INSTITUTUL GEOLOGIC

STUDII TEHNICE ŞI ECONOMICE

SERIA D *Prospecţiuni geofizice* Nr. 10

A XIII-a ADUNARE GENERALĂ A COMISIEI SEISMOLOGICE EUROPENE

(PARTEA A II-a)

Braşov, 28 august — 5 septembrie 1972

BUCUREŞTI
1974

Răspunderea asupra conținutului acestor articole revine în exclusivitate autorilor

INSTITUTUL GEOLOGIC

STUDII TEHNICE ŞI ECONOMICE

SERIA D *Prospecţiuni geofizice* Nr. 10

A XIII-a ADUNARE GENERALĂ A COMISIEI SEISMOLOGICE EUROPENE

(PARTEA A II-a)

Braşov, 28 august — 5 septembrie 1972

BUCUREŞTI
1974

GEOLOGICAL INSTITUTE

TECHNICAL AND ECONOMICAL STUDIES

D SERIES | *Geophysical Prospecting* | No. 10

THE XIIIth GENERAL ASSEMBLY OF THE EUROPEAN SEISMOLOGICAL COMMISSION

(PART II)

Brașov, 28th August — 5th September 1972

BUCHAREST
1974

TABLE OF CONTENTS

INSTRUMENTATION AND DATA PROCESSING

INSTRUMENTS

SUR L'ASTATISATION DES SÉISMOGRAPHES VERTICAUX À RESSORT MAGNÉTIQUE

PAR

EUGEN BERCEI [1]

Les problèmes spéciaux qui apparaissent à l'astatisation des séismographes verticaux ont reçu, au cours du temps, plusieurs solutions. On connaît pour les cas classiques les solutions données par W i e c h e r t, R i c h a r d s o n, W i l i p, L a C o s t e et G r e n e t.

Une synthèse du problème a été faite par A r h a n g h e l s k i i (1960).

Utilisant la manière de A r h a n g h e l s k i i de traîter le problème, on donne, en ce qui suit, les résultats théoriques applicables dans l'astatisation d'un séismographe vertical à ressort magnétique selon l'hypothèse que le ressort magnétique a, dans le domaine d'utilisation, une caractéristique qui peut être considérée linéaire.

Avec référence à figure 1 on usera les notations suivantes :

R_0 — distance du centre de poids du pendule à l'axe d'oscillation,

a — bras de la force F du ressort de compression magnétique,

b — distance entre l'axe d'oscillation et le bout fixe du ressort,

[1] Université de Timişoara, Station Séismologique. Timişoara, Roumanie.

α — angle donné par a avec R_o
β — angle donné par b avec la position d'équilibre,
θ — angle de déviation du pendule avec sa position d'équilibre,
K — moment d'inertie du pendule,
ζ — longueur initiale du ressort,
Z — longueur AB du ressort soumis à la sollicitation envisagée dans figure 1.
Z_0 — longueur du ressort en position d'équilibre
c — rigidité du ressort,
$F = c(\zeta - Z)$ — force du ressort dans ce cas,
T, n — période et fréquance du pendule
$M(\theta)$ — somme des moments extérieurs.

En négligeant les forces dissipatives l'équation du mouvement du pendule est :

$$K \frac{d^2\theta}{dt^2} = M(\theta) \tag{1}$$

Le moment $M(\theta)$ peut être developpé en série Mac Laurin :

$$M(\theta) = M(0) + \theta M'(0) + \frac{\theta^2}{2} M''(0) + \frac{\theta^3}{6} M'''(0) + \dots \tag{2}$$

dans laquelle $M(0) = 0$

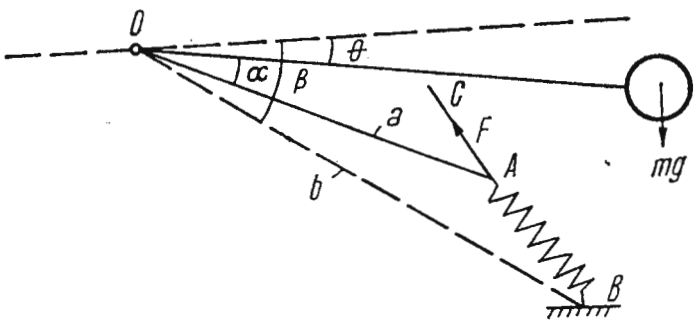

Fig.1. — Ressort magnétique avec caractéristique linéaire.

En négligeant la puissance supérieure de θ l'équation du mouvement devient :

$$\frac{d^2\theta}{dt^2} - \frac{M'(0)}{K}\left(1 + \frac{M''(0)}{2M'(0)}\theta + \frac{M'''(0)}{6M'(0)}\theta^2\right)\theta = 0 \tag{3}$$

D'ici on peut obtenir le période du pendule :

$$T = T_0\left(1 - \frac{M''(0)T_0^2}{8\pi^2K}\theta - \frac{M'''(0)T_0^2}{24\pi^2K}\theta^2\right)^{-\frac{1}{2}} \tag{4}$$

Supposant que $\frac{M''(0)T_0^2}{8\pi^2K}\theta$ et $\frac{M'''(0)T_0^2}{24\pi^2K}\theta^2$ sont suffisament petites nous obtenons :

$$T = T_0 + \frac{M''(0)T_0^2}{16\pi^2K}\theta + \frac{M'''(0)T_0^2}{48\pi^2K}\theta^2 \tag{5}$$

relation qui explique la dépendance de T de T_0, de la déviation angulaire θ et de la position d'équilibre.

Pour éliminer les dissymétries des mouvements propres et la dépendance la période de la grandeur de la déviation angulaire il faut que les expressions en θ et θ^2 de (5) soient négligeables.

Du calcul des trois dérivés de $M(\theta)$ on obtient :

$$M'(0) = -\frac{\zeta a^2b^2c\sin(\beta-\alpha)}{Z_0^3} + abc\left(\frac{\zeta}{Z_0} - 1\right)\cos(\beta-\alpha) \tag{6}$$

$$M''(0) = -M(0) + \frac{3\zeta a^2b^2c\sin(\beta-\alpha)\cos(\beta-\alpha)}{Z_0^3} - \frac{3\zeta a^3b^3c\sin^3(\beta-\alpha)}{Z_0^5} \tag{7}$$

$$M'''(0) = -M'(0) - \frac{3\zeta a^2b^2c\cos 2(\beta-\alpha)}{Z_0^3} + \frac{18\,\xi a^3b^3c\sin^2(\beta-\alpha)\cos(\beta-\alpha)}{Z_0^5} -$$

$$- \frac{15\zeta a^4b^4c\sin^4(\beta-\alpha)}{Z_0^7} \tag{8}$$

Désirant éliminer les dissymetries du mouvement il faudra imposer la condition :

$$M''(0) = 0 \tag{9}$$

D'ici on peut déduire :

$$\cos(\beta-\alpha) = \frac{a}{b} \tag{10}$$

ou

$$\cos(\beta - \alpha) = \frac{b}{a} \tag{11}$$

Prenant pour α la valeur zéro, on déduit que deux variantes de pendules sans boitement sont possibles dans le cas où le ressort occupe la position de cathète dans le triangle OAB.

Le montage le plus avantageux, dans notre cas est donné par la condition (10), pour laquelle on obtient :

$$M'(0) = -a^2c \tag{12}$$

$$M'''(0) = a^2c\left(1 + \frac{3\zeta}{Z_0}\right) \tag{13}$$

$$T_0 = 2\pi\sqrt{\frac{K}{a^2c}} \tag{14}$$

La dernière relation montre que si on désire de grandes périodes, il est avantageux d'avoir un grand moment d'inertie, en même temps qu'un petit lévier a et une petite rigidité du ressort.

La diminuation de la rigidité et le maintien d'une certaine force nécessitée par la construction n'est pas possible dans le cas du ressort hélicoïdal classique.

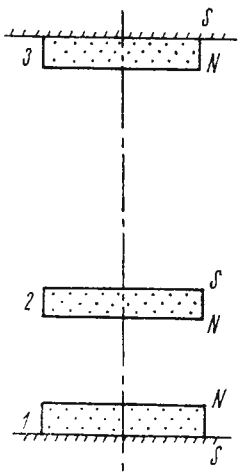

Fig. 2. — Ressort magnétique à trois composantes.

Cela devient possible par l'utilisation d'un ressort magnétique à trois composantes disposées avec les polarités comme en figure 2 dans laquelle les aimants 1 et 3 sont fixes, l'aimant 2 étant le bout mobile du ressort.

Le ressort principal est celui de compression formé par les aimants 1 et 2, l'aimant fixe ayant rôle de "flexuosité".

Les données expérimentales suivantes et les résultats reçus ont été obtenus à l'aide de trois aimants de céramique identiques du point de vue des caractéristiques, la distance entre les composantes fixes 1 et 3 ainsi que le domaine de fonctionnement du ressort choisi étant dicté par des considérations qu'on ne discute pas ici.

Dans le cas du ressort de compression formé par l'aimant fixe 1 et l'aimant mobile 2, la caractéristique expérimentale peut être obtenue en représentant graphiquement des mesurages de la force par rapport à la distance entre les deux aimants.

En considérant ensuite le ressort de traction formé par l'aimant fixe 3 et l'aimant mobile 2 on obtient une caractéristique de la même allure qui peut être considérée comme le reflet de l'allure antérieure par rapport à une droite $x = \text{const}$.

Evidemment, la caractéristique du ressort magnétique à trois composantes peut être obtenue par la composition des deux caractéristiques obtenues, en tenant compte de l'épaisseur de l'aimant mobile.

Dans la partie expérimentale on a tenue compte seulement de la partie de stabilité du ressort à trois composantes.

Les parties qui présentent un intérêt par leurs caractéristiques ont été calculés approximativement par des arcs de parabole cubiques calculés à l'aide du polynôme d'interpolation de Lagrange :

$$P(x) = \sum_{i=0}^{n} y_i \frac{\prod_{\substack{s=i \\ s\neq i}}^{n} (x - x_s)}{\prod_{\substack{s=0 \\ s\neq i}}^{n} (x_i - x_s)} \tag{15}$$

Les résultats obtenue sont des paraboles cubiques :

$$P(x) = -0{,}08533\ x^3 + 5{,}43994\ x^2 - 133{,}86577\ x + 1573{,}99562 \tag{16}$$

pour la partie de la caractéristique de l'arc de compression et

$$Q(x) = -0{,}04266\ x^3 + 5{,}11973\ x^2 - 189{,}72392\ x + 2517{,}88625 \tag{17}$$

pour la partie de la caractéristique de l'arc de traction.

Pour les caractéristiques du ressort à trois composantes on a trouvé l'expression :

$$R(x) = -0{,}12799\ x^3 + 7{,}999\,83\ x^2 - 169{,}99729\ x + 2004{,}29547 \tag{18}$$

En calculant la rigidité dans le cas du ressort à deux composantes et dans le cas du ressort à trois composantes pour une force de 0,8 Kgf, où la caractéristique composée peut être considérée comme linéaire, on obtient une diminuation de la rigidité de presque 3,1 fois, fait qui détermine un accroissement de période de plus de 1,75 fois sans changer aucune des caractéristiques de la construction mécanique des séismographes.

Sauf l'agrandissement de la période par cette voie on propose une astatisation de type ressemblant à celle qui a été proposée par Richardson.

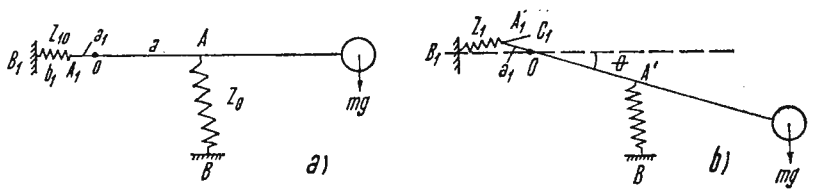

Fig.3. — Ressort de compression : a) Position d'équilibre. b) Déviation angulaire 0.

Pour cela on va introduire un nouveau ressort de compression qui soit monté de telle manière qu'il ait un moment nul en position d'équilibre et qui doit donner des moments contraires à celles données par le ressort d'équilibre, alors qu'une déviation angulaire θ se produit. Un exemple d'un tel montage est donné dans la figure 3, selon laquelle on conduira les raisonnements.

Dans la figure 3a la situation est donnée en position d'équilibre et en figure 3b la situation a une déviation angulaire θ.

Supposons la force F du ressort d'astatisation du même type que la force du ressort d'équilibre

$$F_1 = c_1(\zeta - Z_1) \tag{19}$$

Tenant compte de l'additivité des moments, on peut étudier le moment donné par les ressorts d'astatisation.

À la déviation avec un angle θ on obtient :

$$M_1(\theta) = F_1 a_1 \sin C_1 A_1 O \tag{20}$$

Du triangle OA_1B_1 on obtient :

$$\sin C_1A_1O = \frac{b_1}{Z_1}\sin\theta \tag{21}$$

et tenant compte de (19) :

$$M_1(\theta) = a_1b_1c_1\left(\frac{\zeta_1}{Z_1} - 1\right)\sin\theta \tag{22}$$

En figure 3 on a :

$$Z_1 = \sqrt{a_1^2 + b_1^2 - 2a_1b_1\cos\theta} \tag{23}$$

À l'aide de ces données on peut calculer les premières dérivées de $M_1(\theta)$. On obtiendra :

$$M_1(0) = 0 \tag{24}$$

$$M_1'(0) = a_1b_1c_1\left(\frac{\zeta_1}{b_1 - a_1} - 1\right) \tag{25}$$

$$M_1''(0) = 0 \tag{26}$$

$$M_1'''(0) = -a_1b_1c_1\left(\frac{\zeta_1}{b_1 - a_1} - 1\right) - \frac{3\zeta_1a_1^2b_1^2c_1}{(b_1 - a_1)^3} \tag{27}$$

En même temps avec l'introduction du ressort d'astatisation la fréquence limite du pendule devient :

$$n_0^2 = -\frac{[M'(0) + M_1'(0)]}{K} = \frac{1}{K}\left[a^2c - a_1b_1c_1\left(\frac{\zeta_1}{b_1 - a_1} - 1\right)\right] \tag{28}$$

donc on peut obtenir une période convenable choisissant les léviers des deux ressorts.

On remarque de (26) que l'introduction du ressort d'astatisation ne donne pas de dissymétries de mouvement.

On remarque encore que le terme en θ^2 de (5) peut être considéré comme négligeable.

La solution proposée est facilement réalisable dans le cas d'un ressort de compression et dans la construction les difficultés de la solution Richardson n'apparaîtront pas.

Conclusions : Un séismographe vertical à ressort magnétique peut être astatisé à l'aide des deux solutions combinées exposées ici.

Il est avantageux de réaliser le schéma mécanique donné en figure 3 et qui donne des moments contraires à ceux donnés par le ressort d'équilibre.

BIBLIOGRAPHIE

Arhanghelskii V. T. (1960) Voprosi teorii dliunoperiodnogo vertikalnogo seismometra. *Izv. A. N. SSSR, seria Gheofiz.*, 10, Moskva.

Bercei E., Curea I. (1970) La construction et l'expérimentation d'un séismographe vertical, à courte période, au ressort magnétique. *Annali di Geofisica,* XXIII, 4, Roma.

Sawarenski E. F., Kirnos D. P. (1960) Elemente der Seismologie und Seismometrie. Berlin.

MODERN SEISMOLOGICAL INSTRUMENTS AT MOXA [1]

BY

CHRISTIAN TEUPSER, GERHARD GENSCHEL, ERHARD UNTERREITMEIER[2]

BROAD-BAND SEISMOGRAPHS WITH ULTRA-LONG-PERIOD GALVANOMETER

Continuing our works in long-period seismometry different broad-band frequency responses were tested using a new galvanometer developed by Akademie Werkstätten für Forschungsbedarf. This galvanometer has a period of 330 seconds, a very low air damping of 0.18, and a small inertial moment of 7 g cm^2. The galvanometer is shown in figure 1. Connected with our long-period electromagnetic seismographs the displacement or the velocity of ground motion can be measured in a wide period range (T e u p s e r et al., 1971).

At first two responses have been tested with a maximum magnification of nearly 600 (fig. 2). The response 1 is proportional to the displacement in the range from 10 to 250 seconds. The response 2 is proportional to the velocity in the range from 10 to 330 seconds. Observations with these equipments and with a long-period system of type C(seismometer period 30 s, galvanometer period 90 s) show that in „in scale" records of earthquakes with a magnitude $M<7$ periods longer than 100 seconds cannot be detected by a visual interpretation. But strong earthquakes give periods up to 250 seconds in „out scale" records. Therefore, a low-gain long-period vertical seismograph has been installed with the response 3, which is flat from 2 to 330 seconds. This new equipment with a magnification of 50 gives nearly complete „in scale" records of strong earthquakes at Moxa. Figure 3 shows a record of an earthquake with a magnitude 8.1 occurred at Alëutian Islands July 30 this year. The long-period Rayleigh Waves LR are shown separately in the upper part of the picture. Below

[1] Communication Nr. 300, Central Earth Physics Institute.

[2] Central Earth Physics Institute, AdW der DDR, 69 Jena, Burgweg 11, GDR.

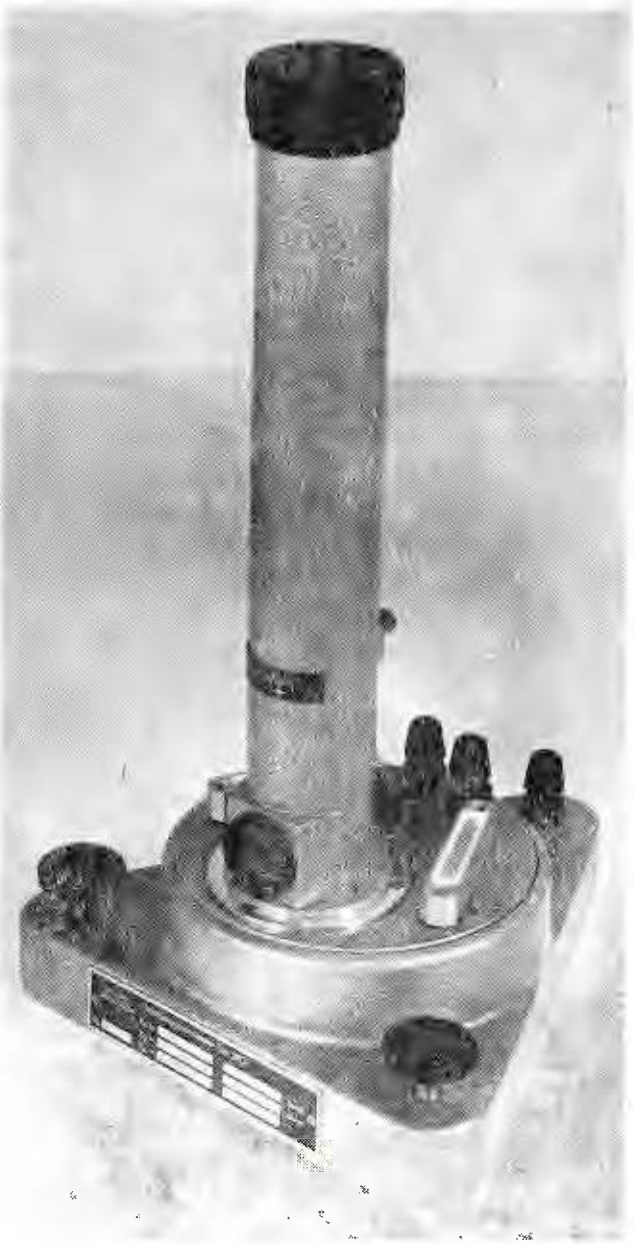

Fig. 1. — Galvanometer SPG—7.

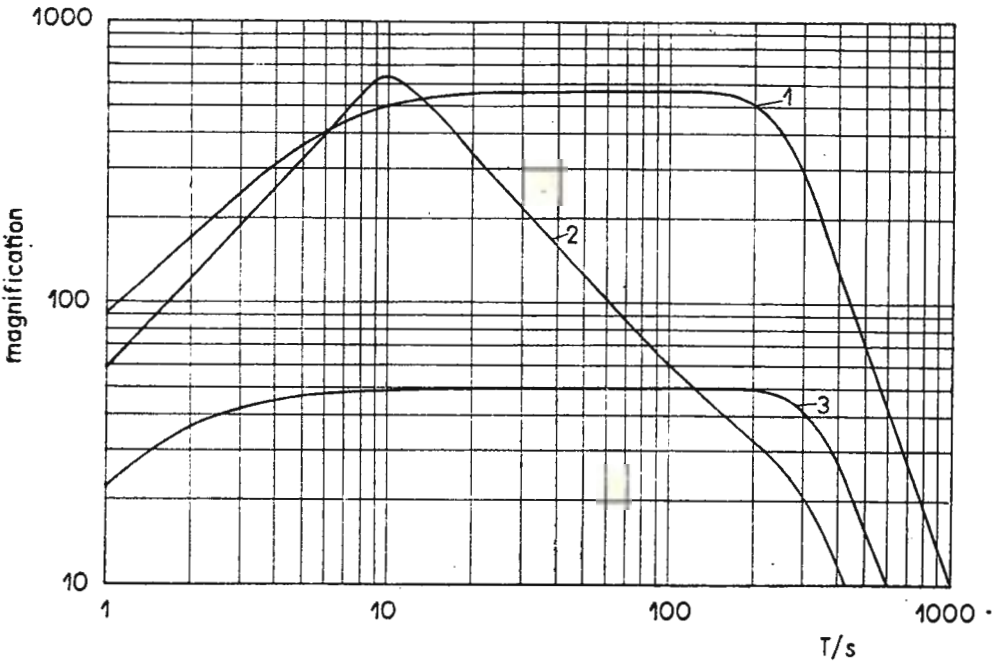

Fig.. 2. — Frequency responses of long-period systems.

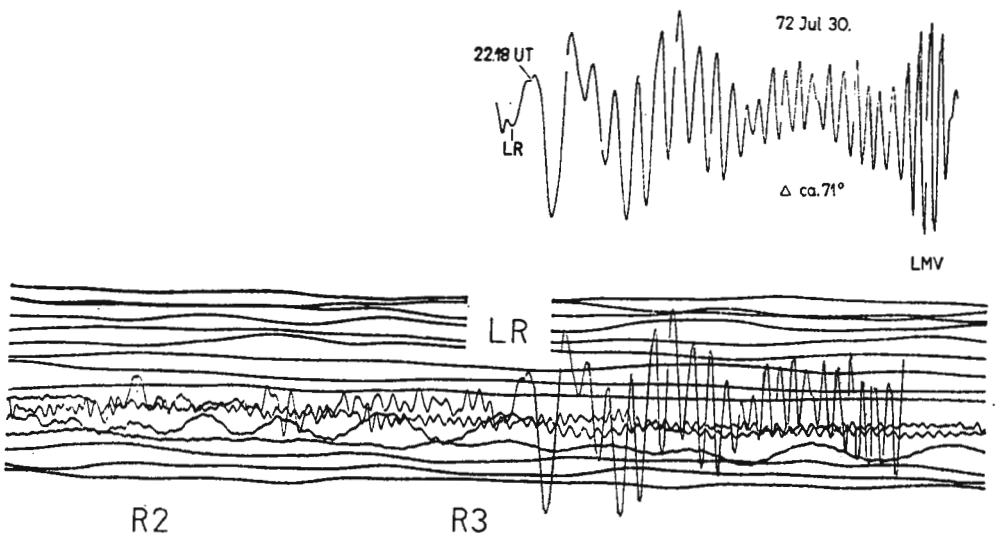

Fig. 3. — Record of Alëutian earthquake 1972 july 30.

the waves R_2 and R_3 with periods of about 3 minutes are to be seen. The LR waves show these long periods, too. The new equipment is good as a standard type for visual interpretation.

AN EVENT-SELECTING SEISMOGRAPH SYSTEM

An event-selecting seismograph system with punched tape record has been developed for digitizing short-period surface waves of earthquakes[3] with magnitudes $M > 6$. Figure 4 gives the block diagram of the system. The output of a seismometer with a period of 20 seconds is amplified for analogue to digital conversion. Using active RC networks the amplifier simulates the parameters of a galvanometer. Bandpass filtering extinguishes d. c. drift and high frequency noise. The output of 1 mV/μm ground displacement is given to a digital voltmeter with a sensitivity of 100 μV

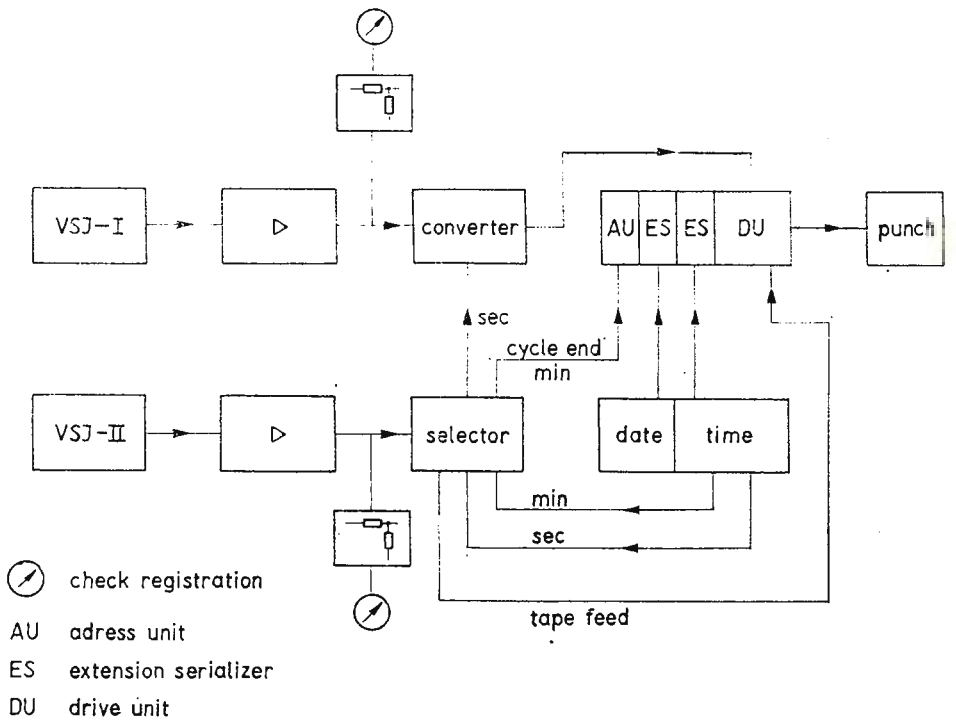

Fig. 4. — Block diagram of the event-selecting system.

[3] Teupser Ch., Unterreitmeier E., Wenk R., Brunner M. An event-selecting seismograph system with digital recording. 1973. *Gerl. Beitr. Geophys.*, 82 (in press).

per unit. An allowed deflection of ± 1 mm of the seismometer boom gives a dynamic range of 80 db. The sampled data are recorded on eight-track strips.

The system shall be triggered by *P*-waves. Therefore, these waves are detected by a short-period vertical seismograph with a period of 1 s. After amplification a ground-displacement of 0.1 μm causes an output voltage of 1 V. An event selector forms the output signal and a threshold switch uses 2 to 5 pulses for starting tape punching. In this way a single pulse does not trigger the system. After triggering the system operates one hour automatically.

A quartz-controlled timing unit gives 1 Hz pulses for sampling. At the beginning and at the first second of each minute a time word is punched. It consists of the day of the year (three figures), GMT (six figures in h, min, s) delivered by the timing system, the date of the year and the number of the measuring point. After operation a sufficient piece of the tape is feeded without punching.

In figure 5 the frequency responses of the registration and the triggering channel are shown in comparison with a standard type B response

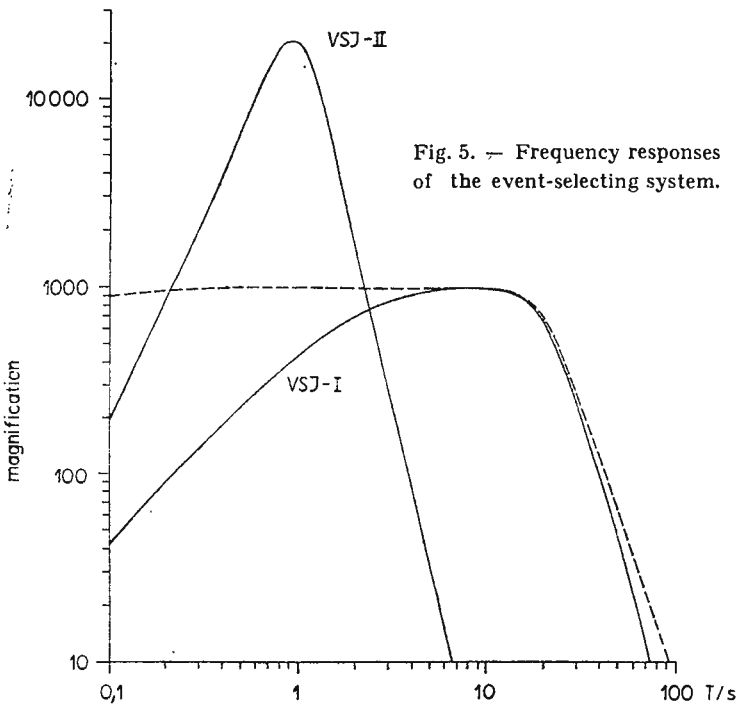

Fig. 5. — Frequency responses of the event-selecting system.

(dashed line). The ordinate gives the magnification of the analogue check registration. Cut-off for periods lower than 2 seconds in the digital registration channel avoids aliasing effects.

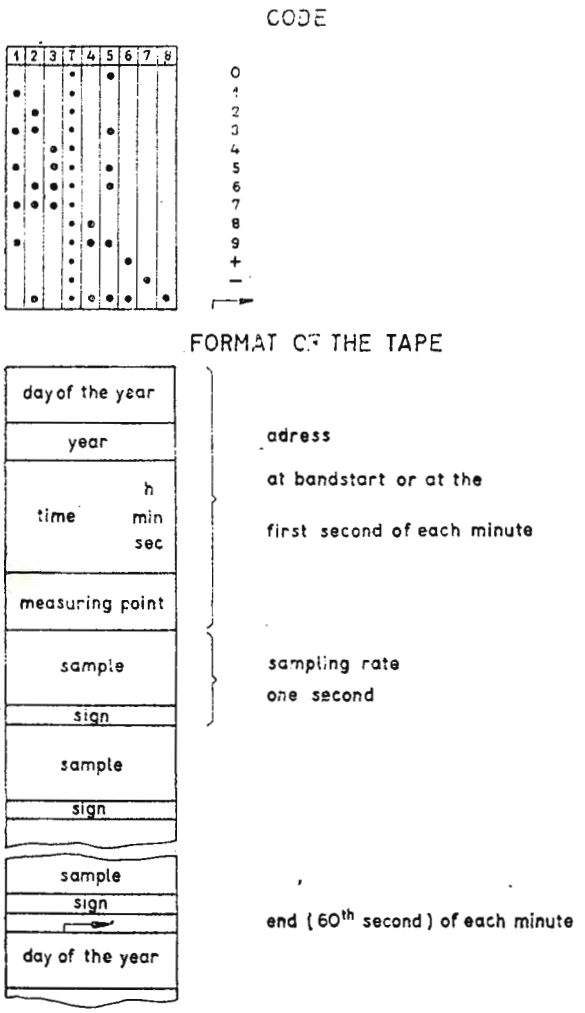

Fig. 6. — Code and tape format of the event-selecting system.

The data are recorded as 4-digit BCD words with the code shown in figure 6. The sign represents the end of the data word and the symbol „carriage returns and a line feed" the end of every minute.

In figure 7 are shown the digital voltmeter, the timing system, the drive unit, the two amplifiers, the event selector, and the paper tape punch.

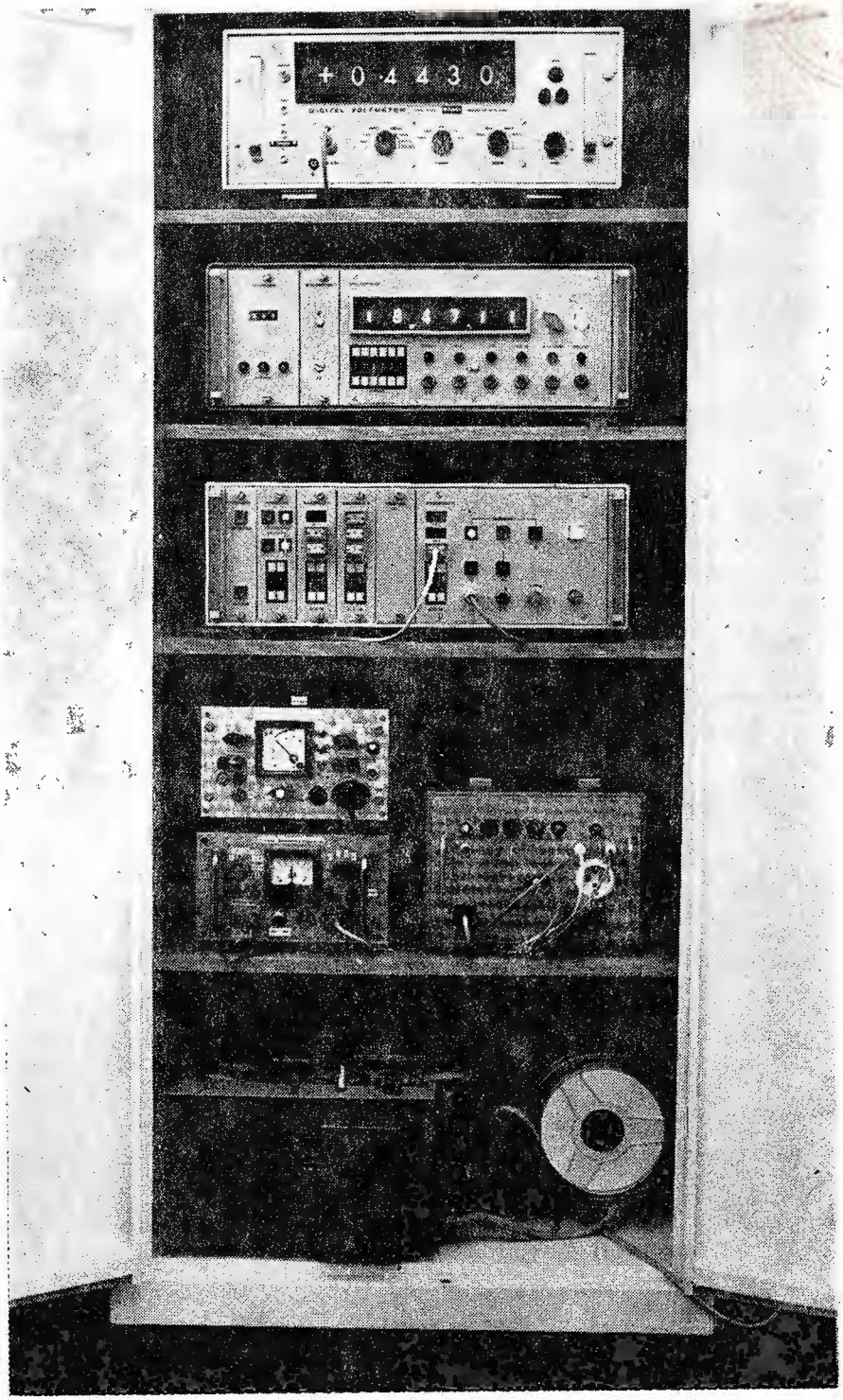

Fig. 7. — The event-selecting system.

THE ELECTRONIC SEISMOGRAPH

In order to minimize drifts in mechanical receivers and to obtain a stable output signal suitable for direct digitization with high accuracy and for telemetering an electronic long-period seismograph has been developed and tested[4]. In the first model a modified vertical seismograph VSJ—I has been used. Figure 8 shows the block diagram of the equipment.

The mechanical receiver is of La-Coste-type with a period of 30 seconds. The two coil and magnet assemblies are used for damping and feedback respectively. The mechanical adjustment of the equilibrium position and the period are carried out at the upper end of the helical spring. The seismic mass M and an isolated plate in a distance of about 1.5 mm from a variable capacitor. Displacements of the seismic mass causes variations of the capacity and a narrow-band frequency modulation of high frequency crystal oscillator. Mixing these modulated frequency with a similar constant one of a second oscillator gives a difference frequency in the low-frequency band from 300 to 3 000 cps. This signal can be used for telemetry with high accuracy. After demodulation the displacements of M give voltage differences ΔU. It follows a high-pass filter and an analogue recording device.

The long-term variations of the equilibrium position of the seismometer boom are reduced by degenerative feedback. A low-pass in the feedback loop decreases the sensitivity against drifts, temperature variations etc.

The output voltage of the demodulator is about 3 mV/μm. Filtering, amplification, and feedback networks are performed by operational amplifiers. The transducer circuit is constructed with silicon transistors. The equivalent input noise is of the order of 10 nm if the seismic mass is clamped. The distortion of the seismometer boom and the vibrations of the helical spring are included in this value. Figure 9 shows the linearity of the transducer assembly. Within ± 1 mm displacement of the capacitor plates the linearity is better than 1% and within $\pm$ 0.5 mm better than 0.4%. The low noise and the high linearity enables registrations with a dynamic range of more than 80 db and the signal-to-noise ratio is better than 20 db.

Earthquakes occuring in different distances were registered at Moxa in 1971. In figure 10 the response of the electronic vertical seismograph

[4] Unterreitmeier E. Zur Erhöhung der Störfreiheit langperiodischer Seismographen. 1973. *Veröff. Zentralinst. Physik der Erde* (in press).

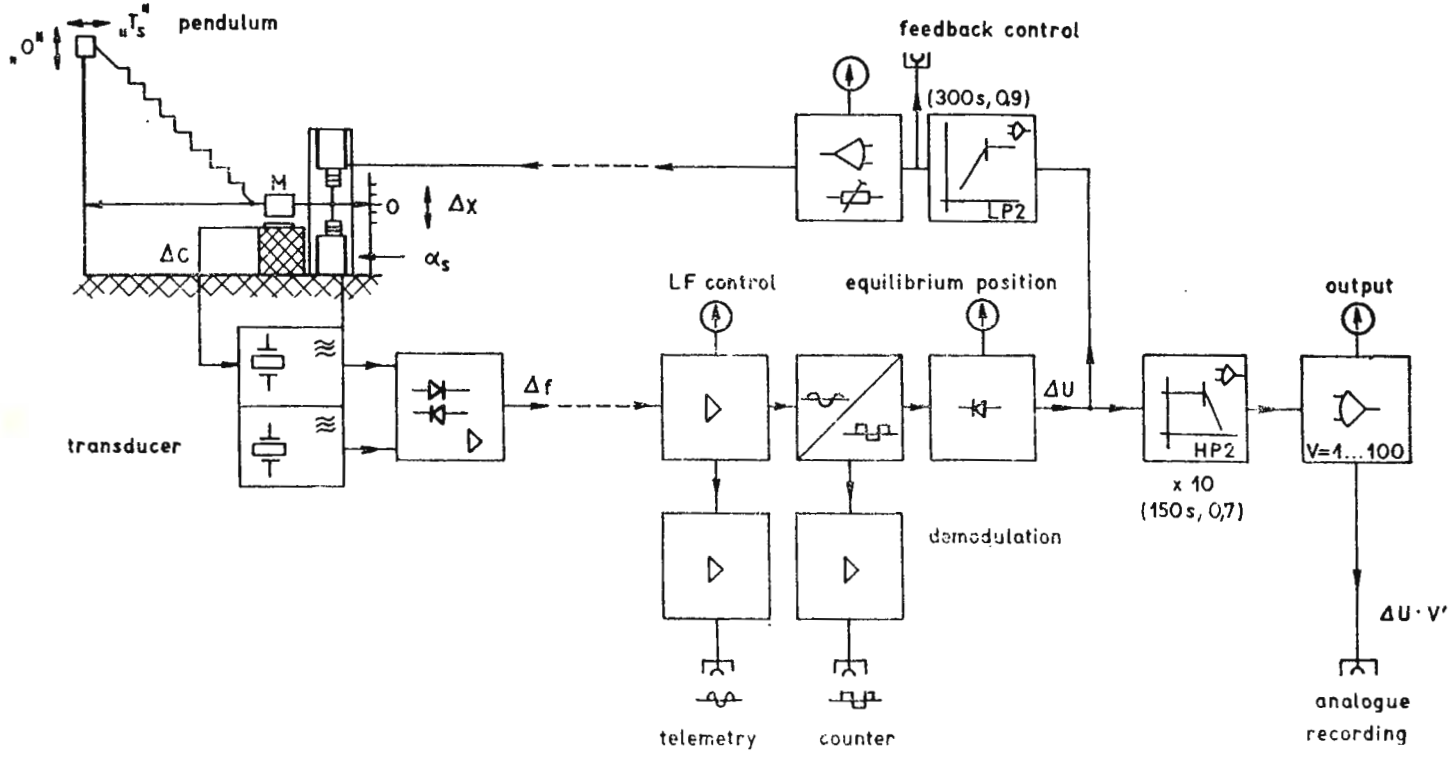

Fig. 8. — Block diagram of the electronic seismograph.

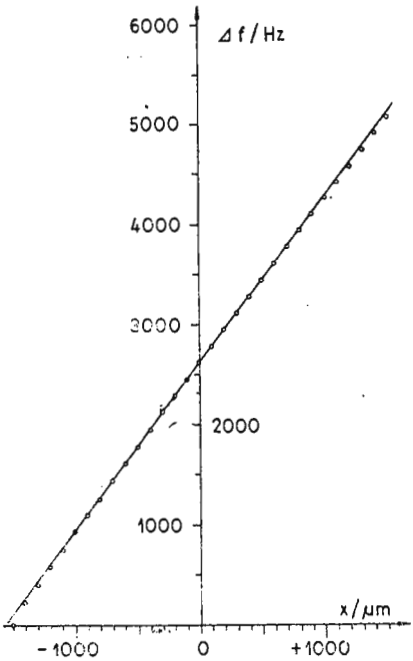

Fig. 9. — Transducer linearity.

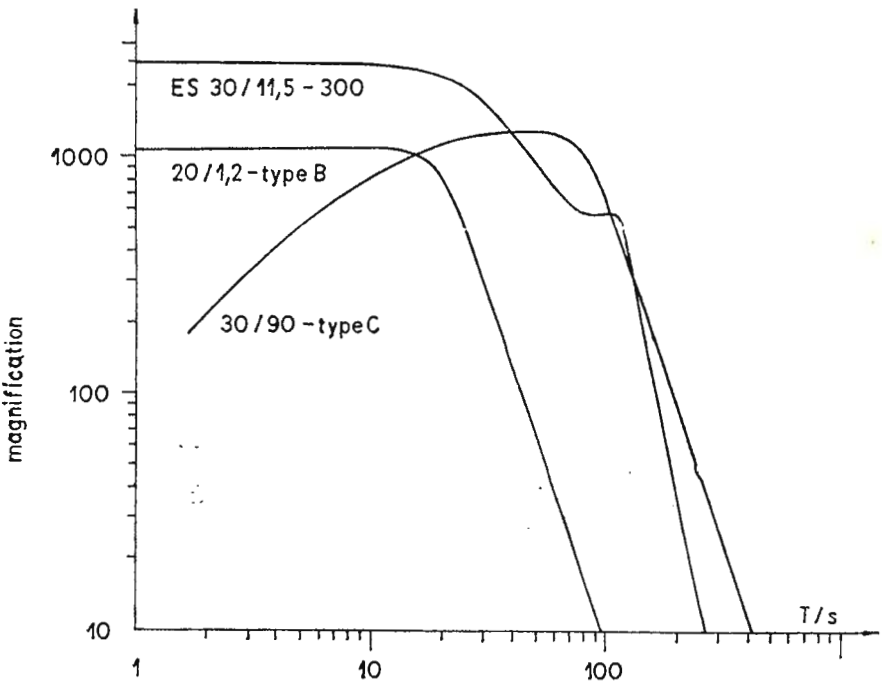

Fig. 10. — Frequency responses of the electronic seismograph and the standard types B and C.

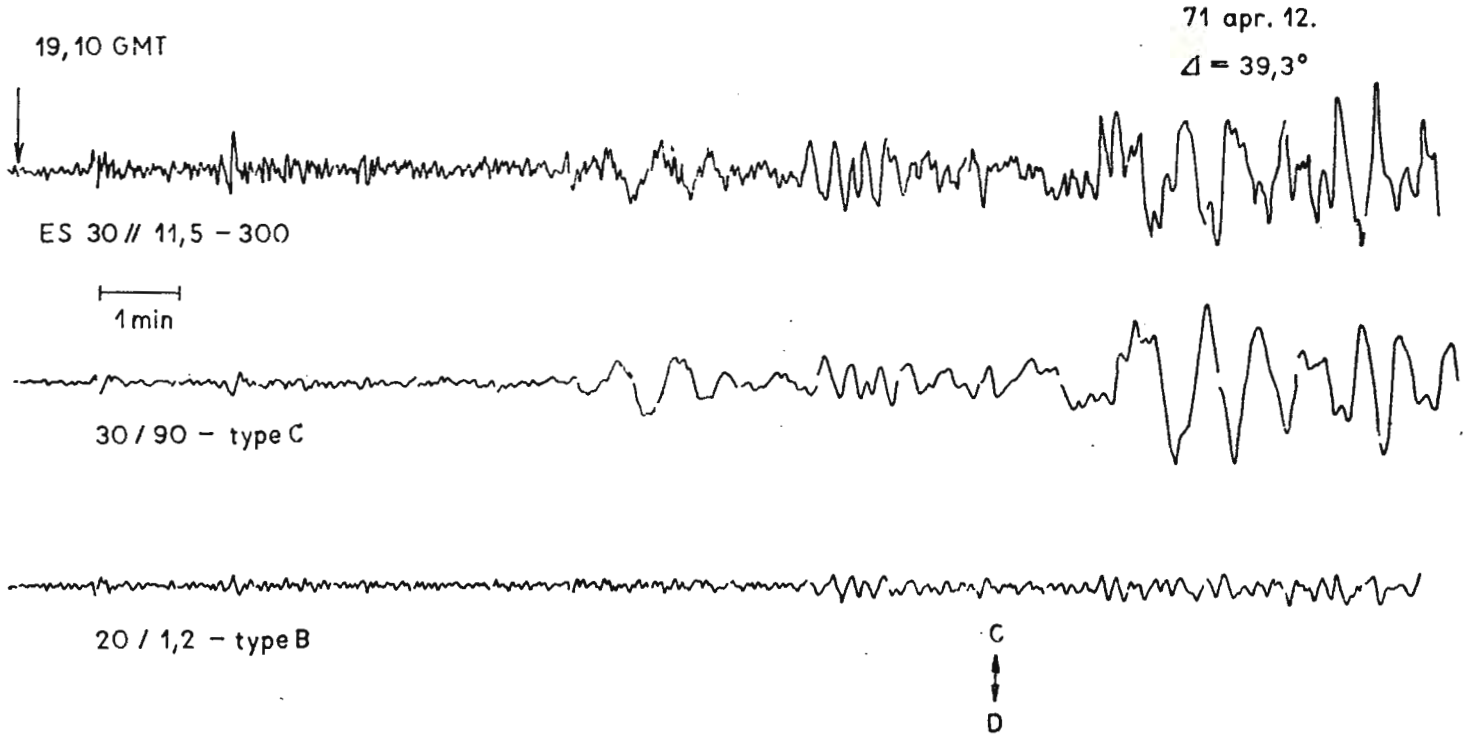

Fig. 11. — Records of Iran earthquake 1971 april 12.

(ES 30/11.5—300) is compared with those of the standard type B and C instruments. The parameters of the electronic seismograph are : the real seismometer period $T_s = 30$ s, the apparent period for long periods $T_s' = 11.5$ s, the corner period of the second-order low-pass filter in the feedback loop $T_T = 300$ s, and the damping constants $\alpha_s = 0.7$ and $\alpha_T = 0.9$.

In figure 11 the records of an Iran earthquake obtained by the electronic seismograph and the standard types B and C are shown. Obviously the record of the electronic seismograph is nearly the sum of the records of the other ones.

The electronic seismograph is applicable for telemetry, direct digitization, visible recording and inverse filtering in order to realize broadband responses up to 300 s.

The authors wish to thank Dr. B o r m a n n for the interpretation of the records of the long-period seismographs and helpful discussions.

REFERENCE

T e u p s e r Ch., G e n s c h e l G., R i b n i t z W. (1971) Langperiodische Seismographen mit 330-s Galvanometer. *Gerl. Beitr. Geophys.*, 80, 6, Leipzig.

NEW PORTABLE SEISMIC EQUIPMENT WITH WIDE-BAND POTENTIALITIES

BY

PATRICK L. WILLMORE[1]

INTRODUCTION

Following some years of experience with magnetic tape equipment, based essentially on the technology of 1960, there has been a growing awareness in the United Kingdom that the state of the art would now permit a substantial step forward in terms of power consumption of the totality of information recorded, packing density on the tape, and of overall system mobility.

These concepts were developed in the UK Atomic Energy Authority, in the Universities of Durham and Reading, in the Institute of Geological Sciences, and by Messrs. Racal-Thermionic and Rank Precision Instruments. The parallel development of strain-meters in the University of Cambridge is being reported separately.

A final stimulus for development arose from a decision of the Natural Environment Research Council of the United Kingdom to establish a pool of recording equipment for the use of universities. In spite of the wide range of technical requirements revealed when the problem was investigated, it appeared that a single new recorder (item 2 below) could meet the whole range of bandwidth envisaged as appropriate for analogue recording, with good prospects of extending to multiplexed digital recording for long-period applications. The areas of application of the various available seismometers and the requirements for ancilliary equipment remain under discussion.

---

[1] Institute of Geological Sciences. Edinburgh, Scotland.

THE „GEOSTORE" RECORD SYSTEM

(RACAL – THERMIONICS)

In considering the available types of recording, the concept of multi-track parallel recording for frequency modulation on slowly moving tape was retained unaltered from the earlier generation of equipment. The basic advantage of this method over systems which multiplex on to a single track of more quickly moving tape is that the desired band width is obtained by means of identical inputs on all channels without requiring frequency transformation or modulators differing in primary frequency.

The concept of radio beams for single channel transmission over distances up to 100 kms has been retained, essentially unaltered, since the last general assembly in Luxembourg but some advance consideration has been given to the possibility of multiplexing three or more components over any given radio link in the expectation that the components would be separated before being recorded.

The comparison between the new „Geostore" and old (T8100) system is as follows:

	T8100		*„Geostore"*	
Number of channels per 25 mm tape width	2×12 interleaved		2×14 interleaved	
Tape speed (mm/s	3.0	2.4	1.2	0.6
Band width (Hz)	10	32	16	8
Running time (hours)	48	170	340	680[2]
Replay facility	No	Yes		
Power consumption (watts)	18	1		
Weight (kg)	55	17		

THE „WILLMORE MARK III" SEISMOMETER

(RANK PRECISION INDUSTRIES)

This new seismometer, like the older „Willmore Mark II" seismometer, is of the moving coil type with suspended magnet 5-spoke constraint and an extra spoke for adjusting the period. The differences from the Mark II instrument are as follows:

a) The magnet has an outer steel tube and a magnetised core with a gap at each end, and there are two coils connected in a hum-bucking con-

[2] Running times for the „Geostore" are obtained by running from one reel to the other in the forward direction, then reversing automatically, switching heads and filling the alternate tracks on the return passage.

figuration. This arrangement reduces the inductive coupling of external A.C. fields into the coil, and also reduces the tendency of external magnetic objects to displace the mass by interacting with the leakage flux.

b) The whole instrument is much smaller than the Mark II and about one quarter of the mass, but the voltage output has been held to a level in excess of 500 V/m/s by increasing the coil impedance to 15 KΩ.

c) Auxilliary coils are wound on the same formers as the main coils so as to permit feedback to be used to modify the characteristics and to permit calibration by the simple injection of electrical current.

d) A new spring system uses triangular leaf springs arranged parallel to the axis of the cylindrical case. These springs are initially formed into a circle. On assembly, they are deformed into vertical planes and attached to the mass. The lower ends of these springs are clamped in levers which pass horizontally across the base of the instrument. The moment caused by straining the springs tends to rotate the levers in such a way as to raise the free ends. The lifting force is transmitted to the mass by thrust acting along the planes of the leaves. This spring system has an internal tendency to compensate for the stiffness of the leaf spring and makes it possible to set the mechanical period to be as long as four seconds.

ULTRA-PORTABLE EQUIPMENT

(UNIVERSITY OF DURHAM)

The University of Durham has developed a small quarter inch tape unit by modifying a high quality, transistorised domestic recorder for recording at low speed on eight tracks. The three channel amplifier, a crystal clock generating modified IRIG code and the tape recorder are produced as three separate elements each one self-powered by dry batteries.

When mounted in a single case, the dimensions of the complete system are approximately 40 × 30 × 30 cms. Total power consumption is 600mw. The internal batteries provide about seven days recording at 2.5 mm/s.

LONG-PERIOD ACCELEROMETER

(UNIVERSITY OF READING AND UK ATOMIC ENERGY AUTHORITY)

A team at University of Reading has been working on the completion of a high-Q medium period system with displacement sensor and feedback control to hold the mass stationary. As a contribution to this system the Atomic Energy Authority are making a La Coste type seism-

ometer with a period of 10 s, a suspended mass of 20 g and $Q = 100$. It is expected that the system will respond to earth accelerations over a range of periods extending from 1—1 000 s.

WIDE-BAND DEVELOPMENTS

(UK ATOMIC ENERGY AUTHORITY)

UKAEA have been conducting experiments on the interchange of characteristics on tape recordings. The original experimental procedure was to use an analogue computer to solve the equations of motion of an actual seismometer to yield true earth motion. A second stage of analogue conversion was then applied to simulate the effect of this ground motion on a second, hypothetical seismometer. This procedure was applied to recordings made from the output of a Willmore Mark II seismometer set to a period of two seconds and to the output of a twenty seconds instrument. Closely comparable recordings were obtained when the simulated seismometer output represented that of a Kirnos-type instrument set to a period of 20 or 30 s, but spurious disturbances appeared on the Willmore derived trace when the response of the simulated instrument was extended to 60 s. Nevertheless, the experiments did demonstrate the interconvertibility of outputs recorded on magnetic tape and went far towards establishing the desirability of wide-band presentation.

Current work by the Authority takes data from a Geotech S11 seismometer using one coil to produce narrow-band long-period recording and a second coil to produce medium-period and short-period output.

GENERAL CONCLUSIONS

Magnetic tape recording has now reached the stage at which complete seismograph systems, having characteristics superior to those realised in the best observatories of a few years ago, can now be packaged into portable units which can easily be set up and maintained in remote locations.

Because the characteristics of these systems are subject to extensive modifications during playback, the conventional calibration parameters (magnification period etc) have lost much of their relevance. It would be better to specify the instrument response in terms of the actual recorded signal (e. g. percentage deviation in F. M. signals, or bits of digital information, per unit of earth motion) and to specify the range of periods for which system noise is below the level of typical earth noise at the point of installation.

Calibration signals of the type needed to provide such information should be recorded on the tape, and can be either single impulses or harmonic wave trains to simulate the system response to known earth movements. A further length of record should be prepared with the seismometer clamped to preserve a sample of instrumental noise. Such calibration signals would survive conversion by processing in advance of final presentation of output, so that the parameters of the original earth motion could always be recovered.

Acknowledgement

This report has been prepared with the support of the Natural Environment Research Council and is published by permission of the Director of the Institute of Geological Sciences of the United Kingdom.

DATA COLLECTING AND PROCESSING

EVENT DETECTION AND LOCATION CAPABILITIES AT NORSAR

BY

HILMAR BUNGUM [1]

Abstract

Data published in the NORSAR seismic bulletin between February and June 1972 has been studied in order to find estimates of the detectability and location accuracy at NORSAR. The detectability is calculated from empirical frequency-magnitude distributions, and the 90% cumulative detectability for the teleseismic zone ($30° < \Delta < 90°$) has been estimated at $m_b = 4.0$, while values for different regions vary from 3.7 to 4.3. These are all NORSAR magnitudes. The magnitude bias between NOAA and NORSAR has been found to be 0.15 ± 0.31 in the teleseismic zone. In this zone, the median location difference between NOAA and NORSAR has been estimated at 160 km, with values for different regions ranging from 130 to 340 km.

INTRODUCTION

The Norwegian Seismic Array came into full operation in the first months of 1971. The array, including the routine data processing, is described in detail by B u n g u m et al. (1971). Figure 1 shows the essential parts of the data processing system at NORSAR. The Detection Processor takes first of all care of the recording of all data on magnetic tapes. Then, the NORSAR SP data is processed in real time in search of seismic events, and a queue of detections is created. Some of these detections are later selected for further analysis by the off-line Event Processor, which

[1] NTNF/NORSAR – Kjeller, Norway.

produces an automatic seismic bulletin. This bulletin is reviewed daily by analysts, and changes are often made before the bulletin can be distributed.

Since 1 May 1971 a reviewed seismic bulletin has been created on a daily basis at NORSAR. This paper is concerned with an evaluation of

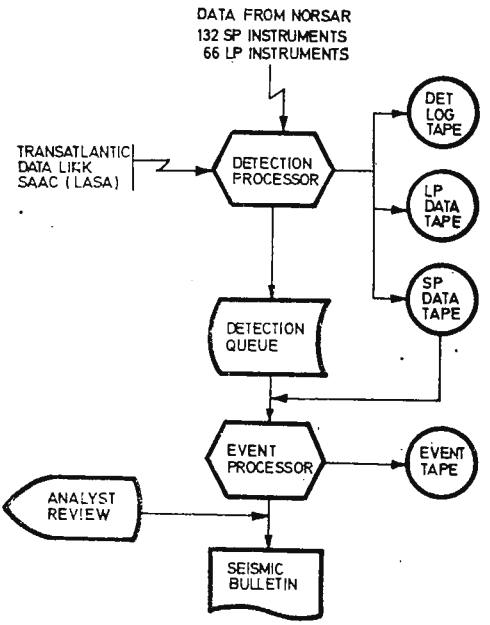

Fig.1. — Schematic view of the NORSAR data processing system.

the data presented in that bulletin, and will be concentrated on the ability of the array to detect and locate seismic events, estimated through a statistical analysis of the data in the seismic bulletin.

DETECTABILITY

Detectability as used in this paper can be defined as the long term operational ability to report, with epicentral information, the occurence of seismic events. The term detectability is therefore used mainly for notational convenience.

Work continues steadily in order to improve the performance of the array. A number of changes have significantly improved both the detectability and the location accuracy. The main changes are :

1) improved analyst performance,

2) a new array beam deployment as of 14 Dec 1971,

3) online filter change from 0.9—3.5 Hz to 1.2—3.2 Hz as of 6 Jan 1972,

4) new time delay and location corrections as of 27 Jan 1972.

The effect of these changes on the detectability can be seen in table 1, which shows the monthly number of events reported by NORSAR for the

TABLE 1

Number of events reported by NORSAR, NOAA and by the two institutions in common

Month	NORSAR	NOAA	Common
1971			
May	230	330	122
Jun	264	277	113
Jul	415	591	184
Aug	320	387	136
Sep	334	359	161
Oct	244	381	150
Nov	154	289	90
Dec	280	368	175
1972			
Jan	283	393	168
Feb	379	393	215
Mar	424	354	187
Apr	605	348	225
May	505	395	163
Jun	470		
Jul	547		
Aug	605		
Sep	742		
Oct	496		

time period May 1971 — October 1972. Also given is the number of events reported by NOAA and the number reported by both institutions. The number of reported events is, of course, also dependent upon other factors, first of all time variations in seismicity and long term variations of the noise level.

One of the aims in the analysis work has been to keep the false alarm rate in the seismic bulletin at a low level. This is not possible unless a large number of true detections are left unreported. Some of these could have been included by devoting more time and effort to the analysis, and some

could probably be confirmed through a study of the bulletins from other networks.

The number of events N above a given magnitude m, within a certain time period, is generally assumed to follow the relationship

$$\text{Log } N = A - b \cdot m$$

both for the entire world and for more limited geographical regions. On this assumption, empirical frequency-magnitude distributions would then make it possible to determine the parameters A and b. Figure 2 shows such a distribution, both incremental and cumulative for the NORSAR teleseismic zone ($30° < \Delta < 90°$). The slope has been estimated by fitting a straight line, in a least squares sense, through the straight part of the cumulative

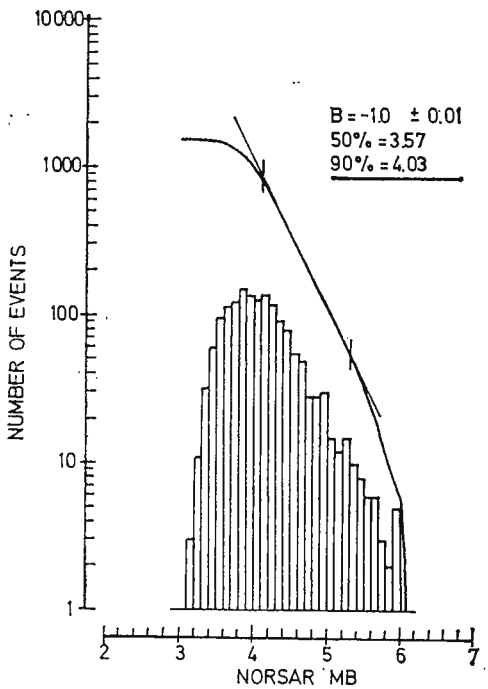

Fig.2. — Interval and cumulative frequency-magnitude distribution for data from Feb-Jun 1972, range 30—90 deg. Straight line is a least squares fit through data within bars.

frequency-magnitude curve. Then, the 50% and 90% levels for detectability are determined, based on computation of the assumed number of missed events at any particular magnitude. As figure 2 shows, the NORSAR teleseismic data from Feb-June 1972 has a slope of $b = 1.00 \pm 0.01$, and the 50% and 90% detectability levels are m_b 3.6 and 4.0 respectively.

It is important to point out that the magnitudes which are quoted above are all NORSAR estimates. In order to facilitate comparisons with other networks, the relation between NORSAR and NOAA magnitudes has also been investigated. Another point worth noticing is that by presenting data from the entire teleseismic zone, one is combining data with possible different statistical distributions. Therefore, all the results are also presented regionalized, where the regions are defined in distance and azimuth from NORSAR, as given in table 2.

TABLE 2

Regionalized results for magnitude thresholds (NORSAR m_b), NOAA/NORSAR magnitude bias and NOAA/NORSAR location differences

Region		Regional limits (deg)		Magnitude threshold			Magnitude bias		Location difference		
No	Name	Azimuth	Distance	Events	50 %	90 %	Events	NOAA-NORSAR	Events	50 %	90 %
A		0–360	30–90	1555	3.6	4.0	848	0.15±0.31	509	160	510
A1	Atlantic	180–260	30–90	88	3.6	4.3	13	0.45±0.28	11	340	780
A2	N. America	260–340	40–90	114	3.8	4.2	100	0.20±0.33	61	260	810
A3	Aleutians	340–15	30–90	131	3.4	3.9	119	0.17±0.35	57	150	370
A4	Japan	15–70	50–90	738	3.7	4.1	441	0.10±0.29	271	130	530
A5	C. Asia	40–110	30–60	211	3.2	3.7	89	0.20±0.34	43	130	270
A6	Iran	110–180	30–90	262	3.5	3.8	39	0.23±0.29	53	180	520

Note: The data for magnitude thresholds is from Feb-June 1972, except for region A1 with data from May 71–June 72. The data for magnitude bias is all fromMay 71–June 72, while the data for location differences is from Feb–May 72.

The regionalized results for the magnitude thresholds are all listed in table 2. As one can see, the 90 % detectability level is $m_b = 4.0$ when all teleseismic data is used, while the values for different regions vary from 3.7 in Central Asia to 4.3 on the Mid-Atlantic Ridge. As mentioned above, this cannot be fully evaluated before the possible magnitude bias between NORSAR and some known reference, say NOAA, has been investigated. Figure 3 shows the NOAA/NORSAR magnitude difference as a function of epicentral distance, where a clear negative bias in the NORSAR data is observed for epicentral distances smaller than 30°. A likely explanation of that bias is the fact that magnitude is measured on the array beam, and more local events have, due to poor coherence across the array, a significant beamforming loss which is not compensated for in the magnitude calculation. As figure 3 shows, the scatter in the magnitude data is quite large.

Table 2, which gives all the detailed results also for the magnitude bias, shows a bias of 0.15 ± 0.31 for all data within 30°—90°, while the different regions have values ranging from 0.10 in Japan to 0.45 on the Mid-Atlantic

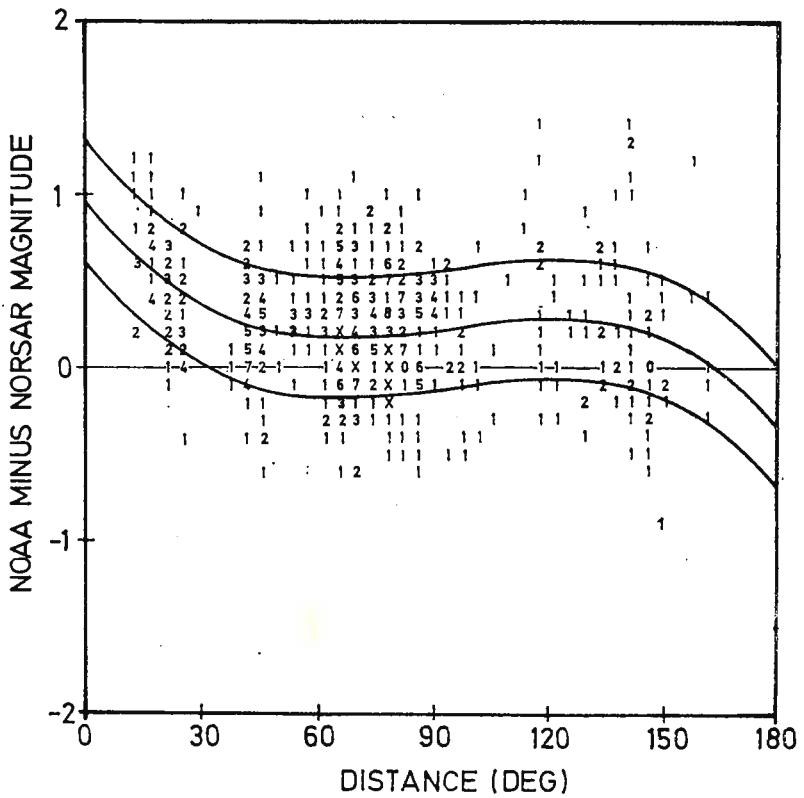

Fig.3. — NOAA/NORSAR magnitude differences vs. epicentral distance for data from May 71—March 72. The curves represent a third degree least squares fit through data, with upper and lower bounds (STD).

Ridge. The scatter in the data is approximately of the same size for all regions.

Now, if one should express the NORSAR magnitude thresholds in terms of some „NOAA equivalent magnitude", one would have to add the bias to the threshold values in table 2. By doing so, one would get a 90 % level of m_b = 4.2 for all data within the teleseismic zone, with values for different regions ranging from 3.9 in Central Asia to 4.7 on the Mid-Atlantic Ridge.

It is important to keep in mind when reading table 2 the special definition of detectability given above. There could easily be a significant difference between the operational and the optimum ability to detect and report events. Another factor of significance is that some of the regions presented in table 2 so far have not very much data. The regional differences are, however, so large that the trends are quite clear.

One should also notice that the data presented herein is mainly from a time of year when the background noise level is moderate. The noisiest time period so far has been October-December 1971, a period which also shows a minimum in the number of reported events (tab. 1). This has been found from an extensive study of the long term short period noise level within the on-line processing frequency band. For the time period January-May 1972, the median noise level within the frequency band 1.2—3.2 Hz has been found to be 1.15 mμ. Some uncertainties apply to the ground motion conversion in this case, while the estimates for the relative variations are more accurate. The 90 % level is 2.0 dB above the median and the 10 % level is 2.7 dB below, and the long term average can be well approximated by a Gaussian distribution (Bungum)[2].

LOCATION DIFFERENCES

The location differences between NORSAR and NOAA have also been studied. Since new location corrections were implemented in January 1972, only four months of data were available for investigation. Figure 4 shows the location differences within the teleseismic zone, incremental and cumulative. From curves like that, the 50 % and 90 % levels of location differences have been found, and the detailed regionalized results are also here given in table 2. The teleseismic zone shows a median location difference of 160 km, while Japan and Central Asia as the best regions have 130 km and North America as the poorest has 340 km. The expression location difference (and not location error) has been used because the comparison is made between two estimates which both are affected by uncertainties. Since the NOAA standard error of location is in the range of 10—40 km, this clearly becomes significant for regions where table 2 shows a location difference of about 130 km, as for Japan.

The regionalized results for the location differences would also here have some uncertainties caused by the limited amount of data. Another

[2] Bungum H. Array Stations as a Tool for Microseismic Research. 1972 (in press).

factor worth mentioning is that the comparison is made only for events above the NOAA reporting threshold, which for some regions is significantly higher than the NORSAR threshold. One should expect that the location error for small events on an average is somewhat larger, but not

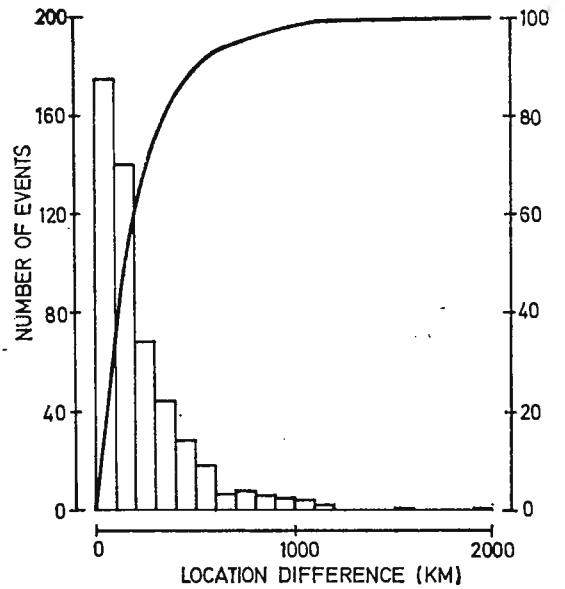

Fig.4. — Interval and cumulative distribution of location differences between NOAA and NORSAR for data from Feb—May 1972, range 39—90 deg.

much, since the error in most cases would still be within the beam radius typically 2—3 degrees.

Acknowledgement

The NORSAR Project has been sponsored by the United States of America under the overall direction of the Advanced Research Projects Agency and the technical management of the Electronic Systems Division, Air Force Systems Command.

REFERENCES

Bungum H., Husebye E. S., Ringdal F. (1971) The NORSAR Array and Preliminary Results of Data Analysis. *Geophys. J. R. Astr. Soc.*, 25, London.

SEISMOLOGICAL APPLICATIONS OF JACOBI POLYNOMIALS

BY

IMRE CSIKÓS[1]

Abstract

For various problems such as the spectral analysis of transient seismic pulses, the Fourier series expansion is generally used. This process requires a lot of numerical work, because transient phenomena must be expanded in a series of steady state functions.

In this article we develop a more efficient approach to expand such transients in a series of functions with properties similar to the transients themselves. Two examples are given to demonstrate the usefulness of the method.

DESCRIPTION OF THE METHOD

A seismic signal $f(t)$ has some properties which we can consider as valid for all of them : if $t = 0$ then $f(t) = 0$ and if $t = \infty$ then $f(t) = 0$. Furthermore we can take into account the different initial conditions which can appear at the observed seismic signals.

We shall examine three sets of functions, each set being characterized by one of the following three sets of properties :

$a)$ if $t = 0$ then $f(t) = \dfrac{df(t)}{dt} = \dfrac{d^2f(t)}{dt^2} = 0$ and *if* $t = \infty$ then $f(t) = 0$

$b)$ if $t = 0$ then $f(t) = \dfrac{df(t)}{dt} = 0$ and if $t = \infty$ then $f(t) = 0$

$c)$ if $t = 0$ then $f(t) = 0$ and if $t = \infty$ then $f(t) = 0$

[1] Royal Netherlands Meteorological Institute. De Bilt, Netherlands.

a) If we approximate the observed seismic signal by a polynomial of the following form :

$$f(t) = a_1 e^{-t} + a_3 e^{-3t} + \ldots + a_{2k+1}\, e^{-(2k+1)t} \tag{2}$$

then the last conditions of equ. (1) are automatically realized. We now write the function $f(t)$ in the following form :

$$f(t) = c_0\Phi_0(t) + c_1\Phi_1(t) + \ldots + c_n\Phi_n(t) \tag{3}$$

where the functions $\Phi_n(t)$ in order to satisfy the conditions of equ. (1a), have the form :

$$\Phi_n(t) = e^{-t}\,(1 - e^{-2t})^3\,(1 + a_{n,1}\, e^{-2t} + a_{n,2}\, e^{-4t} + \ldots + a_{n,n}\, e^{-2nt}) \tag{4}$$

If further

$$\int_0^\infty \Phi_n(t)\,\Phi_m(t)\,\mathrm{d}t = 0 \qquad \text{for } n \neq m \tag{5}$$

then the functions $\Phi_k(t)$ are also orthogonal, which gives us the opportunity to calculate the coefficients c_0, $c_1 \ldots c_n$ of equ. (3) in an easy way.

Let us now write

$$e^{-2t} = x \text{ and } \Phi_n(t) = P_n(x) \tag{6}$$

then equ. (4) is :

$$P_n(x) = \sqrt{x}\,(1 - x)^3(1 + a_{n,1}\, x + a_{n,2}\, x^2 + \ldots + a_{n,n}\, x^n)$$

$$\text{or } P_n(x) = \sqrt{x}\,(1 - x)^3\, S_n(x) \tag{7}$$

$$\text{where } S_n(x) = 1 + a_{n,1}\, x + a_{n,2}\, x^2 + \ldots + a_{n,n}\, x^n$$

According to (6) and (7), equ. (5) takes the following form :

$$\frac{1}{2}\int_0^1 (1 - x)^6\, S_n(x)\, S_m(x)\,\mathrm{d}x = 0 \text{ if } n \neq m \tag{8}$$

and it is satisfied by the polynomials of Jacobi :

$$J_n(\alpha;\gamma;\ x) = 1 + \sum_{k=1}^{n} (-1)^k \left(\frac{n}{k}\right) \frac{(\alpha + n)\,(\alpha + n + 1)\,\ldots\,(\alpha + n + k - 1)}{\gamma(\gamma + 1)\,\ldots\,(\gamma + k - 1)}\, x^k \tag{9}$$

which obey the integral relations :

$$\int_0^1 x^{\gamma-1}\,(1-x)^{\alpha-\gamma} J_n(\alpha;\gamma;x)\,J_m(\alpha;\gamma;x)\,dx = 0 \text{ if } n \neq m \tag{10}$$

$$\int_0^1 x^{\gamma-1}\,(1-x)^{\alpha-\gamma}\,J_n^2(\alpha;\gamma;x)\,dx =$$

$$\frac{\Gamma(\gamma)\,\Gamma(\alpha+1-\gamma)}{\Gamma(\alpha)}\;\frac{(\alpha+1-\gamma)\,(\alpha+2-\gamma)\ldots(\alpha+n-\gamma)}{\alpha(\alpha+1)\ldots(\alpha+n-1)\,(\gamma+1)\ldots(\gamma+n-1)}\;\frac{n!}{\alpha+2n} \tag{11}$$

According to (8) and (10) : $\gamma^{-1} = 0$ and $\alpha - \gamma = 6$ or

$$\alpha = 7\ \gamma = 1, \text{ thus } S_n(x) = J_n(7;1;x)$$

We can deduce now from equ. (9) :

$$S_n(x) = 1 + \sum_{k=1}^{n} (-1)^k \binom{n}{k} \frac{(7+n)\,(8+n)\ldots(6+k+n)}{k!}\,x^k \tag{12}$$

and according to (6) and (7), equ. (4) gets the form :

$$\Phi_n(t) = e^{-t}(1-e^{-2t})^3 \left\{ 1 + \sum_{k=1}^{n} (-1)^k \binom{n}{k} \frac{(7+n)\,(8+n)\ldots(6+k+n)}{k!}\,e^{-2kt} \right\} \tag{13}$$

In accordance with equ. (10) and (11), we must have :

$$\int_0^\infty \Phi_n(t)\;\Phi_m(t)\;dt = \frac{1}{2}\int_0^1 (1-x)^6 S_n(x)\,S_m(x)\,dx = 0$$

$$\int_0^\infty \Phi_n^2(t)\,dt = \frac{1}{2}\int_0^1 (1-x)^6\,S_n^2(x)\,dx = \frac{1}{14+4n} \tag{14}$$

Because the functions $\Phi_0(t)$, $\Phi_1(t) \ldots \Phi_n(t)$ of equ. (3) satisfy the integral relations of (14), the coefficients c_0, $c_1 \ldots c_n$ of (3) can be easily calculated by the equation :

$$c_n = (14+4n)\int_0^\infty f(t)\;\Phi_n(t)\;dt \tag{15}$$

where $f(t)$ is the observed seismic pulse, and $\Phi_n(t)$ is the polynomial, which can be calculated by equ. (13).

We save time in the further calculations, if we are able to deduce a recurrence formula for the polynomials of $S_n(x)$ or $\Phi_n(t)$ of equ. (12) or (13).

Let us suppose for this recurrence formula the following expression :

$$S_n(x) = a\, S_{n-2}(x) + b\, S_{n-1}(x) + c\, x\, S_{n-1}(x) \tag{16}$$

The combination of (12) and (16) gives us the correct form of the formula :

$$n(n+6)(2n+4)\, S_n(x) = -2(n-1)(n+3)(n+5)\, S_{n-2}(x) +$$
$$+ (4n^3 + 30n^2 + 38n - 30) S_{n-1}(x) - (2n+4)(2n+5)(2n+6)x\, S_{n-1}(x) \tag{17}$$

According to equ. (12) the first two polynomials are :

$$S_0 = 1 \text{ and } S_1 = 1 - 8x$$

and equ. (17) gives us the succeeding polynomials :

$$S_2 = 1 - 18x + 45x^2$$
$$S_3 = 1 - 30x + 165x^2 - 220x^3$$
$$S_4 = 1 - 44x + 396x^2 - 1144x^3 + 1001x^4$$
$$S_5 = 1 - 60x + 780x^2 - 3640x^3 + 6825x^4 - 4368x^5$$

. . . .

For the numerical integration of equ. (15) we use Gauss quadrature :

$$c_n = (14 + 4n) \int_0^\infty f(t)\, \Phi_n(t) dt = (14 + 4n) \sum_{i=1}^{N} A_i f(t_i)\, \Phi_n(t_i)$$

$$f(t) = \sum_{n=0}^{N-1} c_n \Phi_n(t) \qquad n = \text{p}, 1, 2, \ldots N-1$$

The sampling points t_i are the zeros of the N^{th} Jacobi polynomial, and the A_i are the Christoffel numbers.

This numerical integration avoids the difficulties that follow from the inaccuracies of the other integration methods and gives the exact value of the Jacobi coefficient for all $n < N$.

We turn back to equ. (1) and write down — without derivations — the polynomials which belong to the initial conditions *b*) and *c*).

b) if $t = 0$ then $f(t) = \dfrac{df(t)}{dt} = 0$ amd $t = \infty$ then $f(t) = 0$

$$f(t) = c_0\Phi_0(t) + c_1\Phi_1(t) + \ldots + c_n\Phi_n(t)$$

where $\Phi_o(t) = e^{-t}\,(1 - e^{-2t})^2$; $\Phi_n(t) = e^{-t}(1+e^{-2t})^2\,(1 + a_1e^{-2t} + \ldots + a_ne^{-2nt})$

$$e^{-2t} = x \quad \Phi_n(t) = P_n(x) = \sqrt{x}\,(1 - x)^2\,S_n(x)$$

$$n(n + 1)\,(n + 4)\,S_n(x) = -\,(n - 1)\,(n + 2)\,(n + 3)S_{n-2}(x)$$

$$+ (2n^3 + 9n^2 + 5n - 6)\,S_{n-1}(x)$$

$$- (n + 1)(2n + 3)(2n + 4)\,xS_{n-1}(x)$$

$$S_0 = 1$$

$$S_1 = 1 - 6x$$

$$S_2 = 1 - 14x + 28x^2$$

$$S_3 = 1 - 24x + 108x^2 - 120x^3$$

$$S_4 = 1 - 36x + 270x^2 - 660x^3 + 495x^4$$

$$S_5 = 1 - 50x + 550x^2 - 2200x^3 + 3755x^4 - 2002x^5$$

.
.
.
.
.

$$c_n = (10 + 4n)\int_0^\infty f(t)\;\Phi_n(t)\;dt$$

c) if $t = 0$ then $f(t) = 0$ and $t = \infty$ then $f(t) = 0$

$$f(t) = c_0\Phi_0(t) + c_1\Phi_1(t) + \ldots + c_n\Phi_n(t)$$

$$\Phi_0 = e^{-t}(1 - e^{-2t});\ \Phi_n(t) = \Phi_0(t)\,(1 + a_1e^{-2t} + a_2e^{-4t} + \ldots + a_ne^{-2nt})$$

$$e^{-2t} = x \quad \Phi_n(t) = P_n(x) = \sqrt{x}\,(1 - x)S_n(x)$$

$$n^2(n + 2)\,S_n(x) = -\,(n - 1)\,(n + 1)^2\,S_{n-2}(x)$$

$$+ (2n^3 + 3n^2 - n - 1)S_{n-1}(x)$$

$$- 2n(n + 1)\,(2n + 1)x\,S_{n-1}(x)$$

$$S_0 = 1$$

$$S_1 = 1 - 4x$$

$$S_2 = 1 - 10x + 15x^2$$

$$S_3 = 1 - 18x + 63x^2 - 56x^3$$

$$S_4 = 1 - 28x + 168x^2 - 336x^3 + 210x^4$$

$$S_4 = 1 - 40x + 360x^2 - 1200x^3 + 1650x^4 - 792x^5$$

.
.
.
.
.

$$c_n = (6 + 4n)\int_0^\infty f(t)\,\Phi_n(t)\mathrm{d}t$$

Examples

Two examples are calculated to demonstrate the efficiency of the method. The first is a known function which has been approximated by 10 polynomials (fig. 1). The full line is the exact function $f(t) = te^{-4t}\sin 2\pi t$, which is of the type b. The crosses are values calculated from an approximation of the function by a series of 10 polynomials.

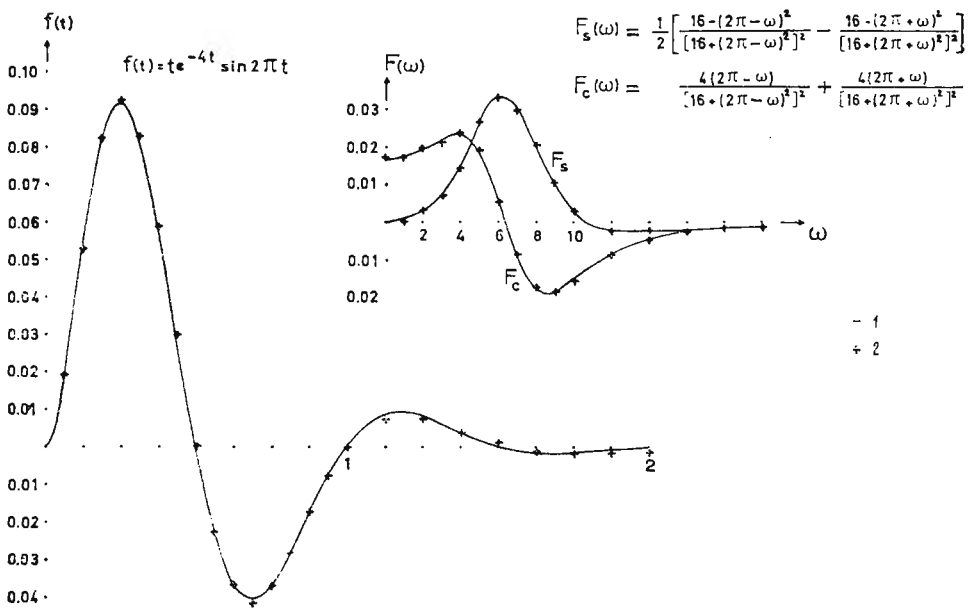

Fig. 1. — The first example :
1, postulated curve; 2, approximations with 10 polynomials.

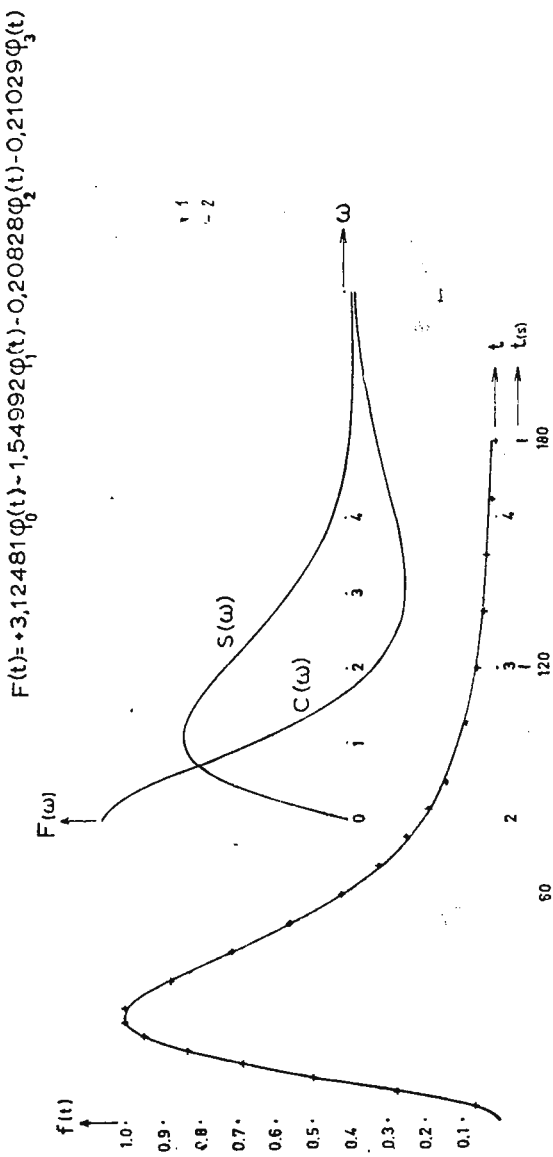

Fig. 2. — The second example :
1. observed values from pulse record; 2. approximations with 4 polynomials

The second example is an observed control pulse as recorded by a Press-Ewing seismograph. The record of this pulse (the curve in fig. 2) has been approximated by 4 polynomials of the type *a*.

In both cases the approximation is very good. For both curves the Fourier integrals are also given.

REFERENCES

Båth M. (1968) Mathematical Aspects of Seismology. Elsevier Publishing Company, Amsterdam — London — New York.

Morse P. M., Feshbach (1953) Methods of Theoretical Physics. McGraw-Hill Book Company, New York — Toronto — London.

SIMULATING ARRAY EVENT LOCATION CAPABILITIES

BY

H. GJØYSTDAL, EYSTEIN S. HUSEBYE, D. RIEBER-MOHN[1]

INTRODUCTION

The large aperture arrays like LASA and NORSAR both detect and locate many events which are left unreported by an organization like NOAA (previously USCGS). We have investigated the event location capabilities of such stations emphasizing the estimate of 95 % confidence ellipses for locations based on data from one or two arrays. The latter restriction is introduced as the LASA and NORSAR arrays have a direct communication link for mutual data exchange. Moreover, we have chosen whenever possible to simulate on the computer the array location process in terms of random and biased errors in the observational data like arrival time, azimuth and velocity of the incoming wavefront.

The purpose of this paper is to present a method for simulating the event location capabilities of one and two arrays. Finally, its usefulness is demonstrated utilizing NORSAR and LASA bulletin data.

ONE-ARRAY EPICENTER LOCATION

Routine processing of events detected by large aperture arrays like LASA and NORSAR comprises calculations of azimuth and apparent velocity of the incoming P-waves. The latter parameter is easily converted to epicentral distance using standard travel time tables. Considering the spherical triangle whose corners are the North Pole, the array center and the event location (fig. 1a), we are now in a position to compute the latitude and longitude of the epicenter using the basic trigonometric equations for spherical triangles. The next step is to obtain a random Gaussian distribution of the parameters azimuth and slowness ($DT/D\Delta$). Specifying

[1] NTNF/NORSAR, N–2007 Kjeller, Norway.

their mean values and variances 200 paired values of these two parameters are simulated by using a random number generation routine. These observations determine a distribution of event locations in geographic space. For computational convenience, we are pointing the array towards a specified point on the equator, i.e., o.o. N and o.o. E. In other words, when

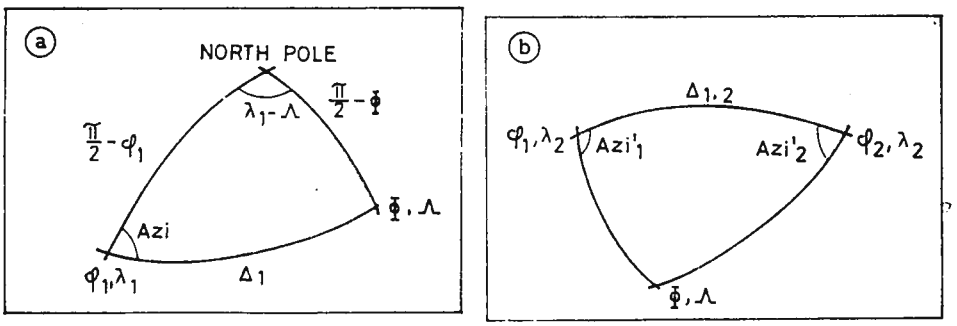

Fig. 1. — Principles for epicenter locations using one and two arrays. In each case at least two sides and angles are known in the given spherical triangles. Array and epicenter coordinates are denoted by (Φ, λ) and (Φ, Λ) respectively. The indices 1 and 2 denote different arrays.

dealing with different epicentral distance intervals, the fictive array may be moved northwards in steps of say 10 deg as actually used. The simulated epicenters are considered in a Carthesian coordinate system, the x and y axes pointing east and north, and the axes of the 95 % confidence ellipse are computed using a method described by E v e r n d e n (1969). These axes would be oriented in the x (azimuth errors) and y (epicentral distance errors) directions, or E—W and N—S, or along and perpendicular to the station azimuth direction.

In table 1 the simulated one-array event location capability in terms of specified standard deviations of the $DT/D\Delta$ and azimuth parameters are tabulated for different distances. The calculated semi-axes of the 95 % confidence ellipses correspond to paired values of the σ $(DT/D\Delta)$ and σ (AZI) parameters, in combinations like $[\sigma(DT/D\Delta) = 0.5$ s/deg, $\sigma(AZI) = 1.0$ deg], etc.

EPICENTER LOCATION USING TWO ARRAYS

In this section the joint epicenter location capability of two arrays is simulated. The analysis is restricted to azimuth and arrival time differences, i.e., the slowness parameter is omitted. The reason is that in most cases the difference in arrival times gives a better distance estimate than that based on slowness measurements. Given the observed azimuth at

TABLE 1
Semi-axes of 95% confidence ellipses in deg.

EPI : DIST. (deg)	$\sigma(DT/D\Delta)$ IN S/DEG							σ (*AZIMUTH*) IN DEG						
	(1) 0.05	(2) 0.10	(3) 0.15	(4) 0.20	(5) 0.25	(6) 0.30	(7) 0.35	(1) 1.0	(2) 1.5	(3) 2.0	(4) 2.5	(5) 3.0	(6) 3.5	(7) 4.0
20	0.3	0.5	0.7	1.0	1.3	1.6	1.8	0.8	1.1	1.6	2.2	2.4	2.9	3.2
30	3.3	5.5	7.4	8.5	10.5	11.5	12.9	1.3	1.7	2.3	3.0	3.5	4.1	5.3
40	2.0	4.0	5.8	7.7	8.6	11.1	12.7	1.5	2.4	2.9	3.9	4.7	5.4	6.4
50	1.8	3.4	4.8	6.6	8.3	10.4	12.1	1.6	3.0	3.6	4.3	5.9	6.6	7.8
60	1.8	3.5	5.8	7.3	8.4	10.7	11.9	2.2	3.0	4.3	5.2	6.7	7.0	9.2
70	1.5	3.2	4.7	6.3	8.3	10.4	12.3	2.4	3.7	4.4	5.8	7.0	7.4	9.4
80	1.7	3.4	4.1	6.3	7.7	8.7	10.8	2.0	3.3	4.6	5.9	6.9	9.1	9.8

Note : Length in degrees of the semi-axes of the 95% confidence ellipses as a function of epicentral distances and standard deviations of observed slowness and azimuth. The given semiaxes are based on paired values of σ ($DT/D\Delta$) and σ (*AZI*).

two different stations we can easily calculate the event position in geographic space as evident from figure 1b. The simulation of the epicenter location process is quite similar to that one discussed in the previous section. As before, we can determine the point distribution in geographic space and then the probability density function which gives the axes and orientation of the 95% confidence ellipse.

When working with body waves it is logical to constrain the above arrival time differences. For a specific event location this parameter defines a curve in geographic space. We may assume that the associated probability density function is represented by a Gaussian surface along the curves of constant arrival time differences which may be considered to be parallel straight lines. Using the notations $f(x, y)$ and $g(x, y)$ for the azimuth and time difference probability distributions, it is possible to determine the epicenter or the point of maximum likelihood by forming the product

$$F(x, y) = f(x, y) \cdot g(x, y)$$

and then differentiating. The above method is described in detail in another paper by the authors (Gjøystdal et al.)[2].

The two-array epicenter location methods are demonstrated in figure 2, using the data simulation approach outlined above. The procedure

[2] Gjøystdal H., Husebye E. S., Rieber — Mohn D. One-array and two-array location capabilities. 1972. (in press).

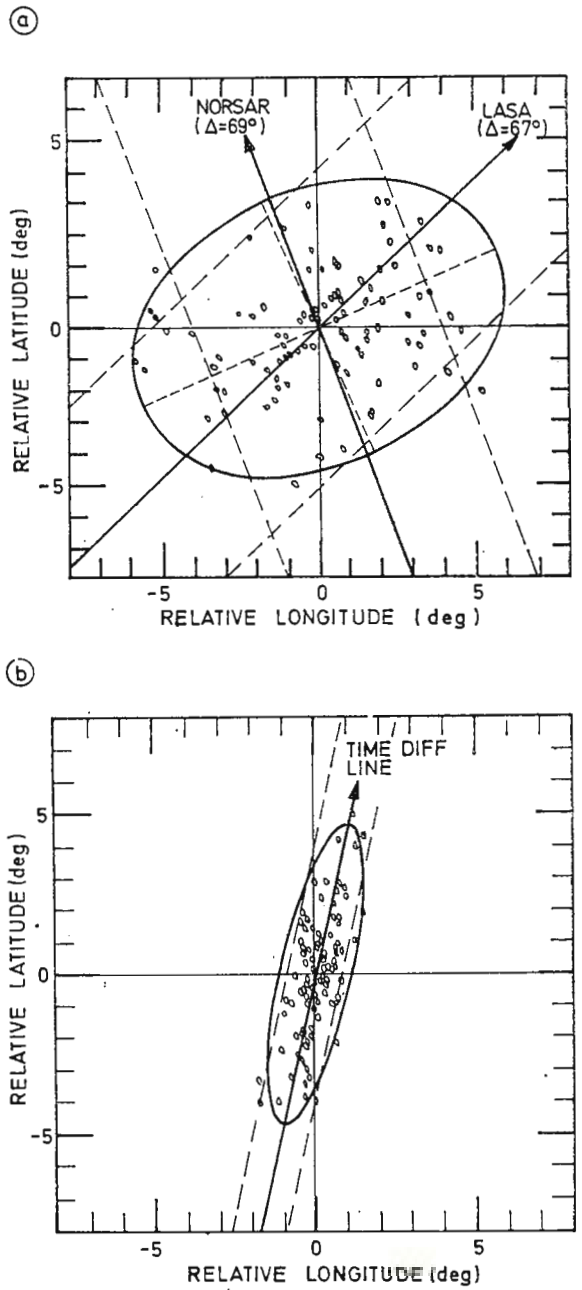

Fig. 2. — Simulated two-array event locations at 45.3°N, 149.3° E. The standard deviations of both azimuth observations are 2.0 deg, and those of arrival times 2.0 s.

will be especially effective in case the confidence ellipse has a considerable eccentricity and the time difference line is nearly parallel to the shortest axis, e. g., when the two azimuth lines intersect under a very sharp angle.

A small test of the joint location capabilities of the NORSAR and LASA arrays has been performed, using a number of the Kurile Islands events which are listed in table 2. The results are displayed figure 3

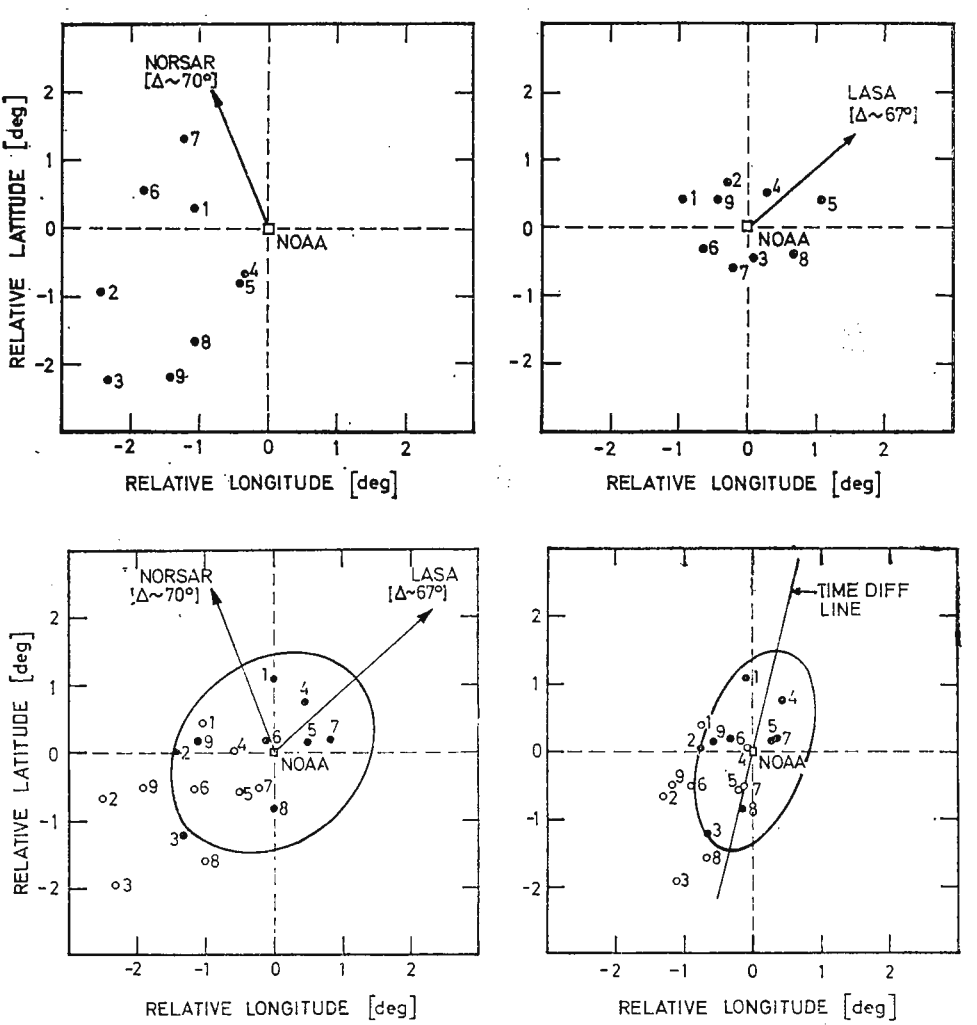

Fig. 3.—NORSAR and LASA epicenter locations for 9 earthquakes in the Kurile Islands region compared to those of NOAA. A biased error in azimut of 1.0 deg seems to occur in NORSAR data. The open and closed rings indicate biased and unbiased observations. The given 95 % confidence ellipses are based on standard deviations of 0.5 deg in azimuths and 2.0 s in arrival times.

TABLE 2

The NOAA focal parameters for earthquakes in the Kurile Islands used in analysis (fig. 3)

NO.	DATE m/d/y	O. TIME h/m/s	$T_N - T_L$ s	MAG m_b	D km	NOAA		LASA		NORSAR		AZIMUTH		AZI. & TIME	
						lat	long	lat	long	lat	long	lat	long	lat	long
1	06/06/71	10/38/05	252.5	4.1	35	8.6 N	79.3 W	10 N	78 W	10.7 N	76.1 W	8.8 N	77.3 W	10.2 N	78.2 W
2	06/12/71	19/18/48	162.0	5.0	43	18.9 N	64.3 W	19 N	65 W	22.8 N	63.4 W	19 .7 N	65.6 W	19.3 N	64.5 W
3	07/08/71	05/54/12	194.0	5.0	48	19.1 N	68.0 W	18 N	69 W	23.2 N	67.1 W	19.2 N	69.9 W	18.5 N	68.8 W
4	08/27/71	06/37/53	193.1	4.7	33	19.2 N	68.1 W	18 N	69 W	23.2 N	67.2 W	19.2 N	69.9 W	18.5 N	68.7 W
5	09/13/71	09/00/26	203.4	4.7	44	6.9 N	71.8 W	7 N	72 W	6.4 N	72.7 W	7.4 N	72.2 W	7.2 N	72.5 W
6	09/21/71	20/31/09	208.5	4.8	150	6.8 N	73.1 W	6 N	73 W	7.7 N	72.5 W	6.6 N	73.3 W	6.3 N	73.1 W
7	09/30/71	20/27/58	161.2	4.9	152	18.1 N	64.5 W	17 N	65 W	20.0 N	63.9 W	17.7 N	65.5 W	17.2 N	64.7 W
8	11/15/71	00/02/09	208.7	4.8	164	6.8 N	73.1 W	6 N	72 W	8.6 N	71.3 W	6.9 N	72.4 W	7.2 N	72.7 W
9	11/22/71	04/55/00	202.9	4.8	36	8.8 N	71.2 W	8 N	72 W	10.4 N	69.1 W	6.9 N	71.3 W	7.4 N	71.7 W
10	11/25/71	11/12/25	209.7	5.1	159	6.8 N	73.0 W	6 N	73 W	8.9 N	71.0 W	5.9 N	72.9 W	6.2 N	73.2 W
11	12/23/71	00/08/50	132.2	4.8	16	14.6 N	60.9 W	14 N	61 W	17.8 N	58.9 W	14.3 N	61.1 W	14.2 N	61.0 W
12	12/23/71	13/17/08	135.0	4.7	170	15.1 N	61.4 W	13 N	61 W	14.2 N	62.4 W	14.6 N	62.3 W	14.2 N	61.6 W
13	12/30/71	05/00/13	226.7	4.9	43	5.6 N	77.7 W	6 N	74 W	6.4 N	78.0 W	10.0 N	76.2 W	9.0 N	75.4 W
14	01/03/72	07/25/23	143.3	5.0	67	10.7 N	62.7 W	11 N	62 W	12.7 N	60.6 W	10.9 N	61.8 W	11.2 N	62.4 W
15	01/20/72	16/31/47	239.3	4.5	82	6.7 N	75.6 W	7 N	74 W	9.0 N	73.6 W	7.8 N	74.4 W	9.8 N	76.0 W

Note: The event locations given in the LASA and NORSAR bulletins are included, and also the epicenter solutions based on two-array azimuth and azimuth and arrival time observations. The LASA and NORSAR azimuth values used were computed from respective one-array locations while arrival time differences are listed in the $T_N - T_L$ the column.

and a few comments are as follows : Due to its larger aperture LASA is expected to have in general a better location performance than NORSAR and this is valid for the events analyzed. The preliminary location distribution vectors in use at NORSAR seem to be troubled by small systematic errors, and a bias correction of 1 deg in the azimuth estimate was introduced for the Kurile Islands event. Even better epicenter locations should be obtainable if absolute travel time corrections for the two arrays were available. Another factor of some importance is the shape of the azimuth confidence ellipse as the intersection between this and the line of constant time difference determines the final solution. Unfortunately, estimates of azimuth variances for LASA and NORSAR were not available.

BIASED OBSERVATIONAL ERRORS

Heterogeneous structures in the site and source regions may cause systematic delays in the *P*-wave travel times across an array, and henceforth biased errors in the estimated azimuth and slowness of the incoming wavefronts. From our point of view the most interesting aspect of the above problem is how large the biased errors could be and whether source or site structural anomalies dominate. In order to investigate the above problem, a reasonable approach may be as follows : The first step is to establish a model for time anomalies for the individual subarrays, which are representative for structural inhomogeneities in the array site area. The next one would be to locate a number of events using both observed and simulated data. In the latter case, the subarray arrival times would be predicted from NOAA epicenter solutions, H e r r i n' s tables (1968) and the above time anomalies for the siting area.

The method outlined above has been tested on data from the NORSAR array. Altogether 126 events recorded during interim NORSAR operation (Plan D) Jan-Jun 1970 were analyzed. At this time only 18 subarray center seismometers were operative (fig. 4) and the high-quality *P*-signals used were in each case clearly visible on at least 14 out of the total of 18 sensor traces. The station corrections on the subarray level were computed in the ordinary way, i.e., taking the average of the difference between observed and predicted arrival times across the array. The resulting one-dimensional model for the subarray station time delays for NORSAR is shown in figure 4 and is considered acceptable as a first order

approximation for simulating biased location errors. In the latter case, the obtained results are shown in figure 5 where the mislocation vectors are split into epicentral distance, independent azimuth and velocity bias

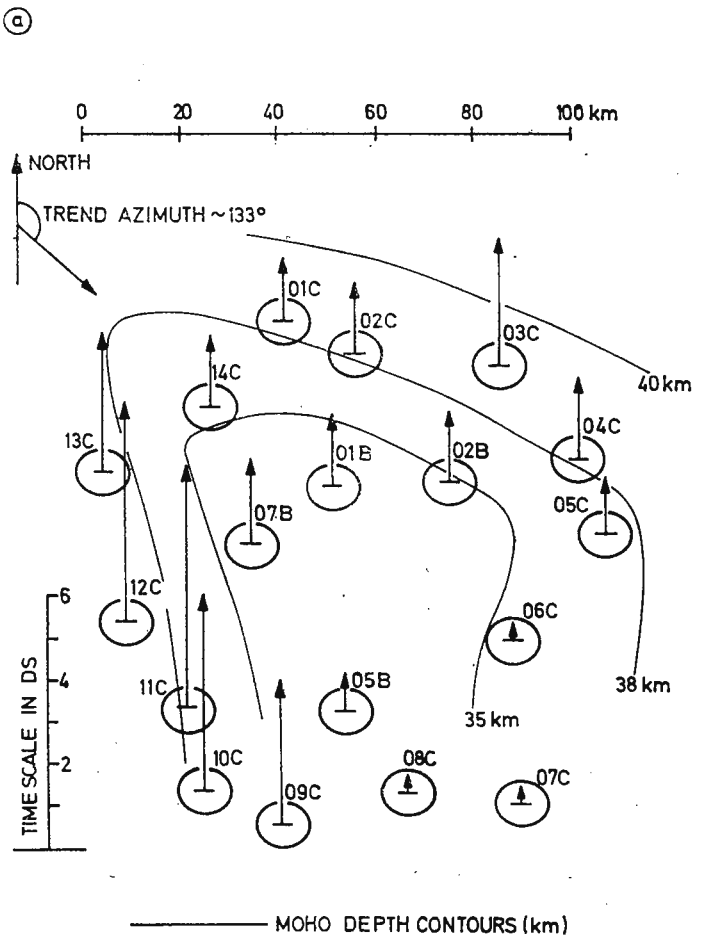

Fig. 4. Observed time delays plotted as a function of NORSAR subarray configuration. The MOHO depth contours are taken from a paper by K a n e s t r ø m , H a u g l a n d (1971).

components. For computational details we again refer to G j ø y s t d a l et al .[3]

The result presented in figure 5 exhibits several interesting features. First of all, structural anomalies in the siting area account for around 45 per

[3] *Op. cit.*, p. 2

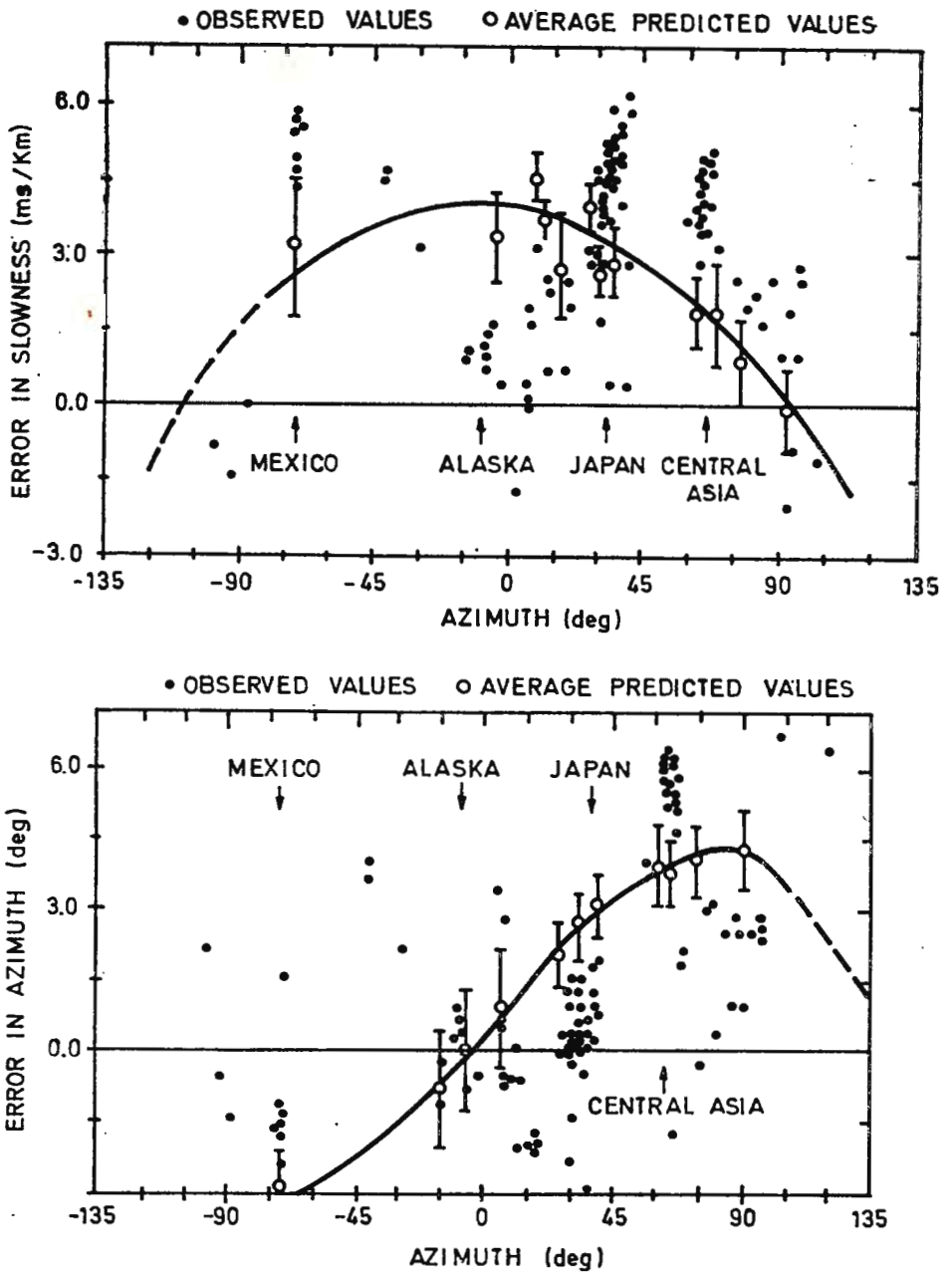

Fig. 5. Observed and simulated biased observational errors in slowness and azimuth for the NORSAR array.

cent of the bias in P-wave slowness, but no improvement is seen in the azimuth values. Moreover, the absolute values of the azimuth and slowness anomalies and also their gradients are relatively large, especially in view of NORSAR's array diameter of around 110 km. In practice, this means that in order to avoid excessive errors in event locations based on a single array like NORSAR, extensive calibration files are part of its software system. However, for epicentral distances beyond 85 degrees and including most of the core shadow zone, where the gradients of the slowness curves are small, large mislocations are likely to occur, unless secondary arrivals, seismicity or exernal information are available.

Acknowledgements

Mr. K. A. Berteussen assisted in the subarray time delay measurements, and his help is greatly appreciated.

The NORSAR research project has been sponsored by the United States of America under the overall direction of the Advanced Research Projects Agency and the technical management of the Electronic System Division, Air Force Systems Command, through Contract No. FI9628—70—C—0283 with the Royal Norwegian Council for Scientific and Industrial Research.

REFERENCES

Evernden J. F. (1969) Precision of epicenters obtained by small numbers of world-wide stations. *Bull Seism. Soc. Am.*, 59, Berkeley.

Herrin E. et al. (1968) Seismological tables for P phases. *Bull. Seism. Soc. Am.*, 58, Berkeley.

Kanestrøm R., Haugland K. (1971) Crustal structure in southeastern Norway from seismic refraction measurements. Sci. Rep. No. 5, Seismological Observatory, Univ. of Bergen, Norway.

PROBLEMS OF RECORDING AND ANALYSIS OF RAPID TILTS ACCOMPANYING EARTHQUAKES

BY

JOSEF HORDEJUK[1]

The possibility of recording rapid changes of ground tilt by means of seismographic equipment was noted by A h o r n e r and V a n G i l s (1963). Analysing a nontypical recording (fig. 1) obtained at the Uccle and Bernsberg stations with Golitsyn seismographs they came to the conclusion that it represents a record of ground tilt. An analogous pheno-

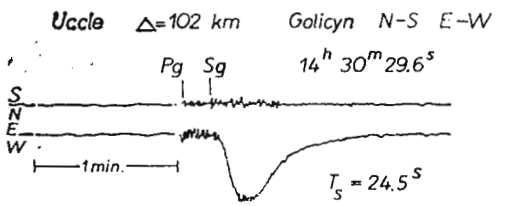

Fig. 1. — Nontypical recording with Golitsyn seismographs at the Uccle and Bernsberg stations.

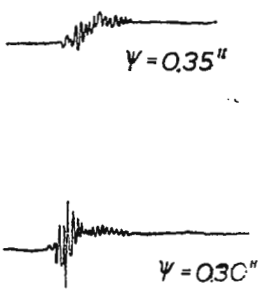

Fig. 2. — Shock recordings with mechanical Mainka-type seismographs from Upper Silezia

menon was observed by T e i s s e y r e and S o b o l e w s k a (1965) on the recordings of shocks from Upper Silesia obtained with Mainka-type mechanical seismographs (fig. 2). Up to now, the problem of occurrence of rapid changes of ground tilt, which accompany earthquakes in

[1] Institute of Geophysics, Polish Academy of Sciences, 3, Pasteur Str., Warsz awa, Poland.

epicentral regions, has not been much investigated. One of the reasons is that such records are usually misinterpreted, being trated as distortions introduced by the instrument, since their shape resembles free oscillations of a seismograph pendulum produced by a short pulse.

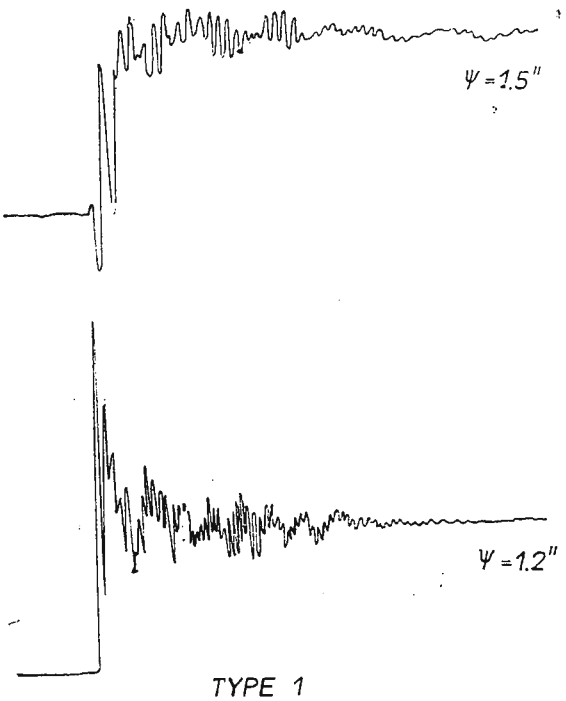

Fig. 3. — Recording of the step-like ground tilt type (type 1).

The above-mentioned characteristic recordings were commonly observed at the Upper Silesian stations equipped with short-period electrodynamical seismographs, as well as in the mining exploitation regions with the occurrence of rockbursts.

Similar phenomena were also recorded by means of Mainka-type mechanical seismographs. The detailed examination of the seismographic equipment and the statistic of occurrence of such phenomena on several stations excluded the possibility that the recordings represent distortions produced by the equipment itself.

An analysis of recordings obtained by means of seismographs with mechanical recorders made it possible to determine two types of the ground tilt. Figure 3 shows the recording of the first, step-like type; the seismic

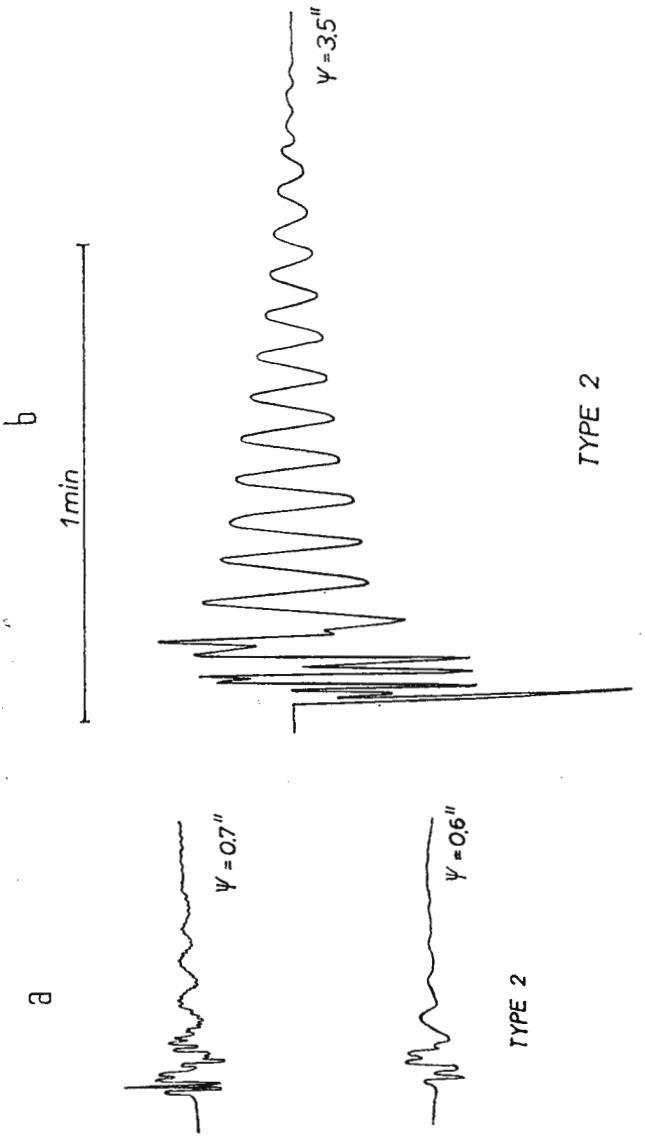

Fig. 4. — Recording of the pulse-like ground tilt type (type 2).

waves produced by the shock accompanying the tilt formation are superimposed on it. Figure 4 shows the recording of the second, pulse-like type, also accompanied by the seismic waves produced by the shock.

To describe the above-mentioned tilt types we analysed theoretically the recordings of which can be obtained by seismographs with mechanical recorders. We assumed that the tilts are described by the formula

$$\psi = \psi_0 \left[1 - e^{-\frac{t}{\tau}}\right] \qquad t \geqslant 0 \tag{1}$$

in the case of the so-called type 1, and

$$\psi = \psi_0 \left(\frac{\pi}{\tau}\right) \sin \left(\frac{\pi}{\tau} t\right) \qquad 0 \leqslant t \leqslant \tau$$

$$\psi = 0 \qquad t > \tau \tag{2}$$

in the case of the so-called type 2.

Figures 5, 6, 7 and 8 present the pattern of theoretical tilt records of type 1 in a nondimensional form. The following notation is used : $u = 2\tau/T_1$, $\xi = 2\pi t/T_1$. The curves were calculated for the attenuation of the seismograph pendulum $D_1 = 0.2$, and for four values of parameter $u = 0.4$; $u = 0.2$; $u = 0.04$ and $u = 0$.

Figures 9, 10, 11 and 12 present theoretical tilt records of type 2, for $u = 1$; $u = 0.4$; $u = 0.2$; $u = 0$ respectively, and for $D_1 = 0.2$.

The consistence of the theoretical and experimental curves is striking.

Apart from the above, we have analysed the theoretical records of substratum tilts of both types, which can be obtained by instruments with galvanometric recorders. Figure 13 and 14 present such records for jumps of a tilt of type 1 and 2, respectively. In both cases it was assumed for simplicity that $\tau = 0$. The parameters of the instrument were adopted as follows : $T_1 = 1.46$ s, $T_2 = 0.42$ s, $D_1 = 0.58$ s, $D_2 = 3{,}75$, $\sigma^2 = 0.07$, and $V_0 = 12000$. From the character of a record one can easily determine the tilt type as well as its magnitude in seconds of arc. Our considerations are illustrated by a recording of a tilt of type 1 (Fig. 15) and two recordings of type 2.

The mechanism of the tilts described above can be explained by an abrupt displacement of rock masses which takes place in a seismic focus region. Such displacement causes changes in the level of the surface and the release of elastic energy. Figure 16 shows the manner in which such

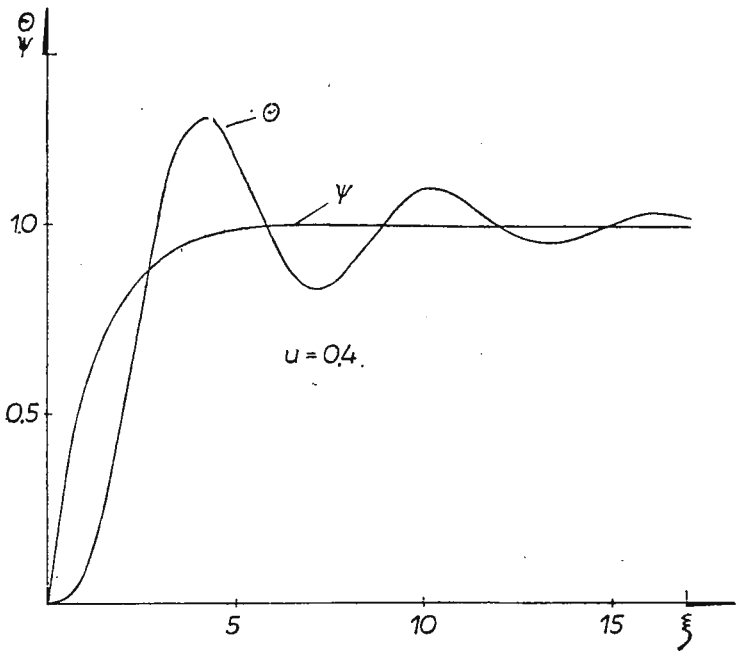

Fig. 5. — Theoretical tilt records of step-like type (type 1), with $u = 0.4$.

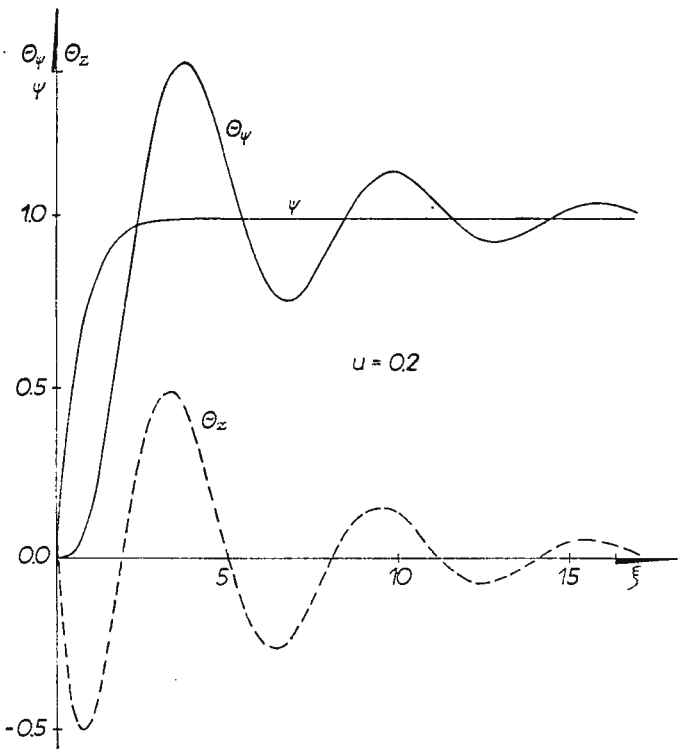

Fig. 6. — Theoretical tilt records of step-like type (type 1), with $u = 0.2$.

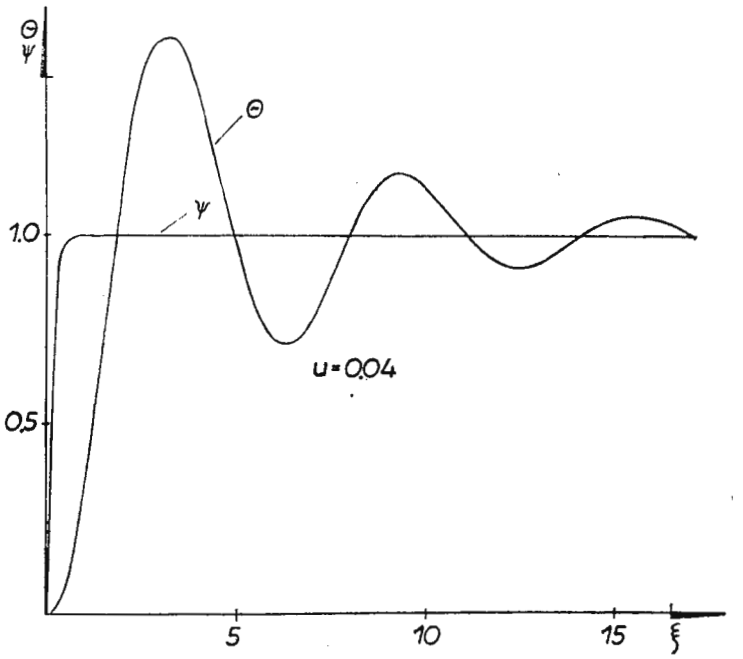

Fig. 7. — Theoretical tilt records of step-like type (type 1), with $u = 0.04$.

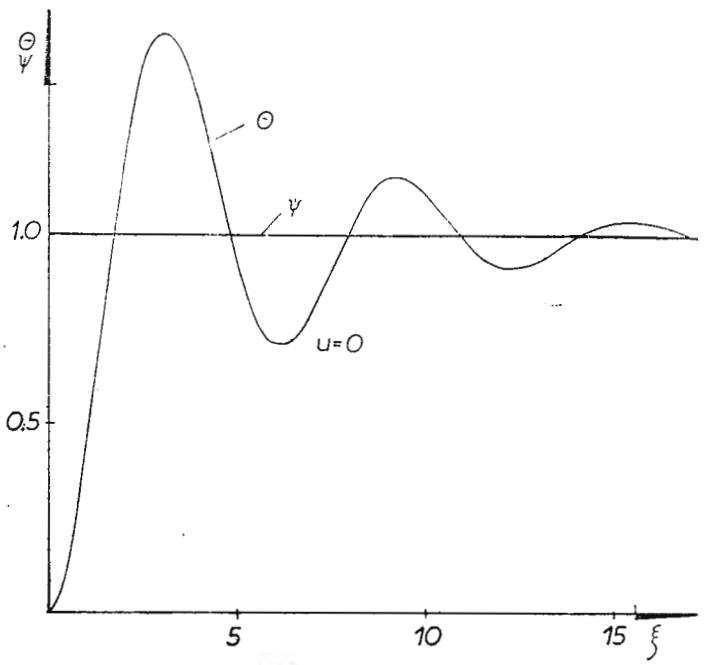

Fig. 8. — Theoretical tilt records of step-like type (type 1), with $u = 0$.

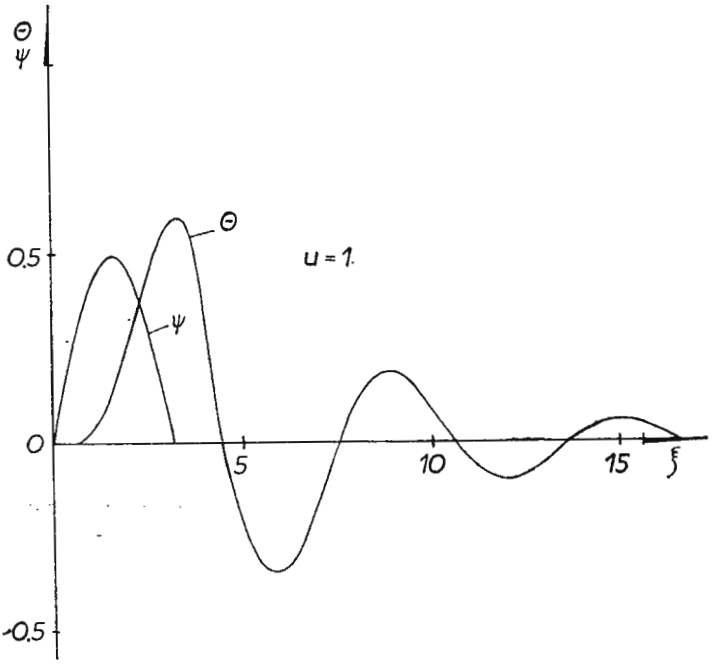

Fig. 9. — Theoretical tilt records of pulse-like type (type 2), with $u = 1$.

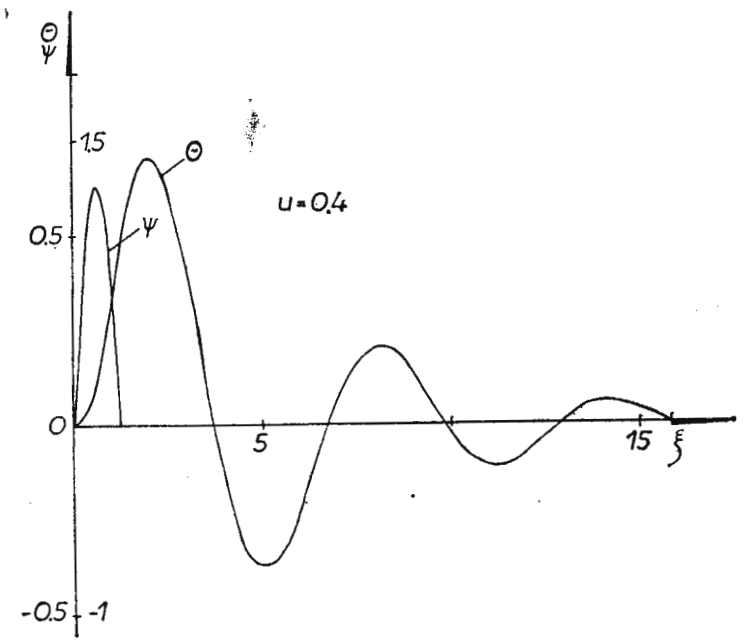

Fig.10. — Theoretical tilt records of pulse-like type (type 2), with $u = 0.4$.

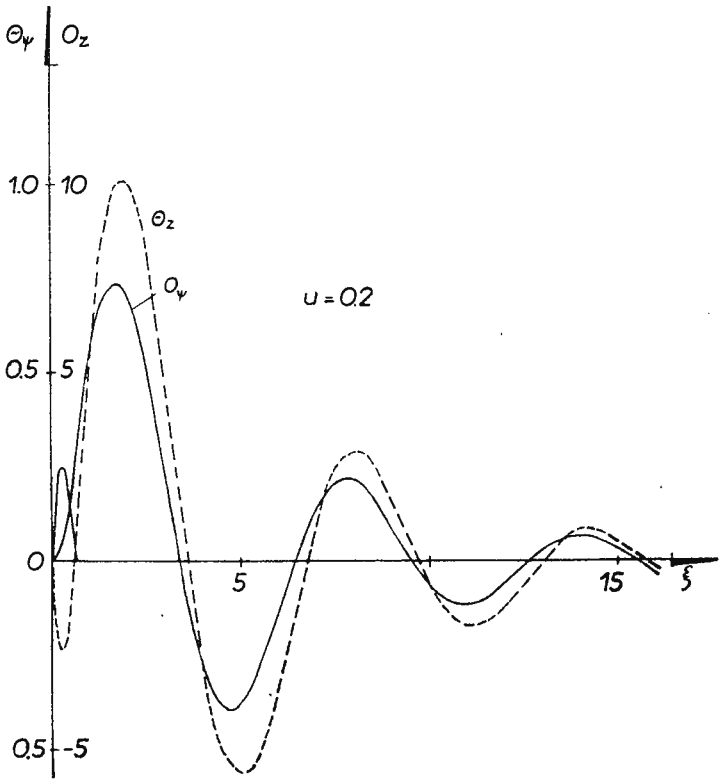

Fig. 11. — Theoretical tilt records of pulse-like type (type 2), with $u = 0.2$.

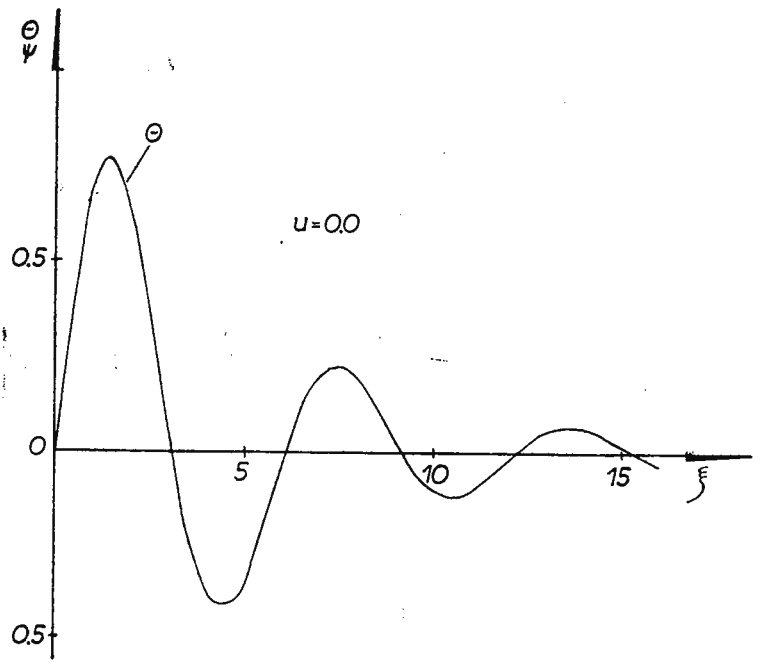

Fig. 12. — Theoretical tilt records of pulse-like type (type 2), with $u = 0$

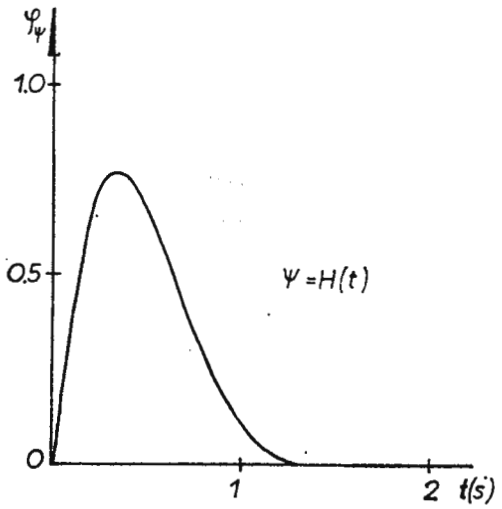

Fig. 13. — Theoretical records of substratum tilts of step-like type (type 1).

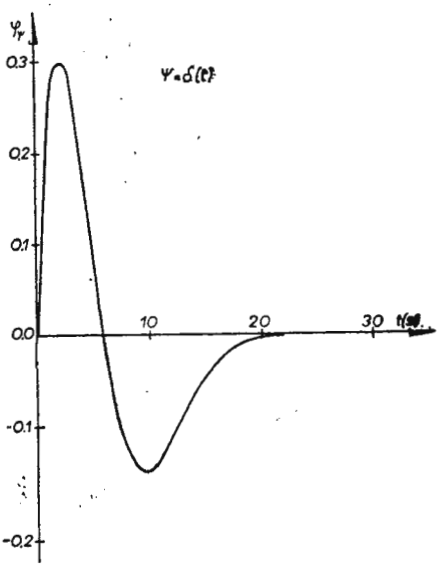

Fig.14. — Theoretical records of substratum tilts of pulse-like type (type 2).

TYPE 1.

TYPE 2

Fig. 15. — Determination of the tilt type from the character of the record.

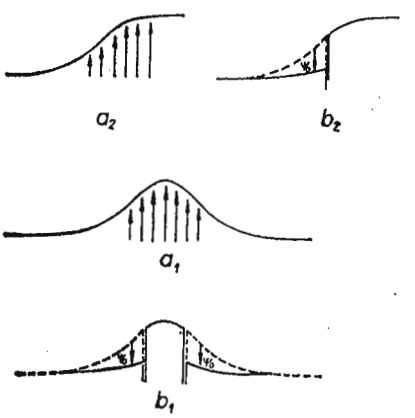

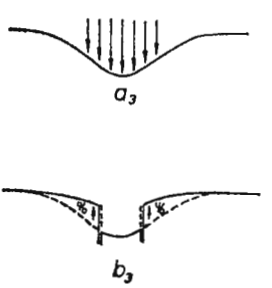

Fig. 16. — Model of the tilt mechanism.

a phenomenon can be created. The stresses acting in a given medium produce its deformations; such deformations cannot be recorded by means of seismographs because the process of their formation is very slow. Upon exceeding the strength limit the medium disrupts, its central part rising up and side parts going either down (model b_1) or up (model b_2). This produces a tilt jump of type 1. The disruption of a medium is accompanied by a release of seismic energy. If the elasticity of the medium is high, the free edges can move in both directions, up and down or vice versa, which produces a tilt jump of type 2.

The occurence of rapid tilt changes in epicentral regions, as well as the recording and detailed analysis of such changes can provide new data on the dynamic processes taking place in seismic foci.

At the same time it should be noted that the effects of deformation in the vicinity of hypocenters can be also recorded by vertical seismographs. To the tilt phenomenon recorded by a horizontal seismograph corresponds a vertical displacement recorded by a Z seismograph. In figures 6 and 11 the dashed line represents the recordings which accompanied the tilts of type 1 and 2, respectively. A comparison of recordings obtained by horizontal seismographs with those obtained by vertical ones provides complementary information to the recording system of the discussed phenomena.

REFERENCES

Ahorner L., Van Gils J. (1963). Das Erdbeben vom 25. Juni 1960 im belgisch-niederlandischen Grenzgebiet. Rheinische Erdbeben III. *Ber. Erdbebenstation Bensberg.* Köln.

Sobolewska Maria (1965) Obserwacje nachyleń powierzchni Ziemi na Górnym Śląsku wedlug zapisów sejsmografów mechanicznych. *Materialy i Prace,* 8.

A DIGITAL PROCESS FOR DEEP SEISMIC SOUNDINGS

BY

MARC SOURIAU, L. STEINMETZ [1]

Two years ago, it was decided to build a digital process for deep seismic soundings, at Institut de Physique du Globe in Paris. This is now a routine procedure. This paper shortly deals with the process from the transducer up to the digital tape and the first analog output.

FIELD RECORDING

Due to the large distance between our recording points, it was necessary to use independent stations. Each one is defined by a 4-channel magnetic tape recording, 3 seismic components and a time track for radio time signals. These channels are multiplexed on a single magnetic track by 4 frequency modulations given by a 6.4 khz quartz pilot, which is the Lennartz recording device, with a 50 db dynamics. The automatic time window is given by a clock and can be adjusted from 3 minutes to 1 hour. (fig. 1).

THE ANALOG-DIGITAL CONVERTER

This step is done by a single converter coupled with a digital computer. The magnetic track is demultiplexed. Each seismic channel goes through a low-pass analog filter adjusted to cancel the frequencies higher than the Nyquist frequency. Two parallel and independent outputs are used, the paper output and the analog-digital converter; the 6.4 khz frequency given by the tape recorder is used by the converter so as to cancel any shift (fig. 2).

The sensitivity of the whole process, as shown by figure 3, must be multiplied by the gain of the amplifier. It is obvious that within the

[1] Institut de Physique du Globe. 11, Quai St. Bernard, Paris V-ème, France.

range 4—40 hz it is a velocity recorder. With the usual gain, we obtain for 1 bit a ground velocity of 4 mμ/s.

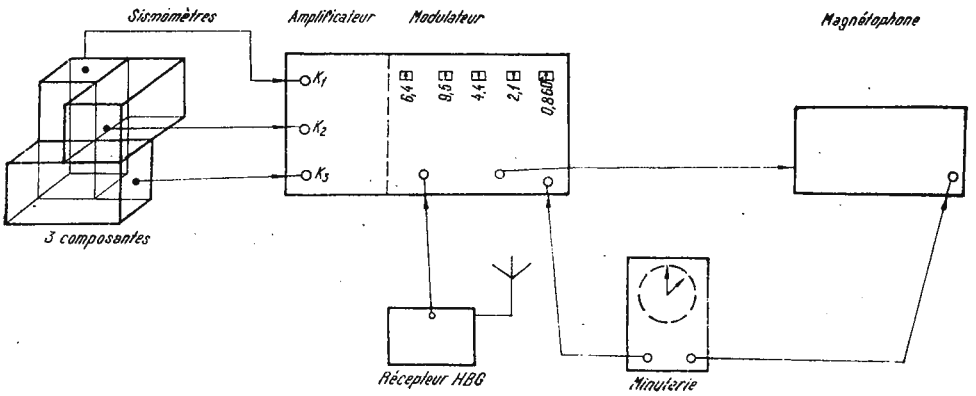

Fig. 1. — Field recording device.

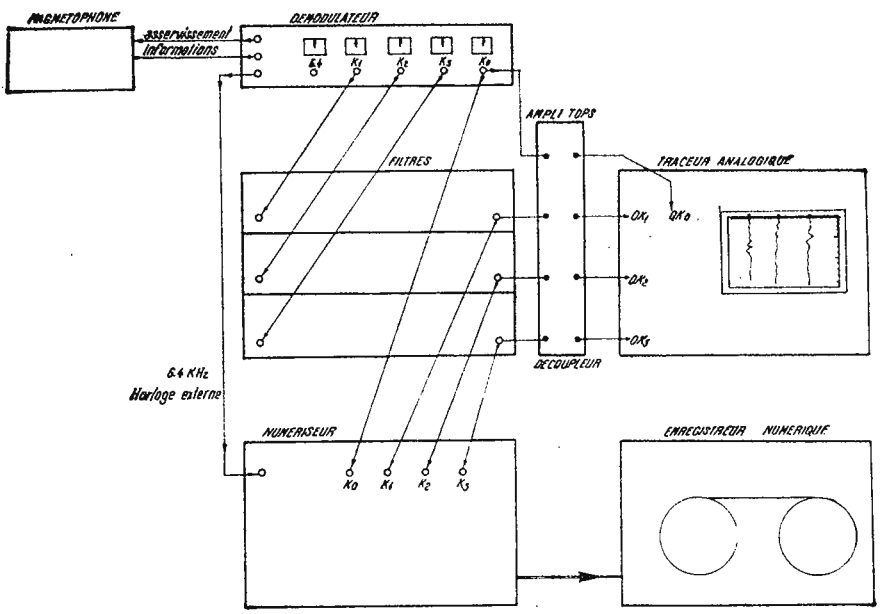

Fig. 2. — Analog-digital converter from analog tape recorder to digital tape.

TAPE PROCESSING

The main parameters of digitalization are :

a) sampling rate 200 by second (Nyquist frequency 100 hz);

b) dynamics 11 bits (a little higher than the analog dynamics);

c) multiplexing the 4 channels with a 40 μs delay.

A software process is used with the following goals

a) recognizing the time signals within the noise according to a confidence level defined over the first seconds;

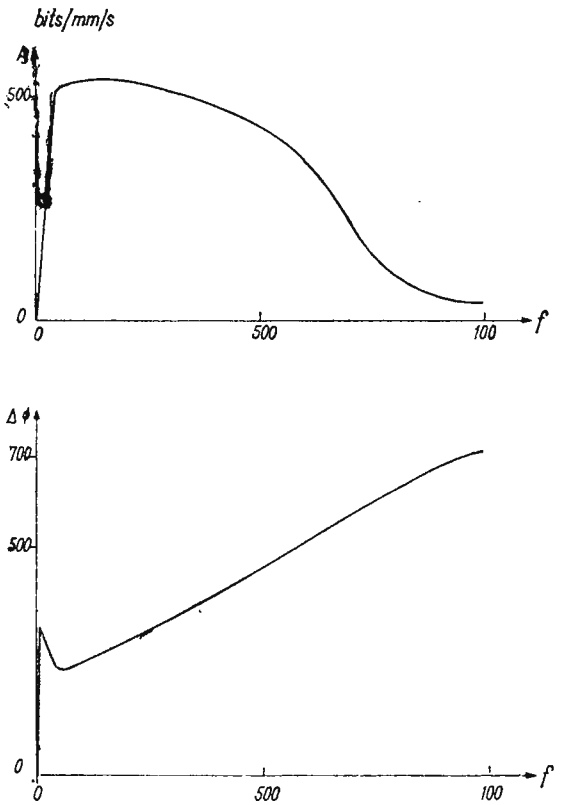

Fig. 3. — Magnification and phase of the whole process from the transducer to the digital tape (Amplifier gain = 1).

b) adjusting the sampling rate to time signals; due to the little shift, adding or canceling one value is enough for 1 second out of 10;

c) defining the time window with the seismic information;

d) building a new tape with

1) a label with all information necessary for further processing;

2) blocks with the 3 seismic channels multiplexed, each block containing 1 second in universal time.

PLOTTER OUTPUT

From the processed tape, we use a plotter for the stacking of a whole profile according to a chosen reduced time and with the time window $(t_1 + \Delta/v_1,\ t_2 + \Delta/v_2)$. For each channel recursive digital filters are used, a high-pass filter to delete the time drift and a band-pass filter with boundaries given by the user.

PRÉPARATION SUR ORDINATEUR DU BULLETIN SÉISMIQUE DES STATIONS DU RÉSEAU BELGO-LUXEMBOURGEOIS

PAR

JEAN-MARIE VAN GILS, BERNARD DUCARME [1]

LE RÉSEAU

Jusqu'en 1966 le réseau belge comportait trois stations : Uccle, Dourbes et Warmifontaine (UCC, DOU, WRM) et permettait la surveillance des régions séismiques du Massif Cambrosilurien du Brabant ainsi que celles qui bordent ce massif sur ses flancs sud et est (tabl. 1).

En 1967 le réseau s'est aggrandi par la création de la station de Luxembourg (LUX) au Grand-Duché. Grâce à cette extension la station de Warmifontaine a pu être abandonnée fin 1970 sans toutefois compromettre l'efficacité du réseau pour la détermination des épicentres belges.

Afin de compléter le réseau d'une part, et en vue de surveiller efficacement les barrages de l'est du pays d'autre part, il a été installé en 1968 une station temporaire à la Gileppe.

Après deux années son fonctionnement a été suspendu, mais elle sera transferée cette année encore dans un site plus propice à Membach et reprendre ses activités.

En 1973 le réseau se verra adjoindre une station située dans le nord de la Belgique de façon à détecter plus efficacement les séismes ayant leurs épicentres le long des failles bordières méridionales du fossé tectonique de Roermond. La configuration ainsi obtenue répondra parfaitement aux besoins des deux pays.

[1] Observatoire Royal de Belgique. 1180 Bruxelles, Belgique.

LE DÉPOUILLEMENT DES OBSERVATIONS

Collecte des données. Le réseau est organisé de façon à ce que tous les séismogrammes parviennent deux fois par semaine au bureau de dépouillement de l'Observatoire Royal de Belgique à Uccle. De plus en ca

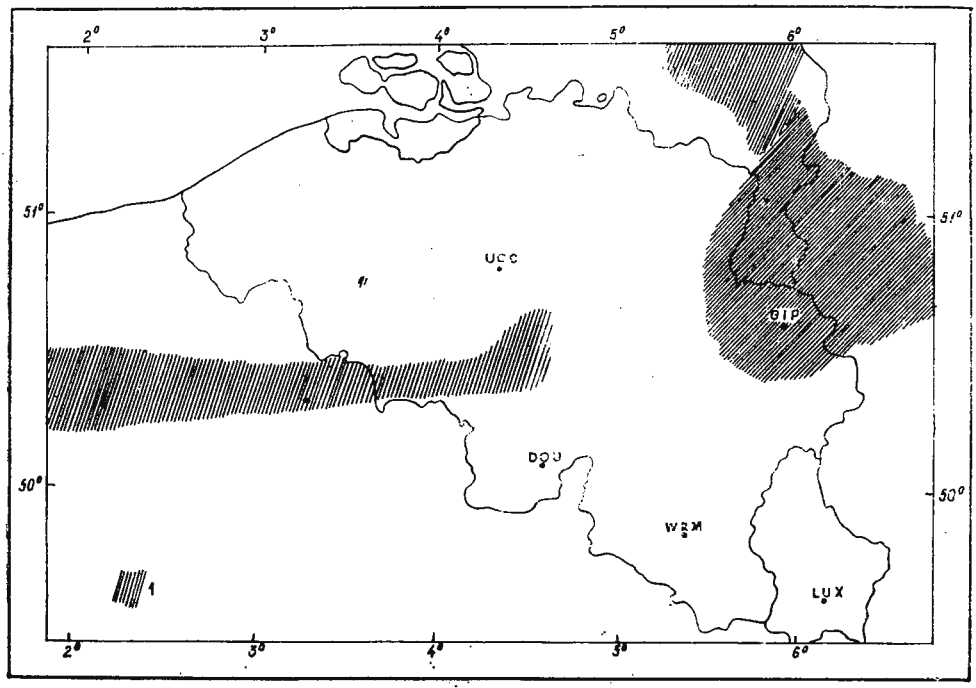

Fig. 1. — Le reseau belge des stations séismiques
1, région sélsmique.

d'évènement exceptionnel les enregistrements sont envoyés le jour même. Les données de la station fondamentale à Uccle sont dépouillées quotidiennement. En outre cette station est pourvue d'un enregistrement en ligne permettant une surveillance constante des évènements locaux.

Dépouillement préliminaire. Les séismogrammes ainsi rassemblés font l'objet d'une première lecture qui a pour but d'informer les stations voisines et les grands centres des évènements enregistrés.

Bulletin provisoire. Après réception des données provisoires des centres internationaux un dépouillement plus complet est effectuée et les

résultats sont perforés sous forme de cartes phases (tabl. 2). Ces cartes sont transposées sur ordinateur dans le code de l'ISC et envoyées à Edimbourg.

Jusqu'en juin 1970, un "listing" de ces cartes était publié sous forme d'un bulletin provisoire.

Bulletin définitif. Ce n'est qu'avec un certain retard (quatre mois pour ERL, un an pour BCIS) que l'on entre en possession des données épicentrales définitives et qu'il devient possible de procéder à l'identification définitive des phases et de consigner les observations dans un bulletin définitif.

Il faut d'abord fixer l'optique dans laquelle ce dernier sera rédigé. Le but du réseau belgo-luxembourgeois n'est pas la détermination des épicentres, ce qui est du ressort des grands organismes internationaux, excepté pour les séismes locaux.

Ce bulletin vise essentiellement à informer les chercheurs du matériel disponible pour d'éventuelles études approfondies. Parmi les recherches souhaitables, citons l'étude des résidus des temps de parcours des différentes ondes en fonction de l'azimut ce qui est indispensable pour améliorer les tables en usage.

Par contre les études de dispersion sur les ondes de surface exigent la digitisation des enregistrements.

C'est pourquoi un bulletin définitif se doit d'abord d'identifier les phases principales et de donner ensuite les écarts entre temps d'arrivée observés et calculés $(O-C)$. Quant aux temps d'arrivée des ondes de surface ils n'ont pas la même signification et seul importe le rattachement à un épicentre donné.

Parmi les autres éléments utiles à renseigner dans un bulletin, signalons la détermination de la magnitude ainsi que le sens du mouvement du sol (compression ou dilatation) si nécessaire pour mieux connaître le mécanisme au foyer.

Pratiquement toutes ces opérations peuvent être confiées à un ordinateur, le problème principal demeurant l'identification automatique des phases. Le problème d'identification en pose un autre : celui du calcul de la distance épicentrale et celui de la consultation de tables de temps de propagation.

Il faudrait donc, d'abord choisir l'expression mathématique permettant de calculer la distance épicentrale de manière à s'approcher au mieux de la distance vraie et ensuite, adapter les tables des temps de propagation.

CALCUL DES DISTANCES ET AZIMUTS

Avant toute chose il faut noter que ce calcul est lié directement à un certain nombre de constantes géodésiques fixées par les Unions. Nous avons adopté les conventions du „GEODETIC REFERENCE SYSTEM 1967"

Aperçu des differentes méthodes de calcul des distances. Initialement les coordonnées géographiques d'un épicentre étaient calculées à l'aide des distances épicentrales Δ de plusieurs stations. Ces distances se mesuraient le long d'arcs de grand cercle d'une sphère de référence. Quoique pour la sphère les géodésiques coïncident avec les grands cercles, il demeurait toujours une grandeur aléatoire due aux choix de la sphère de référence. Du point de vue du calcul, cela se réduit à une simple application de la formule fondamentale de la trigonométrie sphérique :

$$\cos \Delta = \cos \theta_1 \cos \theta_2 + \sin \theta_1 \sin \theta_2 \cos (\lambda_2 - \lambda_1)$$

θ_1 et θ_2 désignant les colatitudes de deux points et λ_1, λ_2 les longitudes correspondantes.

En procédant de la sorte et en considérant que la Terre a une forme ellispoïdale plutôt que sphérique, la distance Δ est entachée d'une erreur qui peut atteindre plusieurs dizaines de kilomètres.

Si, au contraire, comme le préconisaient G u t e n b e r g et R i c h t e r (1933), nous utilisons les coordonnées géocentriques, cette erreur diminue considérablement. En désignant par ω la latitude géocentrique d'un point de latitude géographique Φ, e étant l'excentricité d'une ellipse méridienne, la transformation s'obtient à partir de la relation

$$\operatorname{tg} \omega = (1 - e^2) \operatorname{tg} \Phi$$

Ce procédé ne lève toutefois pas l'ambiguïté due au choix de la sphère de référence : sphère équivolume, sphère équiméridienne, etc. G u t e n b e r g et R i c h t e r se sont servis dans tous leurs calculs de la sphère de rayon

$$R = 6366 \text{ km.}$$

A la distance ainsi calculée, ils appliquaient un terme correctif, dépendant de la hauteur H_0 de l'ellipsoïde par rapport à la sphère. Cette correction atteint 12 km à l'équateur et 10 km aux pôles.

En utilisant les „latitudes réduites" u, liées aux précédentes par la relation

$$\operatorname{tg} u = \sqrt{1 - e^2}\, \operatorname{tg}\Phi$$

le problème reste identique et l'erreur possible est du même ordre de grandeur.

En 1937, B u l l e n suggérait l'introduction d'une „latitude séismologique" afin de corriger au mieux les temps de propagation des ondes P et S des erreurs résultant de l'excentricité de la Terre.

Cette „latitude séismologique" B était liée à la latitude géographique Φ et à la latitude géocentrique ω par la relation

$$B = 1{,}1\,\omega - 0.1\,\Phi$$

Outre cette correction, le même auteur suggérait également de tenir compte de hauteur H_1 du point considéré par rapport à la sphère de référence.

Dans les dernières éditions des Tables de Propagation de J e f f r e y s et B u l l e n, il a été tenu compte des corrections en question. Actuellement, grâce aux ordinateurs électroniques, nous croyons qu'il est utile de repenser les anciennes méthodes de travail.

En effet, au lieu de rapporter tous nos calculs de distance et d'azimut à l'une ou l'autre sphère de référence nous avons calculé ces mêmes éléments suivants les géodésiques de l'ellipsoïde international. Ce calcul peut d'ailleurs se faire à l'approximation souhaitée, en limitant le nombre de termes dans le développement en série des géodésiques.

Calcul d'un arc de géodésique. Pour le calcul d'un arc de géodésique nous avons utilisé une méthode renseignée par T a r d i et L a c l a v è r e dans leur Traité de Géodésie. Elle est basé sur l'emploi de la sphère de Jacobi.

Il s'agit d'une représentation sphérique des arcs d'ellipsoïde sur une sphère de rayon a, suivant certaines conventions. Tout d'abord les azimuts Z de l'arc de grand cercle sont égaux aux azimuts ellipsoïdiques et en première approximation les longitudes sont conservées.

Si on choisit une représentation suivant la latitude réduite on a la relation

$$\operatorname{tg} u = b/a\, \operatorname{tg}\Phi$$

On établit les relations différentielles entre l'élément d'arc sur l'ellipsoïde ds et l'élément d'arc sphérique $d\sigma$. Ces relations sont développées en série puis intégrées terme à terme. Suivant la précision requise on arrête plus au moins loin ce développement.

Ecrivons les relations différentielles relatives aux lignes géodésiques de l'ellipsoïde (Φ, λ, s) et aux arcs de grand cercle de la sphère de Jacobi (U, l, σ).

$$\rho d\Phi = ds \cos Z \qquad a dU = e d\sigma \cos Z$$

$$a \cos U d\lambda = ds \sin Z \qquad a \cos U dl = a\, d\sigma \sin Z$$

D'où l'on tire les relations

$$\frac{d\lambda}{dl} = \frac{1}{V} \qquad \frac{ds}{d\lambda} = \rho \frac{d\Phi}{dU}$$

dans lesquelles $\rho = \frac{b^2}{a} \frac{1}{W^3}$ (rayon de courbure du méridien)

$$\left.\begin{aligned} W^2 &= \frac{1}{1 + e'^2 \sin^2 U} = 1 - e^2 \sin^2\Phi \frac{\cos^2\Phi}{\cos^2 U} \\ V^2 &= \frac{1}{1 - e^2 \cos^2 U} = 1 + e'^2 \cos^2\Phi \frac{\sin^2\Phi}{\sin^2 U} \end{aligned}\right\} \frac{W}{V} = \frac{b}{a}$$

$$\begin{cases} e'^2 = \dfrac{a^2 - b^2}{b^2} \text{ étant la seconde excentricité} \\ e^2 = \dfrac{a^2 - b^2}{a^2} \text{ étant la première excentricité} \end{cases}$$

$$E'^4 = \frac{a^4 - b^4}{b^4}, \qquad E^4 = \frac{a^2 - b^4}{a^4}$$

Longueur d'un arc

De la relation $\operatorname{tg} U = \frac{b}{a} \operatorname{tg}\Phi$

on tire aisément $\frac{d\Phi}{dU} = \frac{a}{b} W^2$

et on trouve ainsi

$$\frac{ds}{d\sigma} = \frac{b}{W} = \frac{a}{V} \tag{1}$$

Transfert de la longitude

$$\frac{d\lambda}{dl} = \sqrt{1 - e^2\cos^2 U} = 1 - \frac{e^2}{2}\cos^2 U - \frac{e^4}{8}\cos^4 U - \ldots \tag{2}$$

Sur la sphère on a la relation

$$dl = \frac{\sin Z_e}{\cos^2 U}\, d\sigma \tag{3}$$

où sin Z_e est l'azimut à l'équateur.

Ce qui permet d'expliciter (2) sous la forme

$$d\lambda = dl - e^2 \sin Z_e \left(1/2 + \frac{e^2}{8}\cos^2 U + \frac{e^4}{16}\cos^4 U + \ldots\right) d\sigma \ldots \tag{4}$$

U peut s'exprimer en fonction de σ et de l'azimut de la géodésique à l'équateur Z_e par la relation sphérique

$$\sin \sigma = \frac{\sin U}{\cos Z_e}$$

ce qui nous donne

$$d\lambda = dl - e^2 \sin^2 Z_e \,(A_0 - 2AZ\cos^2 Z_e \sin^2 \sigma + 2A_4 \cos^4 Z_e \sin^4 \sigma + \ldots)\, d\sigma \ldots \tag{5}$$

avec
$$\begin{cases} A_0 = 1/2 + \dfrac{e^2}{8} + \dfrac{e^4}{16} \\ A^2 = \dfrac{e^2}{16} + \dfrac{e^4}{32} \\ A_4 = \dfrac{e^4}{32} \end{cases}$$

Dans ces conditions pour une arc de cercle de longueur σ' comptée à partir de l'équateur l'écart $\varepsilon = 1 - \lambda$ vaut

$$\left\{\begin{array}{l} \varepsilon = A_0 \sin Z_e\, \sigma - 2A_2 \sin Z_e \cos^2 Z_e \int_0^\sigma \sin^2 \sigma\, d\sigma \\ \\ = e^2 \sin Z_e \left\{ \left(A_0 - A_2 \cos^2 Z_e + \frac{3}{4} A_4 \cos^4 Z_e \right)\sigma + 2(A_2 \cos^2 Z_e - A_4 \cos^4 Z_e) \right. \\ \\ \left. \sin 2\sigma + \frac{1}{16} A_4 \cos^4 Z_e \sin 4\sigma \right\} \end{array}\right. \qquad (6)$$

Pour une ligne quelconque considérée comme la différence entre deux arcs équatoriaux

$$\Delta\sigma = \sigma_1 - \sigma_0 \text{ on trouve}$$

$$\varepsilon = e^2 \sin Z_e \{\ldots\ldots\} \Delta\sigma + A_2 \sin \Delta\sigma \cos(2\sigma_0 + \Delta\sigma) \qquad (7)$$

Calcul de la longueur d'un arc

$$\frac{dS}{d\sigma} b (1 + e'^2 \sin^2 U)^{1/2} \qquad (8)$$

U peut s'exprimer en fonction de σ et de l'azimut de la géodésique à l'équateur Ze par la relation

$$\sin\sigma = \frac{\sin U}{\cos Z_e}$$

on a dès lors

$$\frac{dS}{d\sigma} = b \sqrt{1 + e'^2 \cos^2 Z_e \sin^2 \sigma} \qquad (9)$$

En développement par la formule du binôme on a

$$\frac{ds}{d\sigma} = b\left(1 + \frac{1}{2} e'^2 \cos^2 Z_e \sin^2 \sigma - \frac{1.1}{2.4} (e'^2 \cos^2 Z_e)^2 \sin^4 \sigma \right.$$

$$\left. + \frac{1.1.3}{2.4.6} (e'^2 Z_e)^3 \sin^6 \sigma - \ldots \right) \qquad (10)$$

L'intégration se fait en utilisant les formules de Moivre qui permettent d'exprimer les puissances successives de sinσ en fonction des arcs multiples 2σ, 4σ ...

$$\sin^2\sigma = \frac{1}{2} - \frac{1}{2}\cos 2\sigma$$

$$\sin^4\sigma = \frac{3}{8} - \frac{1}{2}\cos 2\sigma + \frac{1}{8}\cos 4\sigma$$

$$\sin^6\sigma = \frac{5}{16} - \frac{15}{32}\cos 2\sigma + \frac{3}{16}\cos 4\sigma - \frac{1}{32}\cos 6\sigma$$

en posant

$$\frac{1}{4}e'^2\cos^2 Z_e = K^2 \text{ on obtient}$$

$$\frac{ds}{d\sigma} = b\left(1 + K^2 - \frac{3}{4}K^4 + \frac{5}{4}K^6\right) - \left(K^2 - K^4 + \frac{15}{8}K^6\right)\cos 2\sigma +$$

$$\left(\frac{K^4}{4} - \frac{3K^6}{4}\right)\cos 4\sigma - \frac{3}{24}K^6\cos 6\sigma \qquad (11)$$

Dans l'intégration nous pouvons considérer deux cas.

a) Prenons d'abord le cas d'une géodésique de longueur s comptée à partir de l'équateur.

Si la quantité entre crochets est exprimée en radians on trouve en kilomètres.

$$s = b\left(1 + K^2 - \frac{3}{4}K^4 + \frac{5}{4}K^6\right), -\frac{1}{2}\left(K^2 - K^4 + \frac{15}{8}K^6\right)\sin 2\sigma$$

$$+ \frac{1}{2}\left(\frac{K^4}{8} - \frac{3K^6}{8}\right)\sin 4\sigma - \frac{K^6}{48}\sin 6\sigma$$

Comme $\frac{1}{4}e'^2 = 1{,}6849313\ 10^{-3}$, la série est rapidement convergente.

En posant :

$$B_0 = 1 + K^2 - 0{,}75\ K^4 + 1{,}25\ K^6$$

$$B_2 = K^2 - K^4 + 1{,}875\ K^6$$

$$B_4 = 0{,}125\ K^4 - 0{,}375\ K^6$$

$$B_6 = 0{,}04\ K^6$$

On a

$$s = b\left(B_0\sigma - \frac{1}{2}\ B_2 \sin 2\sigma - \frac{1}{2}\ B_4 \sin 4\sigma - \frac{1}{2}\ B_6 \sin 6\sigma\right) \qquad (12)$$

À la précision recherchée de 0.001 degré nous négligeons le terme en B^6 et nous adoptons :

$$B_0 = 1 + K^2 - 0{,}75\ K^4$$

$$B_2 = K^2 - K^4$$

$$B_4 = \frac{K^4}{8}$$

b) Si on ne calcule pas un arc équatorial mais un arc Δs joignant un point Q_o de latitude réduite U_o et d'élongation σ_o, à un point $Q_1(U_1, \sigma_1)$, on pourra le considérer comme une somme ou une différence d'arcs équatoriaux de la géodésique.

Application. Le calcul de la distance se réduit donc au calcul de la distance sphérique $\Delta\sigma$, de l'élongation des extrémités σ_o et σ_1 et de l'azimut à l'équateur Z_e.

Toutes ces quantités peuvet s'obtenir à partir des quatres cosinus directeurs principaux :

$$a = \cos\Phi' \cos\lambda$$

$$b = \cos\Phi' \sin\lambda$$

$$c = \sin\Phi'$$

$$-k = \cos\Phi'$$

Φ' représentant la latitude transférés c.à.d., U dans notre cas.

Première approximation sur la distance sphérique $\Delta l = \Delta\lambda$

On assimile les longitudes sphériques à celles de l'ellipsoïde si l'indice *0* désigne la première station et l'indice 1 l'autre.

$$\cos \Delta\sigma = a_0a_1 + b_0b_1 + c_0c_1 \sin Z_e = \frac{a_0b_1 - a_1b_0}{\sin \Delta\sigma}$$

$$\sin \sigma_0 = \frac{\sin \Phi'_0}{\cos Z_e}$$

$$\sin \sigma_1 = \frac{\sin \Phi'_1}{\cos Z_e}$$

L'azimut direct (*0* → *1*) et inverse (*1* → *0*) calculés sur la sphère sont donnes directement à partir de sin Z_e

$$\sin Z_{01} = \frac{\sin Z_e}{\cos \Phi_0} \qquad \sin Z_{10} = \frac{\sin Z_e}{\cos \Phi'_1}$$

Le signe du cosinus de l'azimut est nécessaire tant pour discriminer les quadrants que pour le calcul du terme correctif.
Il suffit pour cela de calculer le numérateur des expressions

$$\cos Z_{01} = \frac{C_1 - \cos \Delta\sigma C_0}{\sin \Delta\sigma \cdot \sigma \cos \Phi'_0}$$

$$\cos Z_{10} = \frac{C_0 - \cos \Delta\sigma C_1}{\sin \Delta\sigma \cdot \sigma \cos \Phi'_1}$$

Nous devons aussi calculer ε à partir de la formule (7)

Seconde approximation $\Delta l = \Delta\lambda + \varepsilon$

Les formules fondamentales deviennent :

$$\cos \Delta\sigma' = (a_0a_1 + b_0b_1) \cos \varepsilon - (b_0a_1 - a_1b_0) \sin \varepsilon$$

$$\sin Z'_e = \frac{(a_0a_1 + b_0b_1) \sin \varepsilon + (a_0b_1 - a_1b_0) \cos \varepsilon}{\Delta'}$$

Les autres formules ne changent pas.

On peut pousser plus loin le calcul en déterminant une nouvelle valeur ε' qui différera très peu de la précédente et recommencer le processus jusqu'à la précision recherchée.

À la première approximation ε vaut environ $\Delta\sigma/300$ et à la seconde approximation il ne varie plus que d'une quantité négligeable à la précision recherchée de 0.01 degré.

Longueur de l'arc de géodésique sur l'ellipsoïde

On a choisi de sortir les distances en degrés moyens de 111 km.

Or on voit dans la formule (6) que la quantité entre crochets est exprimée en radians de la sphère de rayon polaire

$$b = 6.356{,}774 \text{ km}$$

pour laquelle un degré vaut 110 km 947.

On doit donc multiplier les résultats par un facteur correctif 0.99952 pour les exprimer en degrés moyens, ce qui donne :

$$s = 0.99952 \left(B_0 \Delta\sigma - \frac{1}{2} B_2 (\pm \sin 2\sigma_1 + \sin 2\sigma_0) \right).$$

Le signe des termes correctifs est fixé par la position relative des deux stations.

En pratique ce signe est négatif quand le cosinus de l'azimut correspondant (cos Z_{10} pour σ_1 et cos Z_{01} pour σ_0) est positif.

Conclusions. Les distances calculées par cette méthode diffèrent de moins de 0.1 degré des valeurs obtenues par la formule classique utilisée par l'ISC.

Elles sont systématiquement inférieures ce qui provient probablement du choix de la sphère de référence ainsi que du fait que nous travaillons en degrés moyens.

LES TABLES DE TEMPS DE PROPAGATION

Nous avons généralement utilisé les tables de Jeffreys-Bullen (1958). Toutefois pour l'onde *PKP* les tables choisies sont celles de Shimshoni.

Préparation des tables. Les tables de Jeffreys ne se présentent sous une forme directement accessible en ordinateur que pour les phases simples *P* et *S*. Pour les autres seuls les temps de propagation en surface sont renseignés et les corrections de profondeur sont données de façon assez grossière. C'est pourquoi nous avons préféré recalculer toutes les phases composées.

Un autre cas difficile est celui où les phases de deux séismes sont mélangées. Après identification des phases du premier séisme il faut garder en mémoire les phases non identifiées appartenant au second séisme qui elles ne seront reconnues que plus tard. D'où l'utilisation d'une table des stocks où les phases seront gardées jusqu'à ce que leur temps d'arrivée soit entérieur au *P* ou au *PKP* du dernier épicentre lu.

Une phase est considérées comme identifiée quand sont temps de propagation diffère de moins de 5 sec. pour les *P*, moins de 10 sec. pour les autres ondes de volume.

Si deux ondes différentes sont identifiables à une même phase, les phases principales (*P*, *S*, PKP, *SKS*) prennent le pas.

Pour les ondes de surface les bornes d'identification sont élargies considérablement en tenant compte du fait que les retards sont plus plausibles que les avances.

Pour les ondes de surface se pose en outre le problème des identifications multiples. On voit par exemple dans le tableau 3 qu'un même train d'onde peut être identifié comme appartenant à plusieurs épicentres. C'est le cas des séismes :

4 et 5 (9 05 2.9)

7,8 et 9 (11 14 57.2)

14 et 15 (15 20 21.1)

21 et 22 (22 15 1.2)

Pour trancher on pourra inclure des critères basés sur la magnitude et la distance, mais en dernier ressort une intervention humaine sera parfois nécessaire.

Celles-ci ont été réparties en quatre groupes

1) phases mixtes 

2) phases réfléchies sur le noyau 

3) phases traversant le noyau 

ou la graine 

4) phases des séismes profonds *p* et *s*.

Calcul des phases composées. Toute phase peut se ramener à la composition des deux autres.

La règle fondamentale est que la partition des distances s'effectue de telle sorte que l'inverse de la vitesse apparente $\delta t/\delta\Delta$ soit le même pour les portions d'arc parcourus par chacun des éléments de la paire.

Tout le problème se ramène à déterminer par interpolation dans les tables des vitesses apparentes, la partition exacte pour chaque distance angulaire Δ. Les phases interdites en découlent immédiament.

Au départ on a dû admettre un certain nombre de phases élémentaires. Ce sont :

groupe 1 *P* et *S*

d'où l'on tire

PP, *PS*, *SP*, *SS*

PPP, *PSP* $\equiv$ *PPS*, *SPP*, *PSS*, *SPS* $\equiv$ *SSP*, *SSS*

groupe 2 *PcP* et *ScS*

d'où l'on tire

PcS, *ScP*

groupe 3 *PKP* (Shimoshoni)

K : temps de propagation à travers le noyau

KIK : temps de propagation à travers la graine

PcP et *ScS*

d'où l'on tire

PKS, *SKP*, *SKS*

PKKP, etc....

groupe 4 *P* et *S*

d'où l'on tire

p*P*, *sS*, *sP*

*p*PP, *sSS* etc....

Pour les phases réfléchies du groupe 2 on doit combiner la moitié du temps de propagation pour l'arc double, ce qui correspond au temps de parcours surface-noyau ou réciproquement.

Pour le groupe 3 on combine le groupe 2 avec les temps dans le noyau. Le groupe est complexe car la loi de partition est plus difficile à appliquer.

Exemple xY ($\Delta' = \Delta - \Delta_1$)

Il faut

$$\left(\frac{\delta t}{\delta \Delta_1}\right)_{y,s} = \left(\frac{\delta t}{\delta \Delta_2}\right)_{Xs}$$

$$\left(\frac{\delta t}{\delta \Delta_2}\right)_{X_s} = \left(\frac{\delta t}{\delta (\Delta_2 - \Delta')}\right)_{X_h}$$

Fig. 2. — Exemple xY ($\Delta' = \Delta - \Delta_1$)

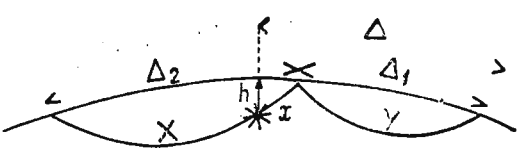

où l'indice s indique que la phase est prise en surface et l'indice h qu'elle est prise à la profondeur h.

$$t_{xY,h,\Delta} = t_{y,s,\Delta 1} + (t_{X,s,\Delta_2} - t_{Xh,\Delta 2} - \Delta')$$

Sur ces bases nous avons été amené à élaborer un programme pour chaque groupe.

Les temps de propagation ainsi déterminés sont en agrément avec les tables au dixième de seconde près.

PROGRAMME D'IDENTIFICATION

D'une part on dispose des données épicentrales de l'ERL et du BCIS ainsi que des distances calculées stockées sur disque. Les données du BCIS sont plus spécialement retenues dans le cas des séismes de la zone européenne. Les séismes proches ($< 1°$) et les explosions sont traités à part.

D'autres part tous les évènements ont été perforé sur des cartes phases (tabl. 2) et regroupés par séismes numérotés dans l'ordre chronologique. Des identifications provisoires ont été faites, mais seules ont été retenues celles concernant les ondes à longue période.

Pour disposer d'une échelle de temps uniforme, le programme commence par transformer toutes les heures origines et les temps d'arrivée des phases en Temps Julien.

On prend un premier épicentre, on dresse une tables des temps d'arrivée théoriques et on cherche à les identifier avec les temps de propagation du premier séisme à déterminer. Si l'identification n'est pas possible on passe à l'épicentre suivant et ainsi de suite. Dès qu'une phase du séisme est identifiée celui-ci est considéré comme déterminé et on passe au suivant.

La logique du programme doit prévoir certains cas particuliers. Tous d'abord les ondes d'un séisme chronologiquement postérieur peuvent arriver à la station avant celles d'un séisme antérieur. A ce moment il faut garder en mémoire les épicentres jusqu'à ce que le temps d'arrivée des dernières ondes possibles (M ou W) soit dépassé par les phases lues. De là la nécessité d'une table des épicentres.

TABLEAU 1

UCCLE

Observatoire Royal de Belgique

$\Phi = 50°47'54''$ N.

$\lambda = 4°21'34''$ E.

Altitude : 105 m.
Sous-sol : sable éocène moyen.

Instruments : (1966 et années suivantes)

1) *a*) 1 séismomètre vertical type Wiechert VEU
b) 1 séismomètre horizontal, type Wiechert á 2 composantes NS et EW NEU—EEU
Transmission du mouvement du sol par transformateur différentiel et enregistrement sur enregistreurs potentiométriques électroniques Brown.
En fonction jusqu'en mars 1972.

2) 2 séismomètres électromagnétiques horizontaux type Galitzine original EGU—NGU
1 séismomètre électromagnétique a composante verticale type Wilip Sombille VGU
Enregistrement photogalvanométrique sur papier.
Ce groupe de séismomètres est toujours en fonction.

3) Trois séismomètres „longue période" type Press-Ewing.

composantes :	verticale	VLU
	EW	ELU
	NS	NLU

a) Enregistrement photogalvanométrique sur papier.
Mise en fonction : 10 mai 1971 et toujours en fonction.
b) Enregistrement sur enregistreurs potentiométriques électroniques Brown a partir de mars 1972.

DOURBES

Centre de Physique du Globe de l'I.R.M.

$\Phi = 50°5'45,7''$ N ;

$\lambda = 4°35'39,2''$ E ;

Altitude : 232 m.
Sous-sol : dévonien.

Instruments : (1966 et toujours en fonction)

1) 3 séismomètres „Longue période" type Press Ewing.
2) 3 sèismomètres „Courte période" type Benioff.

Chaque groupe de séismomètres est relié à un enregistreur triple du type Sprengnether. Enregistrement photogalvanométrique.

WARMIFONTAINE

Station souterraine à 150 m de profondeur

Mise en service en septembre 1964.
Station à l'arrêt depuis le 1er novembre 1970.

$\Phi = 49°50'$ N ;

$\lambda = 5°22'50''$ E ;

Altitude : $\pm$ 300 m.

Instruments :

3 séismomètres type Sprengnether.
Enregistrements photogalvanométriques.

LUXEMBOURG

Ville de Luxembourg — Casemates du Saint-Esprit

$\Phi = 49'36'$ N ;

$\lambda = 6°8'$ E ;

Altitude : 271 m.

Instruments :

3 séismomètres Askania type Galitzine.
Enregistrement photogalvanométrique.
Mise en fonction le 1er mai 1967 et toujours en fonction.

LA GILEPPE

$\Phi = 50°35'32''$ N ;

$\lambda = 5°58'27''$ E.

Instruments :

Un séismomètre courte-période type Grenet.
Enregistrement photogalvanométrique standard.
Mise en fonction le 1er octobre 1968 et mise à l'arrêt au début mars 1970.

TABLEAU 2

UCCLE

CARTES PHASES

JANVIER 1966

1	04	13	06	29	L	EG						
2	05	17	43	41	E	EG						
2	05	17	59	37	L	NG						
2	05	18	09	57	LM	NG						
3	07	21	42	46	L	NG						
4	09	05	02	53	L	NG						
5	10	02	09	23	L	NG						
6	11	14	57	14	L	NG						
6	11	15	05	00	M	EG						
7	13	1	53	03	P	VG						
7	13	11	19	16	L	NG						
8	15	12	19	52	E	NG						
8	15	12	35	31	L	NG						
9	15	18	18	54	L	EG						
10	15	2	21	04	L	EG						
11	16	0	13	30,0	SG	EE						
12	16	01	26	47	L	EG						
0013	16	06	51	41,0	PG	VG, NG	0.36	HO	06	51	33	8
13	16	06	51	45,8	ISG	EN, E						
13	16	06	51	46,5	E	EG						
13	16	06	51	47,7	E	NE, VNG						
13	16	06	51	50,2	E	EG						
14	16	09	50	39	L	NG						
0015	16	12	32	56,5	PG	VE, EE	0.35 C	HO	12	32	49	5
15	16	12	33	01,0	SG	NE						
0016	16	12	32	57,8	PG	VE	0.36 D	HO	12	32	50	6
16	16	12	33	02,4	ISG	EN, E						
16	16	12	33	03,0	I	VG, NG						
17	16	12	32	59,8	PG	NE, NG						
17	16	12	33	03,9	I/SG/	NG						
17	16	12	33	05,9	E	VE						
18	16	19	01	32	E	EG						
18	16	19	04	39	L	NG						
19	17	17	04	28	SG	EG						
19	17	17	04	35	E	NG						
20	17	2	29	08,2	E	VG						
20	17	2	29	11,0	SG	EG						
20	17	2	29	12	E	EE						
20	17	2	29	15,5	E	NE						

(Continuation tableau 2)

21	19	07	01	49	PN	VG						
22	19	1	7	29	E	NG						
22	19	1	7	37	E	NE, NG						
23	19	15	36	29	E	VG						
23	19	15	36	33,6	E	EE						
24	22	0	32	52	S	EG						
24	22	0	35	15	L	NG						
0025	22	14	38	35	P	NG	71.8	HO	14	27	09	
25	22	14	47	55	S	EG						
25	22	14	53	00	/SS/	NG						
25	22	14	55	26	/SSS/	EG						
25	22	15	01	10	L	EG						
26	23	01	33	09	PN	VG						
27	23	01	40	06	L	NG						
28	23	02	36	50	L	NG						
29	24	02	46	49	L	NG						
30	24	07	39	45	S	EG						
30	24	07	51	50	L	EG						
0031	24	22	13	26,9	PG	EG	0.37	HO	22	13	19	5
31	24	22	13	30,0	E	VE						
31	24	22	13	31,6	SG	VG, NG						
32	25	04	15	58	L	EG						
33	26	01	08	56	SG	EG						
33	26	01	09	01	E	EG						
34	28	04	55	26	P	VG						
35	28	06	01	54	P	VE, VG						
35	38	06	02	53	E	VE						
35	28	06	04	44	E	VE						
35	28	06	05	44	E	NG						
35	28	06	06	24	E	VE						
35	28	06	11	40	E	EG						
35	28	06	24	00	E	EG						
35	28	06	25	12	E	NG						
35	28	06	37,3		L	EG						
35	28	06	40,5		L	EG						
35	28	06	58,3		MQ	EG						
35	28	07	01		MR	VEN, E						
36	28	22	49	52	P	VG						
37	29	14	52	50	E	VG						
38	30	02	00	01	P	VG						

TABLEAU 3

									MAGN.	PROF.	DIST.	AZ.
1	SEISME INDETERMINE											
	L	4	13	6	29.0	EG						
2		5	17	21	27.9	13.2 N	95.5 E		5.2	33	80.60	80.59
	S	5	17	43	41.0	EG −0.9						
	LR	5	17	59.6		NG 32.						
	M	5	18	9.9		NG 249.						
3		7	20	17	13.7	62.6 S	155.6 E		5.8	33	160.45	138.39
	LR	7	21	42.8		NG 640.						
4		9	4	6	29.8	21.5 S	69.7 W		5.4	57	96.89	244.51
	M	9	5	2.9		NG 186.						
5		9	4	50	52.5	41.2 N	29.3 W		4.4	33	25.06	260.67
	LR	9	5	2.9		NG 19.			PHASE IDENTIFIEE 2 FOIS			
6	10	1	19	10.8		13.8 N	120.7 E		5.4	124	95.14	60.78
	LR	10	2	9.4		NG 348.						
7		11	14	6	17.4	33.8 N	137.1 E		5.1	23	85.92	37.69
	M	14	11	57.2		NG 221.						
8		11	14	11	8.4	33.9 N	137.1 E		4.3	33	85.83	37.64
	M	11	14	57.2		NG −67.			PHASE IDENTIFIEE 2 FOIS			
9		11	14	16	32.3	33.7 N	137.1 E		5.6	33	86.01	37.74
	LR	11	14	57.2		NG 33.						
	M	11	15	5.0		EG 69.			PHASE IDENTIFIEE 3 FOIS			
10		13	10	41	11.7	52.9 N	172.0 E		5.6	17	76.01	7.65
	P	13	10	53	3.0	VG 3.2						
	LR	13	11	19.3		NG 156.						
11	SEISME INDETERMINE											
	PS	15	12	19	52.0	NG						
12		15	11	32	48.3	18.7 S	169.2 E		4.4	214	145.70	25.90
	LQ	15	12	35.5		NG 91.						
13		15	18	7	42.8	36.7 N	23.0 E		4.7	11	19.40	129.37
	M	15	18	18.9		EG 31.						
14		15	19	28	55.7	33.6 S	70.2 W		5.0	33	106.59	237.15
	LR	15	20	21.1		EG 144.						

(Continuation tableau 3)

15		15	19	19	36.1	33.5 S	69.8 W	5.5	50		
										106.30	236.95
	LR	15	20	21.1		EG 112.				PHASE IDENTIFIEE 2 FOIS	
16	L	16	1	26	47.0	EG					
17		16	9	11	47.3	52.8 N	172.0 E	5.5	8		
										76.11	7.67
	LR	16	9	50.6		NG 201.					
18		16	18	52	0.8	33.2 N	26.2 E	5.0	33		
										23.77	129.31
	LR	16	19	4.6		NG 93.					
19	PN	19	7	1	49.0	VG					
20		22	0	23	42.1	37.7 N	30.0 E	4.9	20		
										22.41	115.81
	LR	22	0	35.2		NG66.					
21		22	14	5	41.3	10.3S	74.7 N	4.2	95		
										91.10	255.23
	M	22	15	1.2		EG 322.					
22		22	14	27	7.9	56.0 N	153.7 W	5.8	33		
										71.89	347.29
	LR	22	15	1.2		EG 29.					
23	SEISME	INDETERMINE								PHASE IDENTIFIEE 2 FOIS	
	PN	23	1	33	9.0	VG					
24		23	0	57	20.8	16.0 N	95.0 W	4.6	43		
										83.51	287.40
	LR	23	1	40.1		NG 227.					
25		23	1	56	38.8	37.0 N	107.0 W	5.5	14		
										73.78	309.20
	M	23	2	36.8		NG—23.					
26		24	1	25	14.7	15.2 S	167.3 E	0.0	111		
										141.48	27.10
	M	24	2	46.8		NG 213.					
27		24	7	23	9.7	29.9 N	69.7 E	5.6	26		
										52.15	87.39
	S	24	7	39	45.0	EG 3.6					
	M	24	7	51.8		EG —1.					
	SEISME	INDETERMINE									
28	L	25	4	15	58.0	EG					
29		28	4	36	46.1	17.6 S	177.0 E	5.5	556		
										146.26	12.61
	PKP2	28	4	55	26.0	VG—2.9					
30		28	5	42	16.3	17.1 S	168.4 E	5.7	23		
										143.95	26.35
	PKP1	28	6	1	54.0	VE 4.1					
	LR	28	6	58.3		EG 531.					
	M	28	7	1.0		VE 27.					
31		28	22	38	13.7	51.6 N	157.0 E	5.7	122		
										75.24	17.18
	PCP	28	22	49	52.0	VG—5.9					
32		29	14	40	30.5	16.6 N	91.2 N	4.7	33		
										80.74	284.93
	PCP	29	14	52	50.0	VG 1.0					
33		30	1	48	47.1	11.2 S	14.5 W	4.9	33		
										63.92	200.71
	PCP	30	2	0	1.0	VG 6.7					

ARRAYS

PREDICTED AND OBSERVED SEISMIC EVENT DETECTABILITY OF THE NORSAR ARRAY

BY

K. A. BERTEUSSEN, EYSTEIN S. HUSEBYE[1]

INTRODUCTION

A drawback in many types of seismicity investigations is that an estimate of seismic event detection capability si not available or neglected. One interesting example here is that observed earthquake activity is higher during nights than in the daytime (S h i m s h o n i, 1972) which most probably reflects diurnal noise level variations (F l i n n et al., 1972).

Obviously, the event detection capability of an ordinary station or a seismic array is mainly governed by the noise level at the site. Thus, in principle it should be possible to estimate the lower magnitude threshold for observable earthquakes for different epicentral distances for a given seismological observatory when its noise level variations are known. This problem is the topic of the paper.

METHOD

We have here focused our interest on the event detectability of the NORSAR array in Norway, and will first dwell briefly on its automated procedures (B u n g u m et al., 1971) which define the system's operational noise level. The event detector is based on a large number of signal-to-noise ratio (SNR) tests on around 310 array beams which are

[1] NTNF/NORSAR, N2007 Kjeller, Norway.

deployed in all active seismic regions. For extra noise suppression, i.e., in addition to that proportional to the square of the number of array sensors, recursive bandpass filtering is applied on the beam traces. The event detection process itself is based on calculations of a short term (STA) and long term (LTA) linear power average through sliding windows.

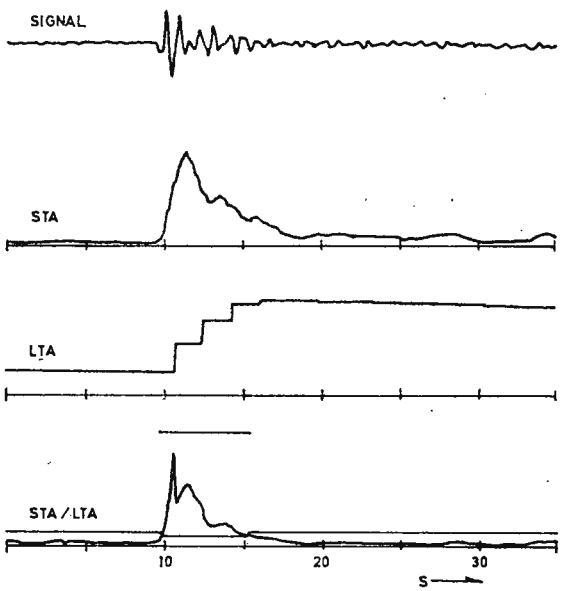

Fig. 1. — Beam, STA, LTA and STA/LTA for earthquake from Tsinghai, China ; arrival time Jan 27 1970, 10.59. 40.1 filtered 1.0—3.0 Hz. STA integration time is 1.8 sec and LTA computation rate is 5/9 Hz. The short line above the STA/LTA curve indicates detection state, and the line crossing the curve is the threshold.

Whenever the ratio between these two parameters on a particular beam trace exceeds a predefined threshold, a detection is declared (fig. 1). The mathematical formulation is given in eq (1) and eq (2).

$$STA(t) = \sum_{i=t-IW+1}^{t} |S(i)| \tag{1}$$

$$LTA(t') = (1 - 2^{-\eta}) \cdot LTA(t' - IW) + 2^{-\eta} \cdot STA(t' - IW) \tag{2}$$

where t and t' are STA and LTA sampling times in dsec, $S(i)$ is array beam amplitude, IW = integration window, and the parameter $\eta = 4$ or 5. For computational convenience a linear power detector is used, while a more common power detector $PSTA/PLTA$ is easily defined from eq (1), i.e., STA replaced by $PSTA$ and $|S(i)|$ by $S(i)^2$, etc. For noise and small signals we have $STA \cong (PSTA)^{1/2}$, an approximation used in this paper.

The short term average is of special interest when an event is detected. The reason is that the STA parameter essentially is an estimate of the square root of the kinetic energy per unit mass of the signal and thus related to the dominating A/T term in the standard magnitude formula given below :

$$m_b = \log(A/T) + Q(\Delta, h) + S \tag{3}$$

where A = signal amplitude, T = period, $Q(\Delta, h)$ = depth distance function for P-waves and S = station constant. It has been shown (IBM, 1967) that the relation between $PSTA$ and (A/T) is of the form

$$PSTA \sim \pi^2(A/T)^2 \tag{4}$$

In the case of NORSAR, a direct approximation of the quantity A/T can be obtained as indicated in eq (4) as the instrument velocity transfer function is essentially flat in the frequency band 0.7—4.0 Hz.

The probability of detecting a P-signal with given log A/T and thereby a specific magnitude value (F e l i x et al., 1972), ignoring the $Q(\Delta, h)$ and S terms in eq (3), may be formulated as :

$$Prob\,(m_b) = Prob\,(20 \log A/T > NL + TH + SL) \tag{5}$$

where NL = noise level in dB relative to 1 nanometer at 1 Hz, TH = = the SNR value in dB to be exceeded before a detection is accepted as an event, and SL = signal loss during the one-line detector processing. It should be noted that m_b in this kind of analysis always refers to NORSAR P-wave magnitude.

DATA ANALYSIS AND RESULTS

In order to solve equation (5) we must know the cumulative probability density distributions (PDD) for the above parameters. It is no problem in the case of the TH parameter as it is a constant having a value of 11.5 dB in the time interval considered. An estimate of the PDD for the STA parameter on an individual beam trace has been obtained from analysis of 2400 noise samples equivalent to 60 min of data in 6 different periods in the interval Dec 71 to Apr 72. The results are shown to the left in figure 2, and it should be noted that the 6 subsamples always within the 2—98% probability interval fell inside the 90% confidence limits also

included in the figure. The given STA distribution passed a lognormal distribution test at the 0.05 level.

The first NORSAR estimation of the magnitude of a specific event is the on-line STA calculation by the event detector. The final magni-

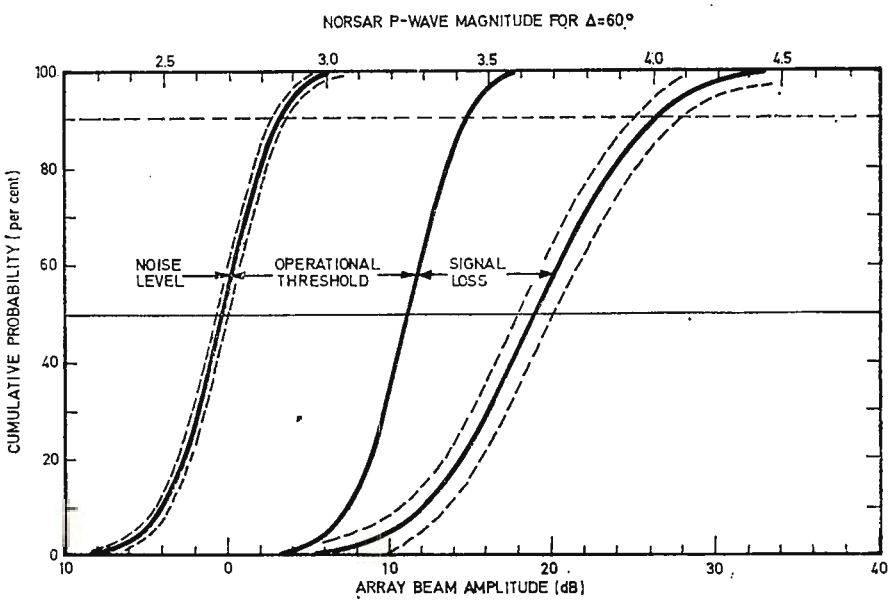

Fig.2. — The first or leftmost curve gives the observed cumulative noise distribution. The second or center curve is obtained by adding the operational threshold parameter of 11.5 dB to the first curve. The rightmost curve is the sum of the center curve and the observed cumulative loss distribution for Zone 1 in table 1. The dotted lines show the 90 % confidence intervals of the leftmost and rightmost curves.

tude value is based on the analyst's measurements of P-wave amplitude and period after the best possible array beam has been found. In other words, the difference between log (A/T) and log (STA), which in this case is measured on different types of array beams, is an estimate of the signal losses encountered during the detection processing. In figure 3 log (STA) versus log (A/T) for 800 NORSAR recorded events are plotted. As a rule, STA is significantly less than the corresponding A/T value, which is interpreted in terms of signal energy losses during the on-line event detection processing. Factors of importance here are the inevitable smoothing operations in the array software system, linear instead of square

detector, a finite number of beams deployed (fig. 4), signal incoherency, travel time anomalies, etc. The sum of the cumulative distribution for *NL*, *TH* and *SL* is shown to the left of figure 2 where also the corresponding m_b magnitude for an epicentral distance of 60 deg is included. The

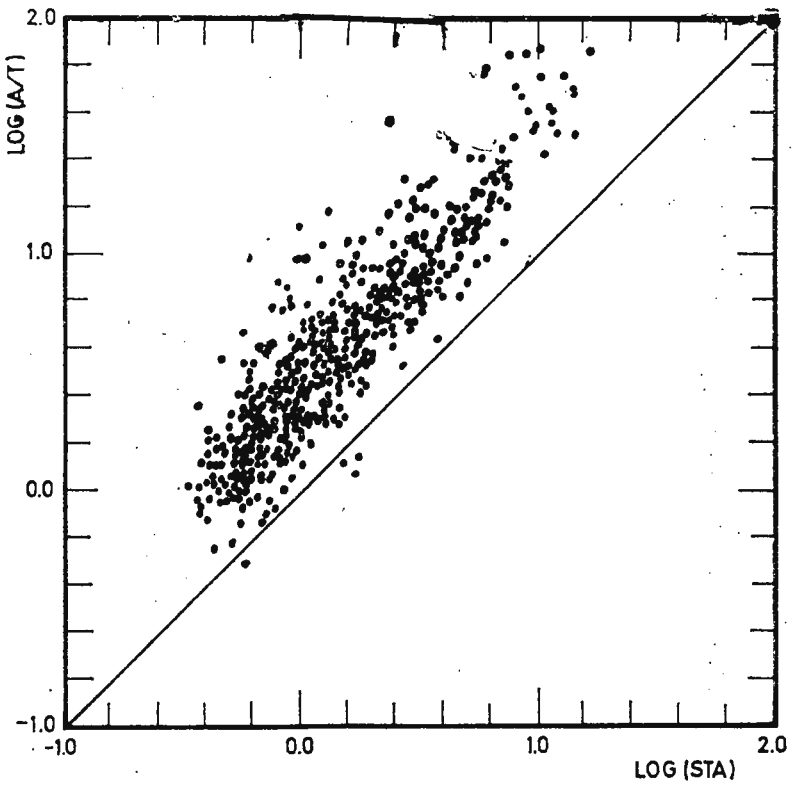

Fig. 3. — Log A/T versus log STA after special scaling factors have been removed for 800 *P*-signals recorded in March and May 1972. The STA values are those measured on the actual array beam at signal detection, while the A/T values are those measured by the analyst after the best possible array beam has been found.

50 and 90 per cent m_b probability event detection levels are given by solid and broken lines.

CONCLUSIONS

As a check of the validity of the procedure we have undertaken a comparison between predicted and observed event detection capabilities (B u n g u m, 1972) in terms of NORSAR m_b thresholds. The results

are given in table 1. For the individual regions, the *PDD* models of the signal loss parameter *SL* have been recomputed. In the case of predicted magnitude levels, the $Q(\Delta, h)$ term in eq (3) was given a value corresponding to the average epicentral distance and normal focal depth for the events located within the respective zones.

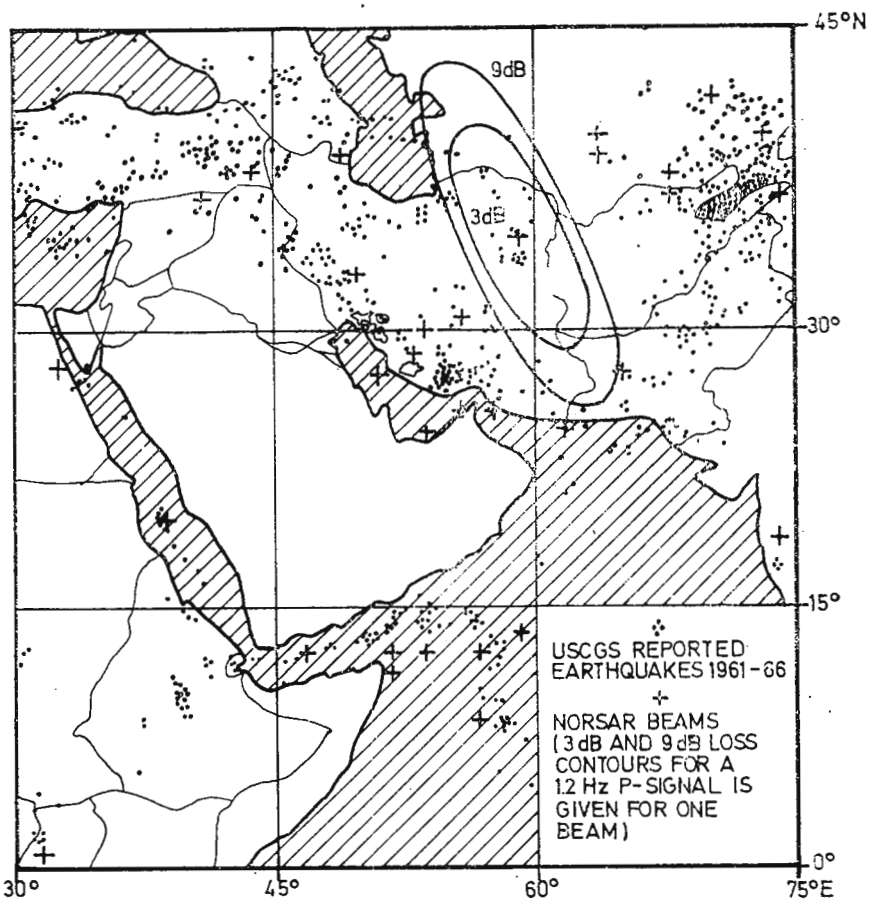

Fig.4. — Earthquake activity and NORSAR beam deployment in the Iran region. It should be noted that due to special array time delay corrections it is no simple relationship between beam locations and seismic activity.
(NORSAR magnitude recurrence relation for observed events in zone 8 in table 1).

DISCUSSION

From table 1 it is obvious that the predicted and observed 90 per cent cumulative m_b event detectability exhibit good similarities, and this result confirms the validity of the method used. For more details here,

TABLE 1

Observed and predicted m_b detectability levels for the NORSAR array

No.	ZONE Name	ZONE LIMITS		OBSERVED m_b LEVELS			PREDICTED m_b LEVELS		
		Azi (deg)	Dist (deg)	No. of Events	50 %	90 %	No. of events for *SL* estimates	50 %	90 %
1	P-zone	0—360	30—90	1555	3.57	4.03	548	3.63	4.01
2	Atlantic	180—260	39—90	88	3.64	4.26	13	3.69	4.23
3	N. America	260—340	40—90	114	3.72	4.06	98	3.66	4.05
4	Aleutian Is.	340—15	30—90	131	3.40	3.90	17	3.62	3.95
5	Japan	15—70	50—90	738	3.66	4.07	236	3.61	3.95
6	C. Asia	40—110	30—90	211	3.21	3.60	58	3.45	3.87
7	Iran (1)	110—180	30—90	262	3.45	3.80	38	3.51	3.88
8	Iran (2)	110—130	35—50	188	3.42	3.78	31	3.49	3.83

Note: The observational data (B u n g u m, 1972) covers the interval Feb—June 1972

we refer to a forthcoming paper by B e r t e u s s e n, H u s e b y e[2]. The above approach may be adapted to the problem of predicting event detection thresholds for conventional seismograph stations. In this case we also have to define the operational noise level, try to estimate the threshold of the subjective analyst event detection procedure and finally replace the *SL* parameter with a regionalized station sensitivity parameter.

Acknowledgement

The NORSAR research project has been sponsored by the United States of America under the overall direction of the Advanced Research Projects Agency and the technical management of the Electronic Systems Division, Air Force Systems Command, through Contract No. F19628—70—C—0283 with the Royal Norwegian Council for Scientific and Industrial Research.

REFERENCES

B u n g u m H. (1972) An evaluation of the routine processing of events at NORSAR. *Proceedings*, Seminar on Seismology and Seismic Arrays, NTNF/NORSAR.

[2] B e r t e u s s e n K. A., H u s e b y e E. S. Predicted and Observed Seismic Event Detectability of the NORSAR Array. 1972. NORSAR Techn. Rep. No. 42, NTNF/NORSAR, Kjeller, Norway.

— Husebye E. S., Ringdal F. (1971) The NORSAR array and preliminary results of data analysis. *Geophys. J.R. Astr. Soc.*, 25, London.

Felix C. P., Gilbert W. L., Wheeler S. G. (1972) Preliminary results from the NORSAR system. *Proceedings*, Seminar on Seismology and Seismic Arrays, NTNF/NORSAR.

Flinn E. S., Blandford R. R. , Mack H. (1972) Comments on 'Evidence for higher seismic activity during the night' by Michael Shimshoni. *Geophys. J. R. Astr. Soc.*, 28, London.

Shimshoni M. (1972) Evidence for higher seismic activity during the night. *Geophys. J. R. Astr. Soc.*, 24, London.

IBM (1967) Third Quart. Tech. Rep., ESD—TR—68—149, IBM *Fed. Sys. Div.*, Gaithersburg, Maryland, USA.

ON-LINE EVENT DETECTION USING A GLOBAL SEISMOLOGICAL NETWORK

BY

EYSTEIN S. HUSEBYE, F. RINGDAL, J. FYEN[1]

Abstract

Joint processing of seismic *P*-wave data from the global seismological network has in general been considered impossible due to lack of signal coherency. However, replacing the P-waves with their envelopes will theoretically give high signal similarity, and this has been confirmed by analysis of 2 earthquakes and 1 explosion as recorded by WWSSN stations. Average signal cross-correlation coefficients were around 0.75. Moreover, global envelope beamforming processing is discussed as a method to improve seismic event detectability and the importance of the approximately lognormal P-amplitude probability distribution across the network is demonstrated.

INTRODUCTION

The characteristic feature of a seismic array is real-time processing of data from a large number of sensors organized in a certain pattern on the surface of the earth. The principal aim of array operation is suppression of unwanted noise and at the same time preserving the seismic signals of interest. To achieve the above goal, the noise at different sensors should be independent random processes and the signals should be approximately identical across the array. As is well known, when sensor separation increases, the signal similarity, in general, decreases. The consequence here is that when processing signals from a continental array or the global seismological network, the signal suppression is approximately equal to the noise suppression, resulting in a processing gain close to zero. One possible way to circumvent this problem might be to replace the

[1] NTNF/NORSAR. Post Box 51. N—2007 Kjeller, Norway.

individual signal trace by its envelope as we intuitively should expect this kind of signals to exhibit a large degree of signal similarity independent of sensor separation, seismometer type, etc. The topic of this report is to discuss the feasibility of multiarray analysis through simultaneous processing of signal envelopes from the global seismological network.

P-SIGNAL ENVELOPES AND DATA ANALYSIS

For certain rather simple signal models it is fairly easy to deduct the relationship between the signal and its envelope. Let us assume that the wave profile is split into an infinite number of harmonic waves of the type

$$exp\,|\,2\,\pi i\,(kx - vt)\,| \tag{1}$$

where k is wave number, v is wave velocity, x is distance and t is time. The amplitudes of these component waves are assumed to have a Gaussian distribution, i.e.,

$$a\,(k) = A \cdot exp[(k - k_o)^2 \cdot \sigma] \tag{2}$$

In this case the envelope Y of the so-called Gaussian wave packet would be for non-dispersive signals (C o u l s o n, 1961)

$$Y = A \cdot (\pi/\sigma)^{1/2} \cdot exp[-\pi^2 (x - vt)^2/\sigma] \tag{3}$$

If we define the half-width of the envelope as the value $(x - vt)$ that reduces the amplitude to $1/e$ times its maximum value, it would then be $(\sigma^{1/2})\,/\pi$ for the wave packet considered. As the signal envelope shape is a function of only σ or signal spectral bandwidth we would expect high similarities between short period P wave envelopes even if the signal waveforms are uncorrelated.

It has been verified, using the Kolmogorov-Smirnov test on normality, that the above model is not unreasonable for describing the dominant part of P-signal spectra. However, the straightforward way of checking P-wave envelope similarity is to perform correlation and coherency analysis of digitized seismic signals recorded by WWSSN stations around the world. This has been done for two earthquakes, Chile 12/20/66 and Solomon Islands 08/20/66, and the Greeley nuclear explosion in Nevada

12/20/66. In figure 1 some of the P-signal and envelope traces for the Chilean event are shown. It should be noted that in this analysis the envelopes have been defined as the average of absolute P-signal amplitudes in a window of 1.5 s length and using a sampling rate of 0.1 s. The average

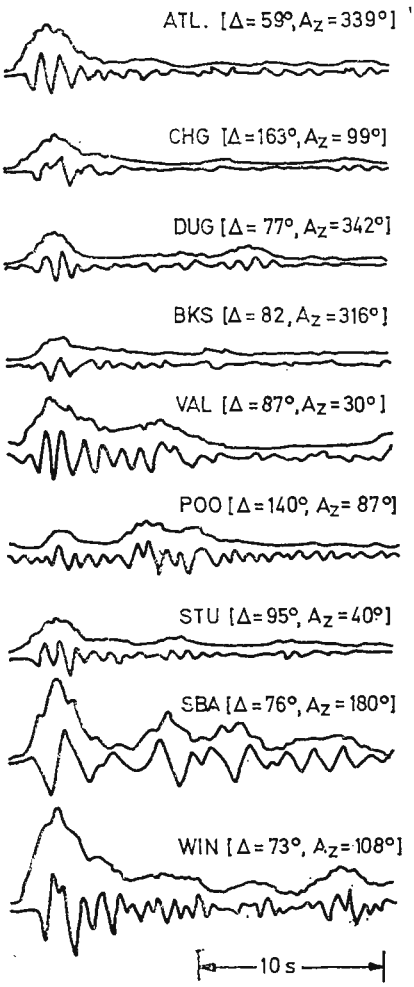

Fig.1. — P-signal and envelope traces for an earthquake in Chile 12/20/66 and recorded by globally distributed WWSSN stations. Distance and epicenter azimuth are given in the figure.

cross-correlation values for all paired envelope combinations for the mentioned events are presented in figure 2 as a function of station separation. A more extensive check on signal envelope similarities was obtained by comparing P-wave envelopes calculated from 20 different earthquakes recorded by the NORSAR array. These events occurred in the interval

Feb-June 1972 and the epicentral distance range was 3—145 deg. Also power spectra of *P*-signal and noise envelopes have been computed, and are displayed in figure 3. A brief summary of the results of the above analysis is as follows:

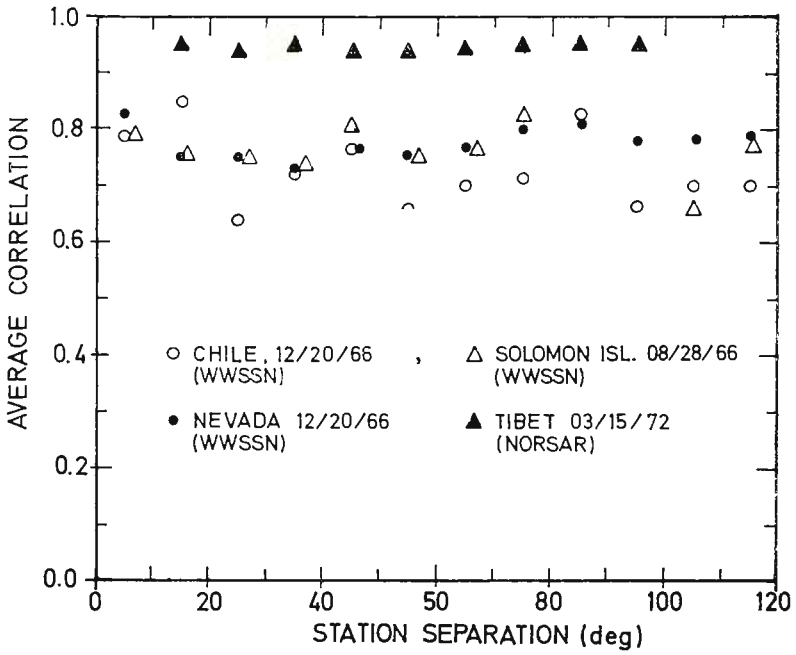

Fig.2. — Average of cross-correlation values for all paired station combinations as a function of station separation. When $\Delta \geqslant 120°$ the distance separation is set equal to 120°. For the NORSAR recorded event, the station separations are in km. Time window length was 12 s.

a) The average envelope correlation coefficient for all station combinations is approximately 0.75. Similar values were obtained for the combination of the 20 different NORSAR recorded events. The corresponding value for the unmodified *P*-signals was around 0.3.

b) Typical values for envelope coherency were around 0.75 units and decreased slowly with increasing frequencies.

c) The noise and signal envelope spectra contain relatively much low frequency energy and have roughly identical shapes. This means that the envelope traces of short periodic signals have a resolution in frequency-wavenumber space which is not unlike that of surface waves and long period *P* and *S* waves.

d) The spectral shape similarity between noise and signal envelopes makes it difficult to obtain signal-to-noise ratio (SNR) improvements by bandpass filtering. However, substantial SNR gains are possible by prefiltering the original P-wave traces as expected from eq (2) and this has also been verified experimentally (F e l i x et al., 1972).

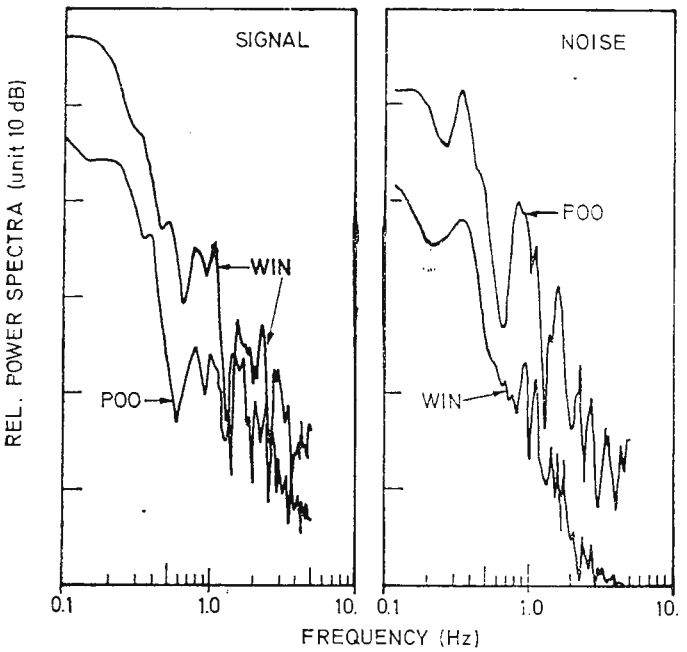

Fig. 3. — Relative signal and noise envelope spectra for WIN (S.W. Africa) and POO (India) for an earthquake in Chile 12/20/66. A spectral window length of 20 s was used.

So far we have demonstrated that the signal envelopes exhibit sufficient signal similarity so that an ensemble of such stations might be considered a continental or global array. The main advantage of such a system would be to improve the global seismic event detectability based on array detection processing on envelope beams. An example of the response pattern for a global network comprising 19 WWSSN stations for the Greeley nuclear explosion is shown in figure 4. In principle, array beamforming is a very simple operation, namely, to add a number of signals which have been properly lined up by using a standard travel time table and certain time correction files. The latter is not very important for envelope signals due to the relatively long periodic nature of these waves. The main

question when considering the potential of the global network is the possible gain in seismic event detectability and whether this kind of processing is technically feasible, and we will try to answer both of these questions.

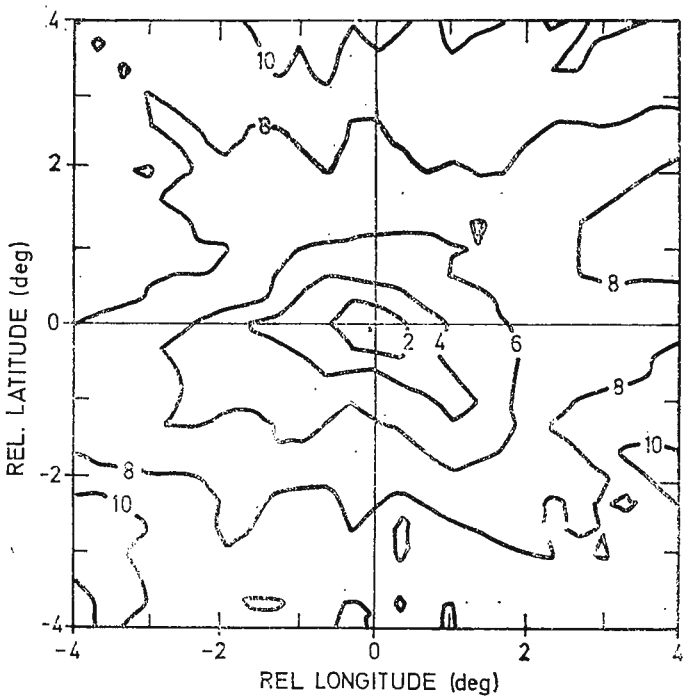

Fig.4. — Response pattern for the Greeley nuclear explosion in Nevada 12/20/1966 based on envelope traces for 19 WWSSN stations.

EVENT DETECTABILITY USING *P*-SIGNAL ENVELOPES

Beamforming processing on envelope traces does not give any noise suppression, and thus does not enhance the signal-to-noise ratio (*SNR*). However, the envelope beam exhibits a noise variance which is reduced by a factor of N (= no. of sensors) from the single sensor level, so that the event detectability is improved by a factor of $\sqrt{N}$. For more details, see Ringdal et al[2].

[2] Ringdal F., Husebye E. S., Dahle A. Event detection problems using a partially coherent seismic array. 1972. NORSAR—Techn. Rep. 45, NTNF/NORSAR, Kjeller, Norway (in press).

Actually, it is possible to have additional pseudo gains in detectability for envelope processing, and two ways are pointed out here. The first is to provide *P*-wave noise suppression by bandpass filtering, as mentioned above. Another gain factor is to restrict the global network to excep-

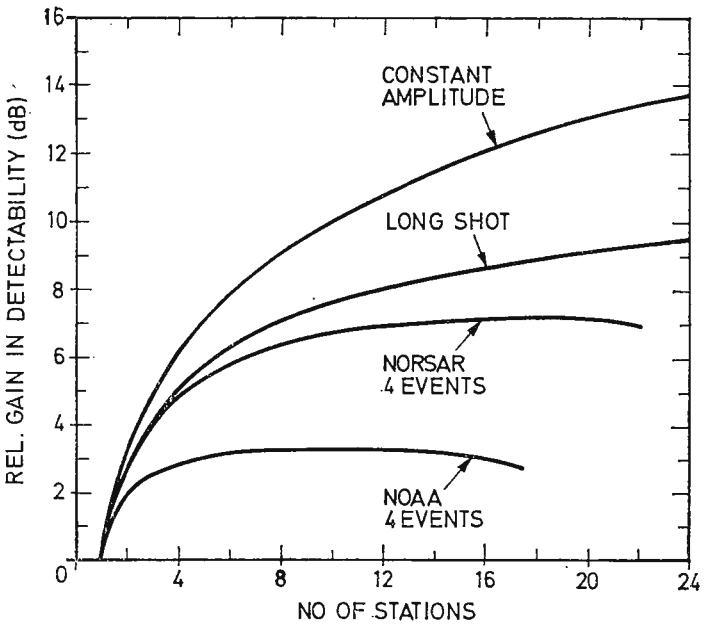

Fig.5. — Gain in event detectability relative to the station having the largest amplitude. Eq (4) was used, and the noise level was taken as a constant. The NORSAR and NOAA events used in analysis, were picked randomly from their respective bulletins.

tionally good stations, thus working on the tail of the signal amplitude probability distribution. From theoretical considerations we should expect the signal amplitude distribution across a number of stations to be log-normal and this hypothesis has been supported by relevant data analysis [3]. Using this model and estimating the parameters involved, it is possible to theoretically predict the cost/performance trade-off regarding the number of stations required for optimum event detectability.

The importance of the statistical amplitude variations of *P*-waves in the teleseismic range 30—90° using data from NOAA, NORSAR and Long Shot (L a m b e r t et al., 1969) is demonstrated in figure 5. Here,

[3] *Op. cit.*, p. 2.

the seismic stations were ranked according to their amplitude value for the event in question, and detectability $D(n)$ was computed using the n best stations as follows:

$$D(n) = \sqrt{n} \cdot \sum_{i=1}^{n} (A_i - N_i) / \sum_{i=1}^{n} N_i \qquad (4)$$

where A_i is maximum signal envelope amplitude and N_i is average noise envelope amplitude for the station with rank i.

It is very interesting to note that the number of stations actually needed for optimum event detectability in a given seismic region is remarkably few, as around 8—16 stations are required for ensuring maximum envelope processing gain for all practical purposes. However, for global seismicity coverage many more stations are required due to intrinsic amplitude variations. A typical example here is the NORSAR array where the signal amplitudes for one subarray may be consistently large for one region and poor for another region as shown in figure 6. Correspon-

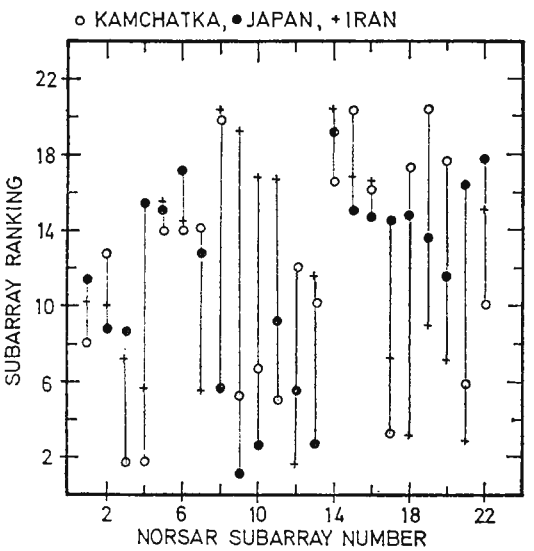

Fig. 6. — NORSAR subarray amplitude ranking for earthquakes occurring in the Kamchatka, Japan and Iran regions. The number of events used in analysis was 21, 16 and 10 respectively. In each case the Kendall rank correlation test (S i e g e l, 1956) gave highly significant results.

ding relations apply to the global network (fig. 7), and the best detectability performance is almost exclusively restricted to small arrays like UBO, TFO, WMO, BMO, LHN and the LF4 subarray in LASA. These results were based on Japanese earthquakes and using data published by ISC for the year 1968.

FEASIBILITY OF GLOBAL NETWORK ENVELOPE PROCESSING

It is difficult to five quantitative values for the potential improvement in event detectability on a global basis as noise suppression due to bandpass filtering and relative station amplitude excitation information are not easily obtainable. However, the essential feature of envelope

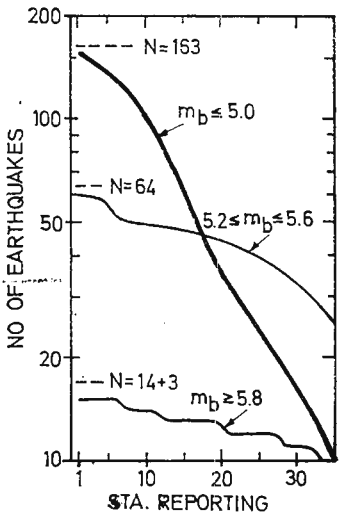

Fig. 7. — No. of stations in the global network reporting earthquakes occurring in the Japan region during 1968. The parameter N gives the total no. of events within each magnitude interval. The data used was taken from ISC bulletin files.

processing as outlined above is a net gain in event detectability when the number of seismic stations considered increases. This is contrary to previously proposed multiarray processing schemes or global network analysis where the final event detectability is taken as a function of the individual station event detection probabilities (Anonymous, 1969; Witham, 1972). In such cases it is difficult to have significant improvements beyond that of the most sensitive station in the network considered.

Finally, we should like to forward some comments on the technical implications of real-time multiarray processing. First of all, restricting the network processing to envelope traces means that a 2 or 1 Hz sampling rate would be sufficient. Data transmission to a common processing center could thus easily be achieved as a standard telephone line can handle at least 75 envelope traces. At present, the large aperture arrays ALPA (Alaska,) LASA (Montana) and NORSAR (Norway) are exchanging seismic data in real time via the telephone network and a communications satellite. It would be feasible within a global seismic network as outlined

above to include the envelopes of the 300 array beams deployed at LASA and NORSAR as single, highly sensitive channels. These beams could then be combined with traces from single stations or smaller arrays in the subsequent joint envelope beamforming. Due to the small sampling rate and relatively long periodic nature of the signal envelopes, a small computer could handle the required detection processing, including deployment of a few thousand beams required for adequate coverage of all seismic regions.

Acknowledgement

The NORSAR research project has been sponsored by the United States of America under the overall direction of the Advanced Research Projects Agency and the technical management of the Electronic Systems Division, Air Force Systems Command.

REFERENCES

Anonymous (1969) Integrated Seismic Research Signal Processing System IBM. 3rd Quarterly Report, ESD—TR—70—25.

Coulson C. A. (1961) Waves. 7th Ed., Oliver & Boyd Ltd., Edinburgh.

Felix C. P., Gilbert W. L., Wheeler S. G. (1972) Preliminary results from the NORSAR system. *Proceedings.* Seminar on Seismology and Seismic Arrays, NTNF/NORSAR, Kjeller, Norway.

Lambert D. B., Von Seggern D. H., Alexander S. S., Galat G. A. (1969) The Long Shot Experiment. *Seismic Data Lab.*, Alexandria, Virginia.

Siegel S. (1956) Nonparametric Statistics. McGraw-Hill, New York.

Whitham K. (1972) An assessment of the present seismological capability for the detection, location and identification of underground nuclear explosions. *Proceedings.* Seminar on Seismology and Seismic Arrays. NTNF/NORSAR, Kjeller, Norway.

EVENT DETECTION PROBLEMS USING A PARTIALLY COHERENT SEISMIC ARRAY

BY

F. RINGDAL, EYSTEIN S. HUSEBYE, A. DAHLE[1]

Abstract

Seismic event detection by conventional beamforming does not always produce good results for a large aperture seismic array. This may be due to poor signal coherency or beamforming loss by missteering. An „incoherent beamforming detector" is described in this paper as a method to improve array detectability in such cases. This detector, which essentially consists of beamforming on *P*-wave envelopes, has been implemented in the NORSAR processing system and relevant results are presented and discussed in this paper. The incoherent detector is shown to be superior to the conventional in detecting near regional events and underground explosions. The statistical distribution of signal amplitudes across a network of sensors is found to be lognormal. Implications of this factor on event detectability by conventional and incoherent beamforming are discussed.

INTRODUCTION

The continuous operation of a large aperture seismic array requires a device for automatically detecting incoming signals generated by earthquakes and underground explosions. The obvious reason for this is the large number of beams that must be deployed to ensure adequate surveillance of the global seismic activity. The individual array beams, which are essentially phased sums of single sensor traces, have to be monitored continuously to identify possible arrivals of seismic wave energy.

The main problem encountered when designing an automatic event detector is to maximize signal-to-noise ratio (SNR) for seismic signals

[1] NTNF/NORSAR, N—2007 Kjeller, Norway.

relative to the variability of the seismic noise. Several factors have to be considered to achieve this goal. Bandpass filtering makes it possible for the detector to operate in that part of the frequency domain where SNR is best in average. For individual sensor traces at NORSAR, this is known to occur at fairly high frequencies, i.e., around 2 Hz. The variability of the seismic noise, and thereby the false alarm probability, has been shown by Lacoss (1972) to be lowest for high filter frequency. On the other hand, array beamforming loss increases sharply with increasing signal frequency, thus necessitating a trade-off between the above factors to improve array detectability. Another factor complicating the array response is the large signal amplitude variations between sensors which in extreme cases may reach a factor of 20. Typically, a few sensors may be consistently good for events in one seismic area, but consistently poor for other regions.

The purpose of this paper is to discuss some topics relevant to seismic array event detection. In particular we want to present results from

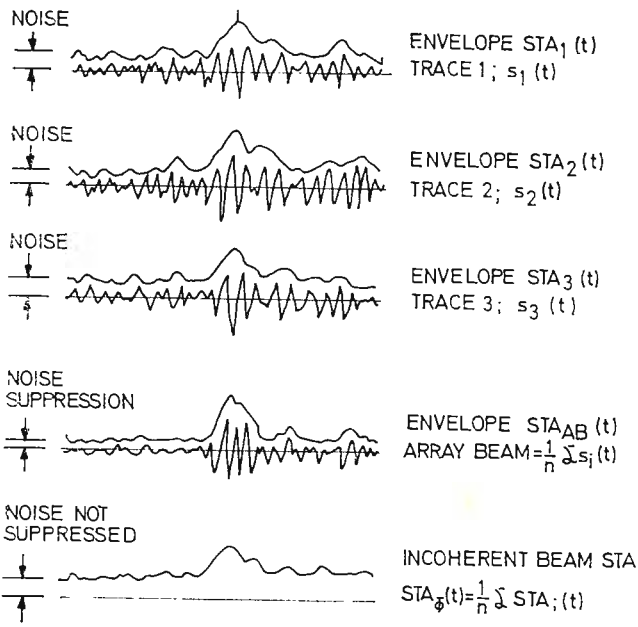

Fig. 1. — Principles of coherent and incoherent beamforming. The signal envelopes represent STA values over a 1.5 second sliding integration window.

the „incoherent beamforming detector" implemented at the NORSAR data center by NTNF personnel in 1972. This detector, which was first suggested by Felix et al. (1972), consists in principle of forming the so-called incoherent array beams by adding together envelopes of subarray beams after proper time delays have been introduced (fig. 1).

We also investigate theoretically the statistical amplitude distribution across a seismic array, and present some implications of this factor for the event detectability.

In Section 2 event detectors will be discussed in general, while Section 3 deals more closely with the relationship between coherent and incoherent beams. A seismic event detectability comparison is worked out in Section 4. In Section 5 a theoretical explanation of the observed log-normal signal amplitude distribution across a network of sensors is given. Finally, relevant data analysis is presented in Section 6 to test the theoretical models described previously on real seismic signal data. Section 7 gives a brief discussion of the obtained results.

EVENT DETECTOR DESIGN

The fundamental characteristics of an array is its capability of suppressing ambient noise by beamforming. In practice, a sensor spacing of minimum 3—4 km and an array diameter of up to a few hundred kilometers ensures uncorrelated noise between sensors while retaining reasonable signal coherency across the array. The NORSAR array has been constructed according to this principle. For a more detailed description of the NORSAR hardware and software, we refer to Bungum et al. (1971).

The event detector implemented by IBM personnel is a conventional beamforming detector, deploying around 300 array beams in real time. Prior to the beamforming, all sensors have been bandpass filtered for additional noise suppression. A near-continuous signal-to-noise ratio test is applied to each individual beam, the signal and noise estimates being based on rectified and averaged amplitudes. In the following, these estimates have been denoted short term average and *(STA)* long term average (*LTA*) respectively. Theoretically, a detector using signal power estimates should be superior to the linear detector, but the practical difference between the two methods appears to be insignificant[2].

Mathematically, the array beamforming may be formulated as follows :

$$AB_C(l) = \sum_{i=1}^{N} S_i(l - \tau_i) \tag{1}$$

[2] Berteussen K. A. Seismic event detection problems with special reference to the NORSAR array. 1972. Thesis, Bergen University, Bergen, Norway.

where $S_i(t)$ is the filtered seismometer trace and τ_i is the appropriate beamforming time delay, $i = 1, 2, \ldots N$.
The short term beam average STA_C is then computed as follows

$$STA_C(t) = \sum_{i=1}^{IW} |AB_C(t - i + 1)| \tag{2}$$

where IW is integration window in deciseconds, typically 15.

The principle of the incoherent detector is to invert the sequence of beamforming and rectification. Mathematically :

$$AB_I(t) = \sum_{i=1}^{N} |S_i(t - \tau_i)| \tag{3}$$

$$STA_I(t) = \sum_{i=1}^{IW} AB_I(t - i + 1) \tag{4}$$

In the NORSAR on-line system, array beamforming has been implemented as a two-step process, the first step being subarray beamforming for each of the 22 subarrays. Signal coherency across a subarray is in general much better than between subarrays. As is shown in Section 3, the incoherent beamforming method is superior to conventional beamforming only if signal coherency is poor. Consequently, it was decided to implement an incoherent detector based on rectified subarray beams rather than single sensor traces in the NORSAR Detection Processor.

The incoherent beamforming method is able to take advantage of high SNR in high frequency bands observed at NORSAR. In the initial implementation, a 1.6—3.2 Hz bandpass filter was used in connection with this method, while the conventional beamforming filter was 1.2——3.2 Hz at the time.

Several other detectors have been developed for seismic arrays, but lie outside the scope of this article. We restrict ourselves to briefly mentioning the Fisher detector which was first suggested by M e l t o n and B a i l e y (1957). The operating principle of this detector is to substract each signal trace from the beam, and then divide the beam power with the average power of all such differences. This detector has a well-known statistical distribution, and has been demonstrated in an

operational mode [3]. The Fisher detector requires coherent signals across the array and well-equalized amplitude responses between sensors for optimum performance.

It should finally be noted that in many cases sophisticated detection algorithms amy be simply ruled out in the design of real-life detectors. This may be due to computer processing limitations, or because the detector may be too sensitive to deviations from the theoretical model.

COHERENT AND INCOHERENT BEAMFORMING

In this section we will study the relationship between signal-to-noise ratios for the coherent and incoherent beams. Suppose n channels are available for the beamforming process. The time series may e.g.be filtered seismometer traces, filtered subarray beams or a combination. During noise conditions the channels are assumed to be independent, stationary Gaussian processes $N_i(t)$, $i = 1, \ldots, n$. The occurrence of a seismic signal implies an additional term $S_i(t)$ to be added to each channel. We assume also that the $S_i(t)$ are Gaussian processes of short duration.

The signal-to-noise ratios SNR_C and SNR_I for coherent and incoherent beams respectively are defined as the quotients between a short term average (STA) and long term average (LTA) for the beams. The STA and LTA are calculated by averaging the rectified beams over short (typically 1.5 seconds) and long (typically 30 seconds) periods of time. A detection is declared if SNR_C or SNR_I exceed predefined thresholds. Note that SNR_I and SNR_C are well defined whether or not a seismic signal is present. We will now develop the relationship between SNR_I and SNR_C a seismic signal occurs and assume that

$$STA\,(S_i + N_i) = c \cdot \sigma\,(S_i + N_i) \qquad i = 1, \ldots, n \tag{5}$$

$$LTA\,(N_i) = c \cdot \sigma(N_i) \qquad i = 1, \ldots, n$$

where σ denotes the standard deviation of the Gaussian process and c is a constant. For simplicity, the time variable in $S_i(t)$ and $N_i(t)$ has been omitted. Note that (5) is a reasonable assumption since $E(|X|)$ is proportional to σ when X is Gaussian $(0, \sigma)$.

[3] Edwards J. P., Benno S. A., Creasey G. Evaluation of the CPO auxiliary processor. 1967. CPO Spec. Rep. No.5, Texas Instrument Sci. Serv. Div., Dallas, Texas, U.S.A.

In the coherent case this yields:

$$SNR_C = \frac{STA\left(\sum_{i=1}^{n}(S_i + N_i)\right)}{LTA\left(\sum_{i=1}^{n} N_i\right)} = \frac{\sigma\left(\sum_{i=1}^{n}(S_i + N_i)\right)}{\sigma\left(\sum_{i=1}^{n} N_i\right)} = \tag{6}$$

$$= \left(1 + \frac{\sigma^2\left(\sum_{i=1}^{n} S_i\right)}{\sigma^2\left(\sum_{i=1}^{n} N_i\right)}\right)^{1/2}$$

Since noise is independent between channels:

$$\sigma^2\left(\sum_{i=1}^{n} N_i\right) = \sum_{i=1}^{n} \sigma^2(N_i)$$

For the signal we will introduce a parameter q by setting

$$\sigma\left(\sum_{i=1}^{n} S_i\right) = \sqrt{q} \cdot \sum_{i=1}^{n} \sigma(S_i) \tag{7}$$

The variable q lies between 0 and 1, and depends upon signal coherency as well as sampling loss and channel misalignment. If sampling and alignment losses can be disregarded, q is related to the average signal cross-correlation $\bar{\rho}$ through the standard gain formula for seismic arrays:

$$q = \frac{1}{n} + \left(1 - \frac{1}{n}\right)\bar{\rho} \tag{8}$$

By combining eq. (5), (6) and (7) the result is

$$SNR_C = \left(1 + q \cdot \frac{\left(\sum_{i=1}^{n} \sqrt{STA_i^2 - LTA_i^2}\right)^2}{\sum_{i=1}^{n} LTA_i^2}\right)^{1/2} \tag{9}$$

where $LTA_i = LTA(N_i)$ and $STA_i = STA(S_i + N_i)$.

In the simplified case that all $LTA_i = LTA$ and all $STA_i = STA$. $i = 1, \ldots, n$, eq. (9) reduces to :

$$SNR_C = \left[1 + n \cdot q\left(\left(\frac{STA}{LTA}\right)^2 - 1\right)\right]^{1/2} \tag{10}$$

For incoherent beamforming, the loss due to signal incoherency and misalignment is assumed to be negligible, and we may then write :

$$SNR_I = \sum_{i=1}^{n} STA_i / \sum_{i=1}^{n} LTA_i \text{ or } SNR_I = STA/LTA \tag{11}$$

in the simplified case considered above.
A combination of eq (10) and eq (11) gives :

$$SNR_C = [1 + n \cdot q(SNR_I^2 - 1)]^{1/2} \tag{12}$$

Thus we have developed a relationship between coherent and incoherent signal-to-noise ratio, assuming that identical bandpass filters are being used and that all sensors are well equalized.

DETECTABILITY CONSIDERATIONS

A theoretical comparison between Receiver Operating Characteristics (ROC) for the two beamforming methods requires a knowledge of the statistical distributions of STA_C and STA_I during noise conditions. Experimentally, it seems reasonable to assume that STA of either a single channel or a coherent beam is lognormally distributed, i.e., log STA is a Gaussian random variable (L a c o s s, 1972). STA_C may therefore be considered lognormal. However, in the incoherent case, we have to consider a sum of independent (lognormal) variables, and by the Central Limit Theorem, STA_I will approach a Gaussian distribution as the number of channels (n) becomes large.

As a first order approximation to a ROC evaluation, we will consider the „normalized" variables :

$$X_I = [STA_I - E(STA_I)]/\sigma(STA_I) \text{ and}$$

$$X_C = [STA_C - E(STA_C)]/\sigma(STA_C) \tag{13}$$

σ and E denote the statistical standard deviation and expectation of the time series STA_C and STA_I during stationary noise conditions.

For a given seismic event, the values of X_I and X_C will then tell how „well" the event can be detected by the two methods.
It is not difficult to see that:

$$\frac{\sigma(STA_C)}{E(STA_C)} = \sqrt{n} \cdot \frac{\sigma(STA_I)}{E(STA_I)} \tag{14}$$

In other words, the incoherent beam suppresses „noise variability" by a factor $\sqrt{n}$, while the coherent beam of course suppresses „noise level" by $\sqrt{n}$.

Setting $STA_I/E(STA_I) = SNR_I$ and $STA_C/E(STA_C) = SNR_C$ and combining expressions (13) and (14) with expressions (10) and (11) we obtain:

$$R = \frac{X_C}{X_I} = q \cdot \sqrt{n} \cdot \frac{1 + \sqrt{1 + (SNR_C^2 - 1)/nq}}{1 + SNR_C} \tag{15}$$

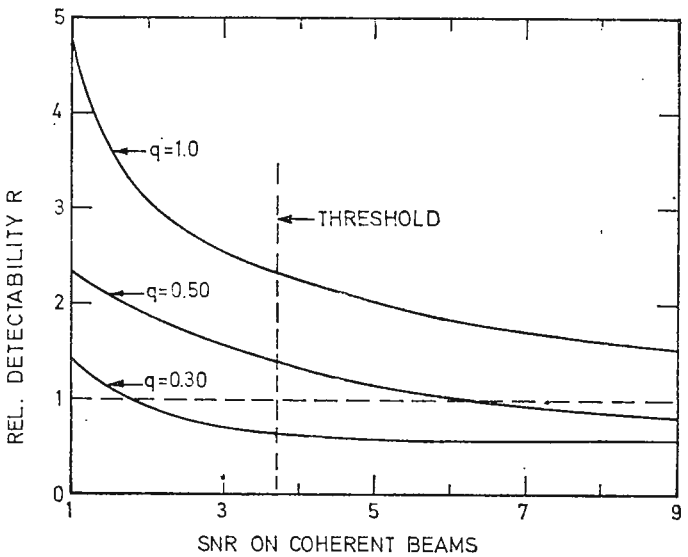

Fig. 2. — Seismic event detectability comparison between coherent and incoherent array beams as defined in eq (15). Only for small q-values will incoherent beamforming be superior to coherent beamforming.

The ratio R is sketched in figure 2 for $n = 22$ and different values of q. From this figure it can be seen that unless q is very small, the conventional beamforming has a better detectability for small events. Even with

$q = 0.5$ the coherent detector is better for events close to the NORSAR false alarm threshold (SNR_C 3.5 to 4.0). Thus only in cases of poor signal coherency, the incoherent detector can be expected to contribute to an array's theoretical detection capability. In practical operation, however, the narrow main lobes of the coherent array beams makes the conventional beamforming vulnerable to loss due to missteering. In should be noted that the main advantage of incoherent beamforming is its good areal coverage due to the relatively long periodic nature of the envelope traces (fig. 1). Thus in an operational environment, where only a limited number of beams may be deployed, the picture will turn out to be greatly more favorable to incoherent beamforming than indicated from the theoretical model.

AMPLITUDE DISTRIBUTION

Seismic recordings by laterally distributed seismometers from an arbitrary event show a substantial scatter in P-wave amplitudes. It is reasonable to assume that the size of a specific signal amplitude is tied to the ray path from focus to the sensor site. In this respect we may consider the geological structures that a ray „sees" as a layered earth model consisting of N discontinuities. When traversing the i-th interface, the signals will be modified by a transmission coefficient R_i of which a first order approximation may be expressed as :

$$R_i = 1 - \frac{K_i - L_i}{K_i + L_i} \tag{16}$$

where K_i and L_i are functions of the angle of incidence, velocity and density contrasts at the i-th discontinuity. The corresponding amplitude modulation effect is :

$$A_i = R_i A_{i-1} \tag{17}$$

The above argument leads to the expression

$$A = R_N \cdot R_{N-1} \cdots R_1 A_0 \tag{18}$$

where $A = A_N$ is the observed amplitude. Thus, the reconstruction of an observed P-wave amplitude might be regarded as the joint, multiplicative effect of N mutually independent causes, acting in an ordered sequence and depending on the geological structures encountered along

the ray path. If signals from a seismic event are received at several stations, a set of such transmission coefficients R_i will apply to each receiving site. For each discontinuity surface, the corresponding transmission coefficient for each station is considered as a random value drawn from some common probability distribution characterized by the ray paths and the geological conditions at the boundary. Sufficient station separation will ensure that these values are statistically independent.
Taking the logarithm on both sides of (18) gives :

$$\log A = \log R_N + \log R_{N-1} + \ldots \log R_1 + \log A_0 \qquad (19)$$

$$= \sum_{i=1}^{N} \log R_i + \log A_o$$

The right hand side of (19) is now a sum of independent variables, and considering N a large number, we infer by the Central Limit Theorem that log A is normally distributed. If log A is normally distributed (m, σ), it is easily seen that the variable. A itself has the probability density function

$$\begin{cases} \dfrac{1}{A} \cdot \dfrac{1}{\sigma\sqrt{2\pi}}\, e^{-\frac{(\log A - m)^2}{2\sigma^2}} & A > 0 \\ 0 & A \leqslant 0 \end{cases} \qquad (20)$$

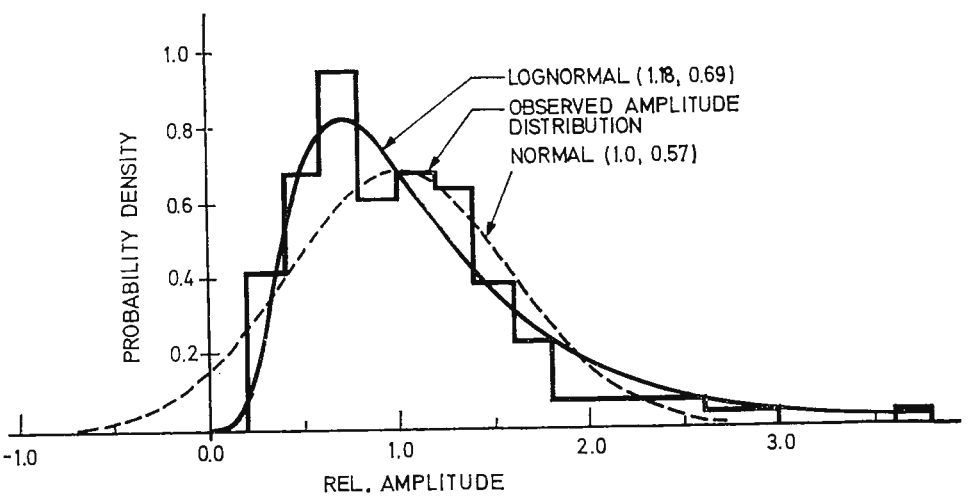

Fig.3. — Observed positive amplitude distribution for an Aleutian Island earthquake with a 1.4—3.8 Hz filter (Event No. 2 in table 4). The normal and lognormal distribution functions estimated from the observed sample mean and variance are also shown.

Purposely, the above discussion is tied to short periodic *P*-waves in the teleseismic range as such signals are likely to „see" many more discontinuities than long periodic *P* and *S* waves. Moreover, attenuation and geometrical spreading effects were ignored in view of the wave type considered. In short, observed *P*-wave amplitudes across a global seismic network or a large array like LASA or NORSAR are expected to be log-normal. In figure 3 the actual amplitude distribution across the NORSAR array for a typical seismic event is shown, together with normal and log-normal frequency functions fitted to the observed data.

DATA ANALYSIS

The on-line implementation of the incoherent beamformer at NORSAR early in 1972 made it possible to monitor closely the performance of this detector over an extended period of time. To verify the relation-

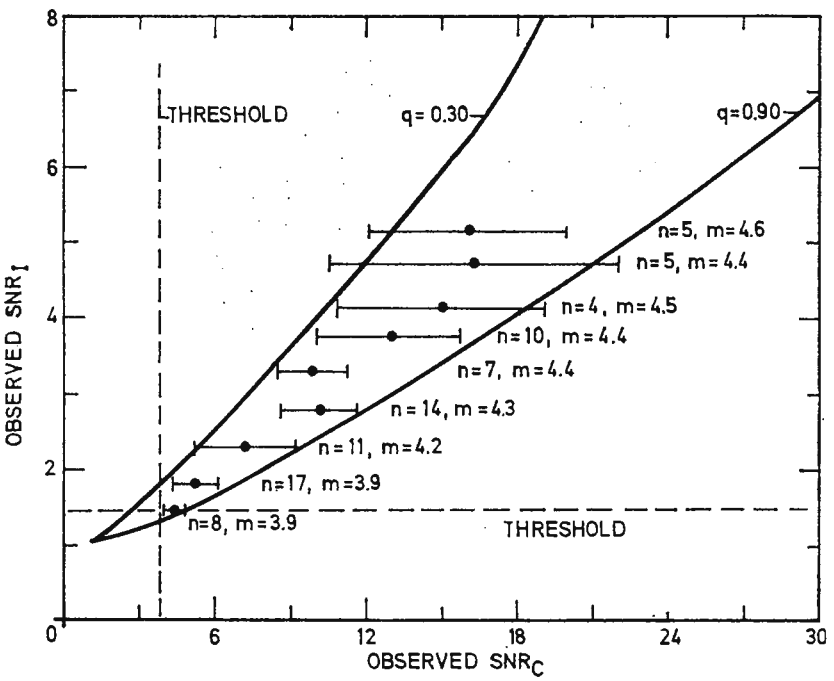

Fig. 4. — A comparison of *SNR* values on the coherent and incoherent array beams as reported by the NORSAR on-line event detector. The 81 earthquakes analyzed occurred in the Japan, Kurile Is., Kamchatka and Aleutian Is. regions in the interval Jan-Mar 1972. Altogether 30 coherent and 3 incoherent array beams were deployed in the above regions, using a 1.2—3.2 Hz bandpass filter. In the figure n is the number of events within a certain SNR_I interval while *m* is the corresponding average of NORSAR observed *P*-wave magnitudes for the *n* events.

ship between signal-to-noise ratios for coherent and incoherent beams developed in Section 3, 81 small and medium size events from the Kamchatka region were selected. A 1.2—3.2 Hz bandpass filter was used for prefiltering of both types of beam traces. The signal-to-noise ratios for these events as determined by the Detection Processor are shown in figure 4.

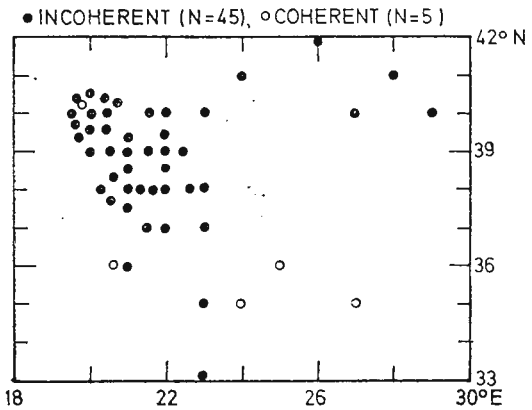

Fig. 5. — Events reported in the final NORSAR bulletin which were detected by either the coherent of the incoherent detector, but not by both. The time period covered is Sept 16-Nov 15, 1972, and typical *SNR* detection thresholds were 3.6 (coherent) and 1.6 (incoherent). The figure shows detection performance in the Mediterranean area.

It appears that the observed data fit the theoretical model reasonably well. The low q values implied from the above figure are mainly caused by the distance separation between the prefixed beam locations and more randomly distributed event locations.

A full-scale incoherent beamforming processor, with a 1.6—3.2 Hz filter, was implemented in the NORSAR Detection and Event Processing system from 16 Sept 1972. This was done while retaining the conventional beamforming detector, which is operated with a 1.2—3.2 Hz filter.

Results from the first two months of parallel operation are presented in figures 5—7, and relevant comments are as follows :

Incoherent beamforming event detection is definitely superior to that of conventional beamforming in the Mediterranean area. This is the case in Western Russia as well, where the conventional beam coverage is poor and the events detected are probably explosions. Also in the Pakistan-Afghanistan region incoherent beams show a better performance. Elsewhere, conventional beamforming, generally, seems to be superior. As to the total number of events detected by the two detectors, regionalization is again instructive as demonstrated in table 1. Coherent beamforming shows the best performance as expected (see Section 4), but this advantage disappears when only high quality events are considered. Here,

„high quality events" refers to clean signal arrivals and dœs not necessarily imply high *SNR* values.

To verify whether the signal amplitude distribution among NORSAR sensors is consistent with the theory developed in Section 5, 9 different events were analyzed (tab. 2). For each event, the largest positive and ne-

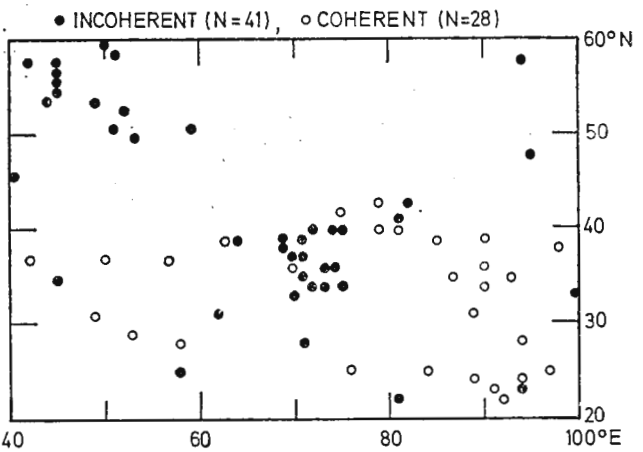

Fig. 6. — Same as figure 5, but covers Russia and Central Asia.

gative amplitude values were extracted for each individual short period sensor. The amplitude data was then subjected to a statistical analysis performed by a Kolmogorov-Smirnov limiting distribution test. A specified theoretical distribution function being the hypothesis, the maximum difference D between the empirical and theoretical cumulative distribution

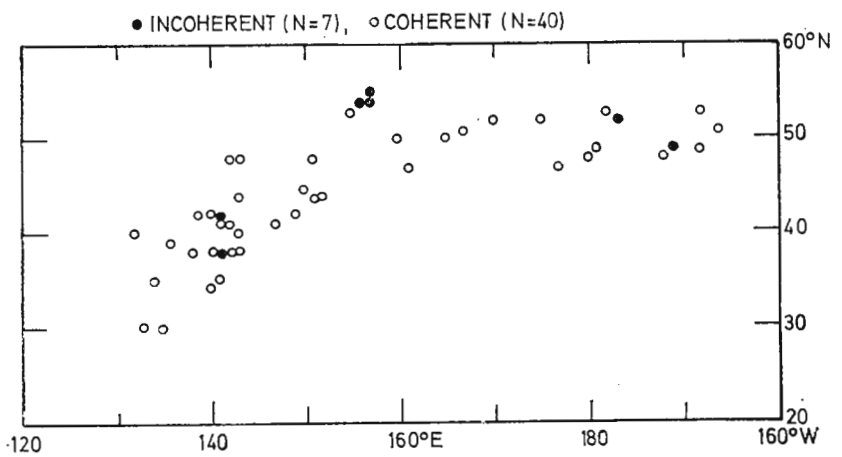

Fig. 7. — Same as figure 5, but covers the Aleutian-Kurile-Kamchatka-Japan area.

TABLE 1

Events reported in the NORSAR seismic bulletin (16 Sep—15 Nov 1972)

No.	ZONE Name	EVENTS Total No.	COH. BF Only No.	INC. BF Only No.	COH. & INC. No.	COH. BF Total No.	%	INC. BF Total No.	%
1	Greece/Turkey	117	5	45	67	72	62	112	96
2	USSR/Cent. Asia	194	28	41	125	153	79	166	86
3	Japan/Kam./Aleu.	168	40	7	121	161	96	128	76
4	USA/Cent. America	64	31	1	32	63	9	33	51
5	Global I (All Events)	1038	242	133	663	905	87	796	77
6	Global II (High Quality Events)	546	24	25	497	521	95	522	95

Note: The table gives the total number and percent of events detected in different regions by the coherent and incoherent beamforming as well as the number of events detected only by one of these detectors.

TABLE 2

Events used for analysis of sensor amplitude distribution

EVENT NO.	DATE 1972	ORIGIN TIME (h min s)	LATITUDE deg	LONGITUDE deg	M_B	REGION
1	12 Aug	09 42 00	50.3 N	177.8 W	5.6	Aleutians
2	28 Aug	15 20 54	50.2 N	178.1 W	5.3	Aleutians
3	03 Jan	06 36 44	52.3 N	158.4 E	5.0	Kamchatka
4	24 Mar	22 56 18	51.7 N	158.8 E	5.0	Kamchatka
5	28 Mar	04 21 45	48.2 N	80.4 E	5.1	Kazakh
6	05 Apr	05 36 57	41.5 N	142.3 E	5.3	Japan
7	11 May	00 44 54	42.2 N	143.9 E	5.6	Japan
8	31 Mar	02 58 19	38.1 N	21.8 E	4.7	Greece
9	11 Apr	02 21 12	0.3 N	29.3 W	6.0	C. Mid-Atlantic Ridge

Note: All epicenter parameters are as reported in the NORSAR seismic bulletin.

function was computed. The statistic $Z = \sqrt{n}\, D$, where n is sample size, was used as a test value. Finally, the probability P_I of doing an error when rejecting the hypothesis was estimated. The theoretical distributions under consideration were: The normal (Gaussian), lognormal and exponential probability functions. Tables 3 and 4 give the scores obtained for the events listed in table 2. Filters of 1.0—3.4 Hz and 1.4—3.8 Hz respectively were applied to the sensor traces prior to the amplitude mea-

TABLE 3

Quality of fit scores for P-wave amplitude distributions obtained in Kolmogorov-Smirnov limiting distribution tests (Filter B — BP 1.0 — 3.4 Hz)

Event No.	Region	Period Sec.	No. Sensors	MB	Ampl.	NORMAL				LOG NORMAL				EXPONENTIAL			
						μ	σ	Z-Value	P_I %	μ	σ	Z-Value	P_I %	μ	σ	Z-Value	P_I %
1	Aleutians	1.0	120	5.6	Pos.	2028	1013	1.626	1.0	7.5027	0.5044	0.8417	47.8	2028	1013	1.187	12.0
					Neg.	2092	1104	0.9193	32.8	7.5009	0.5657	1.1150	16.6	2092	1104	1.643	0.9
2	Aleutians	0.8	132	5.3	Pos.	1143	567	1.132	15.4	6.9152	0.5210	0.8461	47.1	1143	567	1.828	0.3
					Neg.	1224	660	0.9130	37.5	6.9662	0.5552	0.9155	37.2	1224	660	1.752	0.4
3	Kamchatka	0.8	132	5.0	Pos.	618	356	1.269	8.0	6.2630	0.5851	0.8292	49.8	618	356	1.649	0.9
					Neg.	586	329	1.266	8.1	6.2170	0.5679	0.5979	86.7	586	329	1.900	0.1
4	Kamchatka	0.7	132	5.0	Pos.	850	489	1.493	2.3	6.5855	0.5660	0.8673	43.9	850	489	1.654	0.8
					Neg.	777	348	1.162	13.4	6.5305	0.5125	0.9407	33.9	777	384	2.002	0.1
5	Kazakh	0.6	132	5.1	Pos.	1644	892	1.333	5.7	7.2711	0.5187	0.6049	85.8	1644	892	1.393	4.1
					Neg.	1653	1062	2.078	0.0	7.2506	0.5468	0.8296	49.7	1653	1062	0.6418	80.5
6	Japan	0.9	132	5.3	Pos.	1566	928	1.393	4.1	7.1742	0.6228	0.9236	36.1	1566	928	1.741	0.5
					Neg.	1305	648	0.9942	27.6	7.0445	0.5269	1.087	18.8	1305	648	2.263	0.0
7	Japan	0.7	120	5.6	Pos.	2328	1226	0.9829	28.9	7.6103	0.5499	0.7352	65.2	2328	1226	2.100	0.0
					Neg.	2289	1143	1.114	16.7	7.6064	0.5275	0.8556	45.7	2289	1143	1.826	0.3
8	Greece	0.7	132	4.7	Pos.	712	410	2.089	0.0	6.4353	0.4988	0.9786	29.4	712	410	0.5576	91.5
					Neg.	797	486	2.141	0.0	6.5378	0.5104	1.4960	2.3	797	486	1.1820	12.2
9	C. Mid-Atlantic Ridge	1.6	126	6.0	Pos.	718	318	1.110	17.0	6.4753	0.4637	0.8882	40.9	718	318	1.693	0.6
					Neg.	690	327	1.089	18.6	6.4265	0.4787	0.5660	90.6	690	327	1.605	1.2

Note: μ = computed sample mean; σ = computed sample standard deviation; *Z*-value = test statistics; P_I = probability assigned to the distribution by the above test.

TABLE 4

Quality of fit scores for P-wave amplitude distributions obtained in Kolmogorov-Smirnov limiting distribution tests (Filter B—BP 1.4—3.7 Hz)

Event No.	Region	Period sec.	No. Sensors	MB	Ampl	NORMAL				LOG NORMAL				EXPONENTIAL			
						μ	σ	Z-Value	P_I%	μ	σ	Z-Value	P_I%	μ	σ	Z-Value	P_I%
1	Aleutians	1.0	120	5.6	Pos.	1704	985	1.471	2.6	7.2884	0.5620	0.7117	69.2	1704	985	1.278	7.6
					Neg.	1645	909	1.328	5.9	7.2615	0.5510	0.9260	35.8	1645	909	1.461	2.8
2	Aleutians	0.8	132	5.3	Pos.	936	545	1.170	13.0	6.6833	0.5745	0.7070	70.0	936	545	1.594	1.2
					Neg.	970	535	1.008	26.2	6.7192	0.5863	0.7293	66.2	970	535	1.915	0.1
3	Kamchatka	0.8	132	5.0	Pos.	314	191	1.313	6.3	5.6744	0.5693	0.6565	78.2	341	191	2.678	0.1
					Neg.	347	195	1.280	7.6	5.6929	0.5718	0.8497	46.6	347	195	1.741	0.5
4	Kamchatka	0.7	132	5.0	Pos.	746	414	1.243	9.1	6.4613	0.5634	0.9061	38.4	746	414	2.097	0.0
					Neg.	742	409	1.621	1.0	6.4669	0.5379	0.7207	67.7	742	409	1.567	1.5
5	Kazakh	0.6	132	5.1	Pos.	1439	916	1.995	0.1	7.1070	0.5495	1.170	12.9	1439	916	1.150	14.2
					Neg.	1452	902	1.789	0.3	7.1298	0.5322	0.9525	32.4	1452	902	0.8457	47.2
6	Japan	0.9	132	5.3	Pos.	1214	733	1.651	0.9	6.9560	0.5942	0.8955	39.9	1244	733	1.567	1.5
					Neg.	1278	744	1.096	18.1	6.9871	0.5942	0.9153	37.2	1278	744	1.096	0.8
7	Japan	0.7	120	5.6	Pos.	2007	1198	1.121	16.2	7.4269	0.6153	0.5064	96.0	2007	1198	1.552	1.6
					Neg.	1828	950	1.107	17.2	7.3743	0.5377	0.6555	78.3	1828	950	1.917	0.1
8	Greece	0.7	132	4.7	Pos.	565	320	1.737	0.5	6.2094	0.4813	1.1142	14.7	565	320	0.7011	70.9
					Neg.	628	387	2.151	0.0	6.2944	0.5246	0.9666	30.8	628	387	0.6210	83.5
9	C. Mid-Atlantic Ridge	1.6	126	6.0	Pos.	367	187	1.372	4.6	5.7856	0.4931	0.4467	98.8	367	187	1.405	3.9
					Neg.	385	202	1.305	6.6	5.8212	0.5257	0.5098	95.7	385	202	1.425	3.4

Note: μ = computed sample mean; σ = computed sample standard deviation; *Z*-value = test statistics; P_I = probability assigned to the distribution by the above test.

surements. The expectation and variance parameters required in the above hypothesis test, were estimated from the test sample and thus introduce a small positive bias in the calculated significance levels (L i l l i e f o r s, 1967). However, this effect would be partly eliminated if we restrict ourselves to a comparative analysis of test values.

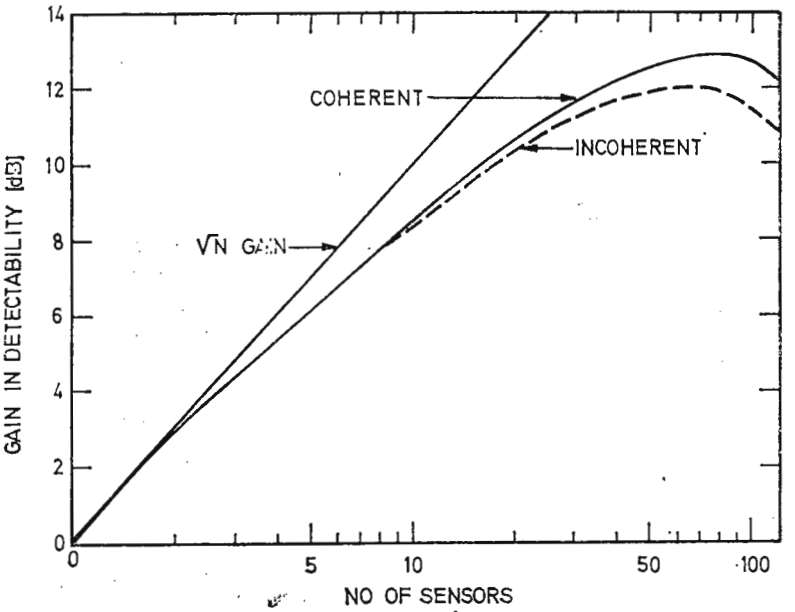

Fig. 8. — Gain in detectability (dB) as function of N when the N best sensors are selected for beamforming (coherent and incoherent). Observed NORSAR amplitudes (120 sensors) for event no. 7 in table 2 were used. Actual beamforming was not performed, instead eq (9) (with $q = 0.8$) and eq. (11) were used for detectability computations.

It should be noticed that the Kolmogorov-Smirnov test is not very stable for the small sample size used here. This is obvious from the great differences between the scores for positive and negative amplitude values, and has also been found when applying the test to samples of data whose distribution was known. Anyway, it is obvious from the tabulated results that the lognormal distribution provides a far better model for the observed amplitude variations than the other two, and in view of the above remarks, we conclude that the test results support our theoretical considerations presented in Section 5.

Considering the large and systematic spread in signal amplitudes across the array, a natural question is whether restricting the beamfor-

ming processing to a few good sensors could improve or match the performance of the full array. The detectability concepts defined in Section 4 have provided a convenient tool for investigating this problem. Several events were selected for this purpose, and the NORSAR sensors were ranked according to their amplitudes. Figure 8 shows an example of gain in event detectability when using the N best stations as a function of N.

It appears that the full array detectability is essentially achieved with less than one third of the sensors, assuming that the best ones have been selected. This holds true for both methods of beamforming. It seems, however, not to be possible to improve the array performance substantially by selective elimination of „low amplitude" sensors or subarrays. Also the fact that sensor performance is strongly dependent upon event location makes it difficult to draw advantages from the amplitude variations as to cost/performance tradeoff.

DISCUSSION

We have shown that incoherent beamforming is generally superior to conventional beamforming in detecting near regional seismic events, events which produce signals with low coherency across the array and very high frequency signals. The main disadvantages of the incoherent detector are its sensibility to local explosions, the poor location estimates caused by the broad main lobe of the beam and the fact that conventional beamforming is superior when it comes to detecting small, coherent seismic signals.

From a computer processing point of view, the incoherent detector has the advantage of providing adequate world coverage with very few array beams (less than 100 for NORSAR), and the computational requirements are also small due to the low sampling rate for the signal envelopes. The lack of location precision is not a major handicap when off-line event analysis is available, as is the case at the NORSAR data center. In the NORSAR implementation, the incoherent detector has required only 20 % of the computer main storage and computational load necessary for the conventional method. Thus as an alternative detector, the incoherent processor can achieve a substantial decrease in computer requirements while retaining most of the detection capability of the array. We still think that the major benefit of an incoherent detector is as supplement to conventional beamforming especially designed to record events of high dominant frequency and underground explosions. Since explosions

may occur at unpredictable sites, where no region corrections may be available for array beamforming, the broad main lobes of the incoherent beams make this method especially useful for detecting this type of seismic events, thereby providing a valuable tool for nuclear test monitoring. We would finally like to mention the interesting aspects of providing a world-wide multiarray seismic detection network using incoherent beamforming. For an outline of this idea, we refer to Husebye et al [4].

Acknowledgement

The NORSAR research project has been sponsored by the United States of America under the overall direction of the Advanced Research Projects Agency and the technical management of Electronic Systems Division, Air Force Systems Command.

REFERENCES

Bungum H., Husebye E. S., Ringdal F. (1971) The NORSAR array and preliminary results of data analysis. *Geophys. J. R. Astr. Soc.*, 25, London.

Felix C. P., Gilbert W. L., Wheeler S. G. (1972) Preliminary results from the NORSAR system. *Proceedings*, Seminar on Seismology and Seismic Arrays, NTNF/NORSAR, Kjeller, Norway.

Lacoss R. T. (1972) Variations of the false alarm rates at NORSAR. *MIT*, Lincoln Lab., 30 June 1972.

Lilliefors H. W. (1967) On the Kolmogorov-Smirnov test for normality with mean and variances unknown. *J.A.S.A.*, 62, New York.

Melton B. S., Bailey L. F. (1957) Multiple Signal Correlators. *Geophysics*, 22, Tulsa, Oklahoma.

[5] Husebye E. S., Ringdal F., Fyen J. On real-time processing of data from a global seismological network. 1972. NORSAR Techn. Rep. No. 43, NTNF /NORSAR, Kjeller, Norway.

STANDARDIZATION AND NORMALIZATION

STANDARDIZATION AND OPTIMIZATION OF FREQUENCY CHARACTERISTICS AT MOXA STATION (GDR)[1]

BY

PETER BORMANN[2]

INTRODUCTION

The Moxa station of the Central Earth Physics Institute of the Academy of Sciences of the GDR is one of the seismological basic network of European socialist countries. The task of this station network is to obtain data for the calculation of the basic focal parameters of earthquakes with magnitudes $M \geqq 4$ and to study the feature of seismic waves for the investigation of the focal mechanisms as well as the structure and the physical properties of the Earth's interior.

Among other things the efficiency of a station network with respect to the solution of the first mentioned task is essentially dependent on that ,whether the characteristics of seismographs at the stations take the best advantage of the local noise conditions. On the other hand the necessary comparability of the data recorded in the different countries with seismographs of different construction requires the standardization of their frequency characteristics.

---

[1] Communication Nr. 297, Central Earth Physics Institute.

[2] Central Earth Physics Institute AdW der DDR, 15 Potsdam, Telegraphenberg, GDR.

THE REGISTRATION EFFICIENCY OF MOXA STATION

Figure 1 shows the inverse spectrum of the maximum peak-to-trough noise amplitudes at Moxa station measured in nanometer (10^{-6} mm) and its seasonal variation in the period range $0.4 \text{ s} \leqq T < 10 \text{ s}$. Additionally the following characteristics are shown in figure 1 :

a) a special characteristic A' operating at Moxa station

b) the standard characteristics of type A, B, and C used at Moxa station and other stations of the basic network of socialist countries

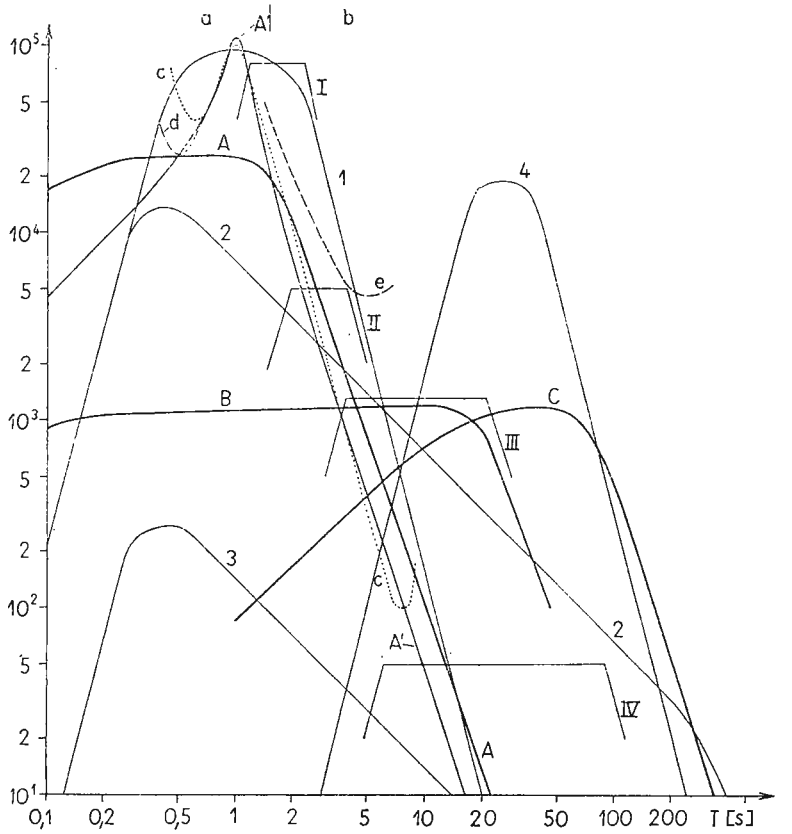

Fig.1. — Frequency characteristics operating at or proposed for seismological stations of the basic network of european socialist countries as well as the inverse spectrum of the maximum peak-to-trough noise amplitudes at Moxa station in times of strongest and smallest microseismic noise and the industrial noise.

a, period range with no remarcable seasonal variations of noise amplitudes; b, period range with strong seasonal variations of noise amplitude; c, the inverse spectrum in times of strongest microseismic noise; d, the inverse spectrum in times of industrial noise; e, the inverse spectrum in times of smallest microseismic noise; V, magnification; T, period of soil motion in seconds; —, operating frequency characteristics; —, proposed frequency characteristics.

c) the „optimal characteristics" I, II, III, and IV discussed in the paper by Kondorskaya and Aranovič, (1971)

d) the characteristics 1, 2, 3, and 4 proposed in connection with other standardization projects in the framework of scientific co-operation of socialist countries.

If we want the maximum peak-to-trough noise amplitude in the record to be 1 mm, then the magnification curve of the „optimal seismograph" has to fit the „inverse spectrum" shown in figure 1. This does the characteristic A′ in the period range $0.3 \text{ s} < T < 9 \text{ s}$ nearly exactly. Claiming a signal-to-noise ratio $SNR \geqq 2$ for *P*-wave detection and considering the *Q* calibrating functions of Gutenberg and Richter, (1956) we found the detection limits of Moxa station for waves with periods $T = 1 \text{ s}$ (Berckhemer, 1971). In some cases we registered events from all epicentral distances between 20° and 100°, the magnitude of which given by USCGS were up to 0.3 units of magnitude smaller than these minimum values of *M* for *P*-wave detection. The standard characteristic of type A is also a good fit to the short-period noise conditions at Moxa station.

As the noise spectrum at Moxa station shows only small seasonal variations in the period range $0.4 \text{ s} < T < 2 \text{ s}$ there is not any possibility of a useful utilization of the characteristics of type 1 and I for photographic analog records. From the characteristic II proposed by Kondorskaya and Aranovič (1971) we can expect a gain of information in comparison with the characteristics A and B only in times with minimal microseismic noise of periods between 2 and 5 s. The characteristic III nearly corresponds to the long-period part of type B characteristic but the latter gives more informative records especially from near earthquakes and is very useful for the identification of teleseismic events (Bormann, 1972). Therefore it seems not necessary to replace the standard characteristic of type B by that of type III one. After figure 1 the records of type B and C are much disturbed in times of microseismic storms. Therefore it should be considered the possibility to switch on a rejection filter at days with microseismic storms.

The high-gain long-period characteristic 4, the maximum of which falls in the range of the global minimum of long-period noise (Savino et al., 1972), could be realized at Moxa station.

SELECTION OF OPTIMAL CHARACTERISTICS OF SEISMOGRAPHS FOR PHOTOGRAPHIC ANALOG-RECORDS AT MOXA STATION

In a comprehensive paper Kondorskaya and Aranovič (1971) studied the methodical fundamentals of optimization of the system of seismological observations for teleseismic earthquakes in the distance range $20° \leqq D \leqq 100°$. As „informative elements" of the wave picture necessary for investigations of the structure of the Earth's interior and the focal processes these authors studied the maximum of amplitude spectra of P and S waves as well as of the Airy phase L. In comparison to this we analysed all visual detectable kinds of waves from different types of seismic events with magnitudes $4.5 < M < 8.5$ in the whole distance range $(0° < D < 180°)$ in photographic records of all electrodynamic seismographs operating or tried at Moxa station, respectively [3].

Comparison of short-period frequency characteristics

Figure 2 shows the short-period characteristics of type HF (high-frequency), A, A′, Fi (with a filter galvanometer, $Tg = 0.48$ s), and Tr (used as a trigger seismograph for digital tape records).

Seismographs of type A and HF give the best records of near earthquakes and rock bursts. The often weak high-frequency first onsets of these events, however, are sometimes detectable only in records of type HF (fig. 3). On the other hand, records of type HF are unsuitable for onsets with predominant periods $T > 0.5$ s and unsuitable, therefore, also for all first onsets of teleseismic events $(D > 20°)$.

The following features resulted concordantly from a comparison of wave onsets with periods $0.6 \text{ s} \leqq T \leqq 1.5$ s from different kinds of seismic events (rock burst, underground nuclear explosions, near and far earthquakes):

a) In comparison to frequency characteristics with a broad flat maximum (e.g. type A) small band characteristics (e.g. type A′) register the first motion of a wave onset much smaller as could be expected from the difference of magnification curves. The relative reduction is greatest for periods in the range of the maximum of the magnification curve (3 to 8 times) and diminish in the range of steep slopes of frequency characte-

[3] Bormann P. Standardisierung und Optimierung von Frequenzcharakteristiken an der seismologischen Station Moxa des Zentralinstituts Physik der Erde. 1972. Unveröffentlichter wissenschaftlicher Bericht des Zentralinstituts Physik der Erde, Potsdam.

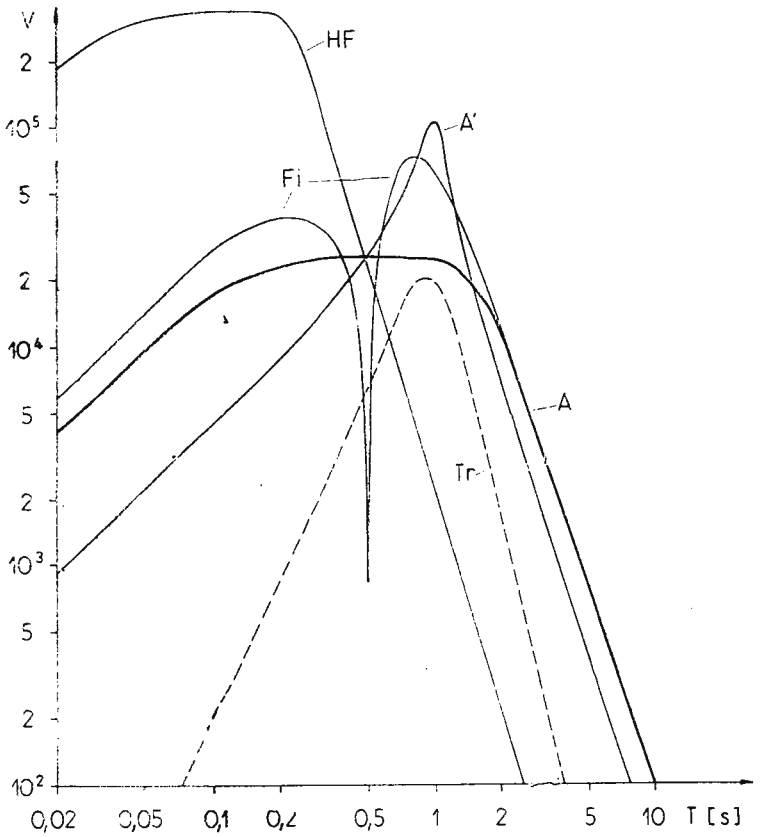

Fig. 2. — Frequency characteristics of short-period seismographs at Moxa station.

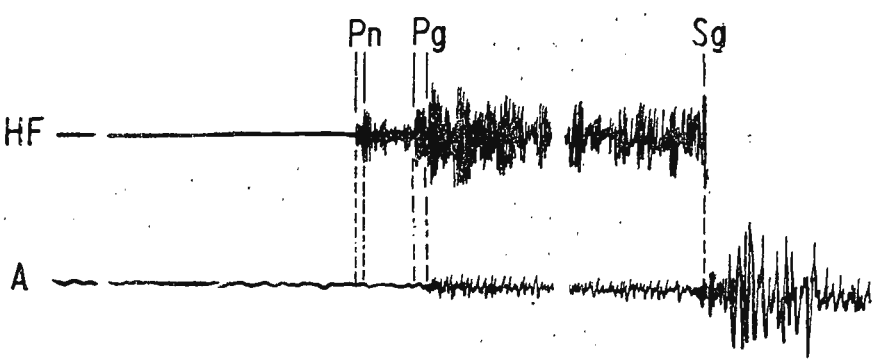

Fig. 3. — Records of types HF and A respectively from a small near earthquake in the Swabian Jura Region/FRG (17.5.1972, $D = 314$ km, $M = 3{,}5$).
The minute marks are indicated as gape in the record line.

ristics and also for the following oscillations (fig. 4). Compared with the type A′ it means that the registration efficiency of type A is the same or a better one for the first motion and about a half for the amplitude maximum, respectively, for wave periods $T = 1$ s despite a four times smaller

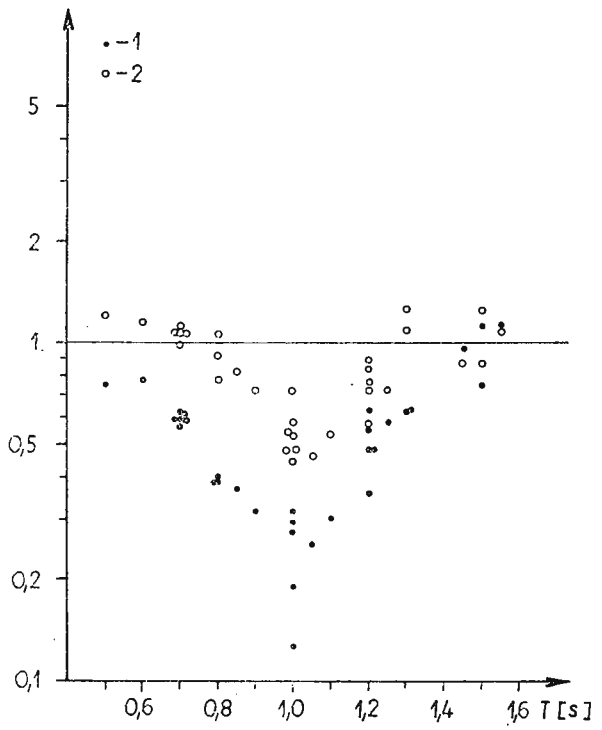

Fig. 4. — Amplitude ratio of the first onsets and of the maximum amplitude of P, respectively, in records of type A′ and A, normalized to the same magnification for stationary harmonic oscillations
1, first onsets, 2, maximum amplitude ot P.

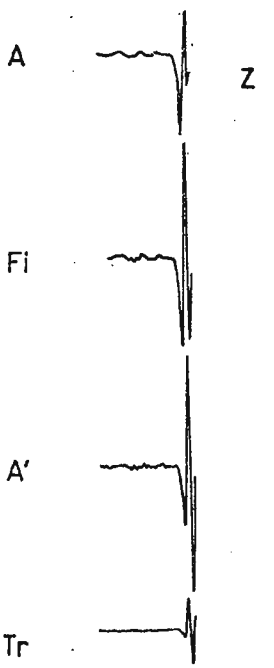

Fig. 5. — Records of types A, Fi, A′ and Tr from a deep earthquake under the Sea of Okhotsk (29.1.1971, $D = 72{,}3°$, $h = 544$ km, MPV = 6,1).

magnification for stationary harmonic oscillations of the same period (fig. 4).

b) In small-band records the first onset is followed by much more oscillations (enlarged wave lets) as in broad-band records (short wave lets). The onset-time determination of following wave onsets, therefore is rendered more difficult or impossible, e.g. for deep phases of shallow

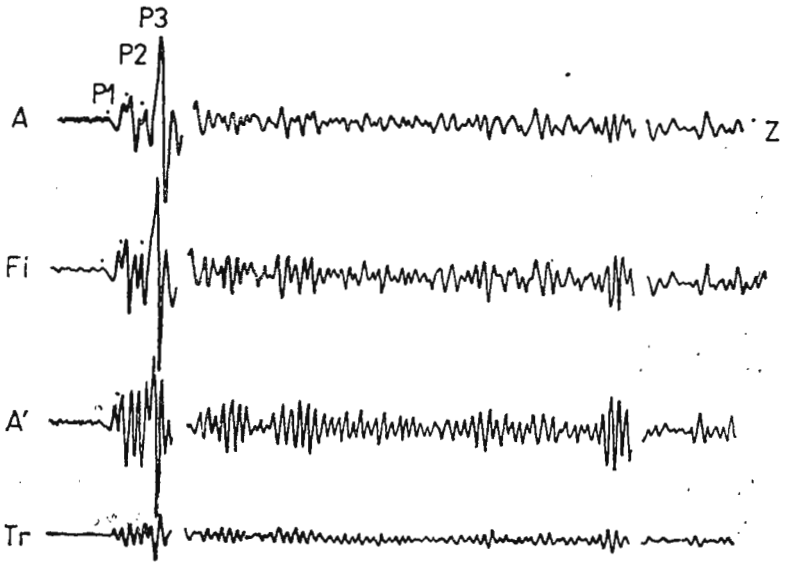

Fig. 6. — Records of types A, Fi, A', and Tr from an earthquake in Honshu/Japan (7.10.1970), (D = 88,0°, h = 179 km, MP1V = 5.8, MP3V = 6.4).

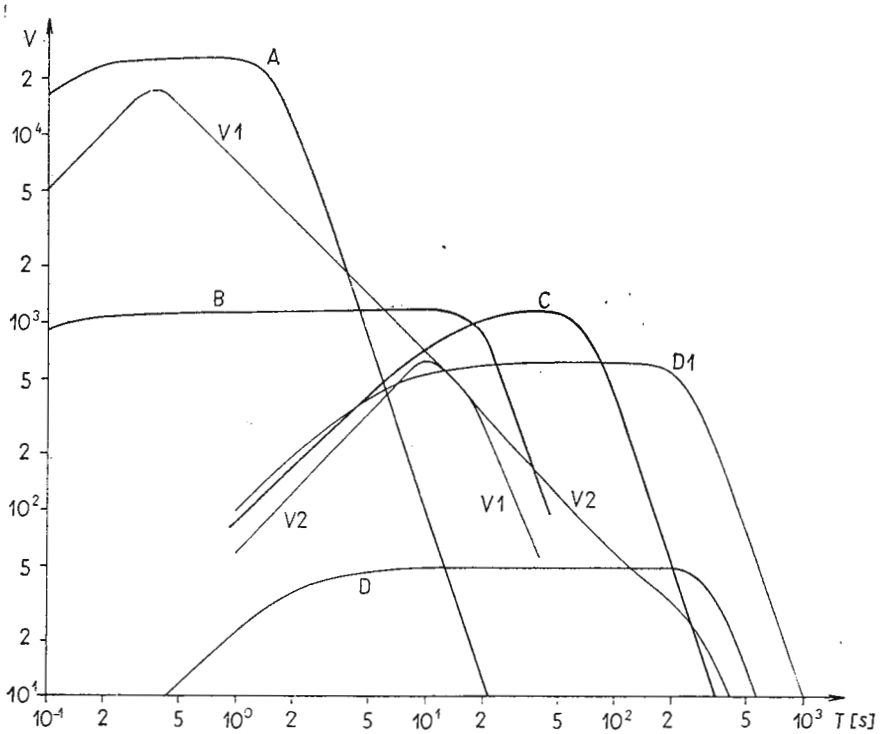

Fig. 7. — Frequency characteristics of short- and long-period seismographs at Moxa station.

focus earthquakes, for onsets of multiple shocks (fig. 6), and of successive core phases.

c) In the case of complex wave spectra as often given, e.g., in records of near earthquakes, a small-band filter characteristic can some times increase the distinctness of wave onsets.

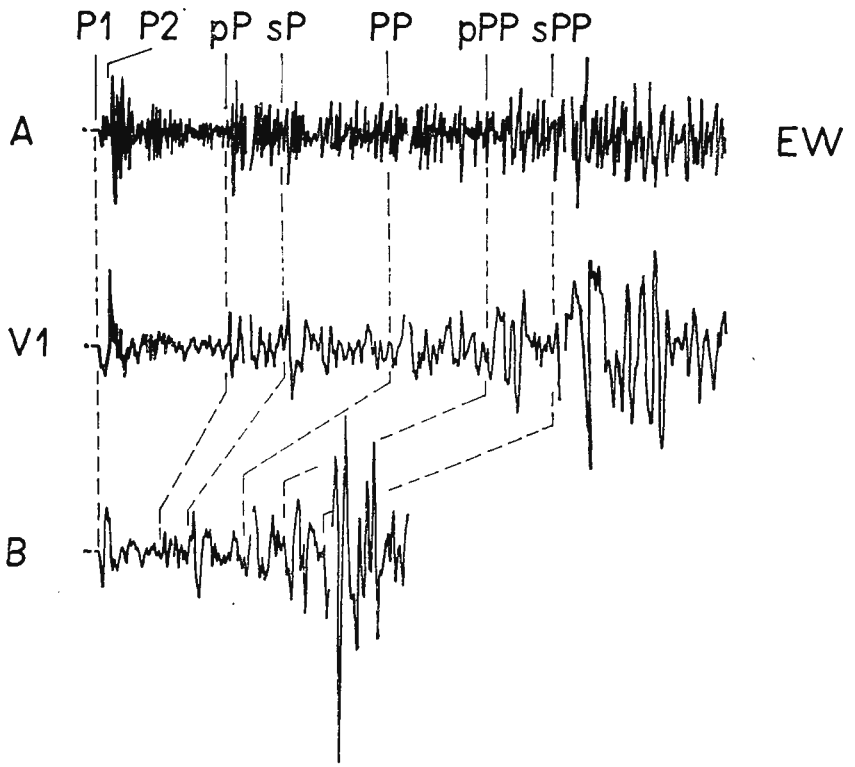

Fig. 8. — Records of types A, V1, and B from a deep earthquake in the Hindukush region (6.6.1966, $D = 44{,}3°$, $h = 225$ km, MPV = 6,6). The opposite direction of the first motions of P1 and P2 in the short-period record of type A is remarkable.

Comparison of the frequency characteristics of type A, V1 and B

The broad-band characteristic of the velocity meter of type 2 shown in figure 1 was realized by the characteristics V1 and V2 at Moxa station (fig. 7). The characteristic V1 falls in the period range of the standard characteristics of type A and B. Its fitness for visual analysis, therefore, was determined by a comparison with photographic records of these standard seismographs. The main results are :

a) If the amplitude spectrum of the first onset also contains a strong long-period portion then multiple P onsets successive in small time intervals can be clearly detected only in records of type A (fig. 8).

b) The magnification of characteristic V1 is much smaller than that of type A and B one, respectively, for periods $T \leqq 3$ s and $T > 10$ s.

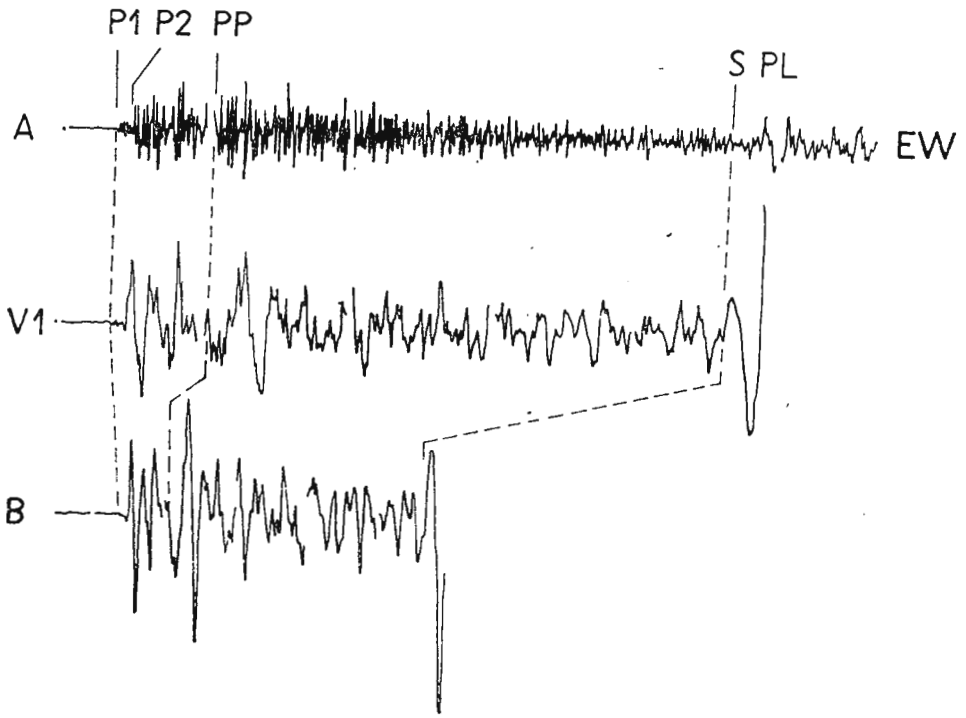

Fig. 9. — Records of types A, V1, and B from an earthquake in Turkey (19.8.1966, $D = 24{,}0°$, MLH = 6,6).

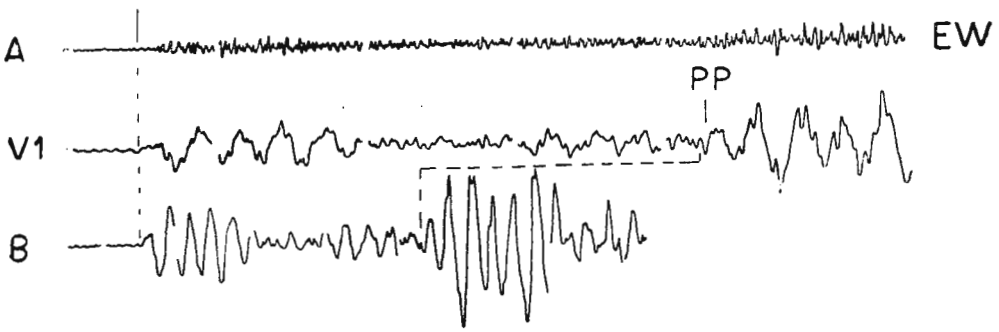

Fig. 10. — Records of types A, V1, and B from an earthquake in Peru (17.10.1966, $D = 98{,}4°$, MPV = 7,8).

The determination of the onset time and of the direction of first motion, therefore, is rendered more difficult in records of type V1 for short-period as well as long-period wave onsets (fig. 9, 10). The combination of characteristics of type A and B provides, therefore much more informations.

Comparison of the frequency characteristics of type B, V2, C, and D1

From a comparison of records of types B, V2, C, D1 and D (fig. 7) the following conclusions could be drawn:

a) Small earthquakes with $M < 5$ do not excite clear waves with periods $T > 20$ s. In the period range $6\text{ s} < T < 18\text{ s}$ records of type V2 are very similar to those of types B, C, and D1.

b) Only in records of types C and D1 from earthquakes with $M > 5$ appear clear long-period waves with periods greater 20 to 30 s. On the

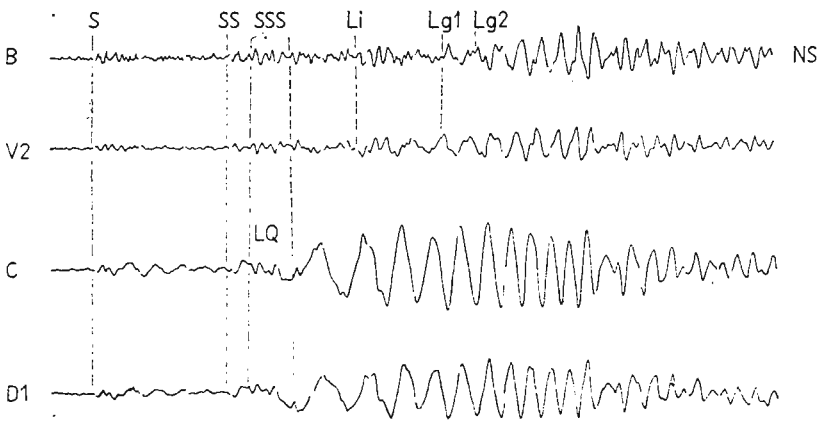

Fig. 11. — Records of types B, V2, C, and D1 from an earthquake in southern Iran (12.4.1971, $D = 39{,}8°$, MPV = 5,7, MLH = 5,7).

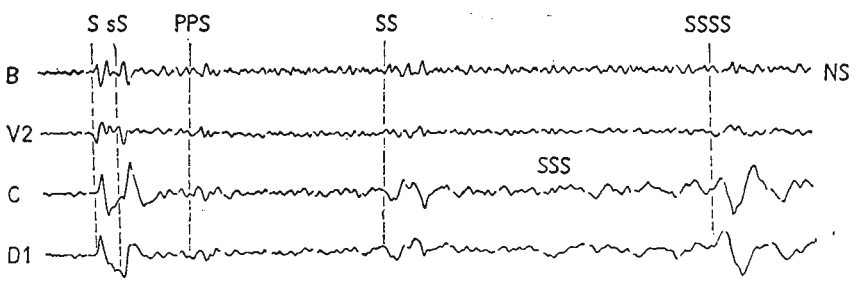

Fig. 12. — Records of types B, V2, C, and D1 from an earthquake in southern Sumatra (8.4.1971, $D = 93{,}8°$, $h = 75$ km, MPV = 6,4).

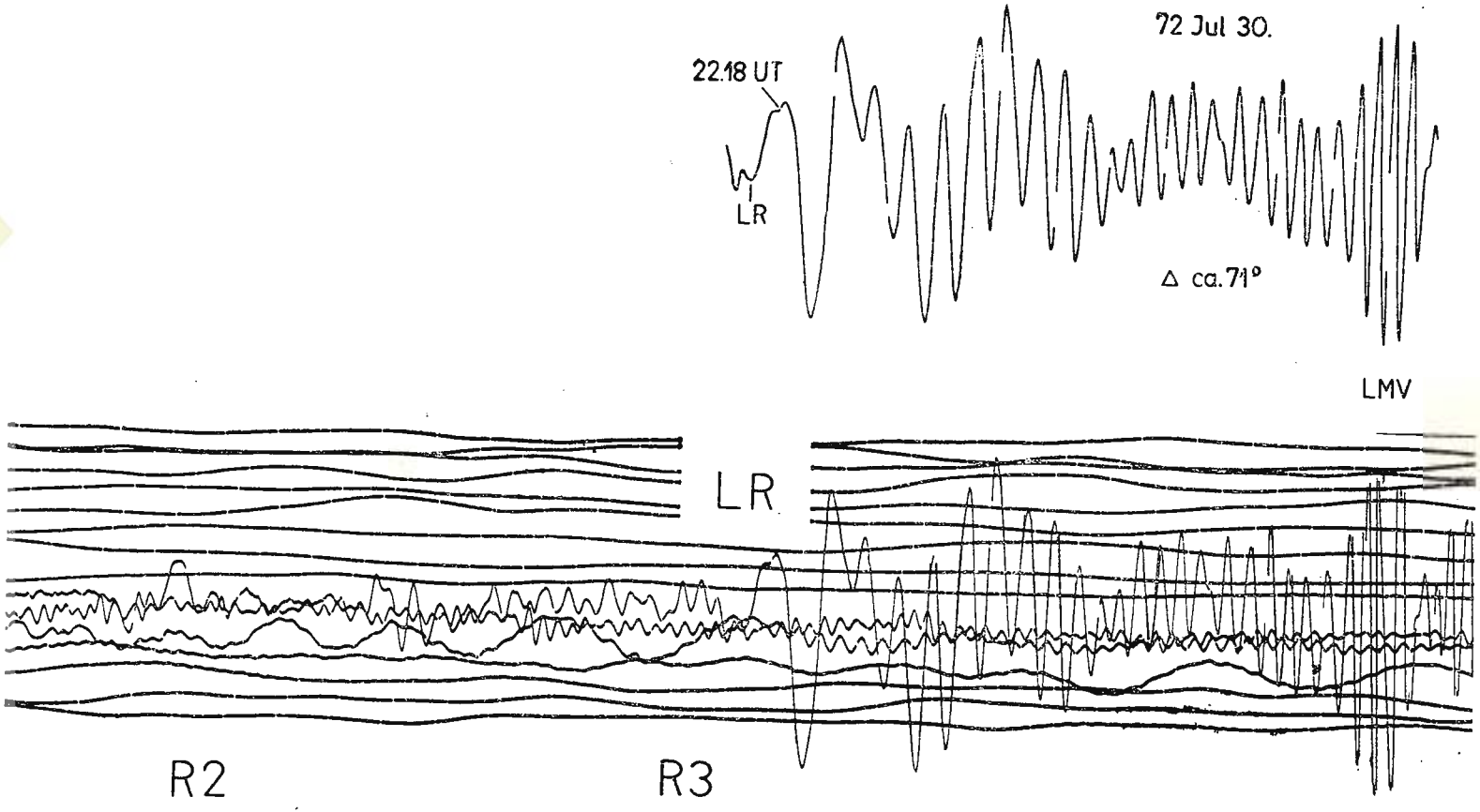

Fig. 13. — Records of the vertical component of type D from an earthquake in Southeastern Alaska ((30.7.1972, $D = 69{,}5°$, $h = 25$ km, MLV = 7,6).

other hand, median-period and rapid succesive body-wave onsets as well as higher modes of surface waves, the onsets of which fall in the range of long-period wave modes are surely detectable only in records of types B and V2, but more better in B's type (fig. 11, 12). Consequently, the combination of standard broad-band characteristics of type B and C is very suitable for a visual recognition and separation of various superimposed wave types with different periods. Its substitution by a broad-band velocity meter of type V2 would result in a considerable loss of information.

c) In records of type C and D1 being in scale by magnifications of about 1200 and 600, respectively ($M < 7$), we could not find clear waves with periods $T > 100$ s by visual analysis. From this follows that photographic records of type D1 with high magnification do not yield much more informations as these of type *C*. On the other hand, we found from earthquakes with $M > 7$ clear periods up to 4 minutes in low-magnification records of type D being in scale but not in the corresponding off-scale records of type C and V2 (fig. 13).

CONCLUSIONS

Short-period and long-period small-band characteristics of type A′ and 4, respectively, fitting the „inverse noise spectra" at Moxa station are most suited for the detection of small teleseismic events. On the other hand broad-band characteristics have a higher effective magnification for pulse-shaped onsets than those of small-band type and they give a more realistic picture of the most interesting features of a seismic record (e.g. direction and amplitude of first motion, multiple onsets, complexity of wave spectra, dispersion). This facilitates the recognization of phases and the identification of seismic events.

Displacement-meter records are more suitable for a visual analysis than those of velocity meters, because in the case of equal soil-oscillation velocity of two waves with different periods the corresponding difference of the soil-displacement amplitudes is a striking additional criterion. Moreover, broadband characteristics of velocity meters do not enable an optimal utilization of natural noise conditions.

A set of well selected displacement-proportional characteristics should be preferred for visual analysis of analog records. The standard characteristics of type A, B, and C used at stations of the basic network of European socialist countries for some years seem to be the most effective set of characteristics for photographic records of teleseismic events

in the magnitude range $4.5 < M < 7.5$. These records, however, are off scale for the strongest earthquakes. Clear periods greater than 100 seconds (up to 4 minutes) could be found out in a low-magnification ($V = 50$) ultra long-period displacement record with a flat characteristic between 2 s and 330 s, but only from earthquakes with magnitudes $M > 7$. Therefore we propose as a new standard type D for an optimal registration of the strongest earthquakes a displacement proportional characteristic with a magnification level of about 50 in the pass-band range from about 1 to 300 seconds.

If we use magnetic-tape or digital paper-tape records, it is of secondary importance whether we register the displacement, the velocity or the acceleration of soil. On the other hand it is very important to record the primary information with minimum distortion in a period range as large as possible and to guarantee a high stability of a velocity- or acceleration-meter system to eliminate the influence of the integration constants in the computer calculated soil displacement. All other desirable operations (e.g. the determination of other derivatives of soil displacement and their spectra; band-pass, noise-prediction, or multi-channel filtering) then can be done by the computer. Thereby the number of seismographs needed at a good station could be strongly reduced. An advantage of a broad-band velocity-proportional record compared to the displacement-proportional one is a dynamic compression up to about 10 db. It is still greater in acceleration records. This can be important if we want a universal broad-band record of all earthquakes over the noise level up to a magnitude of about 7 on a single magnetic tape only with a dynamic range of 70 to 80 db (Berckhemer, 1971).

REFERENCES

Berckhemer H. (1971) The concept of wide band seismometry. XII *Ass. Gén. CSE, Obs. Roy. Belg. Comm. Sér. A*, 13, *Sér, Géophys.*, 101, Bruxelles.

Bormann P. (1972) Identification of teleseismic events in the records of Moxa station. *Gerl. Beitr. Geophys.* 81, 1/2 Leipzig.

Gutenberg B., Richter C. F. (1956) Magnitude and energy of earthquakes. Ann. Geofis., 9, 1, Roma.

Kondorskaya N. V., Aranovič Z. I. (1971) Metodičeskie osnovy optimizacii sistemy sejsmičeskich nabljudenij. *Izv. AN USSR, Fiz. Zemli*, 7, Moskva.

Savino I., McCamy K., Hade H. (1972) Structures in earth noise beyond twenty seconds — a window for earthquakes. *Bull. seism. Soc. Am.*, 62, 1, Berkeley

OPTIMIZATION OF NEW STATION POSITIOS FOR VRANCEA AND CÎMPULUNG SEISMIC REGIONS (ROMANIA)

BY

TRAIAN IOSIF[1], DRAGUTIN SKOKO[2]

Abstract

In order to find the optimum location for new seismic stations to improve the accuracy of the focal-parameters determination, a number of points are assumed as new station positions treated and the calculation of error estimation of foci parameters carried out.

The calculation is done for two seismic areas namely

a) region situated at the bend of the Carpathian arc; deep (Vrancea) and normal (R. Sărat-Urziceni) earthquakes are treated,

b) Cîmpulung region; normal earthquakes are considered.

The distribution of the earthquake-parameter errors in the area around the epicenter position give a general idea of the optimum location of a new station. On this basis the Dobrogea region and southern part of the country are found to be optimal places for setting up new stations.

For the calculation, a model of homogeneous medium is used with the upper boundary, being a flat plane, corresponding in size to the eastern part of the Romanian territory for Vrancea earthquakes, and to all the territory for Cîmpulung earthquakes.

The calculation is based on the Monte-Carlo method and has been carried out at IISEE (Tokyo).

INTRODUCTION

In the Romanian territory there are some seismic zones. In this paper we are dealing with the Vrancea and Cîmpulung seismic regions only.

The most interesting is the zone with the foci at the bend of the Carpathian arc, in the Vrancea region. These foci are characterized by

[1] Institute of Applied Geophysics, Bucure.şti, Romania.

[2] Geophysical Institute, University of Zagreb, Yugoslavia.

the following peculiarities : *a*) they are deep (the term deep focus is used for the intermediate focus) and *b*) they are persistent.

Being persistent, they offer good conditions for the study of many seismological problems. The installation of the seismic network distributed around the epicenter area has permitted obtaining abundant observation data of seismic events which occured in this region.

Since 1935, when the Bucureşti station was put into operation, about 800 earthquakes of magnitude more than 2.8 have been recorded from the Vrancea region, e.g. 20 per year on the average.

All the epicenters of the Vrancea deep foci are distributed within a small area of about 25 km by 55 km in length and the azimuth of approximately 45° (Fig. 1). The area is tangential to the sharp bend of the mountain chains. The foci are placed at depths ranging from 80 km to 160 km. But shocks at smaller depths occur here also.

In the region situated forward of the Carpathian arc, the normal focus earthquakes occur. Their epicenters are distributed in a zone beeing approximately the same direction as the area of deep foci, namely northeast-southwest (fig. 1). The earthquakes taking place in the outermost parts have the depth of 15—25 km and those which occur in the central part have depths of 50—60 km. During the past 35 years, about 50 earthquakes of magnitude more than 3.5 occurred in this region.

Also in the Romanian Plain two relative strong earthquakes ($M = 5-5.5$) occurred in 1960 and 1967 with focal depths of about 80 and 40 km, respectively (Iosif et al., 1972).

Because of the special importance of the foci at the bend of the Carpathian arc, a seismic network has been organized surrounding the seismic area and systematic research of the geometry, kinematics and dynamics of these foci has begun.

To estimate the errors of the earthquake-parameter determination (focus position and origin time) for local earthquakes, using the data of the eastern network, quantitative study has been undertaken.

Besides, an attempt is made to estimate the errors when new stations are added to the existing set.

A similar problem is treated for the Cîmpulung earthquakes, taking into account all the existing Romanian station.

The calculation is based on the Monte-Carlo method (Iosif, Skoko Sato, 1972; Miyatake, Nakayama, 1960; Sato, 1965; Sato, Skoko, 1965; Skoko, Sato, Ochi, 1967).

FORMULATION OF THE PROBLEM

The equations for the errors of epicenter location, focal depth and origin time are

$$(X_k - X_o)x + (Y_k - Y_o)y + Hh + V_oC_kt = V_oC_ke_k \quad k = 1, 2, \ldots \tag{1}$$

where

k — index number of each station,

X_k, Y_k — coordinates of seismic station,

X_0, Y_0 — coordinates of epicenter,

H — depth of focus,

$$C_k = [(X_k - X_0)^2 + (Y_k - Y_0)^2]^{1/2},$$

V_0 — velocity of elastic waves,

e_k — observation error of arrival time and

x, y, h, t — errors of the location of focus and origin time which result from calculation.

The following assumption are adopted :

i) observation points are on a flat surface,

ii) the origin of the coordinate system is assumed the true epicenter,

iii) observation errors e_k follow a Gaussian distribution with mean value 0 and standard deviation ε,

iv) all the stations record all the earthquakes and

vi) velocity of the seismic waves and depth of foci are constant.

For the Vrancea earthquakes the following values are assumed :

depth of focus — 120 km,

P wave velocity — 7.8 km/s,

for the normal earthquake zone :

depth of focus — 25 km,

P wave velocity — 6.5 km/s and

for the Cîmpulung region :

depth of focus — 10 km,

P wave velocity — 6.0 km/s.

Standard deviation of the observation errors $\varepsilon = 0.10$ s.

As the above equations are only intended to be used for the estimation of the error, irrespective of complexities of the path of the seismic waves, only a simple and plausible assumption for the travel time appears

necessary in view of the restricted nature of the problem that is covered by the present investigation.

In this way, the result of the present series of computations do not take into account the effect of focal depth or the heterogenity of the medium.

VRANCEA REGION

OBSERVATION POINTS AND DATA ADOPTED

The seismic network around the Vrancea region contains seven stations (fig. 1) which are listed in table 1 — together with the instrumental setup at each station.

TABLE 1

Eastern station network in Romania

No.	Station	Latitude (North)	Longitude (East)	Instrument	
1	Cîmpulung	45°16′	25°02′	Hiller	— NS, EW, Z
				Mechanic	450 kg — NS, EW
2	Cheia	45°28′	25°57′		
3	București	44°25′	26°06′	Galitzin	— NS, EW
				Kirnos	— Z
				Mechanic	540 kg — NS. EW
					450 kg — NS
4	Vrîncioaia	45°52′	26°44′	VEGIK	— NS, EW, Z
				Mechanic	105 kg — NS, EW
5	Bacău	46°34′	26°54′	VEGIK	— NS, EW, Z
				Mechanic	105 kg — NS. EW
6	Focșani	45°42′	27°11′	Hiller	— Z
				Mechanic	105 kg — NS, EW
					450 kg — NS
7	Iași	47°11′	27°34′	VEGIK	— NS, EW, Z
				Kirnos	— Z
				Mechanic	450 kg — NS, EW

One can see that the position of the stations around the seismic zone is not uniform. Towards the south only one station, namely București, is located, and focus parameters can not be always determined with adequate accuracy. Our experience in such determination indicates the necessity of setting up a new station.

In table 1 seismic station Cheia is also included; its construction has been finished, and it will be put into operation soon.

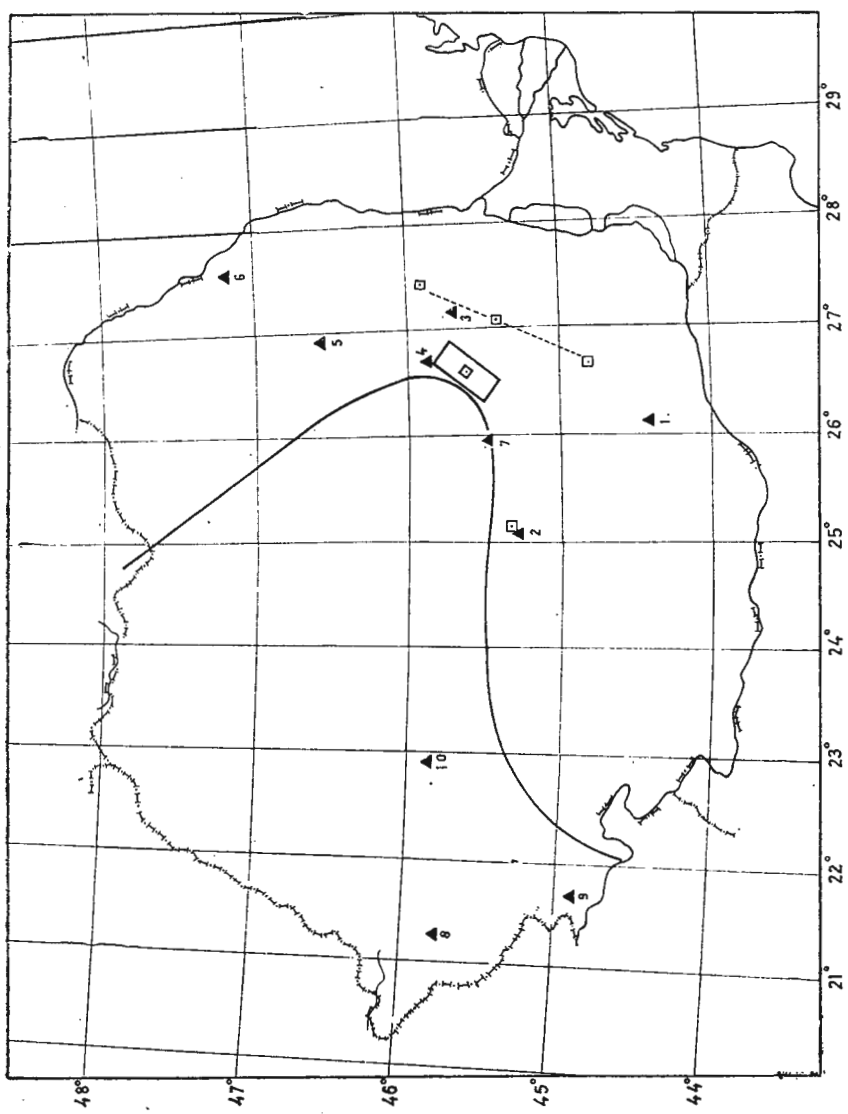

Fig. 1. — Ten existing seismic stations in Romania and the position of the epicenters which have been treated :
1, existing seismic stations; 2, treated epicenters; 3, deep earthquakes area; 4, Carpathian mountain range.

As the stations are equiped with different type of seismographs, the errors of arrival times of the seismic waves at each of the station is different. However, for simplicity's sake, it is assumed than the observational accuracy of all the stations is the same.

Errors of the epicenter position, origin time and focal depth, are alloted to each station from a random number series (Miyatake, Nakayama, 1960) and the equations (1) for a certain epicenter location are solved, using the least square method.

a) *Deep foci.* As the epicenters of the Vrancea earthquakes are placed in a small area, the calculation is done for a medium focus placed at 45°36′ N; 26°36′ E; $H = 120$ km.

b) *Normal foci.* For the normal foci earthquakes, wich take place in the region situated forward of the Carpathian mountain, three different positions of the epicenter have been treated, as listed below:

	I	II	III
φ [N]	44°48′	45°25′	45°50′
λ [E]	26°42′	27°05′	27°20′
H [km]	25	25	25

The points I and III are chosen to be in the outermost parts of the seismic zone, including the earthquakes from the Romanian Plain.

For each of the epicenter locations calculation is repeated 200 times, adopting different sets of random errors. Hence we have 200 different δR's, δT's and δH's for the given epicenter position. Then the standard deviations for r, t and h are calculated and are denoted as ΔR, ΔT and ΔH (ΔR is the vectorial sum of the errors Δx and Δy).

The criterion of the suitability of a new stations position is how small the observation errors will become when that specific station is added.

For that purpose, 91 points of new stations position are treated. These points are chosen east of the 24° meridian, at the intervals of 30′ both in longitude (about 40 km) and latitude (about 55 km). Distribution of the earthquake-parameter errors in all these points gives a general idea of the optimum location of a new station.

RESULT OF CALCULATION

a) **Deep earthquakes.** In order to make clear the problem of where the most desirable location of a future station should be, the errors of the focus parameters as a function of new seismic station, located in different points, are plotted.

Errors ΔR (epicenter location), ΔT (origin time) and ΔH (depth focus) for Vrancea deep earthquakes, as a function of an extra station, are shown in figures 2.

The amount of *error* ΔR decrease when going from epicenter to southeast or north-west and isolines are convex curves to the epicenter.

From the epicenter determination point of view, Dobrogea region is the most convenient for the location of a new station [$\Delta R < 100$ (= = 1.0 km)].

In the area with $\Delta R > 130$(= 1.3 km) along the zone where the existing stations are distributed, addition of a new station is less desirable.

ΔT *isolines* are of a shape similar to ΔH *isolines*, e.g. they are concentric curves with the center in the epicenter of the earthquake; in these cases, the errors have peculiar character. Close to the epicenter they have small values, afterwards they increase, reaching a maximum value in the circular zone, and then they decrease continuously with the epicentral distance. The minimum values are in the Dobrogea region and in the south-western part of the country [$\Delta T < 180$(= 0.18 s); $\Delta H <$ < 180(= 1.8 km)].

Taking into account all the focus parameters (ΔR, ΔT and ΔH) we conclude that the Dobrogea region is the most convenient for setting up a new station in addition to the eastern network for recording the local Vrancea region earthquakes.

b) **Normal earthquakes.** A similar calculation is done for the normal earthquakes wich occur in the Tecuci—R. Sărat—Urziceni seismic zone using the same 7 stations. The error amounts of the focus parameters, for the three choosen epicenters, are shown in figures 3 (ΔR-errors of the epicenter estimation), 4 (ΔT-errors of origin time) and 5 (ΔH-errors of focus depth).

Isolines for ΔR *errors* are of irregular shape, particularly for epicenter I (44°48′ N; 26°42′ E) because the epicenter position is rather outside the seismic network. Generally, the amount of errors are bigger (about twice) than in the other two cases.

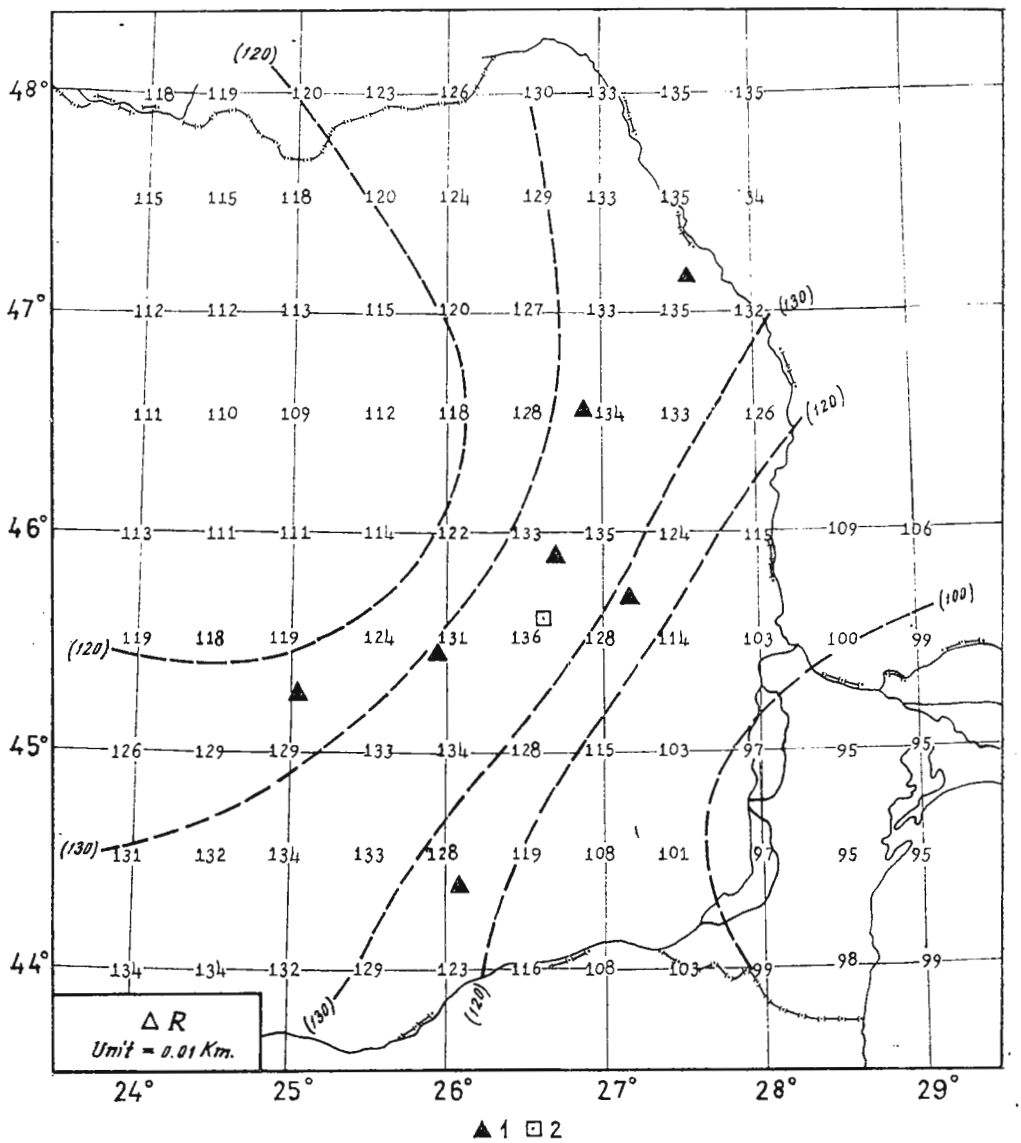

Fig. 2. — Distribution of the errors ΔR, ΔT and ΔH for Vrancea deep earthquakes :
a, The errors of the epicenter location (ΔR);
1, seismic stations; 2 epicenters, $\varepsilon = 0.1$ s.

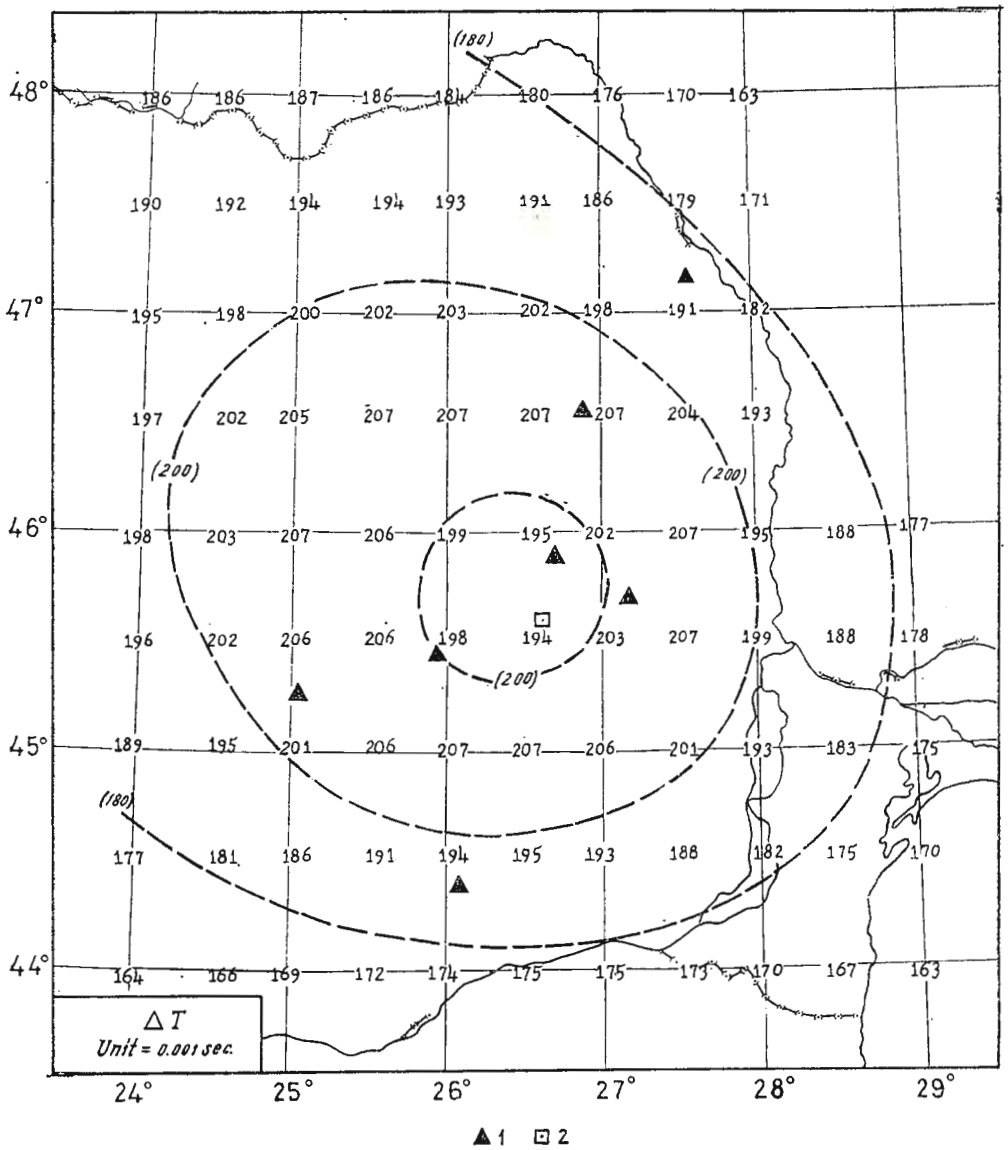

Fig, 2

b, The errors of origin time (ΔT);

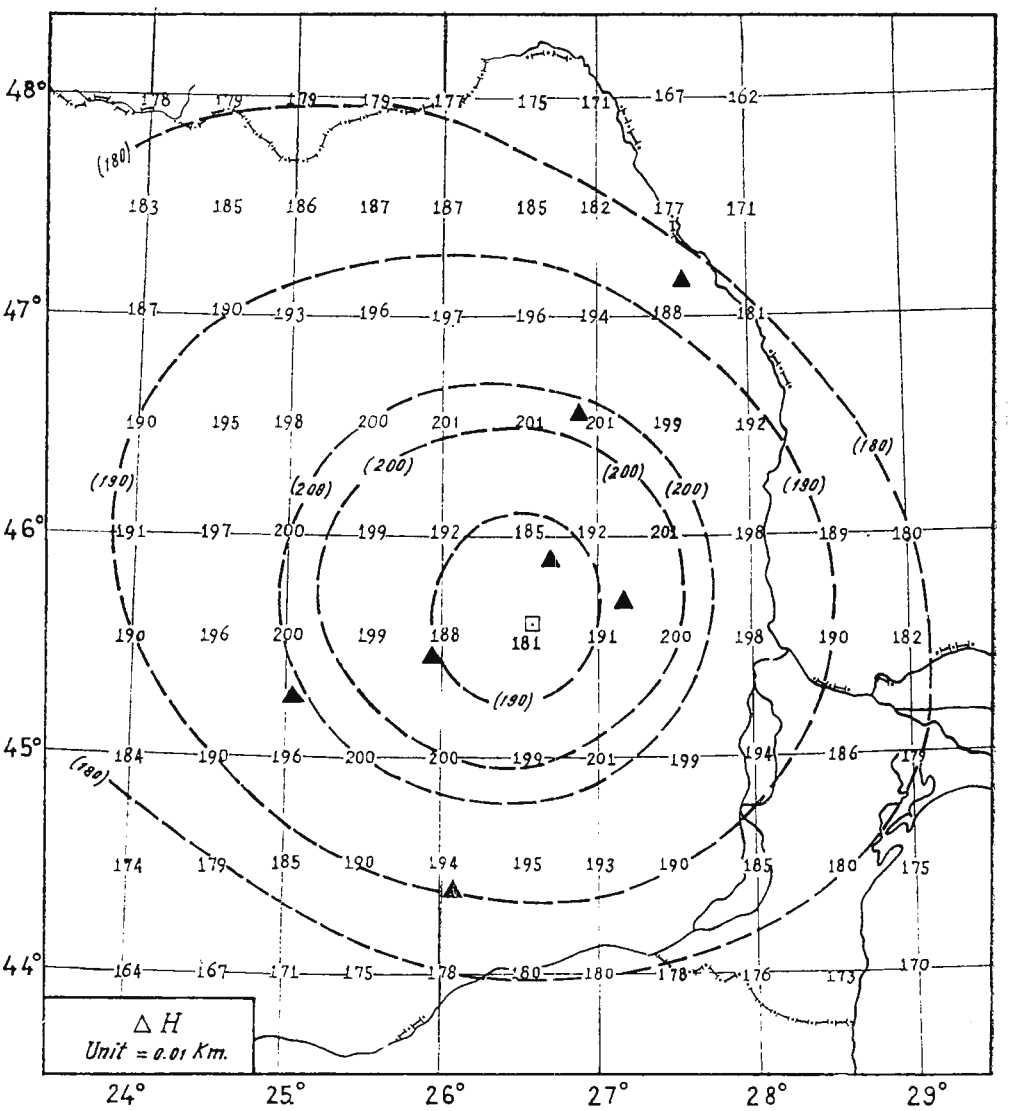

Fig. 2

c, The errors of focal depth (ΔH).

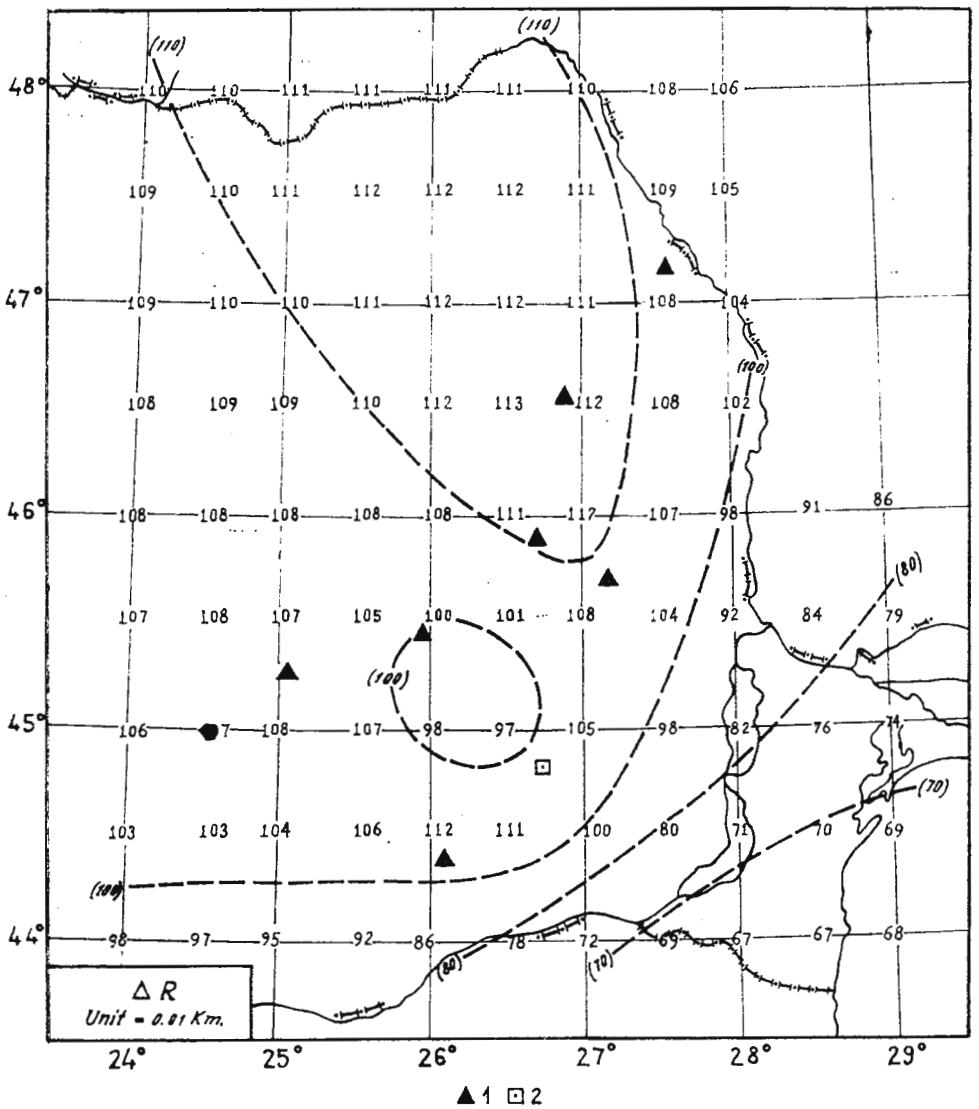

Fig. 3a.— Distribution of the ΔR error for three different epicenter positions of the normal earthquakes :

1, seismic stations; 2, epicenters; $\varepsilon = 0.1$ s.

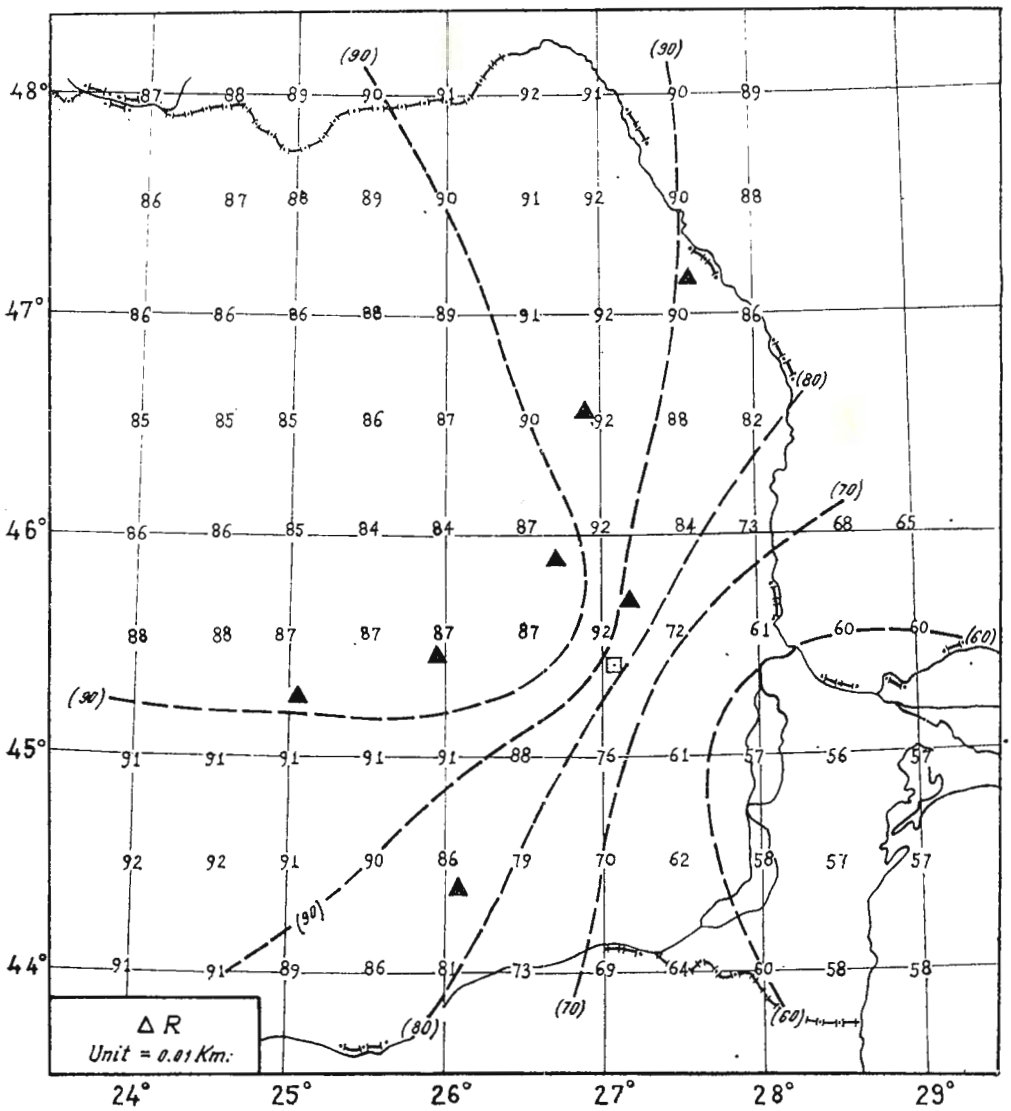

Fig, 3 b

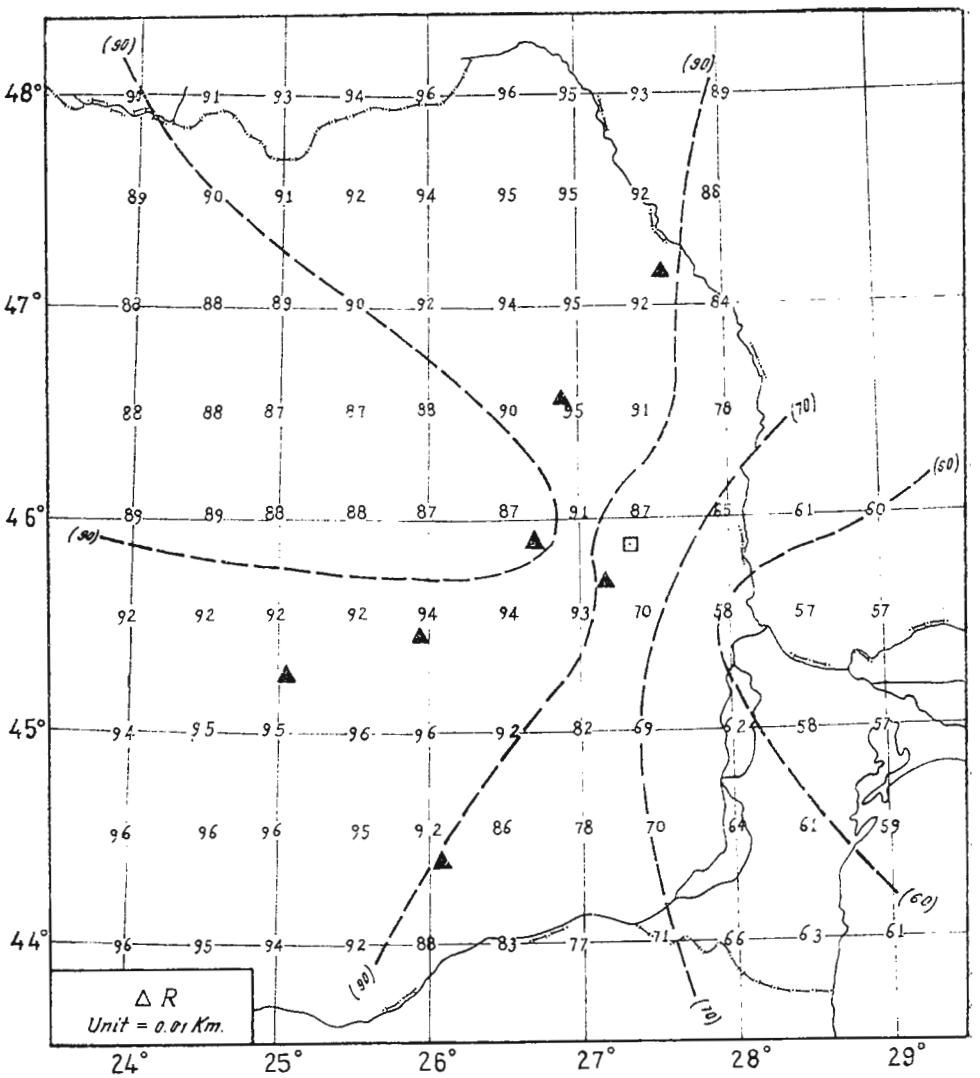

Fig 3 c

In case I, we can notice a relative small zone with $\Delta R < 100 (= = 1.0$ km) in the north-western part of the epicenter, placed inside the area of bigger errors.

The smallest values for all the three epicenter positions are in the south-eastern part of the country and especially in Dobrogea region $R = 60 \div 70$ ($= 0.6 - 0.7$ km).

Similarly to ΔR values, the amount of ΔT *errors*, in the case I, are twice in the other two cases. In cases II and III, the amount of ΔT values decreases with epicentral distance in the south-east direction and the smallest values are obtained in the Dobrogea region.

The shape of ΔT isolines is different for each of the three cases. The ΔT contour lines for cases II and III are curves which follow the direction of the stations distribution.

In case I, T isolines are concentric curves extended to the north-west of the epicenter. In this case the ΔT values are small at first in the vicinity of the epicenter, and then, again, at the bigger epicentral distances. Isolines $\Delta T = 160$ ($= 0.16$ s) encircles a small area about the epicenter in the southern part of the country.

A straight line, drawn along the smallest distances bewteen two consecutive isolines, points to the region of desirable location for new seismic station.

The distributions of ΔH *errors* (depth of focus) for all the three cases (fig. 5) are similar to the error distributions of the deep earthquake.

An area in the vicinity of the epicenter with small amount of errors, is surrounded by the area with bigger errors; going farther away, the amount of errors becomes again small.

Taking into consideration all the foci from the normal earthquakes zone, we can draw the conclusion that for the determination of the focus depth a new observation points is desirable in the southern part of the country, particularly in Dobrogea region.

From the calculation of the ΔR, ΔT and ΔH errors, for deep and normal earthquakes, which occur in the region at the bend of the Carpathian arc, we can get a general idea about the accuracy of determination of the earthquake parameters when a new seismic station is added. Figures 2—5 indicate that the Dobrogea region is the most convenient place for setting up a new station.

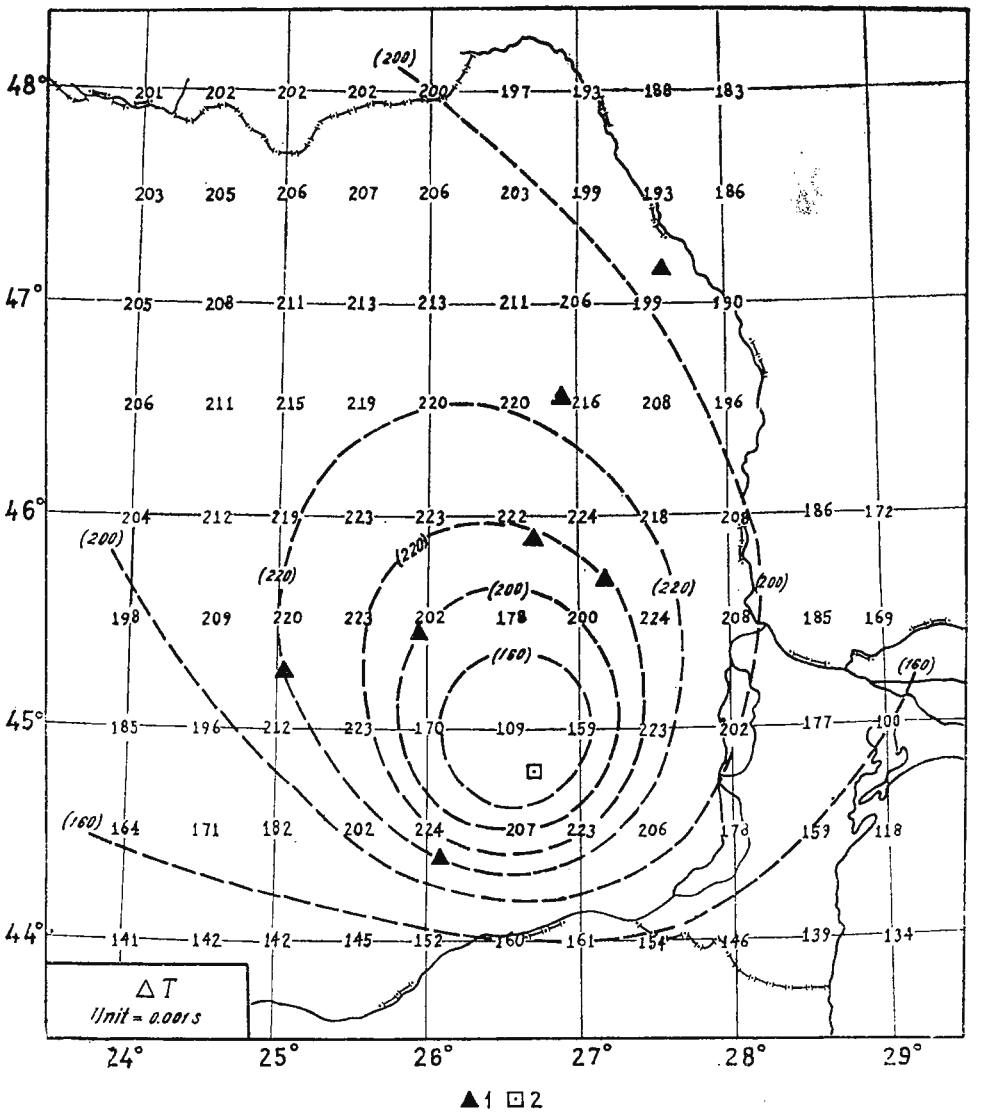

Fig. 4a. — Distribution of the ΔT errors for three different epicenter positions of the normal earthquakes :

1, seismic stations; 2, epicenters; $\varepsilon = 0.1$ s.

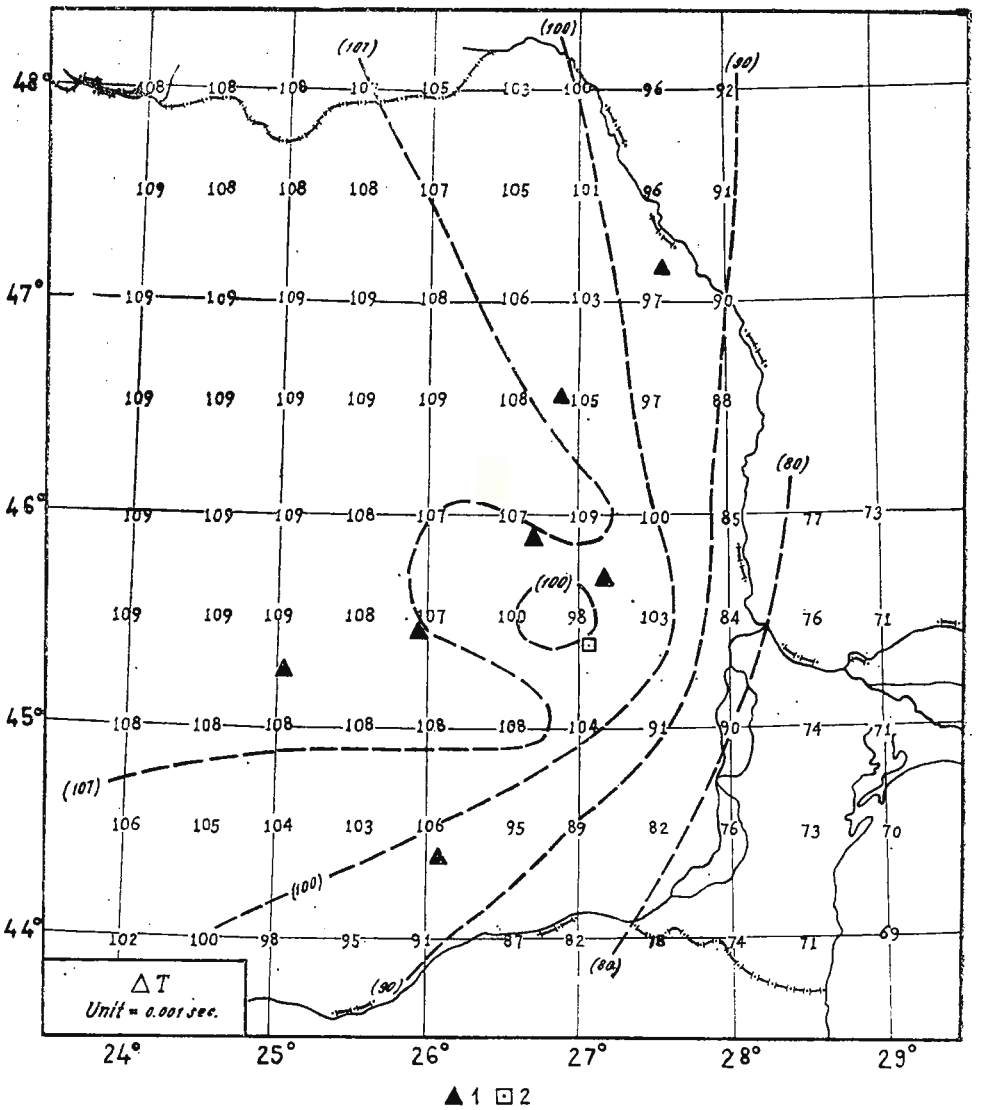

Fig, 4 b

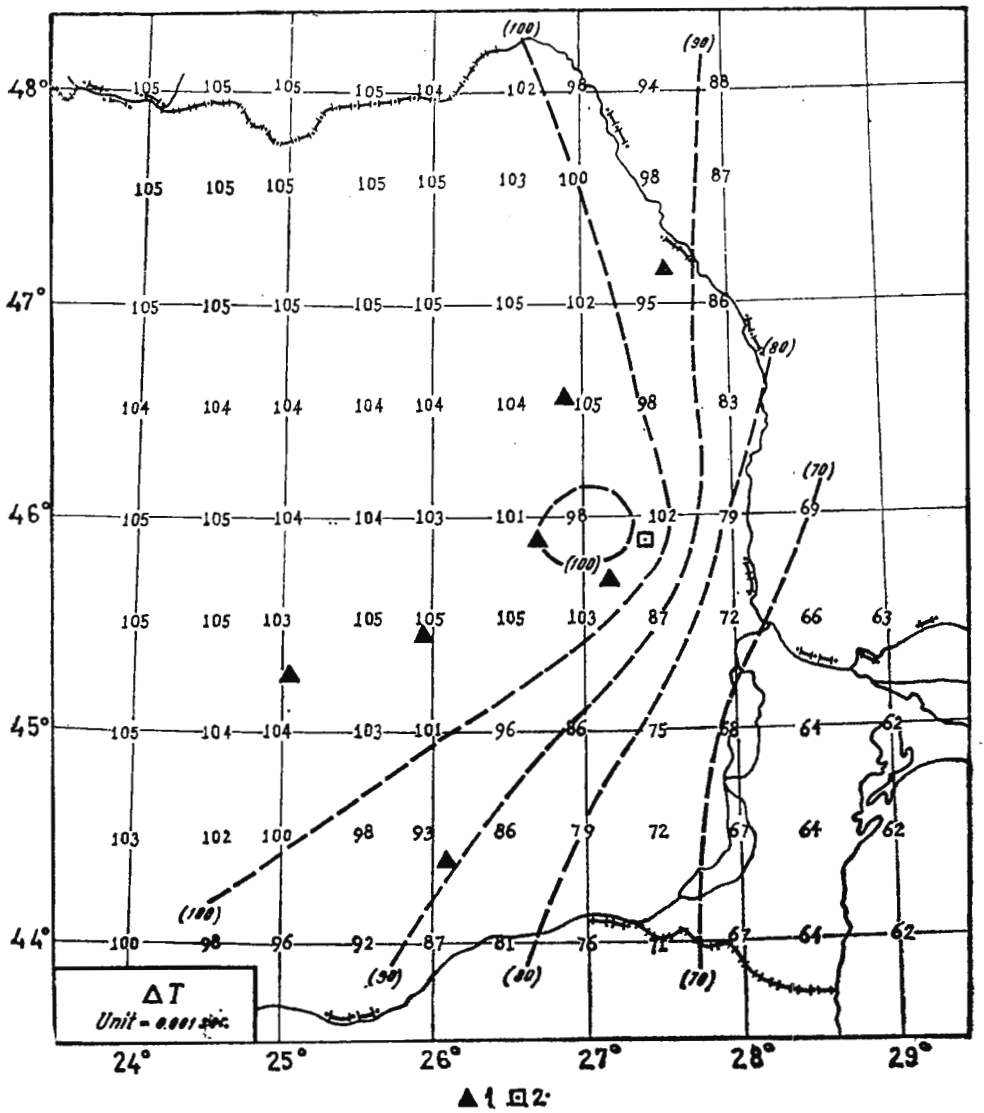

Fig 4 c

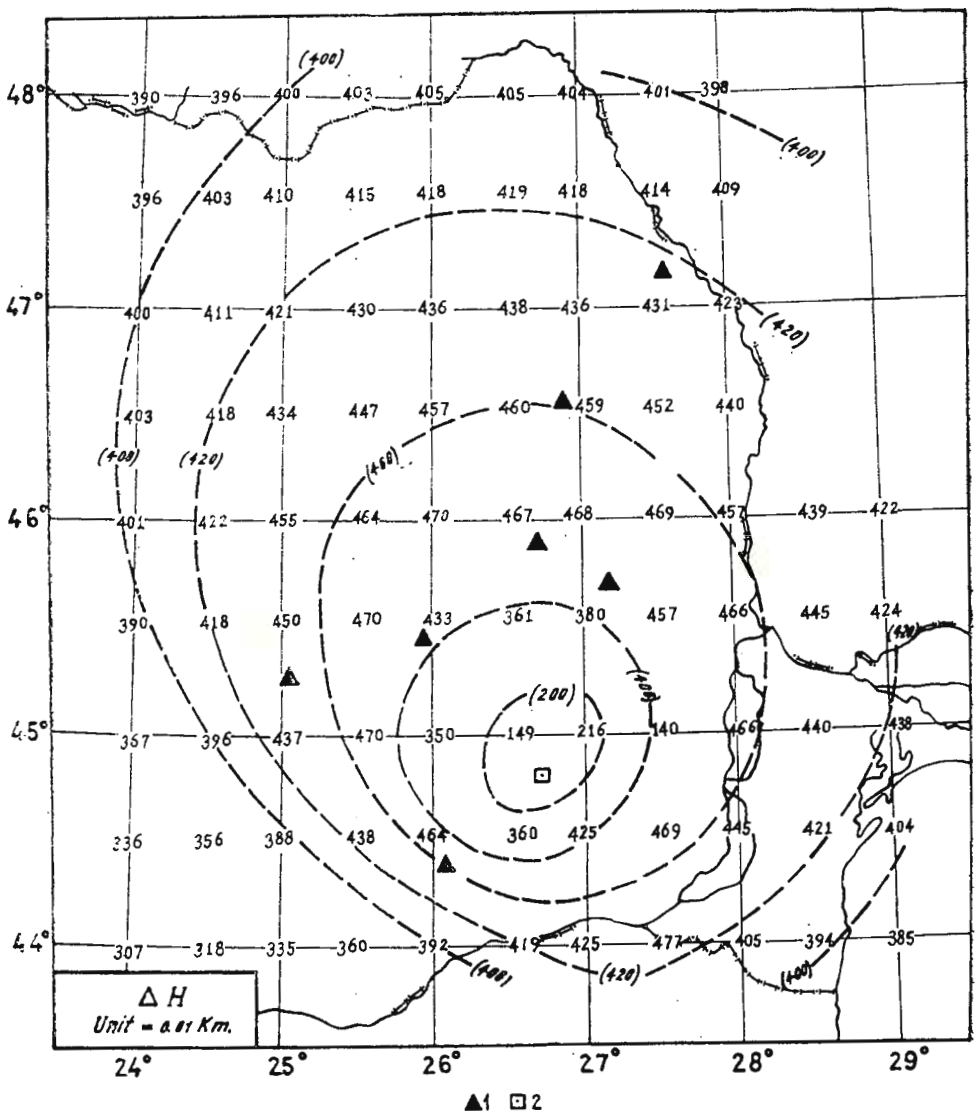

Fig. 5a. — Distribution of the ΔH errors for three different epicenter positions of the normal earthquakes :

1, seismic stations; 2, epicenters; $\varepsilon = 0.1$ s.

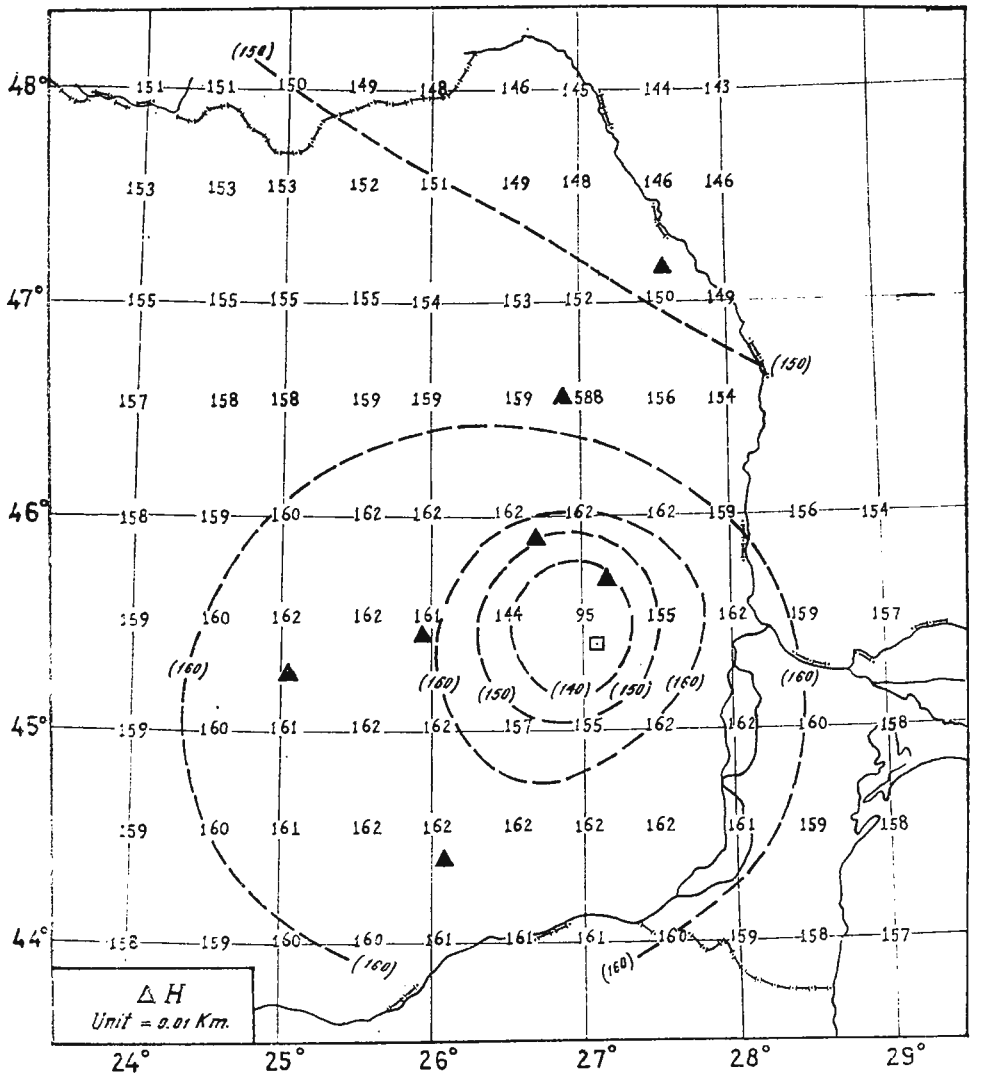

Fig 5 b

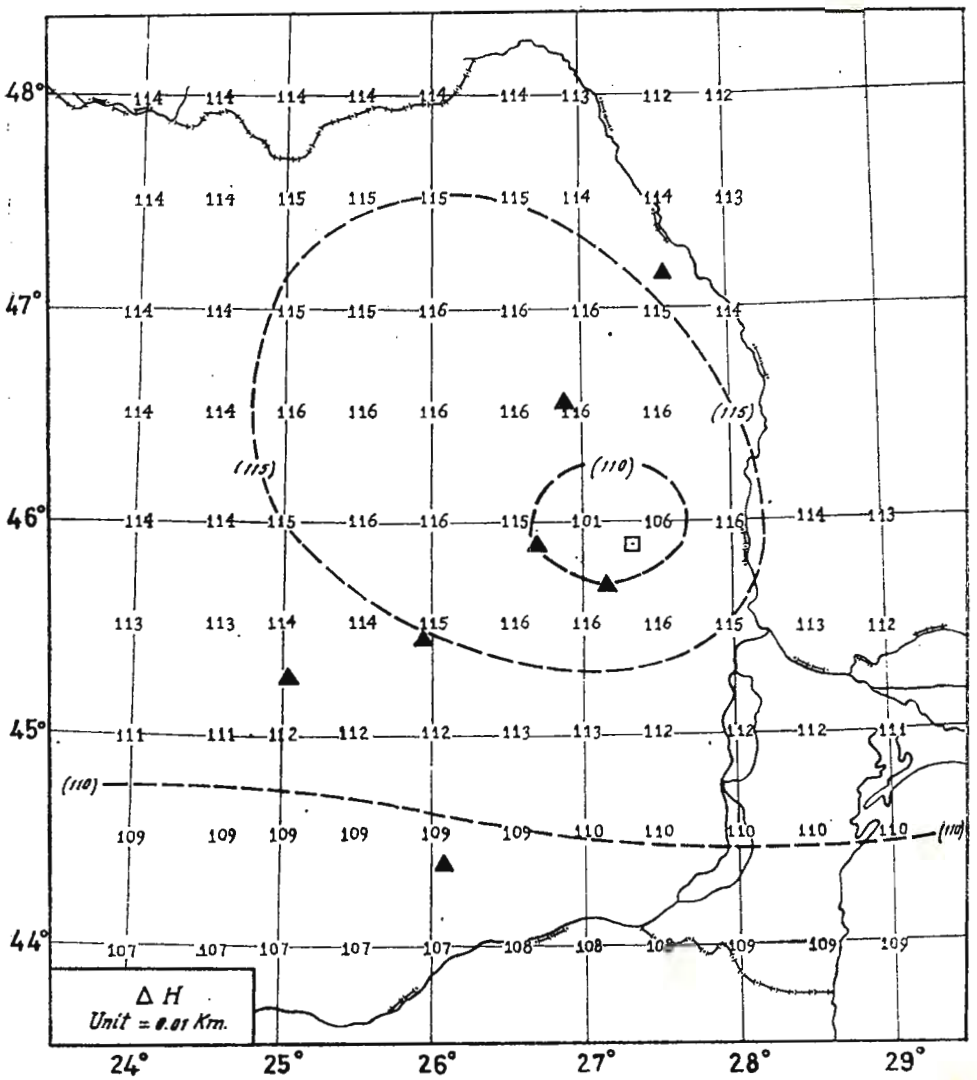

Fig 5 c

CÎMPULUNG SEISMIC ZONE

DATA

In the under Carpathian region, in the immediate neighbourhood of Cîmpulung city, there is another important seismic zone with the foci located in a karstic region of complex tectonics. Several relative large earthquakes have taken place there. Les us mention the earthquake of January 5, 1940 with the maximum intensity of 6° MSK scale (M e d v e d e v, 1968) and the earthquake which occured recently — on the April 12, 1969—with magnitude $M = 5.2$ and maximum intensity of 6° MSK scale.

Both earthquakes have practically the same focal parameters: 45°,3 N; 25°,1 E; $H = 7-10$ km.

The second seismic event mentioned above was followed by a long series of aftershocks (about 500) for two months (C o n s t a n t i n e s c u et al., 1971).

Consequently, when completing the Romanian seismic network, it is necessary to take, also, into account accuracy in the parameter determination of these earthquakes. For this purpose the calculation of focus parameter errors is carried out by the use of data from all 10 existing Romanian stations. Besides the stations listed in the table 1, the following station at the western part of the Romanian territory are included (tab. 2).

TABLE 2

No.	Station	Latitude (North)	Longitude (East)	Instrument	
8	Timişoara	45°45′	21°14′	VEGIK	— NS, EW, Z
				Kirnos	— NS, EW, Z
				Mechanic	450 kg — NS, EW
					200 kg — NS, EW
9	Sasca	44°53′	21°42′	VEGIK	— NS, EW, Z
				SMK	— NS, EW, Z
10	Deva	45°53′	22°55′	VEGIK	— NS, EW, Z
				Kirnos	— Z

RESULT OF THE CALCULATION

The calculation is done assuming 192 positions of one new station added to the present network. The points are distributed all over the territory at the interval of 30′ both in longitude and latitude. For the focal

parameters the following values are adopted : 45°,3 N ; 25°,1 E ; $H = 10$ km. This points is located in the north-eastern part of Cîmpulung.

The amount of ΔR, ΔT and ΔH errors are shown in figure 6.

On can see that the isolines are of particular shape for each of the parameter. The area delimited by the smaller error amounts of the epicenter determination [$\Delta R = 450$ (= 0.45 km)] is localised in the southern part of the country, in the zone 24°,5—26°,5 E ; 43°,5—44°,7 N.

The area with errors $450 < \Delta R < 485$ has three branches, two of then are in Romanian Plain, and the third one extends to the north. Areas with small values of ΔT and ΔH errors are in the southern part of the country, where isolines have the direction WNW—SSE. The isolines wich include area with relative larger values of errors are of a complex form.

Taking into account all the focus parameters for the Cîmpulung earthquakes, we conclude that the optimum place for setting up a new tation is the region around the coordinates 24°,3 E ; 44°,0 N.

CONCLUSIONS

Figures 2—6 give some idea on the weak points of the present network regarding two important seismic regions of the Romanian territory (Vrancea and Cîmpulung), indicating desirable locations for the future observatories.

Parameter determination for the strong earthquakes has been generally done by using data from many stations distributed all over the world. The focus parameters of local shocks have to be determined, however, with data mainly obtained from local network. From this point of view, the distribution of the stations in the epicentral area has great importance to the determination of the earthquake parameters. When a new station is added, its location has to be choosen carefully so that the accuracy of the parameter determination becomes ar good as possible.

For the local earthquakes which occur at the bend of the Carpathian arc, eastern Romanian seismic network, with necessary supplements to the existing set – which result from this study – is adequate. For the Cîmpulung earthquake, which occur in the area situated in the center of the country, all Romanian stations have to be used. In this context, the result obtained from figure 6 have to be correlated with the data obtained in the previous paper (I o s i f, S k o k o. S a t o, 1972) where the optimum distribution of the seismic stations all over Romanian territory is considered. It is concluded there that the distribution of the focus

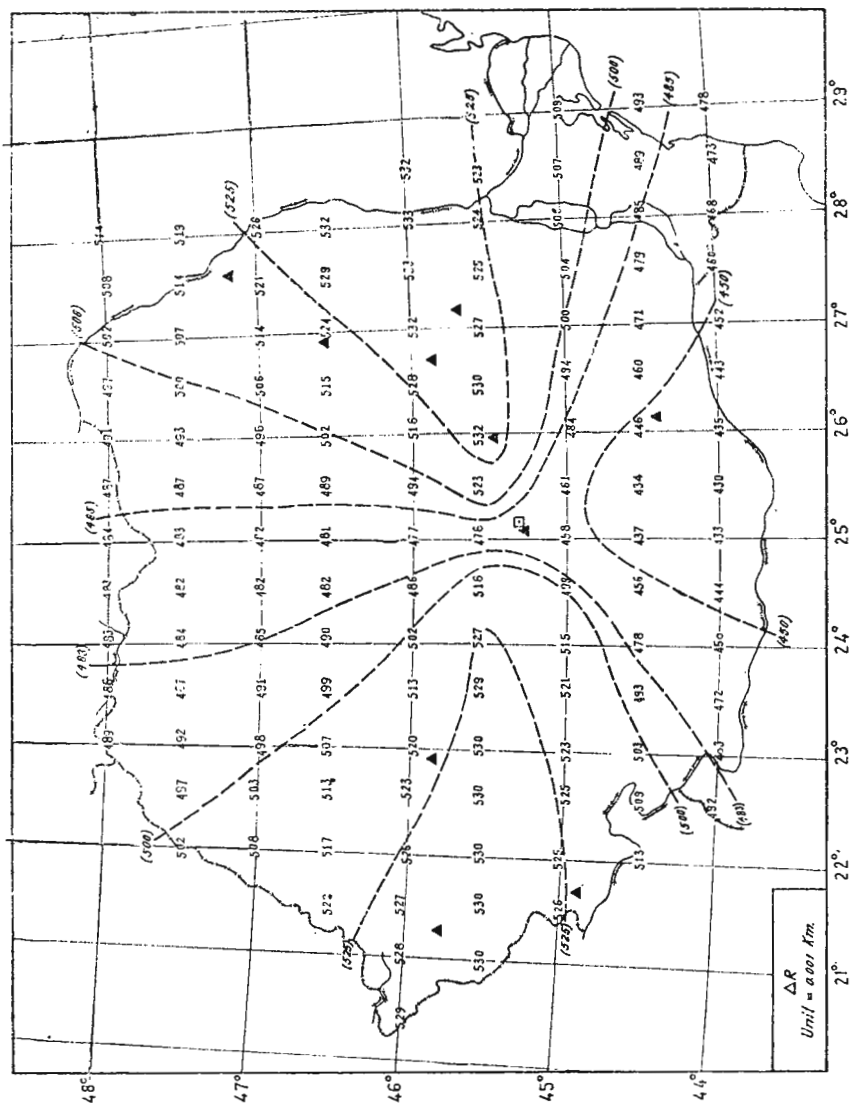

Fig. 6. — Distribution of the errors ΔR, ΔT, ΔH for Cîmpulung earthquakes using all the existing stations : a, The errors of the epicenter location (ΔR),

1, seismic stations ; 2, epicenters ; $\varepsilon = 0.1$.

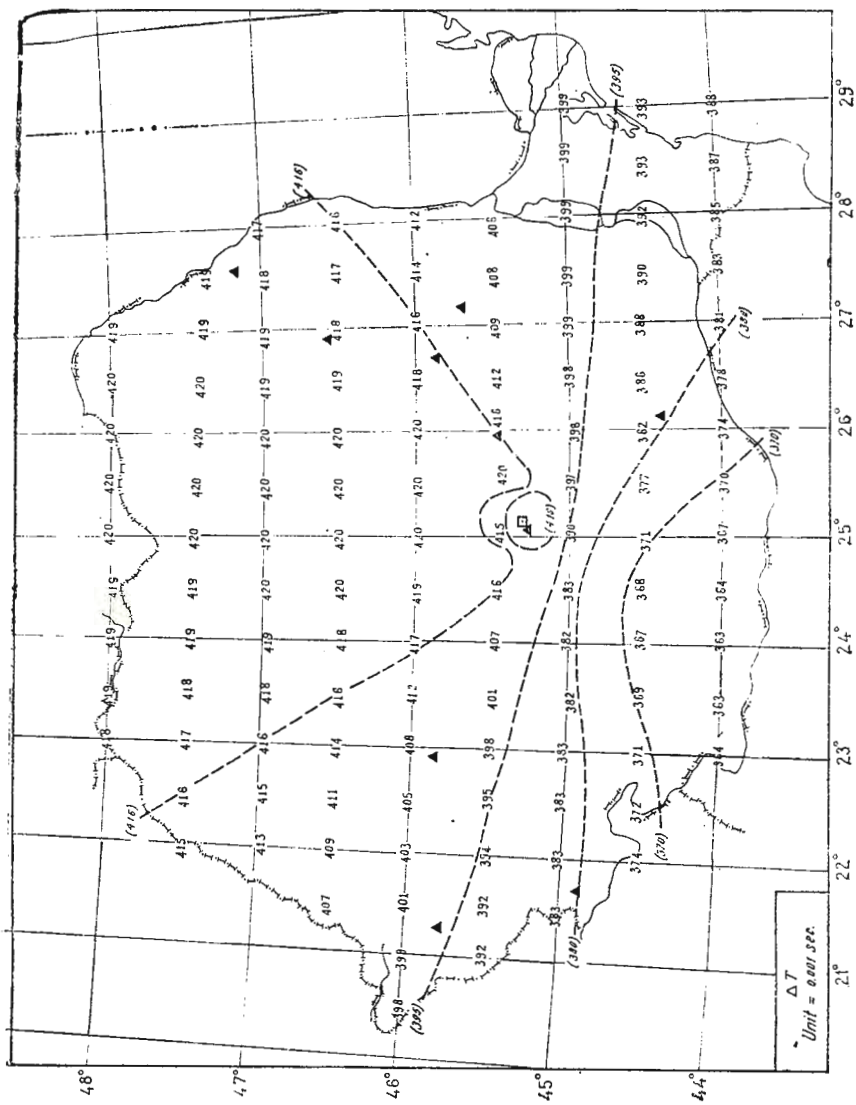

▲1 □2

Fig 6

b, The errors of origin time ΔT;

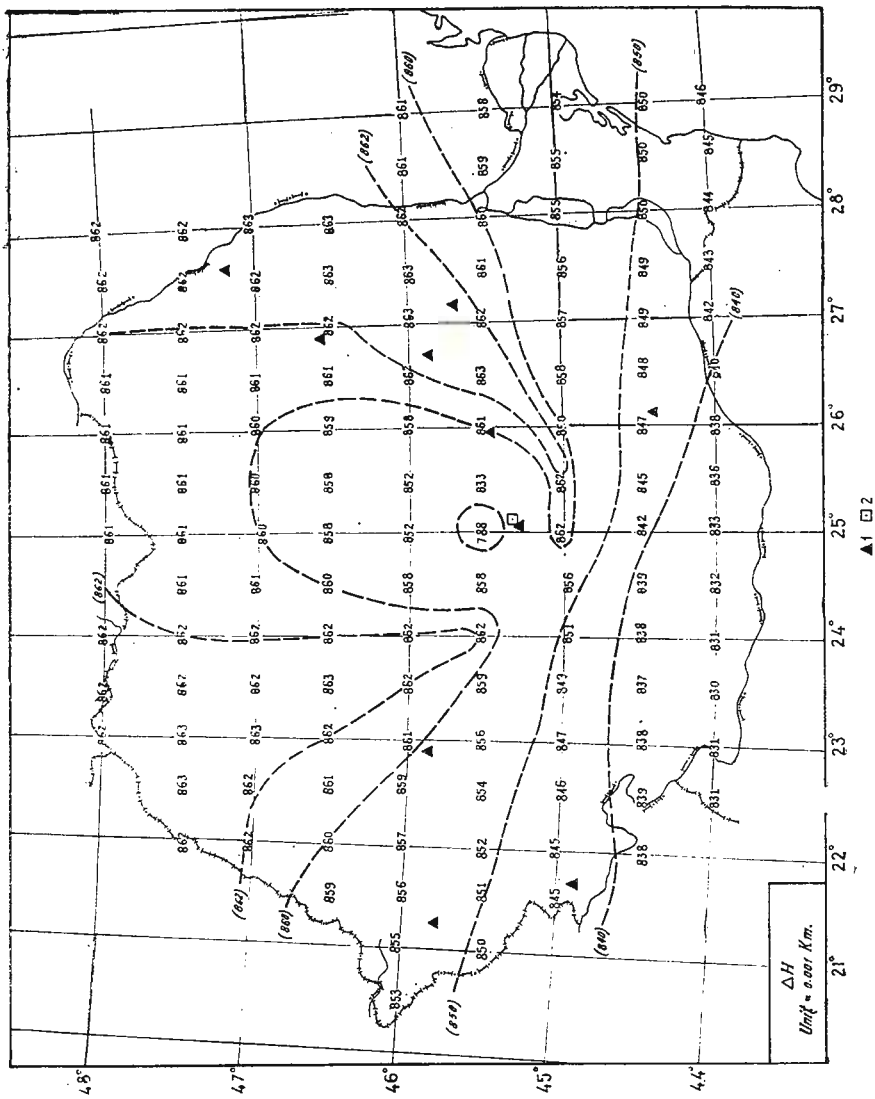

Fig 6

c, The errors of focal depth (ΔH).

parameter errors, using actual Romanian seismic set, indicates that, besides some other areas, the Dobrogea region and the southern part of the country have to be considered for setting up a new seismological observatories.

Acknowledgements

The authors are indebted to Dr. T. Santo Acting Director IISEE, for having provided us the opportunity to elaborate this study at IISEE.

The authors are greatly indebted to Prof. Y. Sato for his valuable advices and kind consideration.

The discussions with Dr. W. Adams, UNESCO Expert in Seismology for Academic Course 1971—1972 are greatly appreciated.

REFERENCES

Constantinescu L. Georgescu A., Radu C. (1971)About a Shallow Earthquake in Romania and its aftershocks. *Rev. Roum. Geol. Geophys. Geogr., Ser. Geophys.*, 15, 2, București

Iosif T., Iosif S. (1971) On Earthquakes with Epicenters in the Romanian Plain. (in Romanian) *St. cerc. geol., geogr., geofiz., Ser. geofiz.*, 9, 2, București.

Iosif T., Skoko D. Satoy. (1972) Optimum Distribution of Seismic Stations in Romania. *Bull. Intern. Inst. Seism. Earthq. Eng.*, 9, Tokyo.

Medvedev S. V.(1968) International Scala of Seismic Intensity. Seismic Zoning of the USSR. (in Russian), *Nauka*, Moscow.

Miyatake O., Nakayama T. (1960) Monte Carlo Method. (in Japanese), *Nikkan Kogya Shimbun*, Tokyo.

Sato Y. (1965) Optimum Distribution of Seismic Observation Points. (in Japanese), *Zisin*, 18, 1, Tokyo.

Sato Y., Skoko D. (1965) Optimum Distribution of Seismic Observation Points. *Bull. Earthq. Res. Inst.*, 43, Tokyo.

Skoko D., Sato Y., Ochi I. (1967) Optimum Distribution of Seismic Observation Points, IV-Desirable Location of a New Station in Yugoslavia. *Bull. Earthq. Res. Inst.*, 45, Tokyo.

GEODYNAMIC INSTRUMETATION

LOCAL ANOMALIES IN STRAIN MEASUREMENT

BY

ROGER BILHAM, GEOFFREY KING[1]

Abstract

Disagreements in the amplitude and phase of measured tidal strains are often found between instruments situated close together. It is not possible to predict or compensate for the variations in local conditions which give rise to these disagreements. A practical method of establishing the degree of homogeneity of the strainfield is proposed which uses several strainmeters installed at individual locations. Using this method it should be possible to isolate locally generated strains from variations in measured strain which are caused by geologically interesting features or by loading tides in shallow seas.

It is well known that measurements of tilt or strain tides near the Earth's surface can show significant disagreement even when measurements are close together. Such discrepancies should not be expected to occur if the surface of the Earth were a uniform half-space. Nor is it be expected from the theoretical strainfield since the wavelength of tidal strains or tidal-loading strains are often much larger than the spacing between measurements. The cause of these discrepancies can be predicted from analysing realistic models of the Earth's surface which incorporate topographical or elastic spacial variations (King, 1971).

Elastic variations can be caused by fissures, faults and cracks in surface rocks as well as by changes of rock type and condition. Topographic

[1] University of Cambridge. Department of Geodesy and Geophysics. Madingley Road, Cambridge, U.K.

surface variations can cause significant distortion to otherwise uniform strainfields as can the geometrical properties of the cavity in which the strainmeter or tiltmeter is installed (K i n g , B i l h a m)[2].

It is not possible to predict the three dimensional elastic conditions prevailing near any isolated measurement of strain or tilt. Thus in measu-

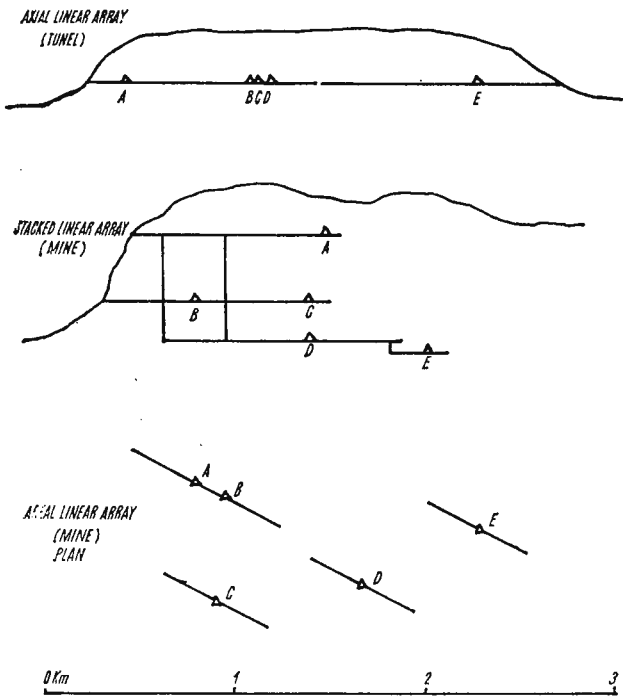

Fig. 1. — Linear arrays of strainmeters :

The axial array above is similar in profile to Queensbury Tunnel. Note that a strainmeter array in this sense is different from the conventional multi-component strain tensor array. It is not „a priori" obvious that the results from multi-component arrays are valid until evidence for elastic homogeneity or the degree of heterogeneity exists.

rements dependent on local elastic conditions the observed phase and amplitude cannot be corrected by calculation.

A practical approach has been devised which can partially overcome the uncertainty that is inevitably associated with isolated measurements of strain. Several measurements are undertaken at a single site and results are compared. This is a simple procedure if the measurements are parallel or colinear to each other. Such measurements form a linear array (fig. 1). The spacing is arranged between measurements such that the homogeneity of the strainfield can be assessed. If a homogeneous strainfield does exist it will be indicated by identical phase and magnitude being monitored by

[2] K i n g G. C. P., B i l h a m R. G. Strain Measurement Instrumentation and Technique. 1972. Royal Society Discussion Meeting, London (in press).

all the instruments present. If inhomogeneity exists on a wavelength much greater than the area covered by the array a gradation in amplitude may be present across the array. If inhomogeneity exists on a wavelength smaller than the array this will be apparent from the scatter of observed values within the array (fig. 2).

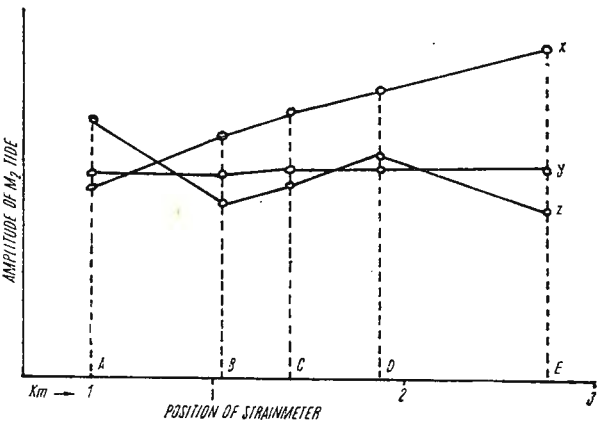

Fig. 2. — Schematic curves obtained from a linear array of strainmeters:

The wavelength of any ealstic heterogeneity can be established from the scatter or trend of observed amplitudes and phases. Curve x obtained in the presence of elastic inhomogeneity outside the measurement area. Curve y obtained if ground is homogeneous. Curve z obtained if lateral variations in elasticity occur within the measurement area. The wavelength of tidal and load tide strains are large compared with the separation of the instruments.

Examples of linear arrays are shown in figure 1. It should be noted that strainmeters installed underground must be installed parallel to the line of the underground cavity in order to avoid distortions in the strainfield associated with measurements which include any component of the width or height of the cavity. (King, Bilham)[3]. In this respect surface strainmeters or trench-installed strainmeters are useful as linear array strainmeters (Berger[4]; Major, 1966).

Having established the degree of homogeneity at a single site or group of sites it is then possible to consider differences or similarities between measurements in an adjacent area which has been similarly examined.

Thus it is possible to start from a single observation and establish the degree of elastic homogeneity over a very large area even when variations in the strainfield occur. A strain survey of Britain has been initiated using these principles. The base station of this survey is Queensbury Tunnel, Yorkshire (Bilham et al, 1972) in which six strainmeters are installed. A network of tunnels are being used to extend the survey from Que-

[3] *Op. cit.*, p. 2.

[4] Berger J. Strain Measurements with Laser Interferometers. 1972. Royal Society Discussion Meeting, London (in press).

ensbury to cover the entire country. It is hoped that the network will be extended eventually to cover the mainland of Europe.

As the network increases in size it is unrealistic to consider using only those underground locations that are parallel to the initial base station.

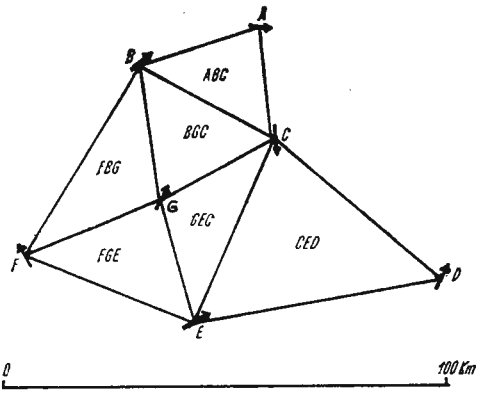

Fig. 3. — Spatial array of tested sites :
Strain measurements (linear arrays) in different azimuths A — G. Strain tensor cobinations of three horizontal measurements shown as circles.

It is often necessary to use every available environment. In these cases amplitude and phase can be compared using a strain tensor derived from groups of three measurements. Since the wavelengths of tidal strains are usually more than 100 Kms it is possible to choose three locations situated within 100 Kms of each other in order to obtain a central strain tensor (fig. 3).

INSTRUMENTS

Strainmeters used to establish homogeneity require individual calibration to within 5%. The wire strainmeters used in Cambridge have a sensitivity of 5.10^{-10} strain and are calibrated to within 3%. The linearity of the instrumental amplitude response and the linearity of the data timing system are of major importance in subsequent frequency analysis. The amplitude response of Cambridge strainmeters has been established as being linear to within 1% for ranges between 10^{-8} and 10^{-4} strain. The timing is dependent on chart speed constancy and 24 hour time marks supplied by an accutron 'tuning-fork' clock. The accuracy of this timing is quoted to better than 1 minute/month.

Since a large number of instruments are proposed it is necessary to simplify maintenance problems. Automatic drift correction is incorporated into the wire strainmeters so that records are not lost between inspection visits. A total drift of 10^{-4} strain can be tolerated before manual adjustment is required which can reduce the number of visits to one or two per year. Slow speed chart recorders enable six months of operation with a

time resolution of half an hour. Low power consumption at 12 V enables continuous operation from caustic soda batteries for $1\frac{1}{2}$ years. Finally, the instruments are waterproof and are designed to be installed beneath the surface of underground cavities. Thus if a tunnel is available an instrument can be installed without its presence being obvious. In practice this means the installation cost is reduced because no security arrangements are required and the tunnel may be left open to the public.

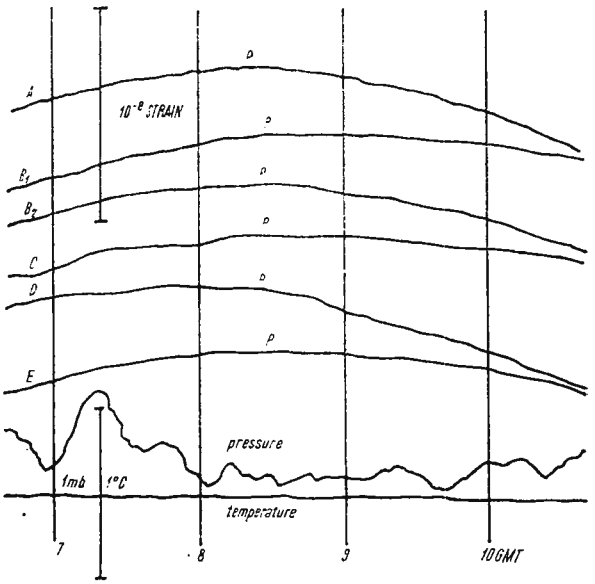

Fig. 4. — Record from Queensbury Tunnel, U.K.:

Strainmetters A – E are located as shown in figure 1. Note that the peak strain total amplitude occurs at different times although each instrument is in the same azimuth (±2°); p = apparent peak amplitude.

DATA COLLECTION AND ANALYSIS

It is possible to ignore long-period drift since this is of little interest in aseismic areas. The phase and amplitude of diurnal and semi-diurnal tides can be extracted from time series which have a sufficiently large signal to noise ratio at these periods and which are sufficiently linear in time and amplitude. The importance of linearity must again be emphasized when using fequency analysis methods.

A continuous length of data from each strainmeter is analysed using Fast Fourier techniques after removing linear drift, (B i l h a m et al., 1970). The length of data required depends on the number of tidal peaks which are of interest and the degree of noise present in the data. Normally, one month is sufficient to examine the semi-diurnal and diurnal peaks but three months are required to resolve the O_1 and K_1 peaks and the M_2

and S_2 peaks. A year of data is required to examine the finer lines of the tidal spectrum.

In order to compare the results from adjacent strainmeters it is important to analyse data covering the same period of time. In this way comparisons may be made of the records directly. The phase and amplitude of each tidal peak can also be compared directly to examine differences attributable to strain variations.

At the time of the Romania meeting long spans of data from the Queensbury strainmeters have not yet been analysed. In the time domain the data shows evident peak shifting (fig. 4) which has been attributed to local effects (King and Bilham)[5].

CONCLUSIONS

Strain measurement technology is presently sufficiently versatile to answer many of the uncertainties that have been associated with previous measurements of strain near the Earth's surface. It is possible to distinguish between propagating and locally induced strains at a particular site using the systematic array techniques that have been outlined. Where such an array has been operated, locally generated strains are seen to form a significant proportion of the total measured strain.

Using an expanded array it is possible to establish strain coherence over large area. When this has been achieved spatial variations in strain caused by geological and tectonic phenomena or by sea-loading strain tides may be studied systematically.

REFERENCES

Bilham R. G., King G. C. P. (1971) Strain Gauges for Geophysics. XII General Assembly of the European Seismological Comission, Comunication 3A, nr. 30. *Geophysics*, 101, Tulsa, Oklahoma.

— Evans R., King G. C. P., Lawson A., Mc Kenzie D. P. (1972) Earth Strain Tides observed in Yorkshire, England, with a Simple Wire Strainmeter. *Geophys. J. R. astr. Soc.*, 29, 4, London.

King G. C. P. (1971) The Siting of Strainmeters for Teleseismic and Tidal Studies. *Bull. R. Soc. N. Z.*, 9, 239, U. K.

Major M. W. (1966) Residual Strain over Large Areas : in E.S.A.A. Symposium on Earthquake Prediction, February 1966, Rockville.

[5] *Op. cit.*, p. 2.

THE EFFICIENCY OF DIFFERENT OPTIMUM MULTICHANNEL FILTERS IN DEEP SEISMIC SOUNDING[1]

BY

BURKHARD BUITKUS[2]

Abstract

Due to the increasing importance of seismic refraction long range measurements for detailed studies of the deeper Earth's crust and the upper mantle with a SNR of frequently about 1 or smaller 1, the efficiency of different optimum multichannel filters is examined for their use in deep seismic sounding.

Originating from the representation of different optimum multichannel filters by means of the correlation theory and their frequency wavenumber characteristics, it is shown which filter processes will be suited best for the signal-noise-improvement of seismic refraction measurements.

Based on the results obtained in spectral-and coherence -investigations of signal and noise, adapted seismometer arrangements are given for the application of multichannel filters in deep seismic sounding.

With the aid of numeric treatment of simulated seismograms which are adapted to the signal-and noise-characteristics in deep seismic sounding, the obtainable signal-noise-improvements are evaluated and by this the enlargement of record-distances is estimated up to which traveltime-measurements can be made with the indicated seismometer-arrangements using suitable optimum multichannel filters.

[1] Full text will appear in *Zeitschrift für Geophysik*, 1973.

[2] Institut für Geophysik der Technischen Universität Clausthal. now : Bundesanstalt für Bodenforschung, Hannover, B.R.D.

MODELAGE ANALOGIQUE D'UN SISMOGRAPHE AVEC UN SYSTÈME DE FILTRES

PAR

CONSTANTIN FÂNTÂNĂ[1]

Résumé

Le calcul des filtres pour les sismographes magnétoélectriques peut être facilité par le modelage du sismographe avec le circuit de filtrage sur une calculatrice analogique.

Deux méthodes sont envisagées : le modelage direct du sismographe à base du système classique d'équations differentielles qui le caractérise, en utilisant un filtre rejecteur et le model ayant comme point de départ le schéma électrique équivalent du circuit pendul-filtres-galvanomètre.

En utilisant pour ce schèma le deuxième théorème de Kirchhoff, on obtient un système d'équations intégro-differentielles, dont le schéma de calcul est aussi présenté.

Une des méthodes modernes d'amélioration du rapport „signal-bruit" dans les enregistrements sismiques est l'utilisation des filtres dans le circuit des sismographes magnéto-électriques.

Mais, le choix du système optimum de filtres suppose de nombreux calculs et essais, qui peuvent être sensiblement simplifiés par le modelage du système sismographe-filtres sur une calculatrice analogique.

Le point de départ pour l'obtention du modèle analogique est l'équation de l'oscillateur linéaire amorti :

$$\ddot{y} + 2h\dot{y} + \omega^2 y = P(t) \tag{1}$$

transformée en „équation machine" :

$$\ddot{y} = P(t) - 2h\dot{y} - \omega^2 y \tag{1'}$$

[1] Institut de Géophysique Appliquée 78, rue Izvor. Bucarest, Roumanie.

Le schéma de calcul correspondant est présenté dans la figure 1, où les éléments opérationnels ont les suivantes fonctions :

I_i = amplificateurs intégrateurs

I_{vi} = amplificateurs inverseurs

$\sum_i$ = additionneurs

P_i = potentiomètres

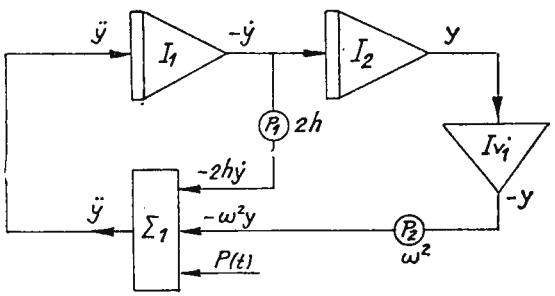

Fig. 1. — Le schéma de calcul pour l'équation (1').

La solution de l'équation s'obtient graphiquement sur un enregistreur X — Y ou sur l'écran d'un oscilloscope. Suivant l'endroit de connexion du celui-ci, on peut étudier n'importe quelle des valeurs y, $\dot{y}$, $\ddot{y}$, représentant, dans ce cas, la réponse du pendul concernant le déplacement, la vitesse ou l'accélération du sol.

La fonction $P(t)$, représentant le déplacement du sol, peut-être simulée soit par une tension sinusoïdale fournie par un générateur de tension, soit avec un dispositif spécial qui livre une tension dont la forme suit le profil d'une sismograme.

La modification du régime du pendul se réalise simplement en manipulant les potentiomètres qui déterminent les coefficients.

Que nous considérions maintenant le système d'équations

$$\ddot{\theta} + 2\varepsilon_1\dot{\theta} + n_1^2\theta = -\frac{\ddot{x}}{l_1} + \sqrt{\sigma^2 4\varepsilon_1\varepsilon_2\frac{k_2}{k_1}}\,\dot{\varphi}$$

(2)

$$\ddot{\varphi} + 2\varepsilon_2\dot{\varphi} + \eta_2^2\varphi = \sqrt{\sigma^2 4\varepsilon_1\varepsilon_2\frac{K_1}{K_2}}\,\dot{\theta}$$

qui décrit le comportement d'un ensemble pendul-galvanomètre et son équivalent en „équations-machine" :

$$\begin{aligned} \ddot{\theta} &= -2\varepsilon_1\dot{\theta} - n_1^2\theta - \frac{\ddot{x}}{l_1} + K\dot{\varphi} \\ \ddot{\varphi} &= -2\varepsilon_2\dot{\varphi} - n_2^2\varphi + K'\dot{\theta} \end{aligned} \tag{2'}$$

où on a noté :

$$K = \sqrt{\sigma^2 4\varepsilon_1\varepsilon_2 \frac{K_2}{K_1}} \; ; \; K' = \sqrt{\sigma^2 4\varepsilon_1\varepsilon_2 \frac{k_1}{k_2}}$$

Le schéma de calcul pour les équations (2') est présentée dans la figure 2.

L'étude analogique d'un sismographe muni d'un, ou de plusieurs filtres, peut être abordé en deux manières :

a) en branchant un filtre de résonance (de rejection) sur le circuit pendul-galvanomètre (le point A de la fig. 2).

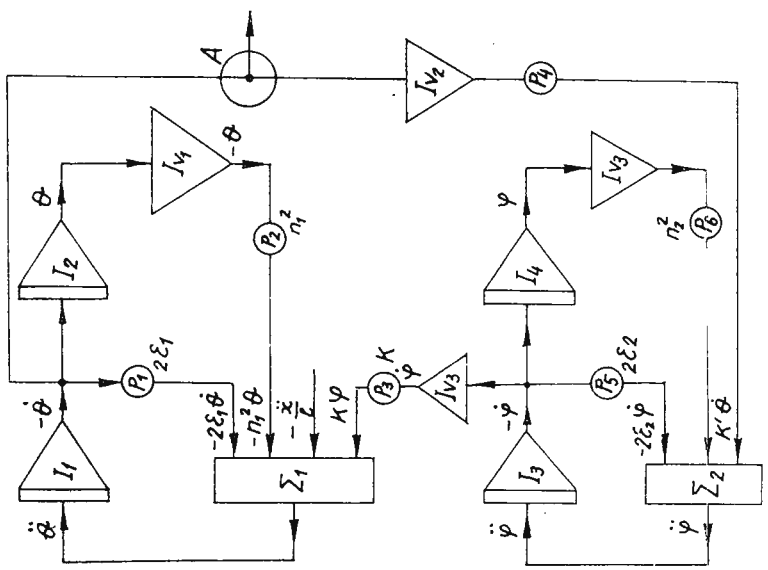

Fig.2. — Le schéma de calcul pour les équations (2').

b) en réalisant les schémas électriques équivalents du pendul et du galvanomètre, y compris le filtre (ou le système de filtres), après quoi on établit le système d'équations intégro-différentielles à base du deuxième théorème de Kirchhoff.

Dans le premier cas, le circuit de rejection, constitué d'un oscillateur résonant sur la fréquance parasite, se modèle simplement d'après un schéma similaire au celui de la figure 1.

Pour le deuxième, le schèma équivalent d'un circuit pendul-galvanomètre, couplés par l'intermède d'un filtre „passe-bas" est présenté dans la figure 3.

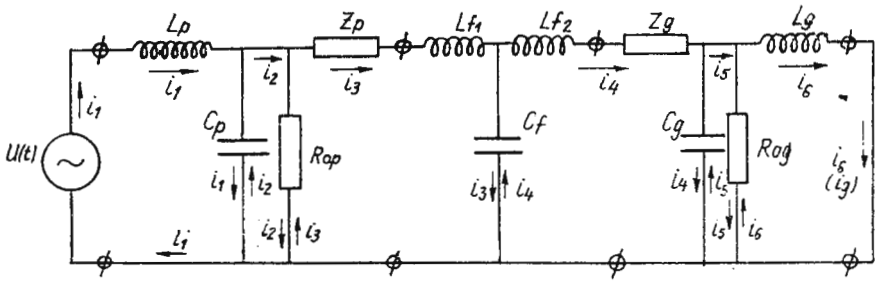

Fig. 3. — Le schéma équivalent d'un circuit pendul-galvanomètre couplés par l'intermède d'un filtre „passe-bas".

Le système d'équations pour ce schéma est :

$$
\begin{aligned}
&L_p \frac{\mathrm{d}i_1(t)}{\mathrm{d}t} + \frac{1}{C_p}\left[\int_0^t i_1(t)\,\mathrm{d}t - \int_0^t i_2(t)\,\mathrm{d}t\right] = u(t)\\
&\frac{1}{C_p}\left[\int_0^t i_2(t)\,\mathrm{d}t - \int_0^t i_1(t)\,\mathrm{d}t\right] + R_{op}\,(i_2(t) - i_3(t)) = 0\\
&R_{op}\,(i_3(t) - i_2(t)) + Z_p\,i_3(t) + Lf_1\frac{\mathrm{d}i_3(t)}{\mathrm{d}t} + \frac{1}{C_f}\left[\int_0^t i_3(t)\,\mathrm{d}t - \int_0^t i_4(t)\,\mathrm{d}t\right] = 0\\
&\frac{1}{C_f}\left[\int_0^t i_4(t)\mathrm{d}t - \int_0^t i_3(t)\,\mathrm{d}t\right] + L_{f2}\frac{di_4(t)}{\mathrm{d}t} + Z_g\,i_4(t) + \frac{1}{C_g}\left[\int_0^t i_4(t)\,\mathrm{d}t - \int_0^t i_5(t)\,\mathrm{d}t\right] = 0\\
&\frac{1}{C_g}\left[\int_0^t i_5(t)\,\mathrm{d}t - \int_0^t i_4(t)\,\mathrm{d}t\right] + R_{og}\,(i_5(t) - i_6(t)) = 0\\
&R_{og}\,(i_6(t) - i_5(t)) + L_g\frac{\mathrm{d}i_6(t)}{\mathrm{d}t} = 0
\end{aligned}
\tag{3}
$$

qui transformé en „équations machine" devient :

$$
L_p\frac{\mathrm{d}i_1(t)}{\mathrm{d}t} = u(t) - \frac{1}{C_p}\int_0^t i_1(t)\,\mathrm{d}t + \frac{1}{C_p}\int_0^t i_2(t)\,\mathrm{d}t
$$

$$R_{op}\, i_2(t) = -\frac{1}{C_p}\int_o^t i_2(t)\ \mathrm{d}t + \frac{1}{C_p}\int_o^t i_1(t)\ \mathrm{d}t + R_{op}\ i_3(t)$$

$$L_{t_1}\frac{\mathrm{d}i_3(t)}{\mathrm{d}t} = -R_{op}i_3(t) + R_{op}\, i_2(t) - Z_p\, i_3(t) - \frac{1}{C_f}\int_o^t i_3(t)\ \mathrm{d}t + \frac{1}{C_f}\int_o^t i_4(t)\ \mathrm{d}t$$

$$L_{t_2}\frac{\mathrm{d}i_4(t)}{\mathrm{d}t} = -\frac{1}{C_f}\int_o^t i_4(t)\ \mathrm{d}t + \frac{1}{C_f}\int_o^t i_3(t)\ \mathrm{d}t - Z_g\, i_4(t) - \frac{1}{C_g}\int_o^t i_4(t)\ \mathrm{d}t + \frac{1}{C_g}\int_o^t i_5(t)\ \mathrm{d}t$$

$$R_{og}i_5(t) = -\frac{1}{C_g}\int_o^t i_5(t)\ \mathrm{d}t + \frac{1}{C_g}\int_o^t i_4(t)\ \mathrm{d}t \qquad (3)$$

$$L_g\frac{\mathrm{d}i_6(t)}{\mathrm{d}t} = -R_{og}\, i_6(t) + R_{og}\, i_5(t)$$

Les notations de la figure 3 représentent :

$$C_p = \frac{K_1}{G_1^2} = \frac{1}{2a_1n_1}\ ;\quad L_p = \frac{G_1^2}{n_1^2} = \frac{2a_1}{n_1}\ ;\quad R_{op} = \frac{G_1^2}{2\varepsilon_1} = \frac{a_1}{D_{10}}$$

où : n_1 = la pulsation des oscillations propres du pendul.

K_1 = le moment d'inertie du pendul.

G_1 = la constante électrodynamique de la bobine du pendul.

a_1 = la constante de l'amortissement électromagnétique du pendul ; $a_1 = \dfrac{G_1^2}{2n_1K_1}\ \Omega$

D_{10} = la constante de l'amortissement libre du pendul.

Pour le galvanomètre les relations sont :

$$C_g = \frac{1}{2a_2n_2}\ ;\quad L_g = \frac{2a_2}{n_2}\ ;\quad R_{og} = \frac{a_2}{D_{20}}$$

n_2, K_2, G_2, a_2, D_{20} ayant les mêmes significations comme ci dessus, en se référant cette fois aux propriétés physiques du galvanomètre.

Le schéma de calcul pour le système (3′) est présentée dans la figure 4.

Dans toutes les deux méthodes l'étude se fait en introduisant en $\sum_1$ une tension $u(t)$, qui contient en outre le signal utile, aussi la tension parasite — $u(t) = u_u(t) + u_p(t)$ — l'action des filtres étant observée dans la

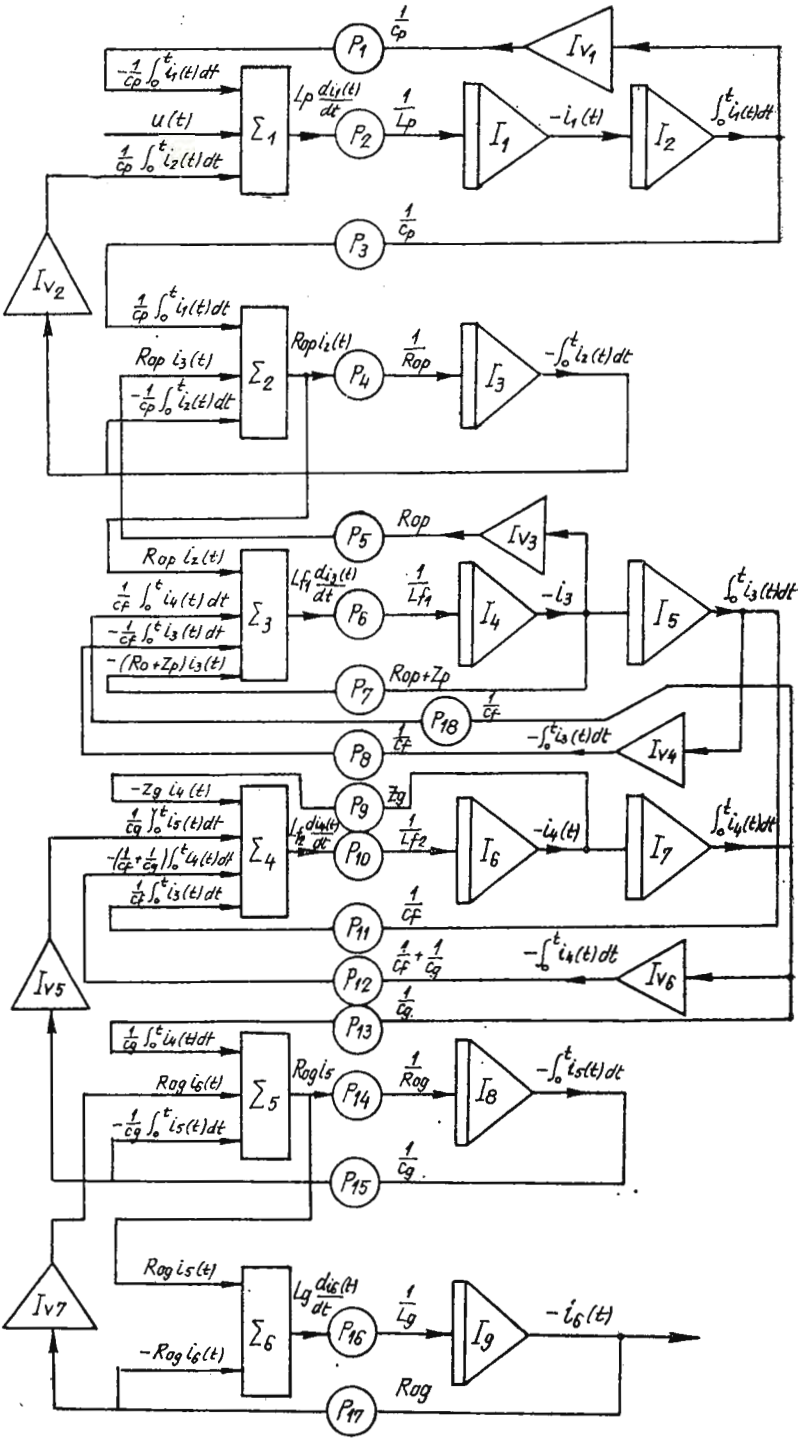

Fig. 4. — Le schéma de calcul pour le système (3′)

première méthode en suivant la grandeur φ (l'angle de déviation du galvanomètre), respectivement le courant i_6 par la bobine du galvanomètre, dans la deuxième méthode.

Malgré la complication apparente du schéma de la figure 4 l'étude du système se fait aisément, l'action des filtres pouvant être suivie rapidement par le manoeuvre des potentiomètres qui déterminent les éléments du filtre.

Les valeurs des coefficients du schèma, calculées préalablement, transformées en unités de machine, s'introduisent à l'aide des potentiomètres, qui se règlent sur les valeurs desirées, en mesurant les tensions à leurs bornes avec un voltmètre électronique ou numérique.

Les schémas de calcul ci-dessus ont été modelés sur un calculateur analogique du Centre de Calcul de l'Université de Iassy.

A COMPARISON OF PERFORMANCE BETWEEN PREDICTION ERROR AND BANDPASS FILTERS

BY

H. GJØYSTDAL, EYSTEIN S. HUSEBYE [1]

INTRODUCTION

The basic difficulty in detecting weak seismic waves from distant sources is to recognize the signals as such in the presence of microseismic noise. Possible solutions to this problem, i. e., to ensure the largest possible gain in the signal-to-noise ratio, would either be to suppress the noise enhance the signal or a combination of these procedures.

The large seismic arrays LASA (Montana) and NORSAR (Norway) are mainly constructed for detecting, locating and eventually classifying small seismic events. In these recording systems, noise suppression is obtained by recursive bandpass filtering and beamforming (delay and sum processing). For more details on the NORSAR array and its operational principles, we refer to papers by B u n g u m et al. (1971) and R i n g d a l et al. (1972). The realtime event detector in the NORSAR software system reports a large number of weak signals, but at the same time many pure noise detections or false alarms. The problem dealt with in this paper is whether more flexible analysis techniques such as prediction error filtering (Wiener filtering), eventually combined with bandpass filters would significantly improve the *SNR* of detected but not verified events, as compared to an ordinary bandpass filter. The performance of the individual filters would be based on criteria like computational efficiency, filter stability and gain in *SNR*.

[1] NTNF/NORSAR, N—2007 Kjeller, Norway.

FILTER THEORY AND METHOD OF ANALYSIS

The filter in use in the event detection processor at NORSAR for additional noise suppression on the array beam level is a digital, recursive 3 rd order Butterworth bandpass filter. Presently, the 3 dB corner frequencies of this filter in the array's on-line system is 1.2 and 3.2 Hz, and in

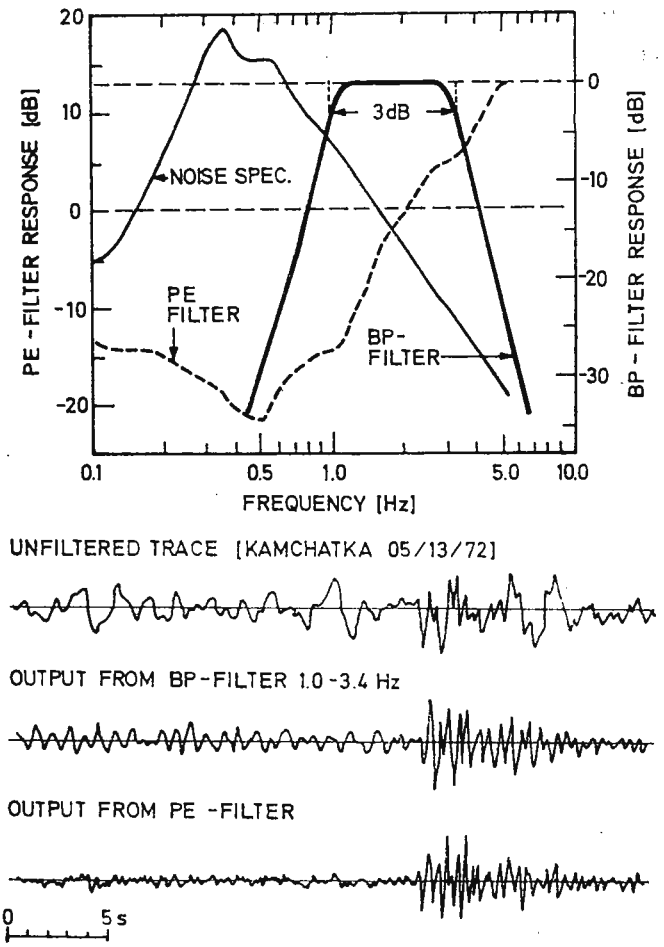

Fig. 1. — Exmaples of filtering a seismic record with *BP* and *PE* filters. The lower part of the figure shows the response of the two filters used, and gives the power gain in dB as a function of frequency. The noise power spectrum shown in the same diagram is given in dB relative to $1nm^2/Hz$ at 1.0 Hz, using the left vertical scale.

average the gain in SNR amounts to around 8—16 dB depending on noise level fluctuations. The response and usefulness of a BP-filter is demonstrated in figure 1.

Another class of filters are the so-called Wiener filters which find wide applications in seismic prospecting. The prediction error filter (PE) is a special type in the group of Wiener filters, all of which are built on the principle of minimizing the energy or power between the actual and desired filter output. This leads to a set of normal equations from which the corresponding set of filter coefficients may be calculated . In case of the PE-filter, it is constructed to predict, with the smallest possible error, a future value of the input trace on the basis of its time history. This error, i. e., the difference between the predicted and the observed value at time t, defines the output time series of the filter. In short, the PE—filter is built upon the statistical properties of the input, the output being expected to be small as far as the assumption of stationarity remains valid. Consequently, the filter tends to suppress inputs possessing the same statistical properties as the time trace from which it is constructed. Time and frequency domain response of a PE-filter is shown in figure 1. For further details on the theory of prediction error filters, we refer to R o b i n s o n , T r e i t e l (1967) and D o u z e (1971).

The aim of this work is as mentioned to investigate whether the PE-filter can be used to further improve the SNR of small teleseismic events. The requirement of computational efficiency at a large array restricts the analysis to a single time series, e.g. the array beam . C l a e r b o u t (1964) has shown that in the n-dimensional case the computer load is proportional to n^2 while the gain in SNR relative to that of a single trace was dubious.

The first step in analysis was to optimize the design of the filter as its performance depends on the prediction distance α, number of filter coefficients and the length of noise interval used for autocorrelation estimation. In order to evaluate the bandpass and prediction error filter performance it was deemed preferable to work in the frequency domain and use synthesized signal and noise models (fig. 2). The shape of the noise spectrum is rather invariant with respect to time while absolute power fluctuations exhibit large seasonal variations. To compensate for this effect the filter gain is measured relative to that of the unfiltered traces. The signal spectrum shape is also assumed to be invariant, while the peak signal frequency is varied from 0.5 to 1.8 Hz in steps of 0.1 Hz.

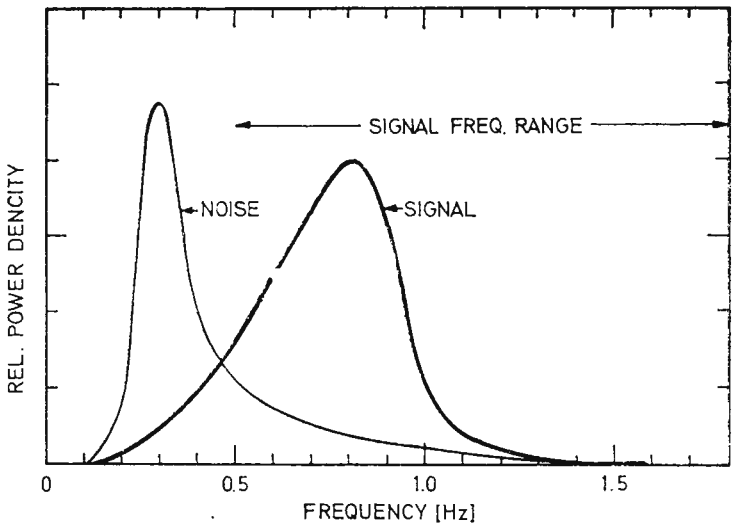

Fig. 2. — Models for signal and noise power spectra. The units for power density are arbitrary.

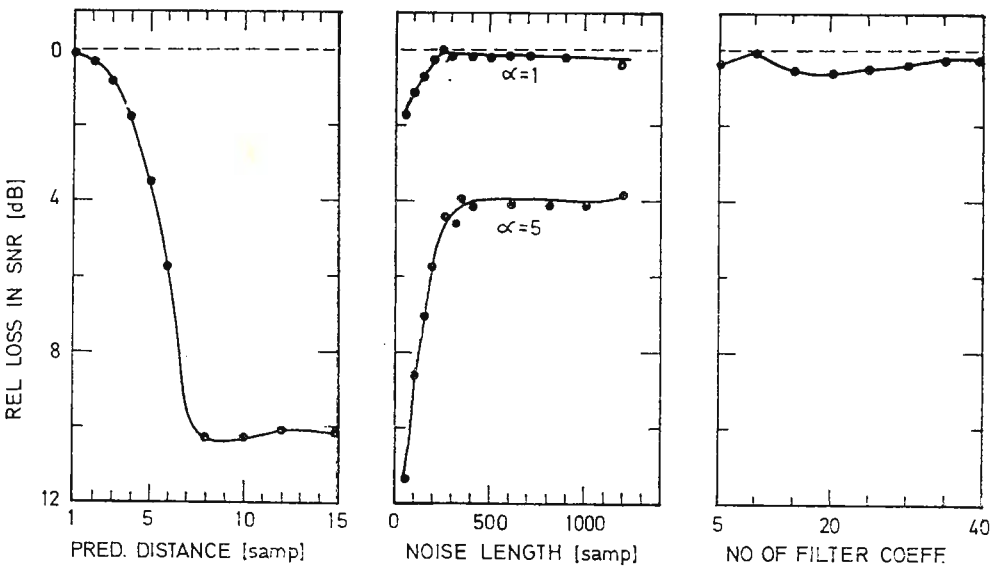

Fig. 3. — Loss in SNR as function of prediction distance (α), noise interval length (m), and number of filter coefficients (n). The values are in dB relative to the maximum value. Two of the parameters above are kept constant in each case ; the values used are $\alpha = 1$ sample, $m = 400$ samples, and $n = 20$. In addition, the second diagram shows the graph for $\alpha = 5$ samples.

RESULTS

The results of the optimum design analysis of the prediction error filter are displayed in figure 3, which shows the variation of SNR with different values of the filter parameters for an earthquake in Kamchatka 05/13/72. It is noticed that a prediction distance of 1 or 2 samples gives the best filter performance. For increasing distances α the filter performance deteriorates rapidly, which means that the PE-filter distortion of the input trace diminishes correspondingly. The length of the noise trace required for autocorrelation calculations stabilizes at 300—400 samples or 30—40 s either a prediction distance of 1 or 5 was used. The number of filter coefficients needed is not critical as long as a minimum number limit of ca. 5 is exceeded. Analysis of other P-signals shows essentially the same picture. The effect of increasing the filter coefficient is to produce ripples on the response curve.

The essential feature of the PE-filter is noise whitening, as easily seen in figure 1. The seismic noise decreases rapidly with increasing frequency, and the filter response increases correspondingly, resulting in an increase in the high frequency noise of the output. Removal of this noise is obtainable by adding constants to the autocorrelation function at zero lag (D o u z e , 1971), or combining the PE-filter with a suitable bandpass or lowpass filter as preferred by the authors.

From the above discussion it is clear that the PE-filter would give a satisfactory gain in SNR only for P-signals which are well separated from the noise in the frequency domain. This has been verified by analysis of the synthesized noise and signal models shown in figure 2. The results are displayed in figure 4 and imply that we always may define a bandpass filter having larger gain in SNR for short period P-waves as compared to the prediction error filter. Time domain analysis of real signals also proved certain BP-filters to have superior performance relative to that of $PE-BP$ filter combinations. However, C l a e r b o u t (1964) in a similar investigation found, contrary to the authors, that the PE-filter gave larger SNR improvements than the BP-filters. The latter results seem to be due to exceptionally large signal and noise sample separation in the frequency domain.

DISCUSSION

In the previous section we dealt with filter performance in terms of SNR enhancement. For routine analysis of seismic signals the computational efficiency of the filtering process is important. It should be mentio-

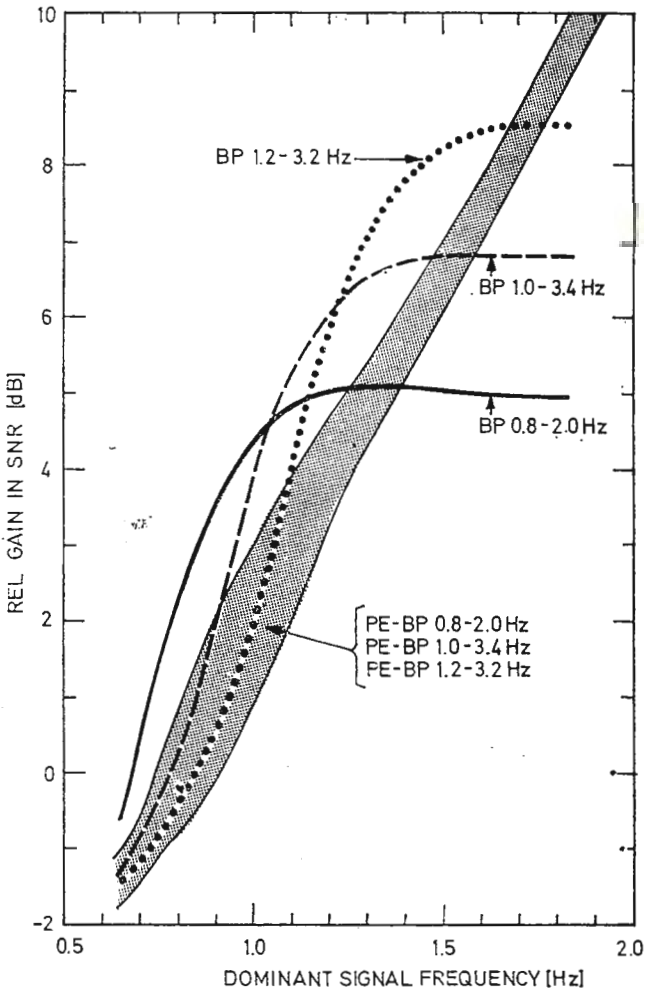

Fig. 4. — Gain in SNR as function of dominant signal frequency for different filters which are indicated for each graph. For simplicity the graphs for the three combination filters are shown as a shaded area, the left boundary corresponding to $PE-BP$ 0.8—2.0 Hz.

ned here that constructing and actually applying a PE-filter of 20 coefficients to a recorded P-signal required approx. 30 s of computer time on an IBM 360/40. Without discussing in detail different types of digital seismic processing systems, we would remark that in the case of the NORSAR array, the performance of bandpass filters is superior to that of the predic-

tion error filter for reasons of flexibility, computer efficiency and SNR enhancement.

Finally, we would like to forward a few comments on the implications of gain in SNR and thus improved seismic event detectability. This is most easily seen through the earthquake occurrence relation (R i c h t e r, 1958) :

$$\log_{10} N = a - b \cdot m_b$$

where N = annual number of earthquakes in a given area, a and b are constants ($b \sim 1.0$), and m_b = P-wave magnitude.

A certain gain in SNR (in dB) is easily converted to magnitude units (2 dB = 0.1 m_b unit), and a possible extension of the above equation is :

$$\log (N + dN) = a - b (m_b - dm_b)$$

Solving the above equations with respect to increments in N in per cent gives

$$\frac{dN}{N} = (10^{dm_b} - 1) \qquad \text{for } b = 1$$

Let us assume that the distribution of dominant P-signal period (say T in the magnitude formula) is known for earthquakes recorded at an arbitrary station. Combining this information with potential gain in SNR relative to that of routine seismometer or array operation, it would be possible to figure out the corresponding improvements in the station's event detectability. Such studies may also be regionalized if deemed necessary for specialpurpose seismic surveillance.

Acknowledgement

The NORSAR research project has been sponsored by the United States of America under the overall direction of the Advanced Research Projects Agency and the technical management of Electronic Systems Division, Air Force Systems Command.

REFERENCES

Bungum H., Husebye E. S., Ringdal F. (1971) The NORSAR Array and preliminary results of data analysis. *Geophys. J. R. Astr. Soc.*, 25, London.

Claerbout J. F. (1964) Detection of P--waves from weak sources at great distances. *Geophysics*, 29, Tulsa, Oklahoma.

Douze E. J. (1971) Prediction error filters, white noise and orthogonal coordinates. *Geophys. Prospect.*, 19, Haga.

Richter C. F. (1958) Elementary Seismology. Freeman & Co., San Francisco.

Robinson E. A., Treitel S. (1967) Principles of digital Wiener filtering. *Geophys. Prospect.*, 15, Haga.

CORRELATION OF THE MAGNITUDES m_{pv} BY INSTRUMENTS WITH DIFFERENT FREQUENCY RESPONSES

BY
I. V. GORBUNOVA[1]

Abstract

Results of analysis of magnitudes m_{pv} by instruments with different frequency responses are presented. It is shown that values of particle velocity A/T depend on a wave period. Maximal values of particle velocity A/T in P wave correspond to periods of 2 to 8 s. Corrections to earthquake magnitudes determined by short-period instruments of SKM-3 type and long-period ones of SKD and P—E types in relation to magnitudes determined by standard medium-period instruments of SK types are received in dependence on earthquake intension and P wave period.

Results of comparison of magnitudes m_{pv} determined in CSO „Obninsk" by short-period instruments of SKM—3 and Benioff types, medium-period ones of SK type and long-period ones of SKD and P—E types are presented here. Frequency responses of these instruments are shown in figure 1.

Analysis of P waves. In connection with determination of magnitudes m_{pv}, analysis of maximal values of A/T in P waves has been conducted. By each type of the instruments, independent measurements of maximal amplitudes and appropriate periods have been done in different parts of P wave spectrum and values of τ, arrival times of maximal phases A/T, have been marked.

$$\tau = t(A/T)_{max} - t_p,$$

[1] Central Seismological Observatory „Obninsk", Institute of Physics of the Earth, AN USSR.

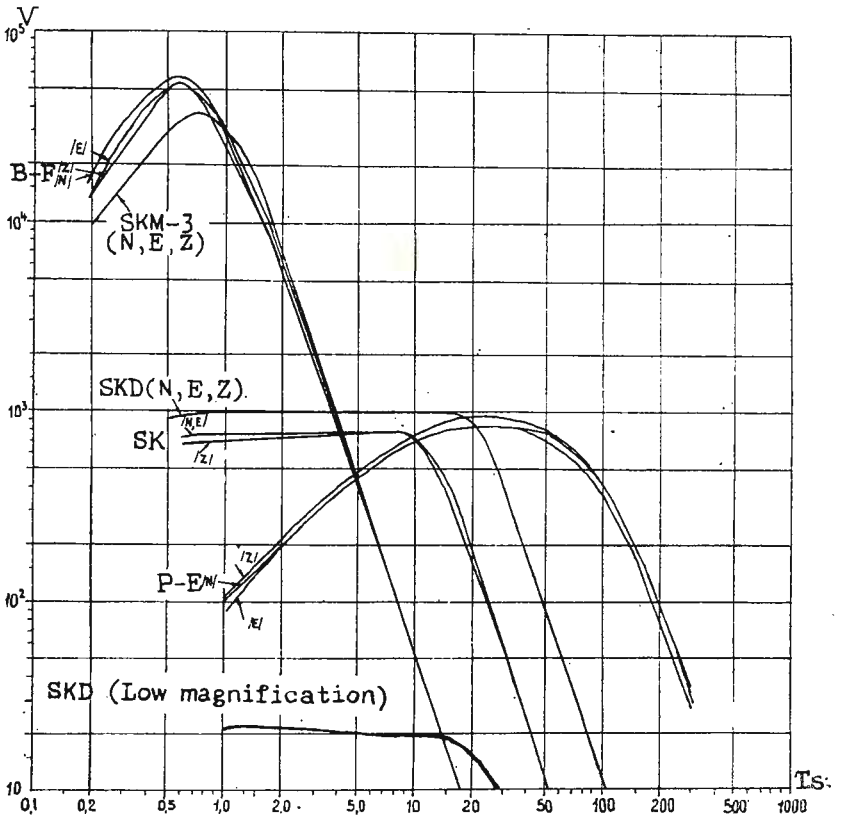

Fig. 1. — Frequency responses of registering instruments:
1, SKM-3 (by D. P. Kirnos); 2, SK (by D.P.Kirnos); 3, SKD (by D.P.Kirnos); 4, B-f (by N. Benioff); 5, P-E (by Press-Ewing).

$t(A/T)_{max}$ being arrival time of maximal phase of (A/T) in P wave, t_p = arrival time of P wave, A = amplitude, T = period.

Examples of P wave records and measurements of A, T and τ are shown in figure 2.

Values of τ for different instruments are shown in figure 3 in conventional symbols. As one can see, τ changes in dependence on earthquake magnitude and a type of registering instrument. It changes from 2 s, when $M = 4.5$ to 5, to 25 s, when $M \sim 7$. By SKD and Press-Ewing insetruments the value τ for some strong earthquakes reaches 30—35 s. In figure 3a one can see that for 75 per cent of P wave records by instruments of SKM—3 type maximal values of A/T dispose in the range of 5 s from P

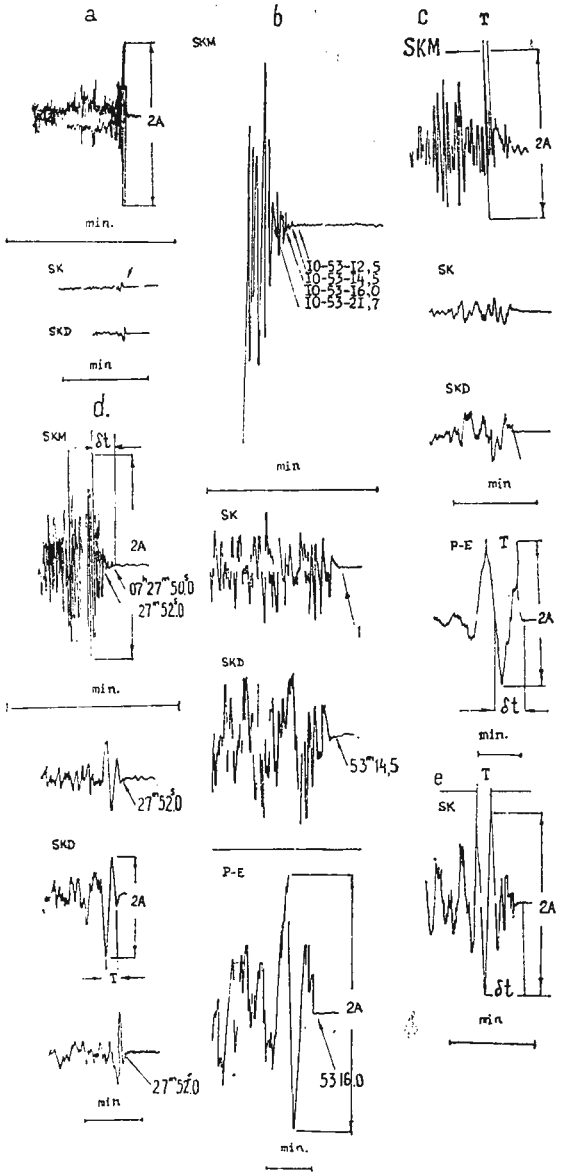

Fig. 2. — Parameters of P wave records by istruments with different frequency responses, for the following earthquakes:

a, 16 August 1969, 15h, $M = 6$ Japan;

b, 30 august 1968 10h, $M = 7.4$ Iran;

c, 28 May 1968, 13h, $M = 7$ New Guinea;

d, 30 November 1967, 7h, $M = 7$ Yugoslavia;

e, 21 November 1969, 02h, $M = 7.7$ Indonezia.

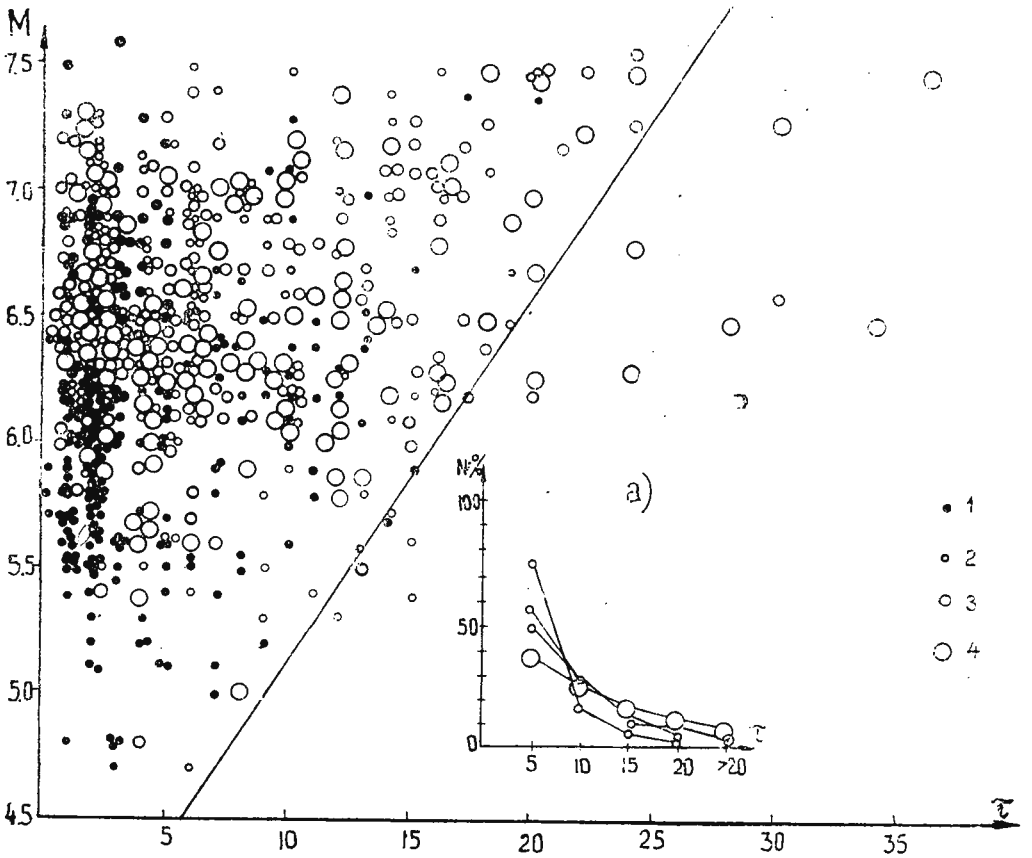

Fig. 3. — Distribution of quantity τ in dependence on earthquake magnitude and registering instrument;
1, SKM-3, 2, SK; 3, SKD; 4, P-E.

wave onset. Values of τ increase when turning to P wave records by more ong-period instruments.

As a result of analysis of values of τ a conclusion has been made that in great majority of cases maximal values of A/T are observed in the range of 2 to 20 s from the beginning of a wave arrival. Therefore, when determining the magnitude, the choice of P wave section with $(A/T)_{max}$ has been done in the limits of 2 to 20 s independently of a quantity of extrema from the beginning of the record. In each individual case, possible arrivals of PcP, pP and sP waves have been allowed for at certain distances.

Calibrating functions. Magnitude determinations have been carried out by all the types of instruments with the use of a standard calibrating curve.

The magnitude has been determined by the formula :

$$m_{pv} = (A/T)_{max} + \sigma$$

being an unified calibrating curve corresponding to instruments of SK type (V a n e k et al., 1962). Proceeding from the assumption that earthquake magnitude should be the same independently of an instrument used, that is

$$m^i_{pv} = m^{sk}_{pv}$$

(i being SKM, SKD or P—E), differents in values of m_{pv} are explained by calibrating functions for different types of instruments.

A calibrating function value is

$$\sigma^i = \sigma + \alpha$$

where

$$\alpha = m^{sk}_{pv} - m^i_{pv} = \log\ (A/T)^{SK}_{max} - \log(A/T)^i_{max}$$

For construction of the calibrating curves, records of earthquakes from different parts of the globe (with foci in the crust) in the range of epicentral distances 20° to 90° and that of magnitudes 4.2 to 7.5 have been used.

Averaged calibrating curves are shown in figure 4, where a calibrating curve σ for medium-period instruments (SK) is given for comparison. When comparing the calibrating curves, we see differents in values of A/T in records by short-period, medium-period, and long-period instruments.

For SKM we see that the difference is less for weak earthquakes at small distances. With increasing earthquake magnitude this difference increases. A mean value of the quantity α for earthquakes with magnitudes in the range 5.5 to 6.5 has been found to be equal to 0.14 ± 0.03 and for earthquakes with $M \geqslant 6.5$ it has been 0.28 ± 0.09.

For SKD instruments with the same frequency response, which SK instruments have in the period range of 0.2 to 10 s, and further the table-shaped one prolonged to 20 s, differents in values of A/T do not exceed determination errors of these quantities. For the range of magnitudes 5.5

$< M \leqslant 6.5$ the quantity α equal to 0.04 ± 0.04 and for earthquakes with $M > 6.5$, $\alpha = +0.03 \pm 0.03$.

In the obtained results, our attention is attracted by the fact that inspite of large possibilities of SKD instrument in comparison with those

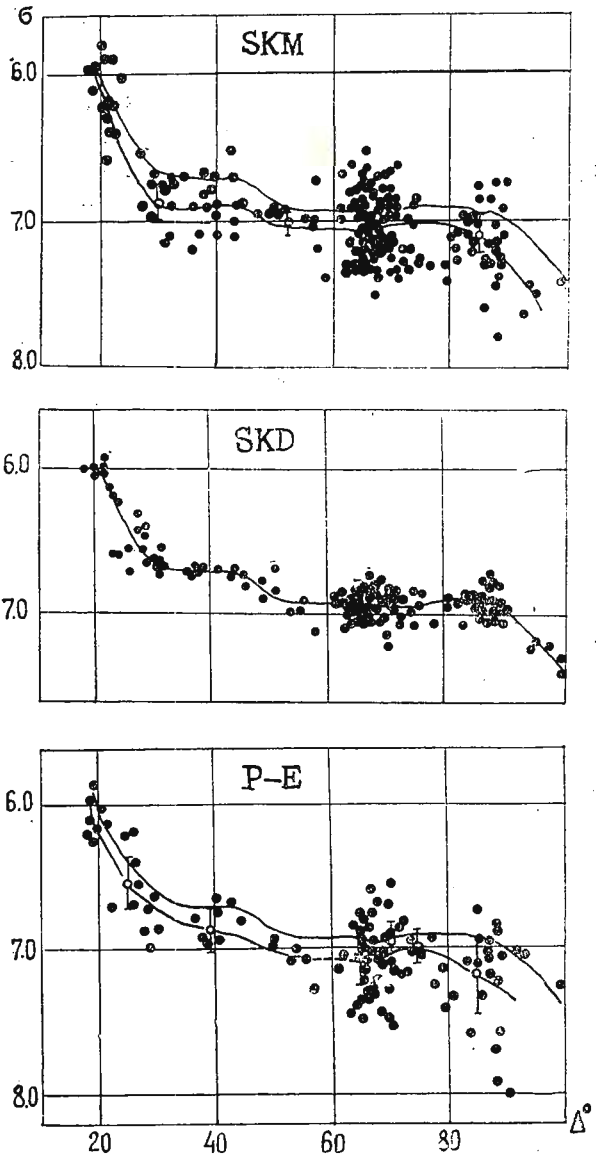

Fig. 4. — Calibrating functions.

of SK in regard to registration of long-period P waves from strong earthquakes (with $M > 6.5$) we have the same magnitude by the both instruments. For periods $T < 10$ s (frequency response of SK)

$$\alpha = 0.01 \pm 0.02,$$

for periods $T > 10$ s

$$\alpha = -0.03 \pm 0.027.$$

Difference in magnitudes by these instruments is within the limits of determination errors of these quantities. However, a negative value itself of α for $T_p > 10$ s, that is for strong earthquakes, indicates some (insignificant in the specified case) but systematic lessening of magnitudes by SKD instruments at long periods.

When comparing calibrating curves for SK instruments and long-period P—E ones, we again see similar picture as when comparing calibrating curves by short-period and medium-period instruments. The quantity for earthquakes registered by P—E instruments with magnitudes $5.5 \leqslant M \leqslant 6.5$ is equal to 0.08 ± 0.03 and for earthquakes with $M > 6.5$ it is 0.25 ± 0.05.

The conducted analysis of α dependence on a registered wave period for different magnitude ranges has revealed significant variations of the quantity.

TABLE 1

$5.5 < M \leqslant 6.5$			$M > 6.5$	
$T_p \leqslant 10$ s	$10 < T_p \leqslant 20$	$T_p > 20$ s	$T \leqslant 20$s	$T_p > 20$ s
α			α	
0.05 ± 0.048	0.13 ± 0.056	0.17 ± 0.020	0.23 ± 0.083	0.33 ± 0.05

The range of P wave periods, for which the quantities were determined, has been chosen to match frequency responses of the instruments. All the earthquakes, for which P wave periods were 10 s both by SK and Press-Ewing instruments, have been selected into first group. Earthquakes with $T_p > 10$ s by SK and P—E have been included into the second group, and into the 3d one those with periods by SK over 10 s and by P—E over 20 s. For earthquakes with $M > 6.5$, the ranges of periods T_p have

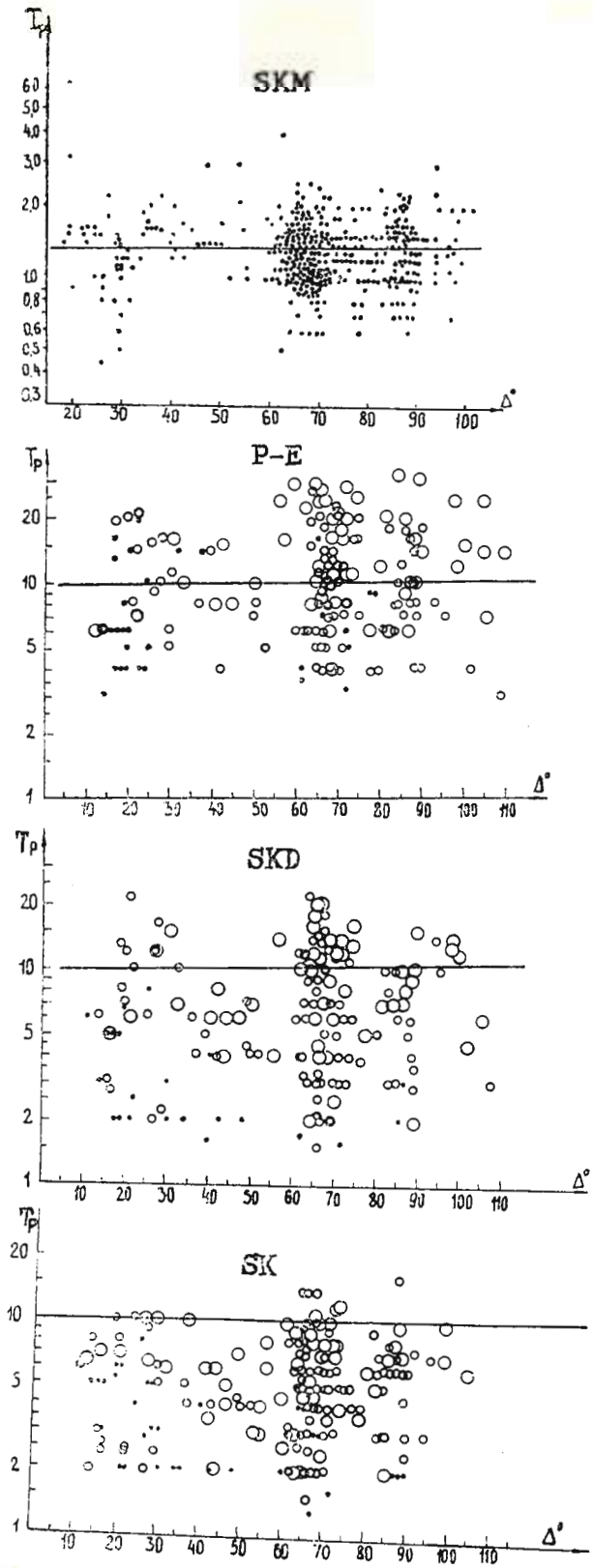

Fig. 5. — Relationship $T = f(\Delta^0)$.

been determined by P—E, though by SK the periods had significantly less values.

The analysis of α values has revealed that within the same interval of magnitudes, difference in the magnitudes by the two instruments is determined by P wave period. In connection with the obtained results of such a nature, P wave periods have been analysed in regard to their change with epicentral distance and in dependence on magnitude: spectral distribution of particle velocity (A/T) of P waves have been drawn.

Change of P wave periods with distance. Periods associated with maximal values of A/T in P wave have been considered (fig. 5). Dependence of period change on distance is poorly manifested and can be written by the next equation (level of confidence 95 %)

$$(\text{SKM})\,T = 0.0006(0.0002 \div 0.0014)^{\circ} + 1.36(1.31 \div 1.41)$$

$$(\text{SK})\,T = 0.016(0.00093 \div 0.034)^{\circ} + 4.5(4.1 \div 4.9)$$

$$(\text{SKD})\,T = 0.024(0.0043 \div 0.053)^{\circ} + 5.6\,(5.0 \div 6.2)$$

$$(\text{P}-\text{E})\,T = 0.024\,(0.019 \div 0.056)^{\circ} + 10.6(9.7 \div 11.6)$$

Dependence of P wave periods on a registering instruments type is seen very clearly.

Dependence of the period T_p on earthquake intensity. $T_p = f(M)$ for the three types of instruments is shown in figure 6, where again the level of disposition of curves of the dependence determined by frequency responses of registering instruments is first of all striking. One can see a tendency of a faint increase of T_p with earthquake intensity, the tendency being more distinct for earthquakes with magnitude over 7.

Distribution of $A/T = f(T)$. Dependences $A/T = f(T)$ by data of SKM, SK, SKD and P—E instruments have been plotted on a graph in a double logaritmic scale for the following magnitude levels:

$$M \leqslant 5.5;\ 5^{3}/_{4} \leqslant M \leqslant 6^{1}/_{4};\ 6^{1}/_{2} < M \leqslant 6^{3}/_{4};\ 6^{3}/_{4} < M \leqslant 7^{1}/_{4},\ \text{then}$$

values of A/T have been averaged for particular periods. The graph constructed in such a way (fig. 7) characterizes spectral distribution of the particle velocity A/T in the period range of 0.5 to 30 s.

Analysis of $A/T = f(T)$ distribution helps to explain the difference in α values in dependence on earthquake magnitude, registering instrument and P wave period.

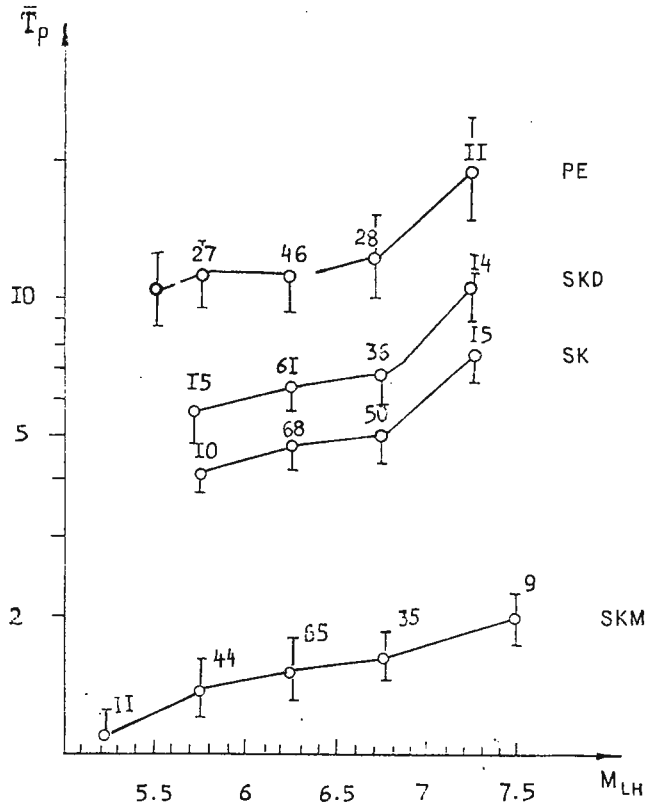

Fig. 6. — Relationship $T = f(M)$.

First of all it should be noted that maximal values of the particle velocity A/T correspond to periods from 2 to 8 s. This period range corresponds to the frequency response of instruments of SK type.

P waves with periods of another frequency range do not give maximal values of the magnitude m_{pv}. For short-period instruments, the magnitudes would be close to maximal ones at periods corresponding to the right slope of their characteristics, while for long-period ones, on the contrary, to the left slope. Magnitude values determined by P waves at periods of 0.8 to about 2 s by SKM and P waves at period of 10 to 30 s by SKD and P—E should be corrected for.

By this means corrections introduced into a magnitude value depend on spectral composition of a wave and an instrument characteristic. A calibrating curve should correspond to P waves of a certain period.

Correlation of m_{pv} by the short period SKM and Benioff instruments. Comparison analysis of m_{pv} values determined by SKM—3 and Benioff

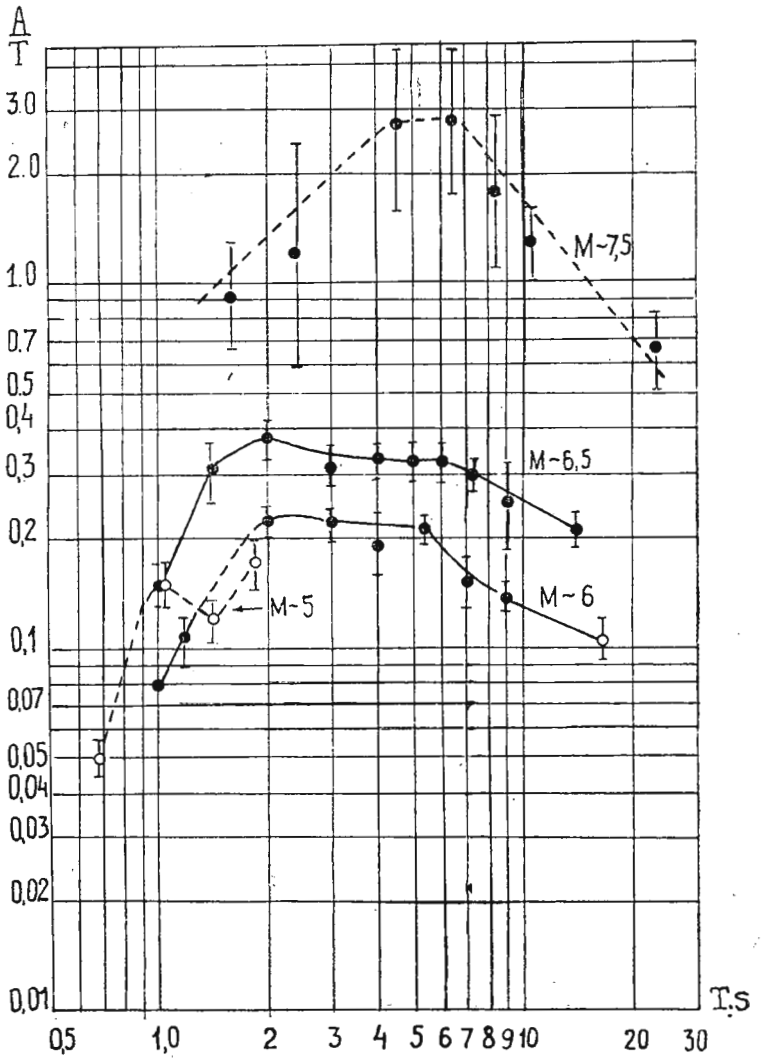

Fig. 7. — Distribution of $A/T = f(T)$ for the following magnitude levels: 1, $M \leqslant 5\ 1/2$; 2, $5\ 3/4 < M \leqslant 6\ 1/4$; 3, $6\ 1/4 < M \leqslant 6\ 3/4$; 4, $6\ 3/4 < M \leqslant 7\ 1/4$.

instruments has been carried out on the basis of experimental data. Results of the comparison for 120 earthquakes are given in figure 8.

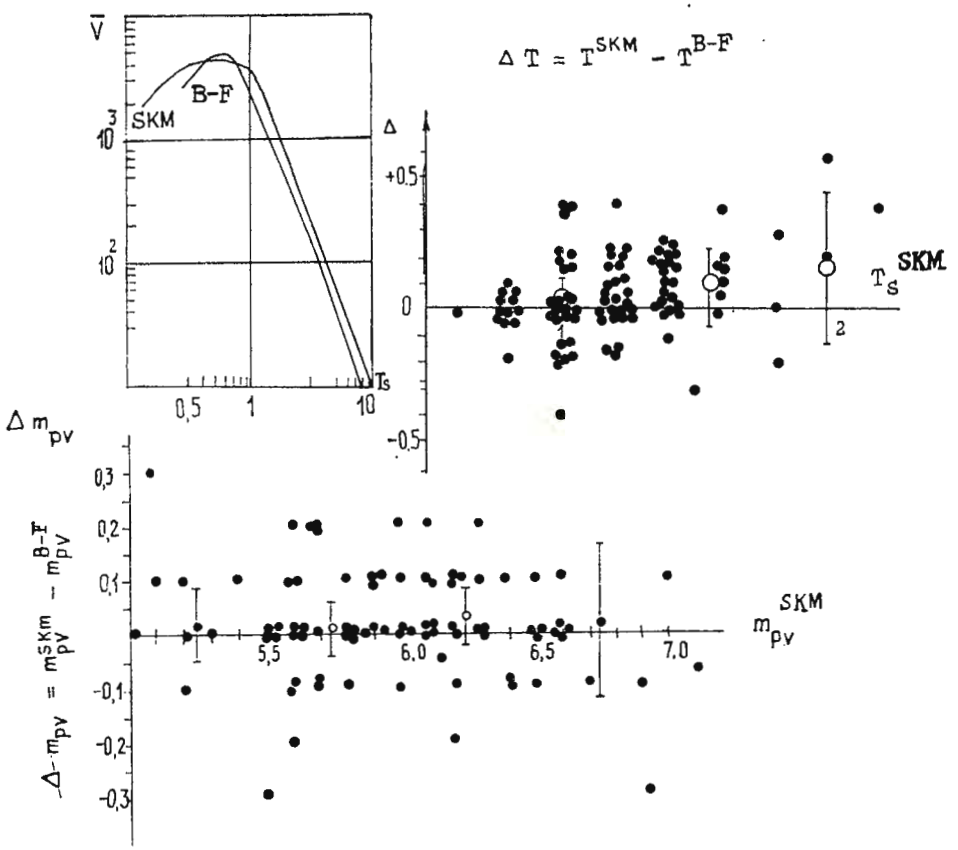

Fig. 8. — Comparison of m_{pv} values by SKM and Benioff instruments.

A systematic difference corresponds to heightening of m_{pv} values by SKM—3 instruments as compared to those by Benioff ones by hundredths of magnitude unit. In some cases the deviations can reach 0.3 of magnitude unit for earthquakes with $M > 6.5$. Insignificant heightening of the values by SKM can be explained by the fact that frequency response of these instruments has a table-shaped part at periods of 0.7 to 1 s. As may be seen from figure 8a, P wave periods increase with earthquake magnitude, this increase being realized by SKM instruments to a greater extent. With the wave period increase, $(A/T)_{max}$, in its turn, also increases nearing to A/T distribution maximum.

REFERENCES

Vanek J., Zatopek A., Karnik V., Riznichenko Y. V., Savarensky E.F., Soloviev S. L., Sheba lin N.V. (1962) Standardization of magnitude scale . *Izv. AN SSSR, Ser. Geophys.*, 2, Moskva.

INTERPRETATION OF SEISMOLOGICAL RESULTS

THEORY

THEORETICAL MODEL FOR THE PROCESS OF UNDERGROUND EXPLOSIONS. CONTRIBUTIONS TO THE PROBLEM OF THE SEPARATION OF LARGE EXPLOSIONS FROM EARTHQUAKES

BY

DUMITRU ENESCU, ANCA GEORGESCU, DUMITRU JIANU, IOANA ZĂMÂRCĂ [1]

Abstract

The theoretical model of source described in this paper is resulted by combining three unequal couples without moment; farther each couple is combined with a simple force, whose intensity is also dependent on the direction in which this force is acting.

This model tries to explain not only the process of explosion radiation of both *P* and *S* wave types, but also the co-occurence of the two anaseismic (compressions) and kataseismic (dilatations) motions in the P-wave.

In the last part of this paper a few examples of large underground explosions are given, whose mechanism may be satisfactorily explained by means of the theoretical model presented in this paper.

INTRODUCTION

In order to study the mechanism of underground explosions, several theoretical models of point or volume sources have been imagined, models by which one has tried to solve the different problems of the explosion process in rocks.

[1] Institute for Applied Geophysics, Departament of Seismology and Seismometry, 5, Cuţitul de Argint st. Bucharest 28, Romania.

In this way, the explosion generating only longitudinal waves has been modeled either by combining three equal couples without moment and mutualy perpendicular (L o v e , 1952; K e y l i s - B o r o k et al., 1957) or with the help of spherical source, on whose internal surface acts a uniformly distributed pressure (S h a r p e , 1942; E n e s c u , C î n d e a, 1971).

The radiation, by explosions, of both longitudinal and transverse waves, has been modeled either by combining three unequal couples without moment and mutually perpendicular (I n g r a m, 1960; E n e s c u, 1963, 1964) or by means of finite length cylindrical (H e e l a n , 1953; W h i t e , S e n g b u s h , 1963) and rectangular (G u p t a , K i s s l i n g e r , 1964) sources. Recently, other authors like A l t e r m a n , A b r a m o v i c i (1967); H u d s o n (1969 a, 1969b); D o u g l a s et al. (1971) have brought important contributions to model explosions and earthquakes by means of point sources radiating both P and S waves.

The theory of seismic sources, by means of which underground explosions have been modeled, shows that the first motion in the P-wave should be anaseismic („from the source") in all the propagating directions of this wave. As it is known, in the case of earthquakes, the first motion in the P-wave is anaseismic in some directions and kataseismic („towards the source") in other directions. Hence has resulted one of the main criteria in the separation of underground explosions from earthquakes.

But seismic records of some underground explosions have proved that the first motion in the P-wave may be, as in the case of earthquakes an anaseismic motion at some stations and a kataseismic motion at other stations.

Consequently, the first motion criterion — one of the earliest criteria proposed for seismic indentification of explosions and earthquakes — has proved to be insufficiently conclusive.

This criterion has been found to have a lesser degree of certainty as it has been observed that for some earthquakes the first motions in the P-wave are anaseismic at all stations (S t a u d e r , 1960). But it has been shown (K e y l i s - B o r o k, M a l i n o v s k a y a , 1962) that these cases seldom occur and they are possible when the forces acting in the focus have such directions that all the stations find themselves in one of the quadrants characterized by anaseismic motions.

In this paper we present a theoretical model of source by means of which we try to provide a more complete solution for the mechanism of underground explosions. This model tries to explain not only the process

of explosion radiation of both P and S wave types, but also the co-occurence of the two anaseismic and kataseismic motions in the P-wave.

FORCES PATTERN ACTING IN SOURCE

As it is known, the source consisting of three equal couples without moment and mutually perpendicular (centre of dilatation) has a perfect spherical symmetry, due to the fact that the intensity of forces acting in it is the same in all directions.

The source analysed by Ingram (1960, 1963) and Enescu[2] has in fact no spherical symmetry, but it represents a particular case since the asymmetry of forces refers only to the direction and not to the sense of forces. That is, the intensity of the force acting in the θ direction is equal with that acting in the $\theta + \pi$ direction.

In fact, due to the shape of explosive charges and especially due to the physico-geological conditions in which the explosions take place, the pattern of forces generating seismic waves is much more complicated. A good discussion of some of the phenomena related to explosive sources is given by Wright, Carpenter (1962). They consider that the explosions may generate S waves too, due to the strong asymmetries of the forces acting in source, the cause of these asymmetries being the Taylor's instability mechanism.

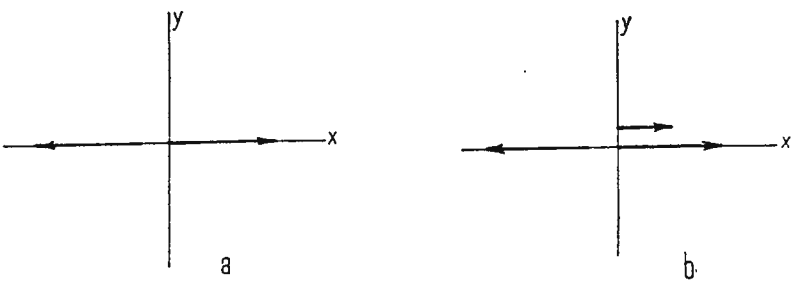

Fig. 1. — Couple without moment (a) and couple without moment combined with simple force (b).

It is known that a couple without moment (fig. 1a) is associated with a symmetrical breaking and a couple without moment combined with a simple force (fig. 1b) produces an asymmetrical breaking (Keylis-Borok et al., 1957).

[2] Enescu D. Curs de seismometrie şi prospecţiuni seismice. 1963. Inst. Petrol, Gaze, Geologie. Bucureşti.

According to the facts mentioned above, we consider that the theoretical model which better corresponds to the process of seismic waves generation by explosion is the source resulted by combining three sources of different intensities, like that source type represented in figure 1b. That

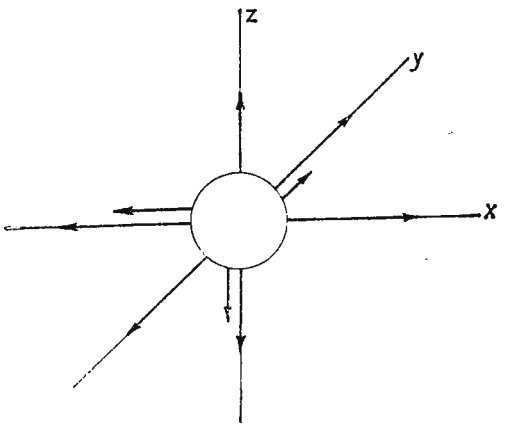

Fig. 2. — Source resulted by combining three unequal couples without moment; farther each couple is combined with a simple force.

is three unequal couples without moment are combined; farther each couple is combined with a simple force, whose intensity is also dependent on the direction in which this force is acting (fig. 2).

EQUATIONS OF THE DISPLACEMENTS FIELD

The solution of the wave equation, given by L o v e (1914) and transformed by K e y l i s - B o r o k (1950), for waves generated by a simple force $\chi(t)$ which is applied at the origin of the coordinate axes, according to a certain direction q, has the form:

$$U^{(1)}_{m,P} = \frac{1}{4\pi\rho}\left\{\frac{\partial^2 r^{-1}}{\partial q\,\partial m}\left[Q\left(t-\frac{r}{V_P}\right)+\frac{r}{V_P}\dot{Q}\left(t-\frac{r}{V_P}\right)\right]+\right.$$

$$\left.+\frac{1}{r\,V_P^2}\frac{\partial r}{\partial m}\frac{\partial r}{\partial q}\chi\left(t-\frac{r}{V_P}\right)\right\}; \qquad (1)$$

$$U^{(1)}_{m,S} = \frac{1}{4\pi\rho}\left\{\frac{\partial^2 r^{-1}}{\partial q\,\partial m}\left[-Q\left(t-\frac{r}{V_S}\right)-\frac{r}{V_S}\dot{Q}\left(t-\frac{r}{V_S}\right)\right]+\right.$$

$$\left.+\frac{1}{r\,V_S^2}\left[\cos(mq)-\frac{\partial r}{\partial m}\frac{\partial r}{\partial q}\right]\chi\left(t-\frac{r}{V_S}\right)\right\}, \qquad (2)$$

where :

$U^{(1)}_{m,P}$ and $U^{(2)}_{m,S}$ are displacement components in the $m = x, y, z$ direction in P and respectively S waves, generated by a first order source (simple force),

ρ is the density,

$r = \sqrt{x^2+y^2+z^2}$ is the distance from the source to a certain point in the medium, the characteristics of this point being the $U^{(1)}_{m,P}$ and $U^{(1)}_{m,S}$ quantities, V_P and V_S are the propagation velocities for longitudinal and transverse waves generated by source.

In the relations (1) and (2) it was considered :

$$Q(t) = \int_0^t \int_0^{t_1} \chi(t_1)\ dt_1\, dt;\ \dot{Q}(t) = \frac{\partial Q}{\partial t}$$

Love's multipole theory and the superposition principle have allowed us to derive by means of the relations (1) and (2), the following equations of the displacements field in P and S waves generated by the source shown in figure 2 :

$$U_{x,P},\ U_{y,P},\ U_{z,P} = \frac{1}{4\pi\rho V_P^3 r^4}\ (x, y, z)\ [b_x x(x \pm rQ_{x,P}) + b_y y(y + r\ Q_{P,y}) + \\ + b_z z\ (z \pm rQ_{z,P})]\ \dot{\chi}\left(t - \frac{r}{V_P}\right) \tag{3}$$

$$U_{x,S},\ U_{y,S},\ U_{z,S} = \frac{1}{4\pi\rho V_S^3 r^4}\ [(b_x x,\ b_y y,\ b_z z)\ r^2 - (x, y, z)\ (b_x x^2 + b_y y^2 + b_z z^2) \pm \tag{4}$$

$$\pm (b_x r Q_{S,x}\ b_y r Q_{y,S},\ b_z r Q_{z,S}) r^2 \pm (x, y, z)\ (b_x x r Q_{x,S} + b_y y r Q_{y,S} + b_z z r Q_{z,S})]\ \dot{\chi}\left(t - \frac{r}{V_S}\right),$$

where :

a_q represents the amplitude of the simple force $\chi(t)$ acting along the $q = x, y, z$ axis, and

b_q characterizes the intensity of the couple without moment acting along the $q = x, y, z$ axis.

With $Q_{q,S}$ and $Q_{q,P}$ we have noted the expressions :

$$Q_{q,P} = V_P \frac{aq}{b_q} \frac{\chi\left(t - \frac{r}{V_P}\right)}{\frac{\partial}{\partial t}\chi\left(t - \frac{r}{V_P}\right)}; \quad Q_{q,S} = V_S \frac{a_q}{b_q} \frac{\chi\left(t - \frac{r}{V_S}\right)}{\frac{\partial}{\partial t}\chi\left(t - \frac{r}{V_S}\right)} \tag{5}$$

In the calculations made in order to obtain the relations (3) and (4), we have neglected the terms decreasing with $\frac{1}{r^n}$; $n > 1$.

Let $\bar{x}$, $\bar{y}$, $\bar{z}$ be the directions East, North and Zenith for the second coordinate system of axes which is considered. As it is known, the relations between the first system of axes ($Oxyz$) and the new one ($O\bar{x}\bar{y}\bar{z}$), may be expressed, by means of direction cosines, as follows :

$$\begin{pmatrix} x \\ \bar{y} \\ \bar{z} \end{pmatrix} = \begin{pmatrix} \alpha_x, & \alpha_y, & \alpha_z \\ \beta_x, & \beta_y, & \beta_z \\ \gamma_x, & \gamma_y, & \gamma_z \end{pmatrix} \begin{pmatrix} x \\ y \\ z \end{pmatrix} \tag{6}$$

or

$$\begin{pmatrix} x \\ y \\ z \end{pmatrix} = \begin{pmatrix} \alpha_x, & \beta_x, & \gamma_x \\ \alpha_y, & \beta_y, & \gamma_y \\ \alpha_z, & \beta_z, & \gamma_z \end{pmatrix} \begin{pmatrix} \bar{x} \\ \bar{y} \\ \bar{z} \end{pmatrix} \tag{7}$$

The displacements corresponding to the SH and SV components of the transverse wave, may be found using the following relations :

$$U_{SH} = \frac{\vec{r} \times \vec{z}_0}{|\vec{r} \times \vec{z}_0|} \cdot \vec{U}_S; \quad U_{SV} = \frac{\vec{r} \times (\vec{r} \times \vec{z}_0)}{|\vec{r} \times (\vec{r} \times \vec{z}_0)|} \cdot \vec{U}_S \tag{8}$$

where :

$\vec{z}_0$ is the unit vector to Zenith ;

$\vec{r} \times \vec{z}_0$ is a vector perpendicular to U_P and $\bar{Z}$;

$\vec{r} \times (\vec{r} \times \vec{z}_0)$ is a vector perpendicular to U_P and U_{SH}.

From the above relations, it results :

$$U_{SH} = \frac{1}{4\pi\rho V_S^3 r^2 \sqrt{r^2 - \bar{z}^2}} [b_x(x \pm rQ_{x,S})(y\gamma_z - z\gamma_y) + b_y(y \pm rQ_{y,S})(z\gamma_x - x\gamma_z) +$$

$$+ b_z(z \pm rQ_{z,S})(x\gamma_y - y\gamma_x)] \dot{\chi}\left(t - \frac{r}{V_S}\right), \tag{9}$$

$$U_{SV} = \frac{1}{4\pi\rho V_S^3 r^3 \sqrt{r^2 - \bar{z}^2}} \left\{ \bar{z} \left[x b_x (x \pm r Q_{x,S}) + y b_y (y \pm r Q_{y,S}, S) + z b_z (z \pm r Q_{z,S}) \right] - \right.$$

$$\left. - r^2 \left[\gamma_x b_x (x \pm r Q_{x,S}) + \gamma_y b_y \ (y \pm r Q_{y,S}) + \gamma_z b_z \ (z \pm r Q_{z,S}) \right] \right\} \cdot \dot{\chi} \left(t - \frac{r}{V_P} \right). \tag{10}$$

$$U_{SP} = \frac{b_x x [x \pm r Q_{x,P}] + b_y y \ [y \pm r Q_{y,P} \ ] + b_z z \ [z \pm r Q_{z,P}]}{4\pi \ V_P^3 r^3} \cdot \dot{\chi} \left(t - \frac{r}{V_P} \right) \tag{11}$$

If

$$Q_{q\,S} = Q_{q,P} = 0$$

and

$$b_x = b_y = b_z = b,$$

the equations (9) — (11) become :

$$U_{SH} = U_{SV} = 0 ; \quad U_P = \frac{b}{4\pi\rho V_P^3 r} \cdot \dot{\chi} \left(t - \frac{r}{V_P} \right) \tag{12}$$

The relations (12) express the displacements field produced by the well known source — the centre of dilatation.
If

$$Q_{q,S} = Q_{q,P} = 0$$

and

$$b_x \neq b_y \neq b_z,$$

the equations (9)—(11) are the same as those obtained by I n g r a m (1960) for the source formed by three unequal couples without moment and mutually perpendicular.

NODAL SURFACES IN THE *S*-WAVE

As it can be noticed from the relations (9) and (10) the displacements U_{SH} and U_{SV} cancel if the following conditions are fulfilled :
for the SH wave

$$b_x (x \pm r Q_{x,S}) \ (y\gamma_z - z\gamma_y) + b_y (y \pm r Q_{y,S}) \ (z\gamma_x - x\gamma_z) + b_z \ (z \pm r Q_{z,S}) (x\gamma_y - y\gamma_x) = 0 \tag{13}$$

for the SV wave

$$\bar{z} \left[x b_x (x \pm r Q_{x,S}) + y b_y \ (y \pm r Q_{y,S}) \ + z b_z \ (z + r Q_{z,S}) \right] - r^2 \left[\gamma_x b_x \ (x \pm r Q_{xS},) + \right.$$
$$\left. + \gamma_y b_y \ (y \pm r Q_{y,S}) + \gamma_z b_z \ (z \pm r Q_{z,S}) \right] = 0 \tag{14}$$

It is known that :

$$\bar{x} = r \sin i_h \sin \alpha ; \qquad \bar{y} = r \sin i_h \cos\alpha ; \quad \bar{z} = r \cos i_h \tag{15}$$

where :

α is the azimuth

i_h is the incidence angle at the source.

With the relations (13) — (15) we performed the nodal lines $U_{SH} = 0$ and $U_{SV} = 0$ for four series of values of the parameters b_q and $Q_{q,S}$. These nodal lines are represented in a Wulf projection in figures 3—6. As it can be seen from these figures, the shape of the nodal lines $U_{SH} = 0$ varies little relative to the change of the parameters b_q and $Q_{q,S}$. But, the shape of the nodal lines $U_{SV} = 0$ is interesting and depends more on the source asymmetry defined by parameters b_q and $Q_{q,S}$.

NODAL SURFACES IN THE *P*-WAVE

The displacement U_P cancels if the following condition is fulfilled [3].

$$b_x x[x \pm rQ_{x,R}] + b_y y\ [y \pm rQ_{y,T}] + b_z z\ [z \pm rQ_{z,P}] = 0 \tag{16}$$

If

$$Q_{x,P} = Q_{Py,} = Q_{z,P} = 0$$

it results

$$b_y x^2 + b_y y^2 + b_z z^2 = 0 \tag{17}$$

The particular case represented by the equation (17) is nothing else but the nodal surface of the *P*-wave for the source analyzed by I n g r a m (1960). Concerning the earthquakes, I n g r a m (1960) considers that the parameters b_x, b_y, b_z may have different signs. For instance, the most simple case $b_z = 0$, $b_x = -b_y$ represents one of the theoretical sources (H o n d a , 1957) equivalent to the earthquakes foci.

In the case of underground explosions, the quantities b_x, b_y, b_z must have the same sign, more exactly all these quantities must be positive. If $b_x > 0$, $b_y > 0$, $b_z > 0$ the equation (17) represents an imaginary cone.

[3] The cancellation of the displacements U_P, U_{SH} and U_{SV} for $r = \infty$, has no importance for the problems dealt with in this work.

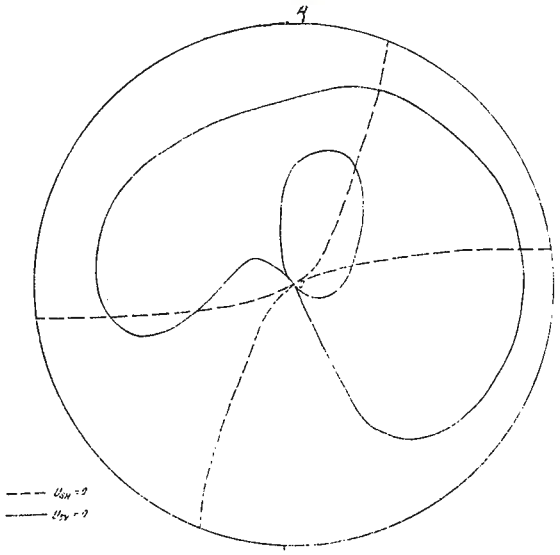

Fig. 3. — Nodal lines $U_{SH} = 0$ and $U_{SV} = 0$ computed for $b_x = 9$, $b_y = 3$, $b_z = 2$, $Q_{x,S} = 1/3$, $Q_{y,S} = 2/3$, $Q_{z,S} = 1/2$.

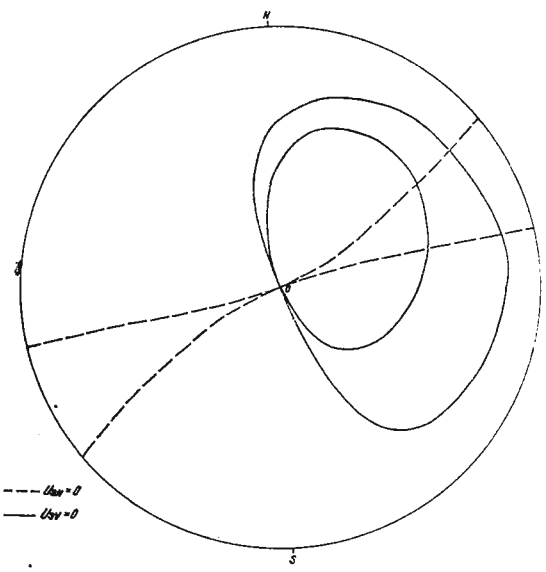

Fig. 4. — Nodal lines $U_{SH} = 0$ and $U_{SV} = 0$ computed for $b_x = 9$, $b_y = 3$, $b_z = 2$ $Q_{x,S} = 1$, $Q_{y,S} = 1$, $Q_{z,S} = 1$.

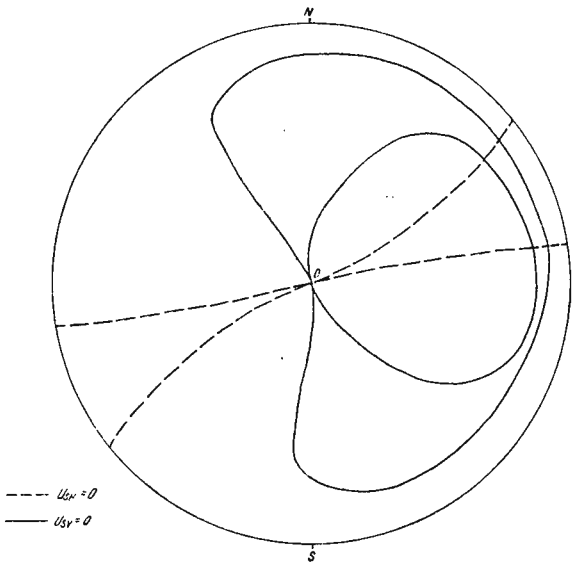

Fig. 5. — Nodal lines $U_{SH} = 0$ and $U_{SV} = 0$ computed for $b_x = 3$, $b_y = 9$, $b_z = 2$, $Q_{x,S} = 3$, $Q_{y,S} = 1/3$, $Q_{z,S} = 1/2$.

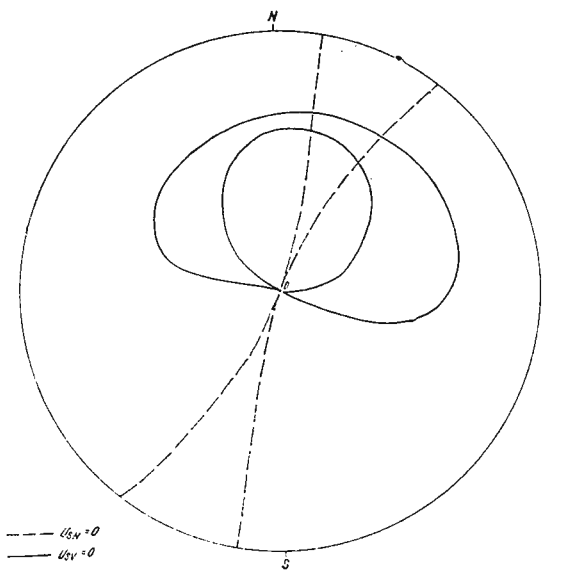

Fig. 6. — Nodal lines $U_{SH} = 0$ and $U_{SV} = 0$ computed for $b_x = 9$, $b_y = 3$, $b_z = 2$, $Q_{x,S} = 1/3$, $Q_{y,S} = 3$, $Q_{z,S} = 2$.

Therefore, in this case, the displacement U_P cancels only at the origin. Hence, it results that the source analyzed by I n g r a m (1960, 1963) and by E n e s c u [4] cannot be considered a theoretical model of underground explosions, for which the first motion in the P-wave is anaseismic at some stations and kataseismic at other stations.

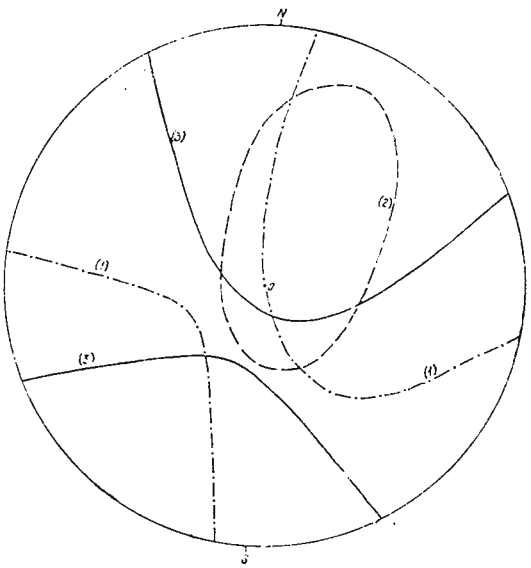

Fig. 7. — Nodal lines $U_P=0$ computed for $b_x = 9$, $b_y = 3$, $b_z = 2$; the lines (1) are computed for $Q_{x,P}=1$, $Q_{y,P}=1$, $Q_{z,P} = 1$; the lines (2) are computed for $Q_{x,P} = 1/3$, $Q_{y,P} = 2/3$, $Q_{z,P} = 2$; the lines (3) are computed for $Q_{x,P} = 1/3$, $Q_{y,P} = 3$, $Q_{z,P} = 2$.

Maintaining the condition regarding the positive sign of the parameters b_x, b_y, b_z, we have tried to compute the nodal lines by means of the equation (16) for values of the parameters $Q_{q,P}$ different from zero. We have noticed that for small values (more precisely for values smaller than the unit) of the parameters $Q_{q,P}$, the nodal lines are in fact imaginary too. The computations show that if one or two of quantities $Q_{q,P}$ are equal or greater than unity the equation (16) represents a real surface. In order to exemplify this, we have computed the nodal lines $U_P = 0$ for three series of values of the parameters $Q_{q,P}$ and we have represented them in a Wulf projection (fig. 7).

The values of the quantities b_q and $Q_{q,P}$, for which the nodal lines were computed, characterize source with strongly asymmetrical distributions of forces. Couples with moment, of the type of those acting in the foci of the tectonic earthquakes, shall appear if only one of the quantities

[4] *Op. cit.*, p. 2.

$Q_{q,P}$ (and $Q_{q,S}$) is equal of higher than unity. These asymmetries and, implicitly the presence of certain couples with moment, are practically possible, if we admit that the forces responsible for the generation of seismic waves, in the case of strong underground explosions, are on the one hand explosive forces and on the other hand tectonic forces (reactivated by the explosive forces). We refer to those reactivated tectonic forces in the explosion cavity zone which are superposed on the explosive forces. Therefore, the forces distribution shown in figure 2 must be, the result of the superposition of those two kinds of forces. We do not make a mistake if we consider that things happen as if these two kinds of forces are summing up. The explosive forces are known to generate seismic waves. It is known that by making more active the tectonic forces these produce seismic waves too. At the seismological observatories, waves resulted from superposition of the waves produced by explosive forces with those generated by reactivated tectonic forces will be recorded. Therefore, according to the superposition principle, the distribution of forces acting in the source may be considered as resulting from summing up the two kinds of forces.

From the point of view of the relative weight of these forces, we can distinguish the following three more important categories :

1) The explosive forces do not reactivate tectonic forces, or, if they do, the latter ones are so weak that they might be neglected. Because, in this case, the seismic wave generation is due to explosive forces only, the theoretical model of the real source is that shown in figure 2, if we consider that $Q_{q,P}$ (and $Q_{q,S}$) quantities are very small or even null. In this case the equation (16) does not represent a real surface.

The cases in which the explosive forces reactivate tectonic forces may be included in this category too, but the tectonic forces act only after explosion and produce aftershocks, whose mechanism is similar to that of the tectonic earthquakes. In these cases too, the mechanism of generating the main shock is determined only by the explosive forces.

2) Another category is that in which the explosive forces and the reactivated tectonic forces are superposed and they have comparable weights. In such cases we can neglect no one these two kinds of forces. As it has been shown above, this summing up may lead to a strongly asymmetrical distribution of forces. The quantities $Q_{q,P}$ (and $Q_{q,S}$) may become great enough, so that the equation (16) should represent a real surface (fig. 7).

3) The reactivated tectonic forces can have a weight much greater than the explosive forces. From the viewpoint of the generating mechanism,

the explosion may be easily taken for a tectonic earthquake. If there are cases in which the weight of the explosive forces may actually be considered negligible as against the weight of the reactivated tectonic forces, then the theoretical model equivalent to the real source can be obtained from the model shown in figure 2 too, for which $b_z = 0$, $b_x = -b_y$ and $Q_{q,S} = Q_{q,P} = 0$. In such particular cases, the nodal surface expressed by the equation (16) degenerates into two real mutually perpendicular planes. This is in fact, the theoretical source equivalent to the tectonic earthquake foci (H o n d a , 1957).

Like the explosions of the first category, the explosions of the second and the third categories, may reactivate tectonic forces responsible for generating aftershocks, whose mechanism is similar to that of the tectonic earthquakes. Aftershocks are frequent only if the larger explosions are considered. In this paper, we are dealing especially with those tectonic forces which, due to their superposition with the explosive forces, take part in the mechanism of generating the main shock (the underground explosion).

The assumption, that the underground explosions may reactivate tectonic forces is not recent ; it is at least as old as the first underground explosion (M c K e o w n , D i c k e y , 1969). In seismological literature many examples of underground explosions are given which have reactivated tectonic forces in the epicentral zone, in its neighbourhood or even in remote areas from it, too (B r u n e , P o m e r o y , 1963 ; M c K e o w n , D i c k e y , 1969 ; H a m i l t o n , H e a l y , 1969 ; B u c k n a m , 1969). The accumulated nuclear explosion experience indicates that the most explosions fit into category 1, a few fit category 2, and there are no known explosions of category 3. We have included the third category, because we have considered it theoretically possible.

There are no known instances in which the total seismic wave energy (the sum of P, S, Rayleigh and Love wave energies) from tectonic energy release exceeded the total seismic energy produced by the explosions alone.

APPLICATIONS. EXAMPLES

In order to show to what extent the theoretical model described in this paper is able to solve the problem of the mechanism of seismic wave generation by means of underground explosion, we have analyzed the data of the first motions in the P-wave for 28 explosions ; 14 explosions detonated in Nevada, 11 explosions detonated in Kazakhstan and 3 explosions

detonated in Sahara. Only 10 of these explosions have provided sufficient data allowing to conclude about the sign distribution of the first motions in the *P*-wave.

Most of the studied explosions belong to the first of the three categories mentioned above. Further on, we present some examples of underground explosions which try to illustrate the validity of the classification made in the previous chapter.

The „Bilby" explosion was detonated on September 13, 1963 at $17^h00^m00^s$, 13 GMT, in Nevada. As one can see in figure 8, this underground explosion belongs to the category in which the generation of seismic waves is due to explosive forces only. The possible tectonic movements which are produced by explosive forces were either negligible or produced at shorter or longer time intervals after the explosion process. McKeown and Dickey (1969) show that the „Bilby" explosion was followed by several seismic events, among which 8 were produced near the Yucca fault.

The „Benham" explosion was detonated on December 19, 1968 at 16^h30^m GMT, in Nevada. The observational data regarding the first motions in the *P*-wave certify that this explosion belongs also to the category in which the explosive forces alone are responsible for the generation of seismic waves. However, the explosive forces reactivated tectonic forces, which produced a great number of aftershocks, whose mechanism is similar to that of the tectonic earthquakes (Hamilton, Healy, 1969).

The explosion which was detonated on February 26, 1967 at $03^h57^m58^s$ GMT in Kazakhstan, in the Semipalatinsk Region, belongs also to the first category (fig. 9), together with the two explosions mentioned above. We have no data showing whether the explosion was followed by seismic events due to the tectonic movements activated by explosive forces.

A few „dilatations" were observed in the case of these explosions (fig. 8, 9). They were caused either by errors due to the lack of recording the first motions in the *P*-wave at the respective stations, or by changes in the process of wave propagation. Whatever the cause of these few anomalies might be, all of the three explosions mentioned above might belong to that category of explosions, in which the distribution of the signs in the first motions of the *P*-wave is the classical one : the first motions are anaseismic at all the stations.

Among the studied cases, we found certain explosions whose relatively great number of first kataseismic motions cannot be assigned only to the misinterpretations of the seismogram or to certain factors belonging to the propagation process, but also to the mechanism of the wave generation in source .

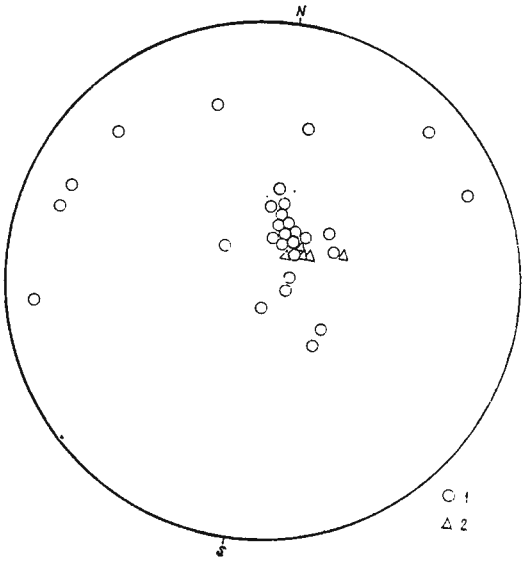

Fig. 8. — The explosion „Bilby" detonated on September 13, 1963 at $17^h\ 00^m\ 00^s$, 13 GMT in Nevada; $M = 5-5{,}25$:
1, Compression; 2, Dilatation.

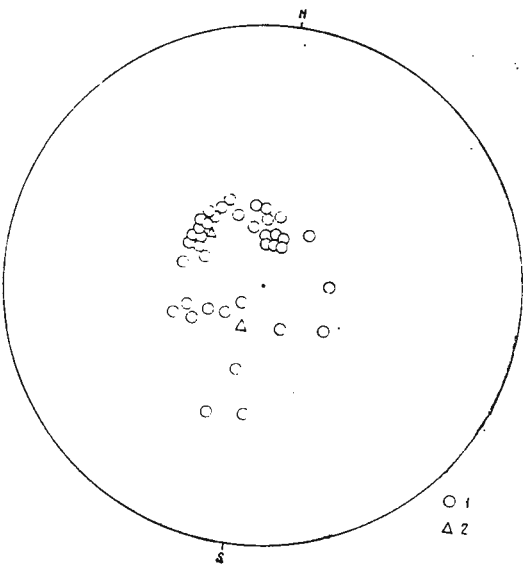

Fig. 9. — The explosion detonated on February 26, 1967 at $03^h\ 57^m\ 58$ GMT in Kazakhstan; $M = 6.6$

The explosion on April 20, 1967 was detonated at $04^h07^m58^s$ GMT in Kazakhstan, in the Semipalatinsk Region. The mechanism solution of this underground explosion is presented in figure 10.

The explosion on October 20, 1963 was detonated ar $12^h\ 59^m\ 59^s$ GMT in Sahara. For this explosion we have presented two possible mechanism solutions (figs. 11, 12).

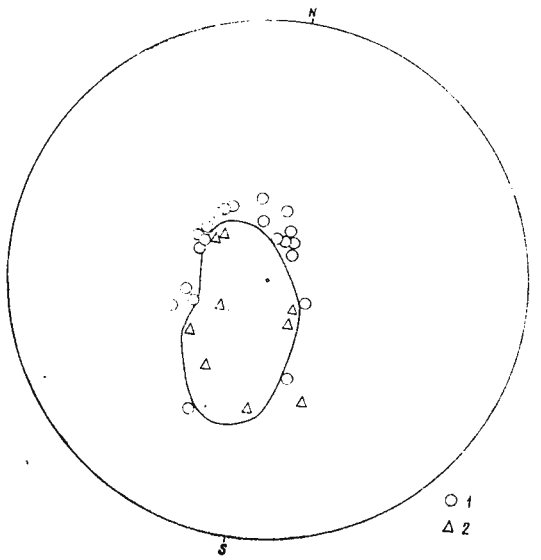

Fig. 10. — The explosion detonated on April 20, 1967 at $04^h\ 07^m\ 59^s$ GMT in Kazakhstan; $M = 6,3$.

The observational data concerning the four explosions for which we have presented the mechanism solutions have been taken from seismic bulletins prepared by well known international centres ISC [5] and BCIS [6].

Comparing the shape of the nodal lines from figures 10 and 11 with that of the nodal lines from figure 7, one can see that these two underground explosions may be included in the category in which the responsible forces for generating seismic waves are the result of the superposition of the explosive forces with tectonic forces (the second category — see previous chapter).

It is very likely that the Sahara explosion released considerable tectonic energy, as it was detonated (like Hardhat) in a granitic massif.

[5] International Seismological Summary for 1963.

[2] Bulletin mensuel : mois de September et October, 1963 ; mois de Février et Avril, 1967.

It is not impossible that the underground explosion detonated in Sahara on October 20, 1963 could belong to the category of explosions in which the reactivated tectonic forces had a greater weight than the explosive forces (the third category), since the „compressions" and „dilatations" observed, may be separated as well as by means of two planes mutually perpendicular (fig. 12). The lack of a larger number of observational data prevents us from deciding where this underground explosion should be included, in the second or in the third category.

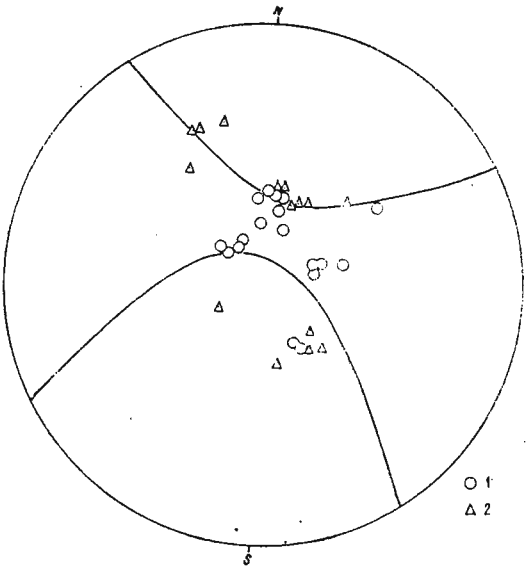

Fig. 11. — The first solution given for the explosion detonated on October 20, 1963 at $12^h\ 59^m\ 59^s$ in Sahara; $M=5.8$.

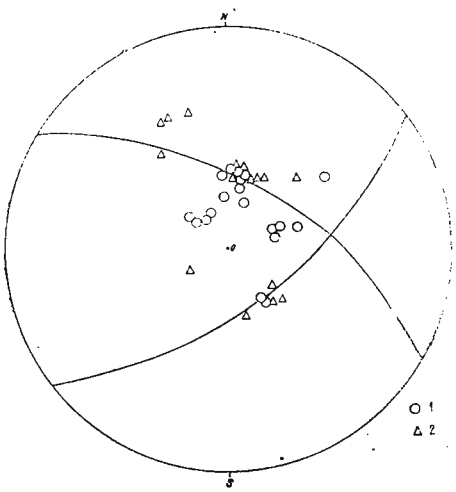

Fig. 12. — The second solution given for the explosion detonated on October 20, 1963 in Sahara.

The „Hardhat" explosion was detonated on February 15, 1962 at $18^h00^m00^s$, 1 GMT in the granite intrusion at the North end of Yucca flat (Nevada). The mechanism of this explosion, studied by means of the surface waves (B r u n e , P o m e r o y , 1963) is a very eloquent proof of superposition of the tectonic forces with the explosive ones. The mechanism of the Hardhat underground explosion was even supposed to be similar to that of a tectonic earthquake (B r u n e , P o m e r o y , 1963).

The granite intrusion in which this explosion was detonated is bordered by two major faults, one of them bein an egxtension of the Yucca fault. There are many minor faults in the vicinity of the explosion. In this case it is better to consider that a superposition occurred of the explosive forces with the tectonic forces. The „Hardhat" explosion was followed by a sequence of aftershocks, which proves that the reactivated tectonic forces acted after the explosion too.

The results obtained by B r u n e and P o m e r o y (1963) concerning the mechanism of the „Hardhat" explosion include this seismic event into the third category (according to the classification made in the previous chapter).

Our opinion is that the „Hardhat" explosion as well as the Sahara explosion, for which due to the insufficient observational data two solutions are possible, may be included into the second category rather than into the third one.

We make the above statement, taking also into consideration the fact that nevertheless the explosive forces cannot be negligible. The proof is given by the „Hardhat" explosion for which, according to B r u n e et al. (1963), the surface waves generated by this explosion were smaller in comparison with those expected for an earthquake of the same magnitude. Therefore, the explosive forces were not negligible in comparison with the tectonic forces because they influenced even the characteristics of the surface waves, by means of which B r u n e and P o m e r o y (1963) have issued the hypothesis that the radiation pattern of „Hardhat" explosion is similar to that expected for a tectonic earthquake.

In this case the third category of underground explosions may be doubtful. The theoretical and observational data establish the existence of at least two categories of underground explosions, the first and the second categories, according to the classification made in the previous chapter.

The data provided by the seismic bulletins as well as those which were observed directly on certain seismograms, demonstrate that the underground explosions generate not only longitudinal waves but transverse wa-

ves as well. The presence of the transverse waves is another reliable proof of the asymmetrical distribution of forces acting in the explosive sources. This asymmetry is present in figure 2, in the most general possible way for a concentrated source.

REFERENCES

Alterman Z., Abramovici F. (1967) The Motion of a Sphere Caused by an Impulsive Force and by an Explosive Point-Source. *Geophys. J.R. Astr. Soc.*, 13, London.

Brune J. N., Espinosa A. F., Oliver J. (1963) Relative excitation of surface waves by earthquakes and underground explosions in the California-Nevada region. *J. Geophys. Res.*, 68, 11, Richmond.

— Pomeroy P. W. (1963) Surface Wave Radiation Patterns for Underground Nuclear Explosions and Small-Magnitude Earthquakes. *J. Geophys. Res.*, 68, 17, Richmond.

Bucknam R. C. (1969) Geologic Effects of the BENHAM Underground Nuclear Explosion. *Bull. Seism. Soc. Am.*, 59, 6, Berkeley.

Douglas A., Hudson J. A., Kembhavi V. K. (1971) The Relative Excitation of Seismic Surface and Body Waves by Point Sources. *Geophys J.R. Astr. Soc.*, 23, London.

Enescu D. (1964) O soluție a problemei generării undelor longitudinale și transversale cu ajutorul exploziilor. *Stud. Cerc. Geol., Geofiz., Geogr., ser. Geofiz.*, 2, 1, București.

—, Cîndea I. (1971) Modèles analogiques électroniques du processus d'explosion dans les roches. *Geophys. Prosp.*, XIX, 3, Haga.

Gupta N. I., Kisslinger (1964) Model Study of Seismic Waves from Explosions in Rectangular Cavities. *Bull. Seism. Soc. Am.*, 54, 4, Berkeley.

Hamilton R. M., Healy J. H. (1969) Afterschocks of the BENHAM Nuclear Explosion. *Bull. Seism. Soc. Am.*, 59, 6, Berkeley.

Heelan P. A. (1953) Radiation from a cylindrical source of finite length. *Geophysics*, XVIII, Tulsa.

Honda H. (1957) The mechanism of the earthquakes. *Sci. Repts.* Tôhoku Univ, 5, 9, supplement 1.

Hudson J. A. (1969 a) A Quantitative Evaluation of Signals at Teleseismic Distances — — I. Radiation from Point Sources. *Geophys. J. R. Astr. Soc.*, 18, London.

— (1969 b) A Quantitative Evaluation of Seismic Signals at Teleseismic Distances.II. Body Waves and Surface Waves from an Extended Source. *Geophys. J.R. Astr. Soc.*, 18, London.

Ingram R. E. (1960) Generalized Focal Mechanism. A Sym posium on Earthquake Mechanism. Hodgson J. H. Ed., *Pub. Dom. Obs.*, XXIV, 10, Otawa.

— (1963) Focal Mechanism of couples without moment. *Bull. Seism. Soc. Am.*, 53, 4, Berkeley.

Keylis-Borok V. I. (1950) K voprosu ob opredelenii dinamiceskih parametrov ociaga. *Tr. Gheofiz. Inst. AN SSSR*, 9, Moscow.

— (1957) Issledovanie mehanizma zemletriasenii. *Izdat. Akad. Nauk SSSR*, Moscow.

—, Malinovskaia L. N. (1962) K voprosu o raspoznavanii zvrîvov po vstupleniiam obiomnih voln. *Trudi Inst. Fiziki Zemli*, 20(187), Moscow.

Love A. E. H. (1914) *Proc. Lond. Math. Soc.*, 1, 1, London.

— (1952) A Treatise on the Mathematical Theory of Elasticity. University Press, Cambridge.

McKeown F. A., Dickey D. D. (1969) Fault Displacements and Motion Related to Nuclear Explosions. *Bull. Seism. Soc. Am.*, 59, 6, Berkeley.

Sharpe J. A. (1942) The production of elastic waves by explosion pressures. *Geophysics*, 7, 2—3, Tulsa.

Stauder W. (1960) Three Kamchatka earthquakes. *Bull. Seism. Soc. Am.*, 50, 3, Berkeley.

White J. E., Sengbush R. L. (1963) Shear waves from explosive sources. *Geophysics*, XXVIII, Tulsa.

Wright J. K., Carpenter E. W. (1962) The Generation of Horizontally Polarized Shear Waves by Underground Explosions. *J. Geophys. Res.*, 67, Richmond.

SIMULATIONS OF THE UNDERGROUND EXPLOSIONS GENERATING LONGITUDINAL AND TRANSVERSE WAVES

BY

DUMITRU ENESCU, ANCA GEORGESCU, VASILE MÂRZA [1]

Abstract

For the purpose to model the process noticed by Kim and Kisslinger regarding the generating of the two wave types (P and S) by underground explosions produced in spherical cavities, a generalization of Sharpe's and Blake's solution in made in this paper.

It has been established the expression of the transfer function of the source by means of which two electronic models for simulating of underground explosions generating longitudinal and transverse waves have been designed.

INTRODUCTION

As it is known, one of the method of studying the physical phenomena is represented by their electrical or electronic simulation. For the simulation of the explosion process generating longitudinal and transverse waves we have considered the cavity in which the explosive charge is placed to be spherical, though the theory shows (Sharpe, 1942; Blake, 1952; Favreau, 1969; Enescu, Cîndea, 1971 and others) that the explosion in spherical cavities generate only longitudinal waves.

The observational data proved (Kim, Kisslinger, 1967) that the underground explosions with spherical charges can generate the two wave types.

[1] Institute for Applied Geophysics. Department of Seismology and Seismometry. 5, Cuțitul de Argint st. Bucharest 28, Romania.

For this reason, the first part of the paper describes a theoretical model of a spherical explosive source generating longitudinal and transverse waves.

Two electronic systems, by means of which the explosion process generating P and S waves can be simulated, are described in the second part of the paper.

The authors do not claim to present a new theoretical model of explosive source, since the theory of the mathematical model taken into consideration in this paper is mere generalization of the solutions of S h a r p e (1942) and B l a k e (1952). This generalization consists in the extension of S h a r p e ' s and B l a k e ' s theory to explosions which generate P and S waves.

The purpose of this paper is the electrical or electronic simulation of the explosion process generating P and S waves. We have chosen from the pertinent literature S h a r p e ' s (1942) and B l a k e ' s (1952) mathematical model, which will be presented under a form suitable to the purpose of this paper.

G u r v i c h ' s theory (1968) is not adequate since we desire to take into consideration the displacements field for any (small and large) distances. Nevertheless, G u r v i c h ' s paper was used by us as a basis for adopting an assumption regarding to the tangential force distribution from the spherical source.

MATHEMATICAL MODEL

Let us assume that the explosive charge is placed in a spherical cavity of radius a (fig. 1). Due to the gas expansion produced by the explosion, a pressure p will act on the walls of this cavity. If the medium in the neighbourhood of the cavity is perfectly elastic, isotropic and homogeneous, a uniform pressure $p(t)$ applied on the internal surface of the cavity will generate only longitudinal waves (S h a r p e , 1942 ; B l a k e , 1952 ; F a v r e a u , 1969 ; E n e s c u , C î n d e a , 1971).

Actually, the medium being imperfectly elastic, the great pressure which acts on the front of the shock wave produces in the vicinity of the cavity of radius a, a zone of breaking, fissuring and shearing which are able to generate both longitudinal and transverse waves. If the medium in the neighbourhood of cavity is prestressed, that is, if in this medium, different kinds of stresses (tectonic stresses, residual stresses caused by others explosions, etc.) are accumulated, the great explosion pressure p reacti-

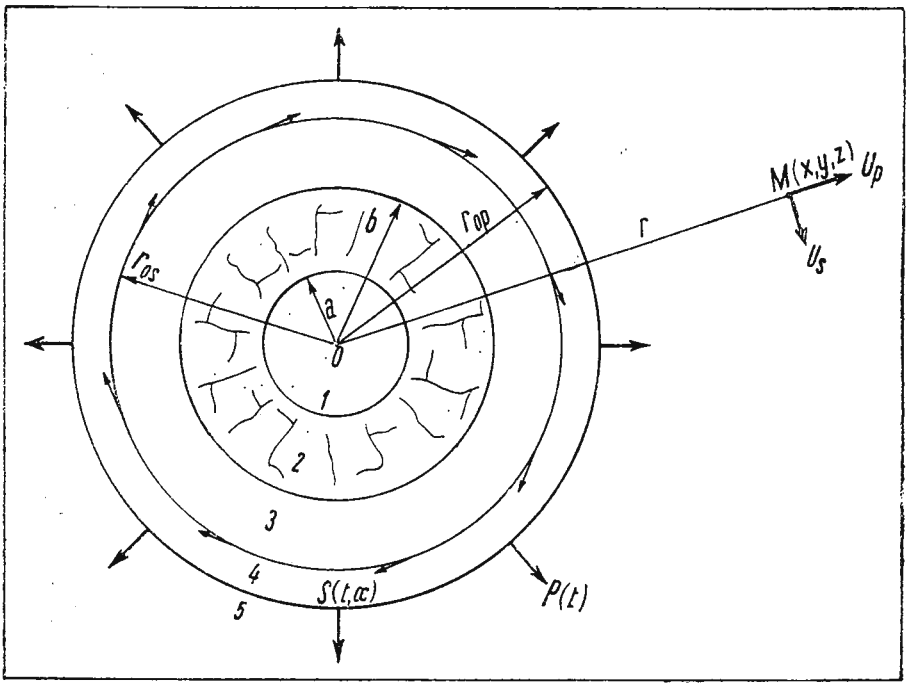

Fig. 1. — Explosive source generating longitudinal and transverse waves:
1, explosion cavity; 2, breaking and shearing zone; 3, zone of inelastic deformation for the S wave; 3,4, zone of of inelastic deformations for the P wave; 5, elastic zone.

vates these stresses which, acting in the directions in which they have been initially oriented, also generate longitudinal and transverse waves.

Let us assume that the processes responsible for the generation of the two wave types take place in the range represented by the sphere of radius b (fig. 1). For $r > b$ (fig. 1), the pressure on the wave front becomes smaller than the breaking strength of the rocks, but remains up to a distance $r = r_0$ greater than the elasticity limit of the medium. Therefore, in the range comprised between the spheres of radii $r = b$ and $r = r_0$ there are both P and S waves, but due to the relatively large strains, they do not behave as elastic waves.

Since the components of the forces generating longitudinal waves differ in intensity from those responsible for the generation of transverse waves, one can admit that the P waves become elastic waves at the distance r_{op} and the S waves at the distance r_{os} (fig. 1); the equality $r_{op} = r_o = r_{os}$ may exist only in a particular case.

From the above considerations it results that the things take place as if we were confronted with two spherical sources of elastic waves : the source of radius r_{op} generating longitudinal waves and the source of radius r_{os} generating transverse waves (fig. 1).

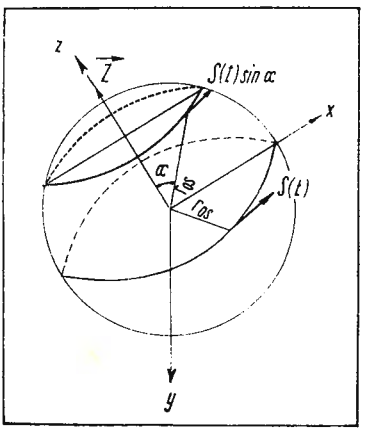

Fig. 2. — The pattern of action of the force $S(t)$.

In order to simplify the solution of the problem we consider, in agreement with S h a r p e and B l a k e , that the displacement in the longitudinal wave is function only of the distance r and the time t. In the case of the transverse wave we assume, in agreement with G u r v i c h , that the oscillations of the particles on the sphere coincide with the rotations variable in time of the sphere around a symmetry axis. If $Oxyz$ is a coordinate system with the origin at the center of the source, the rotations variable in time take place around the z axis arbitrarily orientated (fig. 2). We consider the z axis arbitrarily orientated such that the displacement in the S wave should contain both components (SH and SV).

In view of the above considerations the wave equations, written in spherical coordinates (r, α, β), have the form :

$$\frac{\partial^2\varphi}{\partial t^2} - V_p^2\left(\frac{\partial^2\varphi}{\partial r^2} + \frac{2}{r}\frac{\partial\varphi}{\partial r}\right) = 0 \tag{1}$$

$$\frac{\partial^2\vec{\psi}}{\partial t^2} - V_s^2\left[\frac{\partial^2\vec{\psi}}{\partial r^2} + \frac{2}{r}\frac{\partial\vec{\psi}}{\partial r} + \frac{1}{r^2\sin\alpha}\left(\sin\alpha\,\frac{\partial^2\vec{\psi}}{\partial\alpha^2} + \cos\alpha\,\frac{\partial\vec{\psi}}{\partial\alpha}\right)\right] = 0 \tag{2}$$

α being the colatitude of any point in the medium.

The propagation of the waves generated by the analysed spherical source is governed by the equations (1) and (2).

As concerns the boundary conditions, this paper does not use S a t o ' s (1949) manner of presentation. The mathematical theory of elasticity (L o v e , 1952) shows that the radial stress acting on the front of the longitudinal wave, in the case of the source of the type discussed by us, is of the form

$$\sigma_{rr} = (\lambda + 2\mu) \frac{\partial U_r}{\partial r_r} + 2\lambda \frac{U_r}{r} \tag{3}$$

and the tangential stress on the front of the transverse wave is

$$\sigma_{r\beta} = \mu \left(\frac{1}{r \sin\alpha} \frac{\partial U_r}{\partial \beta} + \frac{\partial U_\beta}{\partial r} = \frac{U_\beta}{r} \right) \tag{4}$$

Taking account of the conditions indicated above, we have :

$$U_r(t,r) = U_p(t,r) ; \; U_\alpha = 0 \; ; \; U_\beta(t,\alpha,r) = U_s(t,\alpha,r),$$

where U_p is the displacement in the longitudinal wave and U_s the displacement in the transverse wave.

The continuity of the forces, according to Newton's third law, imposes the following conditions :

$$P(t) = -\left[(\lambda + 2\mu) \frac{\partial U_p}{\partial r} + 2\lambda \frac{U_p}{r} \right]_{r = r_{op}} \tag{5}$$

$$S(t,\alpha) = -\mu \left[\frac{\partial U_s}{\partial r} - \frac{U_s}{r} \right]_{r = r_{os}} \tag{6}$$

where $P(t)$ and $S(t, \alpha)$ represent the radial and tangential components of the forces acting in the source (figs. 1, 2).

Since the functions $P(t)$ and $S(t, \alpha)$ satisfy Dirichlet's conditions, it can be written :

$$-\left[(\lambda + 2\mu) \frac{\partial U_p}{\partial r} + 2\lambda \frac{U_p}{r} \right]_{r = r_{op}} = \frac{1}{2\pi} \int_{-\infty}^{+\infty} \int_{-\infty}^{+\infty} P(\gamma) e^{-i n(\gamma - t)} \, dn \, d\gamma \tag{7}$$

$$-\mu \left[\frac{\partial U_s}{\partial r} - \frac{U_s}{r} \right]_{r = r_{os}} = \frac{1}{2\pi} \int_{-\infty}^{+\infty} \int_{-\infty}^{+\infty} S(\gamma,\alpha) e^{i n(\gamma - t)} \, dn d\gamma \tag{8}$$

Let us consider the exponential form of the solutions of the equations (1) and (2):

$$\varphi = \frac{1}{r}\, e^{-in\tau_p} \quad ; \quad \vec{\psi} = \frac{1}{r}\, e^{-in\tau_s}\, \vec{Z}, \tag{9}$$

where

$$\tau_p = t - \frac{r - r_{op}}{V_p} \quad ; \quad \tau_s = t - \frac{r - r_{os}}{V_s}$$

$\vec{Z}$ is the potential vector of the rotation forces acting in the source (fig. 2).

Since the rotation is around the z axis, we can write:

$$|\vec{\psi}| = \psi = \psi_z = \frac{1}{r}\, e^{-in\tau_s} \tag{10}$$

Let us set the conditions:

$$\varphi = \frac{1}{2\pi r} \int_{-\infty}^{+\infty} \int_{-\infty}^{+\infty} A(n) P(\gamma) e^{in(\gamma - \tau_p)}\, dn\, d\gamma \tag{11}$$

$$\psi = \frac{1}{2\pi r} \int_{-\infty}^{+\infty} \int_{-\infty}^{+\infty} B(n)(S\gamma,\alpha) e^{in(\gamma - \tau_s)}\, dn\, d\gamma \tag{12}$$

From the considerations presented above there results

$$U_p = \frac{\partial \varphi}{\partial r} \quad ; \quad U_s = \frac{\partial \psi}{\partial r} \sin \alpha \tag{13}$$

The expressions of the functions $A(n)$ and $B(n)$ can be obtained with the aid of the boundary conditions (7) and (8) and taking account of the relations (11)—(13).

As it was to be expected, the relations (11) and (12) are similar with the relation (7) from S h a r p e ' s paper (1942) and with the corresponding relation from B l a k e ' s paper (1952). Applying the procedure used in these two papers, we obtain, with the aid of the relations (11) — (13), the expressions of the displacements U_p and U_s produced by the examined source.

Thus, if

$$P(t) = P_0 \quad \text{and} \quad S(t,\alpha) = S_0 \sin\alpha \text{ for } t > 0$$
$$P(t) = 0 \quad \text{and} \quad S(t,\alpha) = 0 \quad \text{for } t < 0 \tag{14}$$

there results :

$$U_p = \frac{r_{op}P_0}{4\rho V_s^2}\left\{\left(\frac{r_{op}}{r}\right)^2 - \left(\frac{r_{op}}{r}\right)^3 \frac{V_p}{\sqrt{V_p - V_s^2}}\, e^{-h_p\tau_p}\sin\left[\omega'_{op}\tau_p + \operatorname{arc\,tg}\left(\frac{\sqrt{V_p^2 - V_s^2}}{V_s}\right)\right] + \right.$$
$$\left. + \frac{2r_{op}}{r}\frac{V_s}{\sqrt{V_p^2 - V_s^2}}\, e^{-h_p\tau_p}\sin(w'_{op}\tau_p)\right\} \tag{15}$$

$$U_s = \frac{r_{os}S_0}{3\rho V_s^2}\sin\alpha\left\{\left(\frac{r_{os}}{r}\right)^2 - 2\left(\frac{r_{os}}{r}\right)^2 e^{-h_s\tau_s}\sin\left[\omega'_{os}\tau_s + \operatorname{arc\,tg}\frac{1}{\sqrt{3}}\right] + \right.$$
$$\left. + 2\sqrt{3}\,\frac{r_{os}}{r}R^{-h_s\tau_s}\sin(\omega'_{os}\tau_s)\right\}, \tag{16}$$

where :

$$\omega'_{op} = \sqrt{\omega_{op}^2 - h_p^2} = \frac{2V_s}{r_{op}V_p}\sqrt{V_p^2 - V_s^2} \quad ; \quad \omega_{op} = \frac{2V_s}{r_{op}} \quad ; \quad h_p = \frac{2V_s^2}{r_{op}V_p}; \tag{17}$$

$$\omega'_{os} = \sqrt{\omega_{os}^2 - h_s^2} = \frac{\sqrt{3}\,V_s}{2r_{os}} \quad ; \quad \omega_{os} = \frac{\sqrt{3}\,V_s}{r_{os}} \quad ; \quad h_s = \frac{3V_s}{2r_{os}},$$

ρ is the density of the medium.

If

$$P(t) = P_0 e^{-h_p t} \quad ; \quad S(t,\alpha) = S_0 e^{-h_p t}\sin\alpha, \tag{18}$$

there results :

$$U_p = \frac{r_{op}^3 P_0}{4\rho V_s^2 r^2}\left[\frac{V_s^2}{V_p^2 - V_s^2} + 1\right][1 - \cos(\omega'_{op}\tau_p)]\, e^{-h_p\tau_p} +$$
$$+ \frac{r_{op}^2\, e^{-h_p\tau_p}P_0}{2\rho V_s r\sqrt{V_p^2 - V_s^2}}\left[\sin(\omega'_{op}\tau_p) + \frac{V_s}{\sqrt{V_p^2 - V_s^2}}\cos(\omega'_{op}\tau_p) - \frac{V_s}{\sqrt{V_p^2 - V_s^2}}\right] \tag{19}$$

$$U_s = S_0\sin\alpha\left\{\frac{4r_{os}^2}{3\rho V_s^2 r^2}[1 - \cos(\omega'_{os}\tau_s)]\, e^{-h_s\tau_s} + \right. \tag{20}$$
$$\left. + \frac{2r_{os}^2}{\sqrt{3}\,\rho V_s^2 r}[\sin(\omega'_{os}\tau_s) + \sqrt{3}\cos(\omega'_{os}\tau_s) - \sqrt{3}]\, e^{-h_s\tau_s}\right\}$$

In order to designe and calculate electronic or electrical models for the simulation of the explosion process it is necessary to know the transfer function of the source.

The total transfer function of the source is

$$Q(\omega) = Q_p(\omega) + Q_s(\omega) = Q_{p,1}(\omega) + Q_{p,2}(\omega) + Q_{p,1}(\omega) + Q_{s,2}(\omega), \tag{21}$$

where :

$$Q_{p,1}(\omega) = \frac{S_{U_{p,1}}(\omega)}{S_{P_1}(\omega)} = \frac{(V_s/r_{op})i\omega}{\omega_{op}^2 - \omega^2 + 2i\omega h_p} \tag{22}$$

$$Q_{p,2}(\omega) = \frac{S_{U_{p,2}}(\omega)}{S_{P_1}(\omega)} = \frac{q_p\omega_{op}^2}{\omega_{op}^2 - \omega^2 + 2i\omega h_p} \tag{23}$$

$$Q_{s,1}(\omega) = \frac{S_{U_{s,1}}(\omega)}{S_{S_1}(\omega)} = \frac{(V_s/r_{os})i\omega}{\omega_{os}^2 - \omega^2 + 2i\omega h_s} \tag{24}$$

$$Q_{s,2}(\omega) = \frac{S_{U_{s,2}}(\omega)}{S_{S_1}(\omega)} = \frac{q_s\omega_{os}^2}{\omega_{os}^2 - \omega^2 + 2i\omega h_s} \tag{25}$$

We used the notations :

$$q_p = \frac{r_{op}V_p}{4rV_s} \quad ; \quad q_s = \frac{r_{os}}{3r} \quad ; \quad Q_p(\omega) = \frac{S_{U_p}(\omega)}{S_{P_1}(\omega)}$$

$$Q_s(\omega) = \frac{S_{U_s}(\omega)}{S_{S_1}(\omega)} \quad ; \quad S_{U_p}(\omega) = S_{U_{p,1}}(\omega) + S_{U_{p,2}}(\omega) \tag{26}$$

$$S_{U_s}(\omega) = S_{U_{s,1}}(\omega) + S_{U_{s,2}}(\omega)$$

The functions $S_{U_p}(\omega)$, $S_{U_s}(\omega)$, $S_{P_1}(\omega)$, $S_{S_1}(\omega)$ are the complex spectra of the displacements $U_p(t)$, $U_s(t)$ and of the functions :

$$P_1(t) = \frac{r_{op}^2}{\rho r V_p V_s} P(t) \; ; \; S_1(t,\alpha) = \frac{r_{os}^2}{\rho r V_s^2} S(t,\alpha) \tag{27}$$

The calculation of this transfer function has been performed by determining the ratio of the signal spectrum at the source sistem output (response of the medium to the forces applied in the source) to the signal

spectrum at the input of this system. The input signal is represented by the functions $P(t)$ and $S(t)$ and the response of the medium by the displacements U_p (t) and U_s (t).

It is known that the shear and compressional motions are orthogonal and thus can be picked up individually on the three components of a seismometer. However, the total transfer function of the source has been written above since it describes the totality of the filter characteristics of the physical system represented by the spherical explosive source generating P and S waves.

The relations (22)—(25) express the transfer functions of four filters whose differential equations are :

$$\frac{d^2U_{p,1}}{dt^2} + 2h_p \frac{dU_{p,1}}{dt} + \omega_{op}^2 U_{p,1}(t) = \frac{V_s}{r_{op}} \frac{dP_1}{dt}; \tag{28}$$

$$\frac{d^2U_{p,2}}{dt^2} + 2h_p \frac{dU_{p,2}}{dt} + \omega_{op}^2 U_{p,2}(t) = q_p \omega_{op}^2 P_1(t); \tag{29}$$

$$\frac{d^2U_{s,1}}{dt^2} + 2h_s \frac{dU_{s,1}}{dt} + \omega_{os}^2 U_{s,1}(t) = \frac{V_s}{r_{os}} \frac{dS_1}{dt}; \tag{30}$$

$$\frac{d^2U_{s,2}}{dt^2} + 2h_s \frac{dU_{s,2}}{dt} + \omega_{os}^2 U_{s,2}(t) = q_s \omega_{os}^2 S_1(t, \alpha). \tag{31}$$

The transfer function (22), (24) and the differential equations (28), (30) describe resonance filters and the functions (23), (25) and the equations (29), (31) represented low-pass filters.

ELECTRONIC MODELS FOR THE SIMULATION OF UNDERGROUND EXPLOSIONS

In figure 3, one of the models is presented by means of which, the explosion process of generating longitudinal and transverse waves can be simulated. In order to attenuate the mutual influence between certain circuits represented in figure 3, buffer circuits with transistors are used.

For the calculation of the electrical parameters of the model, several conditions must be taken into consideration. The values given to the different electrical parameters (resistances, capacitances, inductances) must cover a large range in order that the simulation of the actual process be made for as large as possible a range of values which the parameters of

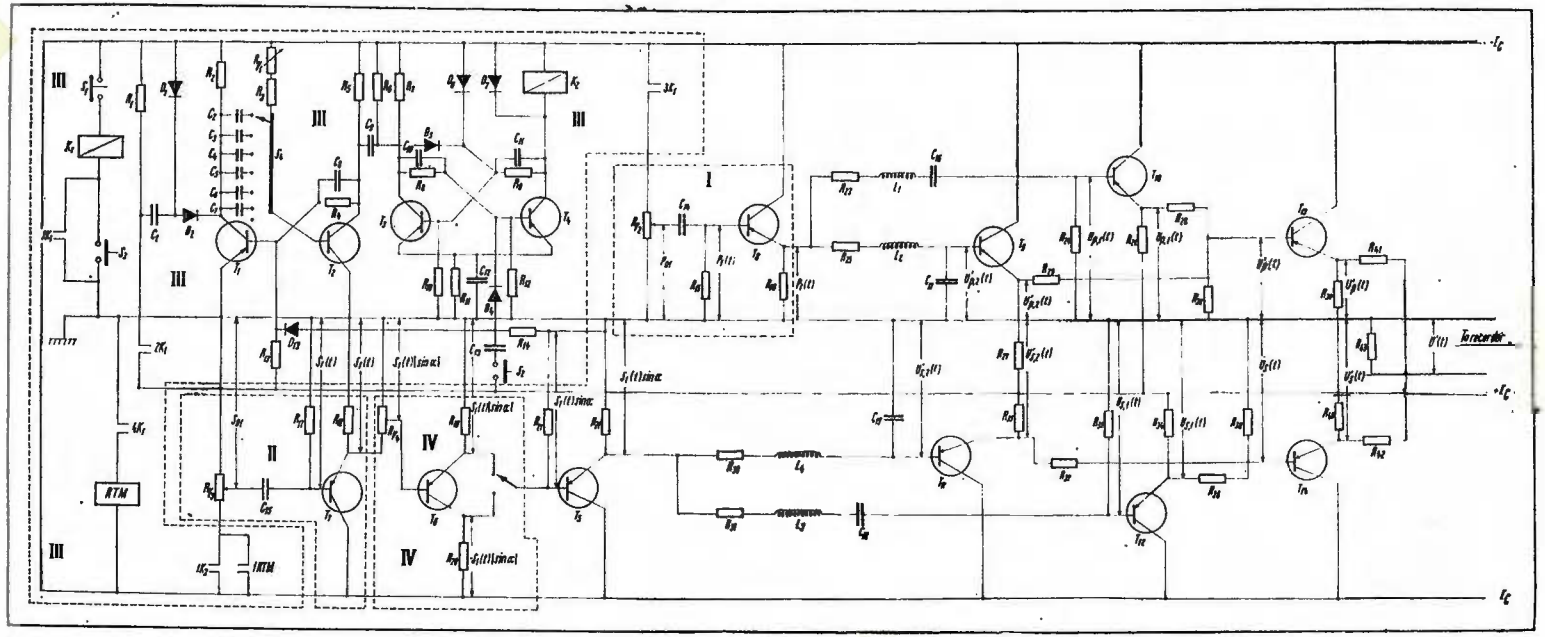

Fig. 3. — Electronic model for the simulation of explosion generating P and S waves.

the medium and explosion may assume. The obeying of this basic condition is restricted by the necessity of choosing those values of the electrical parameters which allow the construction of the model.

The functions $P_1(t)$ and $S_1(t)$ can be simulated by means of RC circuits denoted in figure 3 by I and II. At the input of these circuits the constant tensions P_{01} and S_{01} are applied and at the output we get the functions :

$$P_1(t) = P_{01}\, e^{-\frac{t}{\theta_p}} \; ; \; S_1(t) = S_{01}\, e^{-\frac{t}{\theta_s}}$$

where

$$\theta_p = \frac{1}{h_p} = R_{t,p}\, C_{14} = \frac{r_{op} V_p}{2 V_s^2} \; ; \quad \theta_s = \frac{1}{h_s} = R_{t,s}\, C_{15} = \frac{2 r_{os}}{3 V_s}, \tag{32}$$

in which :

$$R_{t,p} = \frac{R_{15}\, R_{i,8}}{R_{15} + R_{i,8}} \; ; \quad R_{t,s} = \frac{R_{17}\, R_{i,7}}{R_{17} + R_{i,7}} \tag{33}$$

$$R_{i,7} = h_{11e}^{(7)} + h_{21e}^{(7)}\, R_{19} \; ; \quad R_{i,8} = h_{11e}^{(8)} + h_{21e}^{(8)}\, R_{16} \tag{34}$$

The quantities $R_{i,7}$, $h_{11e}^{(7)}$, $h_{21e}^{(7)}$, characterize the emitter follower circuit T_7 and the quantities $R_{i,8}$, $h_{11e}^{(8)}$, $h_{21e}^{(8)}$ characterize the emitter follower circuit T_8, $R_{i,7}$ and $R_{i,8}$ are the input resistances ; $h_{11e}^{(7)}$ and $h_{11e}^{(8)}$ are the input impedances ; $h_{21e}^{(7)}$ and $h_{21e}^{(8)}$ are the current transfer ratios.

It is known that the amplification of the tension of the emitter follower circuit is approximately equal to unity if the following condition

$$h_{21e}^{(7)}\, R_{18} \gg h_{11e}^{(7)} \text{ or } h_{21e}^{(8)}\, R_{16} \gg h_{11e}^{(8)} \tag{35}$$

is fulfilled.

For the parameters R_{18}, R_{16}, C_{14}, C_{15}, $h_{11e}^{(7)}$, $h_{21e}^{(7)}$, $h_{11e}^{(8)}$ and $h_{21e}^{(8)}$ we choose values such as to satisfy conditions (35). By giving different values to the parameters r_{op}, r_{os}, V_p and V_s, the resistances $R_{t,p}$ and $R_{t,s}$ are calculated by means of formulae (32). If the resistances $R_{t,p}$ and $R_{t,s}$ are known, by determining the resistances $R_{i,7}$ and $R_{i,8}$ by means of formulae (34), the resistances R_{15} and R_{17} can be calculated.

Part III of the scheme (fig. 3) releases the path for the longitudinal, wave and delays the release of the path for the transverse wave. This delay

denoted by Δt, represents the difference between the arrival times of the two waves at any point of the medium, namely $\Delta t = r/V_s - r/V_p$.

Actually, the two waves are generated simultaneously. Due to the difference between their propagation velocities, the two waves arrive at any point of the medium at different times. In the model shown in figure 3 we achieved this delay at the outset of the scheme but not at its end. The final result is the same indifferently of the placing of the delay circuit. The way of acting of this circuit is described in several pertinent papers (F e l e a et al., 1964).

To obtain the function $S_1(t, \alpha) = S_{01}e^{-h_s t} \sin \alpha$ we have introduced the circuit IV (fig. 3) which performs the multiplication of the function $S_1(t) = S_{01}e^{-h_s t}$ by $\sin \alpha$.

The buffer circuit with the transistor T_5 has the role to attenuate the mutual influence between the multiplication circuit and the filters.

The calculation of the parameters of the resonance filters described by the transfer functions (22) and (24) or by the differential equations (28) and (30) can be made by means of the formulae :

$$R_{24} = \frac{V_s}{r_{op}} L_1 \; ; \; C_{16} = \frac{r_{op}^2}{4V_s^2 L_1} \; ; \; R_{23} = \frac{4-k}{k} R_{24} \; ; \; K = \frac{V_p}{V_s}$$

$$R_{32} = \frac{V_s}{r_{os}} L_3 \; ; \; C_{18} = \frac{r_{os}^2}{3V_s^2 L_3} \; ; \; R_{31} = \frac{2V_s}{r_{os}} L_3 \tag{36}$$

These formulae result from the analogies made between the equations (28), (30) and the equations describing the two electrical resonance filters shown in the scheme of Figure 3.

The formulae for the calculation of the low-pass filter parameters are obtained in the same manner :

$$R_{25} = \frac{4V_s^2}{r_{op} V_p} L_2 \; ; \; C_{17} = \frac{r_{op}^2}{4V_s^2 L_2} \; ; \; U'_{p,2}(t) = \frac{U_{p,2}(t)}{q_p}$$

$$R_{33} = \frac{3V_s}{r_{os}} L_4 \; ; \; C_{19} = \frac{r_{os}^2}{3V_s^2 L_4} \; ; \; U'_{s,2}(t) = \frac{U_{s,2}(t)}{q_s} . \tag{37}$$

As one can see, the values of the inductances L_1, L_2, L_3 and L_4 must be chosen ; the other electrical parameters (resistances, capacitances)

of the resonance and low-pass filters are calculated by means of formulae (36) and (37) as function of the source dimensions and the elastic parameters of the medium in which the explosion takes place.

The summation of the tensions $U_{p,1}(t)$ and $U_{p,2}(t)$ is made by means of the circuit consisting of the resistances R_{28}, $R_{29} = 1/q_p R_{29}$ and R_{30}; the circuit consisting of the resistances R_{36}, $R_{37} = 1/q_s R_{36}$ and R_{38} makes the summation of the tensions $U_{s,1}(t)$ and $U_{s,2}(t)$. After a short calculation it results:

$$U'_p(t) = m_p\ [U_{p,1}(t) + q_p U'_{p,2}(t)] = m_p\ [U_{p,1}(t) + U_{p,2}(t)] = m_p\ U_p(t)$$

$$U'_s(t) = m_s\ [U_{s,1}(t) + q_s U'_{s,2}(t)] = m_s\ [U_{s,1}(t) + U_{s,2}(t)] = m_s\ U_s(t)\ ,$$

where

$$m_p = \frac{R_{30}}{R_{28} + (1 + q_p) R_{30}}\ ; \qquad m_s = \frac{R_{38}}{R_{36} + (1 + q_s)\ R_{38}}\ .$$

In order to record on the same trace the tensions $U'_p(t)$ and $U_s(t)$ which are shifted in time by the quantity Δt, the circuit consisting of the resistances R_{41}, $R_{42} = R_{41}$ and R_{43} is used. Finally the following tension results

$$U'(t) = m\ [U'_p(t) + U'_s(t)], \tag{39}$$

where

$$m = \frac{R_{43}}{R_{41} + 2R_{43}}\ .$$

In order to attenuate the mutual influences between the adder circuits and the four filters, the buffer circuits with the transistors T_9, T_{10}, T_{11}, T_{12}, T_{13} and T_{14} are introduced in the scheme. For the parameters of these transistors and for the resistances R_{26} R_{27}, R_{34}, R_{35}, R_{39}, R_{40} such should be chosen as to satisfy conditions of the type (35).

By means of the system whose scheme is presented in figure 3, the underground explosions can be simulated for not too large ranges of values of the medium and explosion parameters. However, such ranges cover a great part of the cases met with in practice.

The underground explosions generating longitudinal and transverse waves can be also simulated by means of the system whose scheme is presented in figure 4. For the simulation of the functions $P_1(t)$ and $S_1(t)$

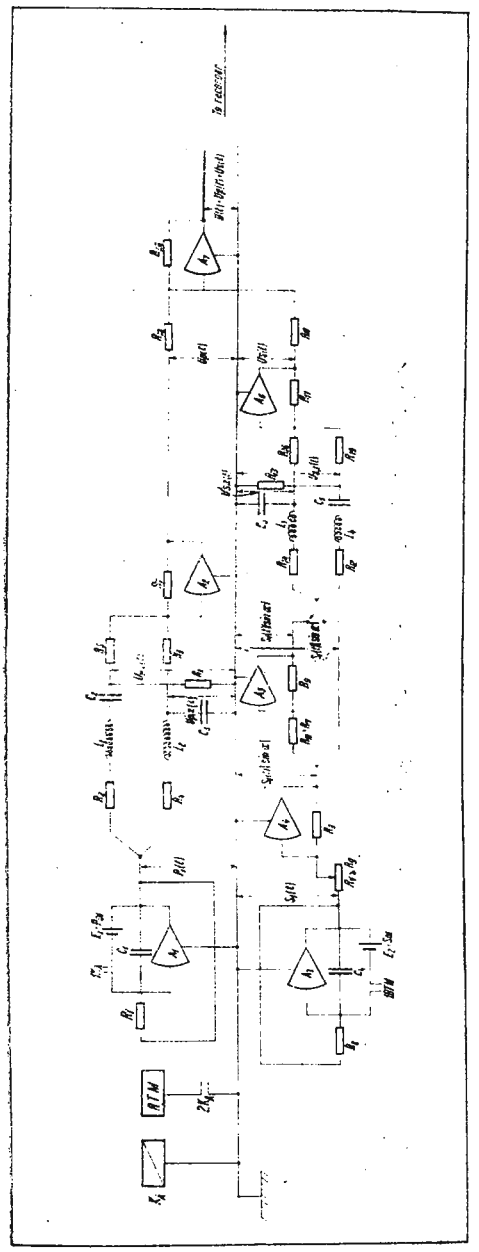

Fig. 4. — Another electronic model for the simulation of explosion generating P and S waves.

one can use calculation schemes which furnish exponential tensions at the output. Such a scheme is represented by an integrator circuit by constant h_p or h_s and initial tension P_{01} or S_{01}, with which the output and the input are directly connected (fig. 4). These circuits simulated the functions $P_1(t) = P_{01}e^{-h_p t}$ and $S_1(t) = S_{01}e^{-h_s t}$ if the following conditions

$$h_p = \frac{2V_s}{r_{0p}V_p} = \frac{1}{R_1 C_1} \; ; \quad h_s = \frac{3V_s}{2r_{0s}} = \frac{1}{R_8 C_4} \tag{40}$$

are satisfied.

The relay K_A (fig. 4) has two contacts. The contact 1 K_A releases the path for the longitudinal wave and the contact 2 K_A feeds up the $R\ T\ M$ time-lag relay. After the elapse of the delay time Δt fixed at $R\ T\ M$ this switches in its contact 1 $R.T.M$ which releases the path for the transverse wave.

The multiplication of the function $S_1(t)$ by sin α is is performed by means of the multiplier consisting of the operational amplifier A_4, the resistance R_9 and the variable resistance $R_v \geqslant R_9$. From the scheme $|\sin \alpha| = R_9/R_v$ results.

The inverter made up of the elements A_5, R_{10} and $R_{11} = R_{10}$ is necessary for obtaining positive values for the product $S_1(t)$ sin α.

The circuits which represent the resonance and low-pass filters are the same as those shown in figure 3.

Since the three adders should carry out the operations shown in figure 4, the following conditions

$$R_7 = R_5 \quad ; \quad R_{17} = R_{15} \quad ; \quad R_6 = \frac{R_7}{q_p} \; ;$$

$$R_{16} = \frac{R_{17}}{q_s} \quad ; \quad R_{18} = R_{19} = R_{20}$$

must be satisfied.

The differential equations (28)—(31) describe the explosion process for any form of the functions $P(t)$ and $S(t)$ because they result from the transfer function of the source. Consequently, the schemes presented in this paper are valid for any form of the functions $P(t)$ and $S(t)$ provided that only the function generators be changed.

REFERENCES

Blake F. G. (1952) Spherical Propagation in Solid Media. *J. Acoust. Soc. Am.*, 24, New York.

Enescu D., Cindea I. (1971) Modèles analogiques électroniques du processus d'explosion dans les roches. *Geophys. Prosp.*, XIX, 3, Haga.

Favreau R. F. (1969) Generation of Strain Waves in Rock by an Explosion in a Spherical Cavity. *J. Geophys. Res.*, 74, 17, Richmond.

Feiea et al. (1964) Circuite cu tranzistoare în industrie. Ed. Tehn., București.

Gurvich I. I. (1968) K teorii sfericeskovo izluciatelia poperecinih seismiceskih voln. Izv. Akad. Nauk SSSR, *Fizika Zemli* 1, Moscow.

Kim W. H., Kisslinger C. (1967) Model investigation of explosion in prestressed media. *Geophysics*, 32, 4, Tulsa.

Love A. E. H. (1952) A treatise on the mathematical theory of elasticity. University Press, Cambridge.

Sato Y. (1949) Boundary condition in the problem of generation of elastic waves. *Bull. Earthquake Res. Inst.*, 29, Tokio.

Sharpe J. A. (1942) The production, of elastic waves by explosion pressures. *Geophysics*, VII, 2–3, Tulsa.

PRINCIPLES OF CORRELATION

BY

PETER GIESE[1]

Abstract

The expression „correlation" is discussed with respect to its meaning in seismic work. It is outlined the necessity to distinguish between the correlation in the time-distance domain (records) and that in the depth-velocity domain (cross sections). It coincides in reflection work, but it is different in refraction in general.

The basic principle of correlation should be the phase correlation as usually used in exploration seismic. But in deep seismic sounding the principle of group correlation must be applied mainly due to the incompleteness of data. The difference between phase-and group correlation, however, is relative when related to the wavelength of seismic pulses. The group correlation means a simplification of the crustal velocity distribution.

INTRODUCTION

When evaluating seismic traveltime data, the procedure of „correlation" plays an important role, perhaps the most important one. Before discussing the principles of correlation the meaning of this term should be studied and dearly defined.

The expression correlation means that a distinct thing or feature is associated with a distinct term. In order to avoid difficulties, a dear definition by aid of the properties of the object under discussion must be given. In consequence, object equally termed can be joined or less precisely expressed „correlated".

The use of the word „correlation" in the seismic language means mainly the identification of the events in the records and their joining.

[1] Institut für Geophysik, Freie Universität Berlin, D—1 Berlin 33, Rheinbabenallee 49.

This correlation in the time-distance domain is regarded as identical with that in the depth-velocity domain. But a critical treatment will show that this conclusion is not valid in all cases. On this base some general considerations on principles of correlation are outlined.

CORRELATION IN REFLECTION SEISMICS

The following considerations are derived from a velocity distribution without any lateral variations. An extension to structures with horizontal inhomogeneities is possible in principle. Reflected waves can be characterized by the property that the derivative dx/dt means in general an apparent velocity. Here, no information on the velocity at the turning point, the reflecting element, can be obtained. The reflection aims to trace sudden changes of wave impedance in the medium under study. The sudden change of wave impedance causing the reflections is the feature that must be traced or correlated from point to point in the cross section. This plane of sudden wave impedance changes is detected by near spaced pointwise observations. The tracing of the arrivaltimes of a reflected wave in the time-distance domain — within one multichannel record or from one record to the next one — corresponds immediately to the tracing of the interface in the cross section. In conclusion the correlation in the record sections coincides with that in the cross section.

CORRELATION IN REFRACTION SEISMICS

Refracted waves, in the very general meaning of penetrating ones, can be described by the feature that the quantity dx/dt allows the determination of the true velocity at the depth in which the ray turns. In general each refracted ray is associated to a certain depth level characterized by a certain velocity. Here one has to check whether the correlation in the time-distance domain corresponds directly to that in the velocity depth one.

The correlation in the record sections means the joining of the arrivaltimes of a wave group from trace to trace, just as in reflection work. A wave group can be defined by a traveltime curve characterized by a curvature without change of sign. If, however comparing and compiling the results of two or more corresponding traveltime curves, a common and joining parameter is necessary. The only possible common parameter in a general velocity distribution is the velocity at the depth of ray turning. Consequently in cross sections, investigated by aid of refracted

waves, the correlation of points showing the same velocity leads automatically to a display with lines of equal velocity.

It is quite evident that the special case of a velocity gradient which becomes infinite — meaning an interface — is involved here. If the inversion of the traveltime data reveals that more than one refracted ray was turned in the same depth an interface is existing. In principle, each sudden velocity increase or decrease can be displayed if the chosen velocity interval Δv of the isolines is sufficiently small. These conclusions can be extended to cases with inclined interfaces, too.

Cross sections are one kind of data representation, contour maps are another one. Here the depths of a distinct velocity or the velocities of a distinct depth can be correlated and displayed.

In conclusion it can be stated that in reflection work correlation in the time-distance domain coincides with that one in the space (depth-distance) — velocity domain. The situation is different in refraction work (penetrating waves in general); the correlation in the time-distance domain cannot be directly transferred to the feature velocity (comparable and correlable in the space (depth-distance) — velocity domain.

The second part of this paper deals with the correlation in the record sections that means in the time-distance domain.

PRINCIPLES OF CORRELATION IN THE TIME-DISTANCE DOMAIN

Phase correlation

The first step of evaluation of x, t data is the identification of arrivaltimes of a wave group in a record section. A wave group can be briefly defined by the conditions having a continuous traveltime curve characterized by increasing traveltime with distance and the quantity dx/dt must be continuous, too. The basic principle of correlation is the phase correlation. In practice, the phase correlation does not use the beginning of an event but the next pronounced minimum or maximum of amplitudes. It is evident that a sure phase correlation requires a spacing of detectors smaller than one wave length (quasi wave length of the seismic pulse recorded).

The inhomogeneous crust passed by a wave field generates many events which travel to the surface. Due to the practical incompleteness of data in seismic crustal studies it is impossible to display the real detailed velocity distribution of the area under study. So here a first simplification has to be introduced in order to separate very local inhomogenei-

ties — here regarded as noise — from major features causing regular signals. Some criteria must be applied when identifying these regular wave groups in the record section:

a) The amplitudes or / and frequencies of the events being correlated must exceed resp. differ those of the noise;

b) the apparent velocity must show values within a possible and reasonable range, and

c) the traveltime branches correlated must be of some length.

There arises the question of how long a segment must be in order to fulfill the criterion of „sufficient length". It depends on the density of data available. In reflection work the scanning density at the reflection horizon is half the detector spacing. But in refraction work in general each observation line (one shot point and the associated observation line) allows only that one velocity isoline is detected once. So it seems reasonable in crustal studies to see the length of regular traveltime curves as at least of some 10 kilometers corresponding to the shot point distances used here.

The principle of phase correlation is applied in exploration refraction work to-day widely performed by automatic picking procedures. In seismic crustal studies a phase correlation is possible when continuous profiling is used. Figure 1a shows an example of a phase correlated reflection whereas the figure 1b demonstrates that of a refracted wave.

The problem of the „length of traveltime branches", established by phase correlation, leads to the principle of group correlation.

Group correlation

The modern view of crustal structure is a sandwich-like structure with components larger and smaller than the wavelength of the seismic pulse (Meissner, 1967; Fuchs, 1969; Davydova, Kosminskaya, Kapustian, Michota, 1972). Especially the classic discontinuities are composed of lamellae causing many wave groups. It depends on the wavelength applied whether these details can be resolved or not. In the case of high resolving power the traveltime branches, phase correlated, are of shorter or greater length and are arranged within a more or less wide stripe. Representing these separated segments by a mean traveltime curve the principle of group correlation is applied, whereby the points of support are individual segments, indicated by phase corre-

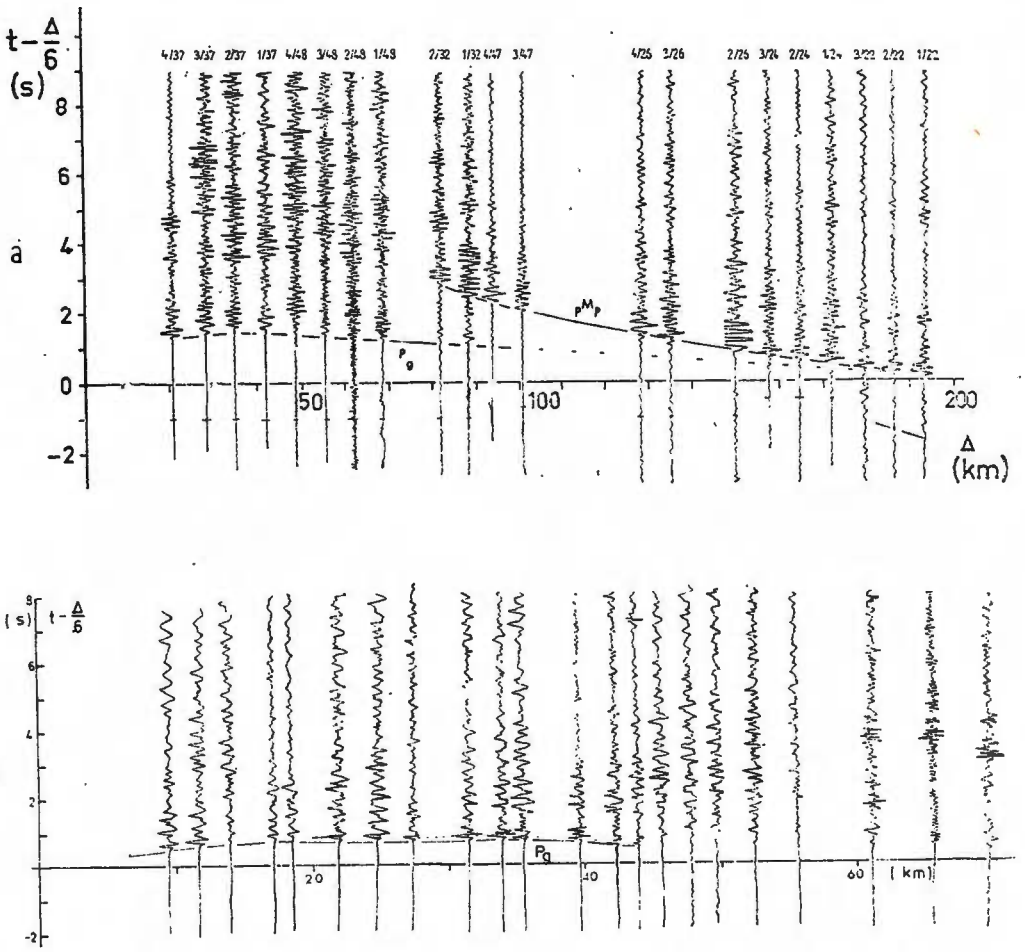

Fig. 1a. — Record section in reduced time scale showing a reversed traveltime curve P^MP established by phase correlation. Profile Jütland, 1962. (data after Hirschleber, Hjelme, Sellevoll, 1966).

Fig. 1b. — Record section in reduced time scale showing a normal traveltime segment P_g established by phase correlation. Refraction profile Rhenish Massif (Baier and Meissner, personal communication, 1971).

lation or even only by groups of large amplitudes. The latter feature is mainly present when in crustal studies the point sounding method is used.

In detail a group correlated traveltime curve can be of different structure. In principle the arrangement of the short elements is statistical or systematic with respect to the average traveltime curve (fig. 2, 3). Evi-

dently the group correlation yields a simplified representation of the real crustal velocity distribution more or less widely. An example is given in figure 3 and 4. Here the classical P^MP-curve is splitted into separated segments which are practically phase correlated. The detailed velocity distribution in the interval of the crust/mantle transition shows a change between high and low velocity layers (G i e s e, 1972). The group correlated traveltime curve yields a wide transition zone with increasing velo-

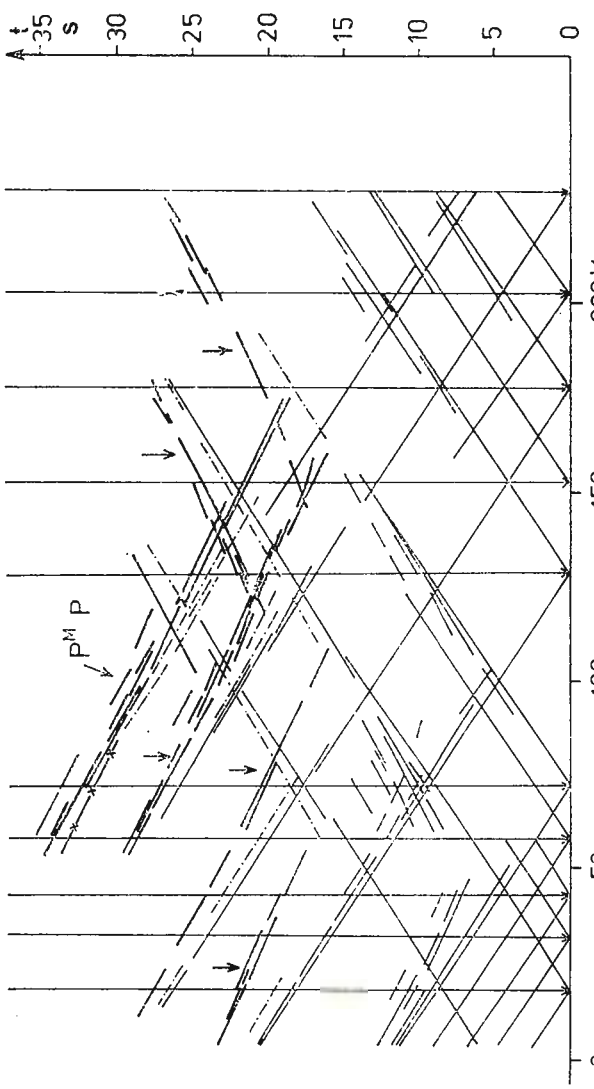

Fig. 2. — Portion of a deep seismic sounding profile observed in the Ukraincan shield showing separated traveltime elements each being phase correlated but without a systematic arrangement along the strip of the P^MP-group [S o l l o g u b, C h e k u n o v, 1972].

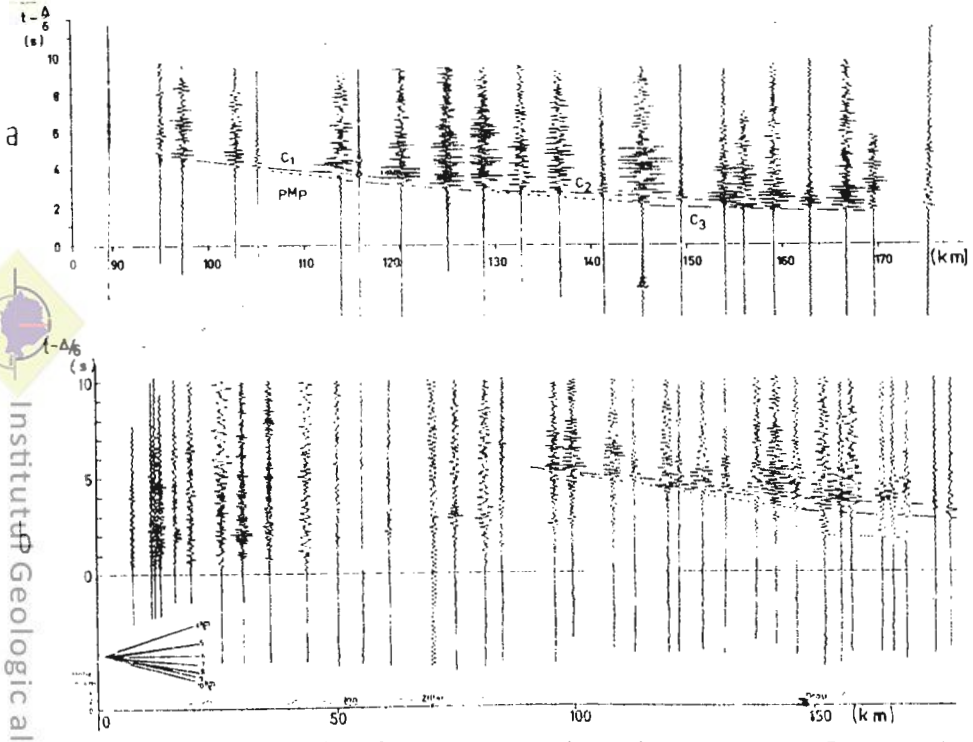

Fig. 3. — Two record sections in reduced time scale observed in the Northern Calcareous Alps :
a, profile Eschenlohe-E[2] ;
b, profile Eschenlohe-SE (A n g e n h e i s t e r, 1970).
The $p^M P$ group is composed of phase correlated segments (full line) which are systematically arranged like roofings. The dotted line envelopes these segments as group correlated traveltime curve.

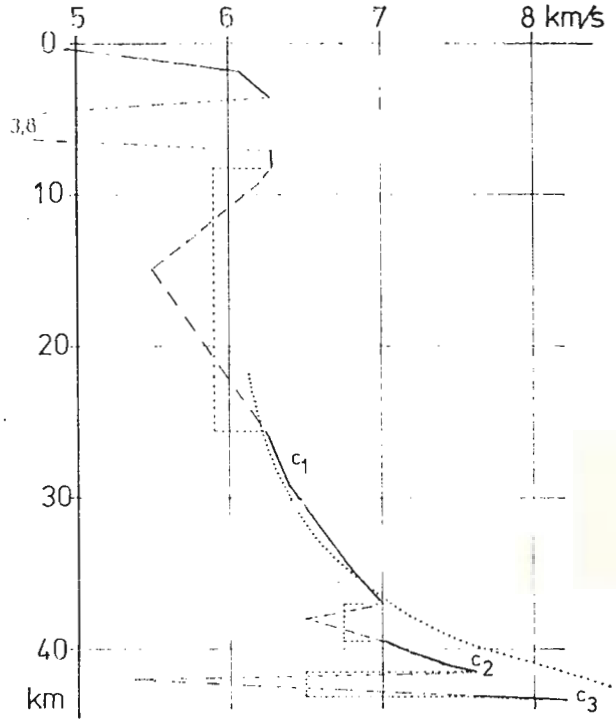

Fig. 4. — Velocity-depth function belonging to the profile Eschenlohe-E (G i e s e 1972). The dotted line in the deeper part corresponds to the group correlated traveltime curve (fig. 3a), whereas the three segments are associated to the phase correlated traveltime branches c_1, c_2, and c_3.

[2] K o s c h y k K. Beobachtungen zur Erforschung der Erdkruste mit der Methode der Refraktions-Seismik längs der beiden Profile Eschenlohe-SE und Eschenlohe-E in den Ostalpen 1965—1969. 1969. Dipl. Arb. Inst. Angew. Geophys. Univ. München.

city gradient with depth. Due to the principle of group correlation the velocity reversals must remain undetected. It is clear that the simplification of crustal structure is stronger if only few traveltime curves are used. Furthermore theoretically calculated seismograms on the base of group correlated traveltime branches are evidently not comparable with the observed amplitudes.

As well as in phase correlation, some criteria are necessary for the application of group correlation :

a) Joining of separated phase correlated segments and/or joining of arrivals characterized by clear and large amplitudes ;

b) the resulting apparent velocity must be within a possible and reasonable range, and

c) the traveltime branch must show „some length".

As briefly remarked previously, the type of correlation must be seen with respect to the wave length used and therefore the terms „phase-" and „group-" correlation are relative. Large wavelengths veil the detailed structure by integration yielding an uninterrupted traveltime curve, thereby allowing a phase correlation. Using shorter wavelengths, this one traveltime branch dissolves into numerous separated shorter segments.

The principle of group correlation in a very general sense is applied, too, if certain time-distance or certain depth-velocity relations are introduced in order to apply the mathematical tool of the least square method. A constant velocity layer is related to a linear time distance curve. Polynomials of higher degree lead to more complicated velocity-depth functions. The points which must be matched by a certain type of curve are based on the traveltimes picked from the arrival time of „distinct" events in the records. Because the individual features of an event (amplitude, frequency) are neglected by the correlation, the principle of group correlation is present.

Some arbitrariness may exist when there is to decide which type of certain mathematical relation and how many branches should be introduced.

A typical application of the method just mentioned is the time-term analysis. The time-term analysis regards the derivations of the real arrivaltimes — mainly first arrivals — from the best fitting curve and interprets these time differences as variations of thickness of the layer under discussion. An example is described by B e r r y and W e s t (1966), here having evaluated the seismic data of the Lake Superior experiments.

REFERENCES

Angenheister G. (1970) Die Erforschung der tieferen Erdkruste, Untersuchungs-Methoden und Ergebnisse. *Physik in unserer Zeit*, 1.

Berry, M. J., West G. F. (1966) A Time-Term Interpretation of the First-Arrival Data of the 1963 Lake Superior Experiment. The Earth beneath the Continents, *Geophys. Monogr.* 10, Am. Geophys. Un., Washington.

Davydova N. J., Kosminskaya J. P., Kapustian N. K., Michota G. G. (1972) Modes of the Earth's Crust and M-boundary. *Z. Geophys.*, 38, Würzburg.

Fuchs, K. (1969) On the properties of deep crustal reflections. *Z. Geophys.* 35, Würzburg.

Giese, O. (1972) The special structure of the P^MP traveltime curve. *Z. Geophys.*, 38, Würzburg.

Hirschleber, H., Hjelme J., Sellevoll M. (1966) A Refraction Profile through the Northern Jutland. *Geodet. Inst. Medd.*, 41, Kobenhavn.

Meissner R. (1967) Exploring Deep Interfaces by Seismic Wide Angle Measurements. *Geopyhs. Prosp.*, XV, 4. Hague.

Sollogub V. B., Chekunov A. V. (1972) The Crustal Structure of Central and Southeastern Europe Based on the Results of Explosion Seismology, part : The Soviet Union, The Ukrainian Soviet Socialist Republic. *Geophys. Trans.*, spec. ed., Budapest.

ON THE PHASE- AND GROUP-VELOCITY CURVES OF THE RAYLEIGH WAVES

BY

ZOLTAN KISS[1]

A number of theoretical dispersion curves have already been plotted for the Rayleigh waves, but the investigation of near-surface structures has required to perform calculations of this kind by using new parameters.

The period equation of the Rayleigh wave for 1-layered medium has been used with the following elasticity constants (tab. 1).

TABLE 1

Parameters of the theoretical dispersion curves calculated for the Rayleigh wave.

σ	$\frac{\mu_2}{\mu_1}$	$\frac{\rho_2}{\rho_1}$	$\frac{a_2}{a_1} = \frac{b_2}{b_1}$	$\frac{a_1}{b_1} = \frac{a_2}{b_2}$
0.25	1.4	1.05	1. 1547	1.73205
0.35				2.08166
0.45				3.31663

Note: $\sigma_1 = \sigma_2 = \sigma$ = Poisson ratio
μ = the constant of rigidity
ρ = the density
a,b = the velocity of the longitudinal—and transversal wave
(Index 1 refers to the upper layer, index 2 to the half space).

[1] MTA GGKI, Bp. XI, Meredek u., 18, Budapest, Hungary.

The fundamental-mode phase and group-velocity curves are shown in figures 1 and 2. The period of the Airy phase corresponding to the minimum value of group velocity changed very little with the growth of the Poisson ratio.

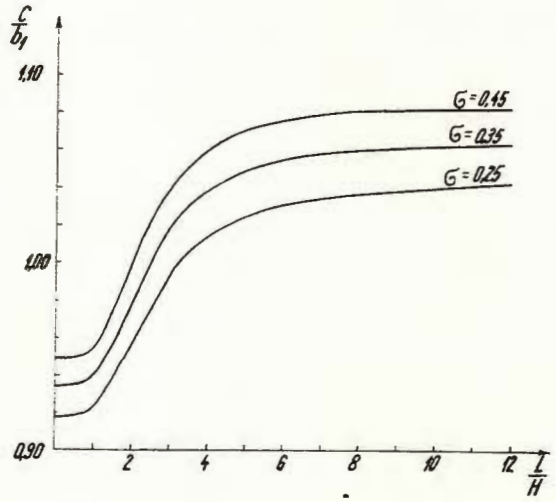

Fig. 1. — Theoretical phase-velocity curves of the Rayleigh wave. (c) $\frac{\mu_2}{\mu_1} = 1{\cdot}4$; $\frac{\rho_2}{\rho_1} = 1{\cdot}05$; L = the wave length; H = the thickness of the layer.

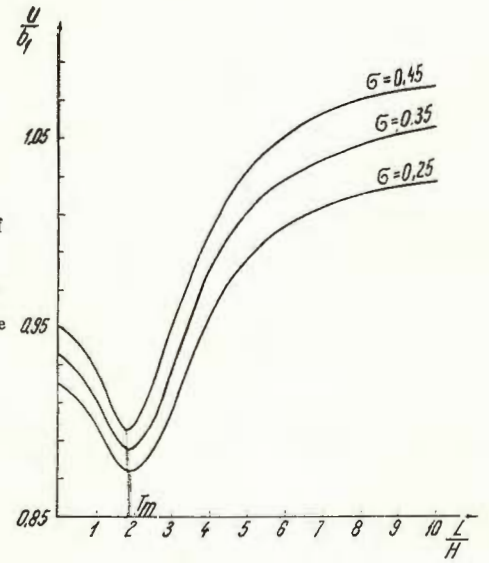

Fig. 2. — Theoretical group-velocity curves of the Rayleigh wave. (U) $\frac{\mu_2}{\mu_1} = 1{\cdot}4$; $\frac{\rho_2}{\rho_1} = 1{\cdot}05$; L = the wave length; H = the thickness of the layer; T_m = the period of the Airy phase.

The same parameters have been used for calculating the horizontal and vertical components of displacement of the Rayleigh waves as referred to the Earth's surface (fig. 3). In case of equal periods the path of the

particle motion is an ellipse. The relation of the components of displacement remains positive for every period. Therefore the direction of particle motion in our case is always a retrograde one.

The analysis of the components of displacement of the dispersive surface waves registered in the practice can be applied to identifying wave

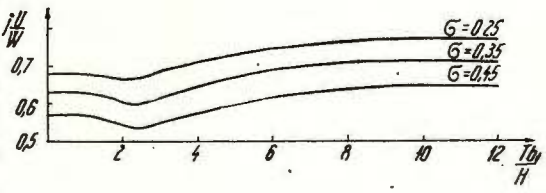

Fig. 3. — Relationship of the horizontal (U) and vertical (w) components of displacement on a free surface of the Rayleigh wave as plotted against values proportional with the period (Tb_1/H) $\frac{\mu_2}{\mu_1} = 1{\cdot}4$; $\frac{\rho_2}{\rho_1} = 1{\cdot}05$; T = the period of the Rayleigh wave; H = the thickness of the layer.

types. In addition, analyses of this kind may give some additional information on the thickness of the respective layer or the velocity of the transversal wave traversing it.

Theoretical dispersion curves with values rather close to the elasticity constants of the Earth's crust and the upper mantle, were published for our hypothetical model by Bolt and Butcher (1960). Their basic data are given in table 2.

TABLE 2

Velocities (a, b) and density conditions, (ρ_2/ρ_1) of the theoretical dispersion curves calculated for the Rayleigh wave by Bolt and Butcher (1960)

	A	B	C	D	E	F	G	H	I	J	K
$a_1 \left[\frac{km}{s}\right]$	5.8	6.0	62	6.0							
$b_1 \left[\frac{km}{s}\right]$	3.6			3.4	3.8	3.6	3.6				
$a_2 \left[\frac{km}{s}\right]$	8.2						8.2	8.0	8.4	8.2	
$b_2 \left[\frac{km}{s}\right]$	4.8									4.6	5.0
	1.296					1.4	1.207	1.296			

The numerical data of 11 fundamental mode theoretical curves have been plotted and the pairs of values corresponding to the minimum

value of group velocity, U_m/b_1 and $T_m b_1/H$, have thus been determined. The latter changed hardly any for the various cases, falling between 2.1 and 2.16. Since the minimum value of group velocity depends first of all on the velocity of the transversal wave in the respective layer, U_m has been plotted against b_1 with consideration of all the 11 cases. (fig. 4).

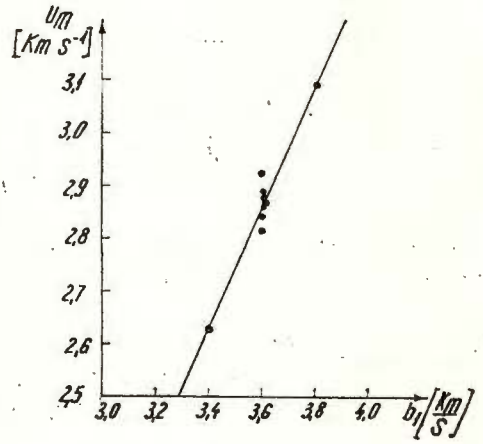

Fig. 4. — The minimum value of group velocity (U_m) as plotted against the transversal wave propagating in the upper layer (b_1) on the basis of the group-velocity curves published by Bolt and Butcher (1960). (The dot o indicates three subequal values).

Using this graph and the afore-mentioned relationship

$$H = \frac{T_m \cdot b_1}{2 \cdot 1 \div 2 \cdot 16}$$

a very rapid estimate for the approximate average thickness of the crust was obtained on the basis of the observation of the minimum value of group velocity of the fundamental-mode Rayleigh wave and of the period of the Airy phase. The period T_m and minimum value of group velocity, U_m, can be measured from the seismogram in most of the cases even when the entire dispersive wave train has not been registered.

We may add to this, that in a later publication Mooney and Bolt (1966) calculated new theoretical dispersion curves for the Rayleigh waves. Their parameters and the minimum values of group velocity read off their published graphs, together with the relevant periods, are shown in figure 5. We can see also from this, that, despite the relatively wide range of variation of the elasticity constants, the $T_m b_1/H$ values are limited to a narrow band. We are of the opinion that, like in the case of

the Earth's crust, an even more subtle recording of parameters might give a possibility for the rapid detecting of certain discontinuities even in near-surface structures.

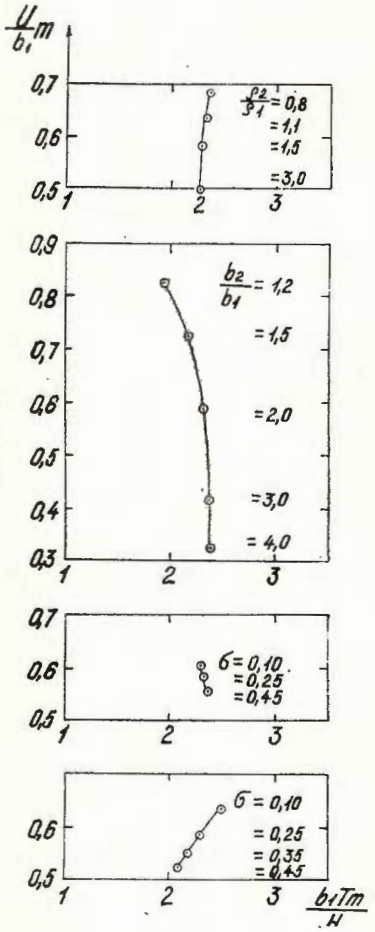

Fig. 5. — The minimum value of the group velocity (U_m/b_1) as plotted against the period of the Airy phase ($T_m b_1/H$) on the basis of the group — velocity curves published by Mooney and Bolt (1966).

$\frac{b_2}{b} = 2{\cdot}0$; $\frac{\rho_2}{\rho_1} = 1{\cdot}5$; $\sigma_1 = 0{\cdot}25$; $\sigma_2 = 0{\cdot}25$.

Al in all, we can conclude that in the case of waves propagating in a stratified medium, at least one period of large amplitude (or a very narrow frequency band) can be distinguished on seismograms obtained for different epicentral distances. An essential characteristic of the thickness of a given layer, this is the period of the Airy phase of the Rayleigh wave or of other types of surface waves. (The higher modes of the surface waves have been disregarded in the present discussion).

REFERENCES

Bolt B. A., Butcher J. C. (1960) Rayleigh wave dispersion for a single layer on an elastic half space. *Austral. J. Phys.* 13, Melbourne.

Mooney H. M., Bolt B. A. (1966) Dispersive characteristics of the first three Rayleigh modes for a single Surface wave. *Bull. Seism. Soc. Am.*, 56, 1, Berkeley

SOURCE FUNCTION OF STRESS WAVES IN NON-ELASTIC AND ELASTIC ZONES OF AN EXPLOSIVE SOURCE

BY

VLADIMIR SCHENK [1]

INTRODUCTION

At present the question of determining the source function of stress waves on the surface of an elastic source of seismic waves is coming to the fore. The definition of its pattern on the basis of the physical properties of the medium and the size of the source makes it possible to solve more reliably the questions connected with the determination of the dynamic parameters of seismic waves in different distances from a given source.

In the solution of the above problems it is a question of computing the particle displacement and its derivatives for the in advance defined physical conditions that are simplified compared with reality. The basis condition for such a computation is the knowledge of the source function of stress waves. In a number of mathematical procedures the presence of non-elastic deformations in the vicinity of the source of seismic waves is not considered and very often a strongly simplified source function on the surface of the spherical cavity of the source is defined. Therefore, the question of determining the stress wave pattern on this source remains still open. That is why in the present work an attempt has been made to approximate the measured wave records in the zone of non-elastic as well as elastic deformations of the explosive source of functions with such a character that would best approach the known patterns.

[1] Geophysical Institute of the Czechosl. Acad. Sci., 141 00 Praha 4 — Spořilov Bočni II., Czechoslovakia.

APPROXIMATION FUNCTION OF STRESS WAVE PATTERNS

The up to now used source functions that would suit the measured stress wave records in the close vicinity of the explosive source were evaluated. These functions can be distinguish into four groups.

In the first group the stress acting on the surface of an elastic source is of a constant value with a limited or unlimited time effect. Its pattern fits the form (Nishimura, 1937; Sezawa, Kanai, 1941, 1942; Sharpe, 1942; Selberg, 1952; Sabodash, 1966; Fadeev, 1968; Ghosh, 1969)

$$p(t) = p_0 \tag{1}$$

or the form (Nishimura, 1937; Sharpe, 1942)

$$p(t) = p_0(1 - e^{-\beta t}) \tag{2}$$

In the second group the stress on the surface of an elastic source reaches its maximum within a short time and then it falls for a considerable time to nought value. This drop can be expressed by the function (Sezawa, Kanai, 1941; Sharpe, 1942; Blake, 1952; Selberg, 1952; Milkulinskiy, 1965; Gurvich, 1966; Ghosh 1969)

$$p(t) = p_0 e^{-\beta t} \tag{3}$$

or functions (Sharpe, 1942; Duvall, 1953; Vaněk, 1953; Berg, Papageorge, 1964; Mikulinskiy, 1965)

$$p(t) = p_0(e^{-\beta_1 t} - e^{-\beta_2 t}), \tag{4}$$

$$p(t) = p_0 e^{-\beta t}\ (1 - k e^{-\beta t}), \tag{5}$$

$$p(t) = p_0 t^{\alpha} e^{-\beta t} \tag{6}$$

and

$$p(t) = p_0\ \beta^{\alpha}\ t^{\alpha}\ e^{-\beta t}, \tag{7}$$

In the third group the stress acting on the surface of an elastic source of seismic waves is of oscillatory undamped character with unlimited time effect and is given by the function (Blake, 1952; Gurvich, 1965)

$$p(t) = p_0\ e^{j\omega t} \tag{8}$$

or functions (S e z a w a, K a n a i, 1941, 1942; M e y e r, 1964)

$$p(t) = p_0 \sin \omega t \tag{9}$$

In the fourth group the stress on the surface of an elastic source of seismic waves is of oscillatory damped character and is given either by one function (S e z a w a, K a n a i, 1941)

$$p(t) = p_0 \, e^{-\beta t} \sin \omega t \tag{10}$$

or two functions linking up to each other (A t c h i s o n, P u g l i e s e, 1964; D u v a l l, P u g l i e s e, 1965; S t a r f i e l d, 1966; S t a r f i e l d, P u g l i e s e, 1968)

$$p(t) = p_0 \, e^{-\beta t} \sin \omega t \ \ldots\ \text{for } 0 < t \leqslant \frac{3\pi}{2\omega}$$

$$p(t) = -p_0 \, e^{-\beta t} \ \ldots\ \text{for } t > \frac{3\pi}{2\omega} \tag{11}$$

A comparison of the above source functions with stress wave records measured in real geological media[2] (S t a r f i e l d, 1966) revealed that these functions in the vicinity of the surface of an elastic source do not by their properties quite suit the obtained records of these waves. The stress wave patterns in the neighbourhood of the explosive source roughly possess the form of a deformed sinusoid, whose first maximum amplitude is manyfold greater than the following amplitude, and the time of the first halfwave is shorter than that of the following halfwave. The properties of stress wave records indicate that the approximation function that would express these records with minimum distortion will be consist from the combination of functions of the second and fourth group.

The above combination nearly fits the Berlage function, which is often used for solving wave problems. However, contrary to stress wave records it has a constant period of oscillation. In order to achieve variability of its period with increasing time, the sinus argument was extended by the member δt, and thus originated new function had the form

$$p(t) = p_0 \, t^{\alpha} \, e^{-\beta t} \sin [(\omega + \delta t) \, t]. \tag{12}$$

[2] S c h e n k V. Study of generation of stress waves near an explosion in soils. 1968. CSC Thesis, Geophys. Inst. Czechosl. Acad. Sci.

The use of this function in a concrete case showed that function (12) fulfils all the above mentioned features of the stress wave pattern in the close neighbourhood of the explosive source. It must be pointed out that individual coefficients in term (12) are of no specific physical meaning but they can be used to express the changes in the form of the stress wave pattern in the medium under investigation in dependence on time, on distance from the source and on its size.

THE SOURCE FUNCTION. OF STRESS WAVES FOR GRAVEL SANDY SOIL

The character of coefficient dependences was sought in stress wave records measured in gravel sandy soil [3]. The individual records were approximated by function (12) in such a way that for the determination of coefficients p_0, α, β, ω and δ the times of their nought and extreme amplitudes together with the amplitude values were taken into account.

By means of statistical methods the changes of these coefficients provided their dependences on the size of the source C (kg) and on the scaled distance r^* (mkg$^{-1/3}$) from the centre of the source. The coefficient β was found to be dependent also on the radius of the elastic source of stress waves r_E^*(mkg$^{-1/3}$). In gravel sandy soil the found dependences have the following form

$$\left.\begin{aligned} p_0 &= 1.7 \times 10^7\, r^{*-3.4}, \\ \alpha &= (1.289 \pm 0.065) - (0.117 \pm 0.037)\ln C, \\ \beta &= (400.0^{+347.7}_{-186.0})\ C^{-(0.287+0.268)}\ r_E^{*}\, r^{*-0.5}, \\ \omega &= (1215.8^{+174.8}_{-152.9})\ C^{-0.2}\ r^{*\,-(0.363\pm0.139)}, \\ \delta &= (9.776^{+26.224}_{-3.639}) \times 10^4\, r^*\, C^{-0.6} \exp\,[-(1.101 \pm 0.612) r^*], \end{aligned}\right\} \quad (13)$$

where $r_E^* = 1.8$ mkg$^{-1/3}$ for gravel sandy soil.

By substituting the relations (13) to (12) we can determine the probable wave pattern of stress waves in gravel sandy medium. The comparison performed between the computed and measured wave patterns suggests that function (12) can reliably express the source function of stress waves on the surface of this elastic source. To be able to demonstrate the changes of stress wave pattern expressed by function (12) with increasing distance from the source, these patterns were computed for $C = 0.05$ kg

[3] *Op. cit.*, p. 2

and for scaled distances $0.4\ \text{mkg}^{-1/3} \leqslant r^* \leqslant 6.0\ \text{mkg}^{-1/3}$. Figure 1 gives these stress wave patterns, in which their first onsets correspond to each other. They can be characterized by the following properties :

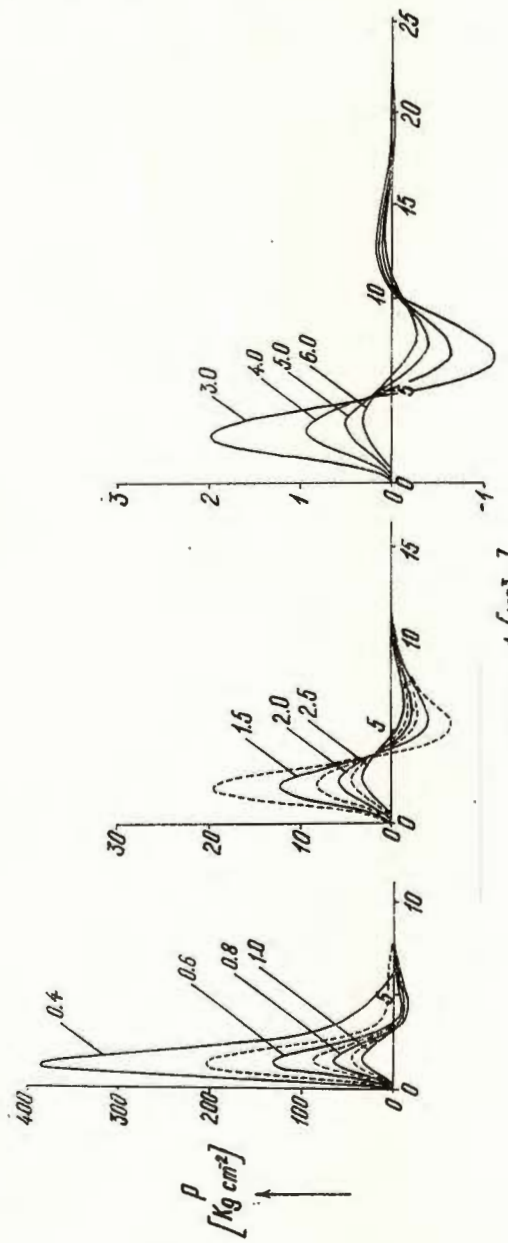

Fig. 1. — Computed stress wave patterns in gravel sandy soil according to relations (12) and (13) for charge $C = 0.05$ kg and for range of scaled distances from 0.4 to 6.0 $\text{mkg}^{-1/3}$.

a) with increasing distance from the source the stress wave pattern changes from shock character into oscillating character;

b) the time of the stress history in the first halfwave in the closest vicinity from the source decreases and approximately from the distance $r^* = 0.9$ to 1.0 $\text{mkg}^{-1/3}$, where the inner plastic zone passes into the outer zone, there again occurs an increase of this time;

c) in the close neighbourhood from the source the duration of succesive halfperiods shortens with time, in greater distances from the source their duration first prolongs and it does not shorten until after several wave lengths;

d) the maximum stress amplitude drops with the distance from the source. With increasing distance from the source there occurs a shift of energy oscillation into the following periods, by which the stress wave pattern acquires the wave character of oscillation.

CONCLUSION

The function (12) characterize fairly well the actual stress wave records in the close neighbourhood from an explosive spherical source. This fact suggests the assumption whether in the future the applicability of function (12) should not be considered in the solution of general problems connected with stress waves propagation in the vicinity of seismic sources. It appears already now that the use of the source function under discussion in some concrete problems of technical practice would make their solution much easier.

In closing I wish to thank Dr. O. Novotný from the Charles University in Prague for preparing the programs for MINSK-22 computer and to Dr. Z. Schenková for valuable advice and assistance in the statistical evaluation of the computed values.

REFERENCES

Atchison T. C., Pugliese J. M. (1964) Comparative Studies of Explosives in Granite: Second Series of Tests. *U.S. BMRI* 6434.

Berg J. W., Jr., Papageorge G. E. (1964) Elastic Displacement of Primary Waves from Explosive Sources. *Bull. Seism. Soc. Am.*, 54, Berkeley.

Blake F. G. (1952) Spherical Wave Propagation in Solid Media. *J. Acoust. Soc. Am.*, 24, New York.

Duvall W. I. (1953) Strain-wave Shapes in Rock near Explosions. *Geophysics*, 18, Tulsa.

— Pugliese J. M. (1965) Comparison Between End and Axial Methods of Detonating an Explosive in Granite. *U.S. BMRI*, 6700.

F a d e e v A. V. (1968) Formirovanie i rasprostranenie vzryvnykh voln napryazheniy v gornykh porodakh. *Fiz. goreniya i vzryva*, 4. Novosibirsk.

G h o s h M. L. (1969) On the Propagation of Spherical Waves due to Large Underground Explosion. *PAGEOPH*, 72, Basel.

G u r v i c h I. I. (1966) Funkciya vozbuzhdeniya vzryvnogo shericheskogo izluchatelya. *Izv. AN SSSR, Ser. Fiz. Zemli*, 4, Moskva.

M e y e r M. L. (1964) On Spherical Near Fields and Far Fields in Elastic and Visco-Elastic Solids. *J. Mech. Phys. Solids* 12, Oxford.

M i k u l i n s k i y M. A. et al. (1965) Analiticheskie issledovaniya parametrov seismovzryvnykh voln v grunte v blizhayshey zone vzryva. *Tr. V. Sessii uchen. sov. po narodn. — khozyaystv. ispol'z. vzryva*, AN Kirg. SSR, Ilim, Frunze.

N i s h i m u r a G. (1937) On the Elastic Waves due to Pressure Variation on the Inner Surface of a Spherical Cavity in an Elastic Solid. *Bull. Earthq. Res. Inst.*, 15, Tokyo.

S a b o d a s h P. F. (1966) O rasprostraneniy shericheskikh voln v uprugo-plasticheskoy srede. *Izv. AN SSSR, Ser. Fiz. Zemli*, 4, Moskva.

S e l b e r g H. L. (1952) Transient Compression Waves from Spherical and Cylindrical Cavities. *Arkiv för Fysik*, 5, Stockholm.

S e z a w a K., K a n a i K. (1941—1942) Transmission of Arbitrary Elastic Waves from a Spherical Source, Solved with Operational Calculus. *Bull. Earthq. Res. Inst.*, 19 and 20, Tokyo.

S h a r p e J. A. (1942) The Production of Elastic Waves by Explosion Pressures. *Geophysics*, 7, Tulsa.

S t a r f i e l d A. M. (1966) Strain Wave Theory in Rock Blasting. *The VIII. Rock Mech. Symp.*, Univ. Minnesota.

— P u g l i e s e J. M. (1968) Compression Waves Generated in Rock by Cylindrical Explosive Charges : a Comparison between a Computer Model and Field Measurements. *Int. J. Rock Mech. and Mining Sci.*, 5, London, New York.

V a n ě k J. (1953) A Contribution to the Theory of Elastic Waves Produced by Shock. *Czech. J. Phys.*, 3, Prague.

SPECTRAL FIELDS OF SEISMIC WAVES PRODUCED BY EXPLOSIVE SOURCE WITH DIFFERENT SHAPE

BY

VLADIMIR SCHENK [1]

INTRODUCTION

When investigating experimentally the origin of individual wave groups, we study the changes of their dynamic parameters in dependence on the properties of the source and its surrounding medium. In near distances from seismic sources, in which the medium is subject to nonelastic deformations, it is necessary to pay great attention to these changes because both the amplitude and the frequency contents of seismic waves characterize the actual wave process of their formation.

In recent years our Institute has solved the problems of the origin of individual wave groups of seismic waves originated by sources with non-spherical radiation patterns. The arrangement of experiments allows to study the succesive changes of the wave patterns of the longitudinal components of the seismic waves up to its transverse components by keeping the same orientation of the pickups over the whole epicentral region of the source. The results, which have been achieved in this research, are presented in this paper.

FIELD TESTS

The measurement of seismic waves produced by an spherical and non-spherical explosive source was performed in gravel sandy soil. The sources, weighted 0.2 kg, were made of cast TNT or plastic explosives and were located to the depth of about 1.5 m. The eight pickup sets with three

[1] Geophysical Institute of the Czechosl. Acad. Sci., 141 00 Praha 4 — Spořilov, Boční II., Czechoslovakia.

e lectrodynamic geophones of type GP—2 were placed on the earth's surface in a circle of the radius of 10 m at 45° intervals round the epicentre of each source. In this way the geophones measured in 8 places on the circle three components X, Y and Z perpendicular to each other of the

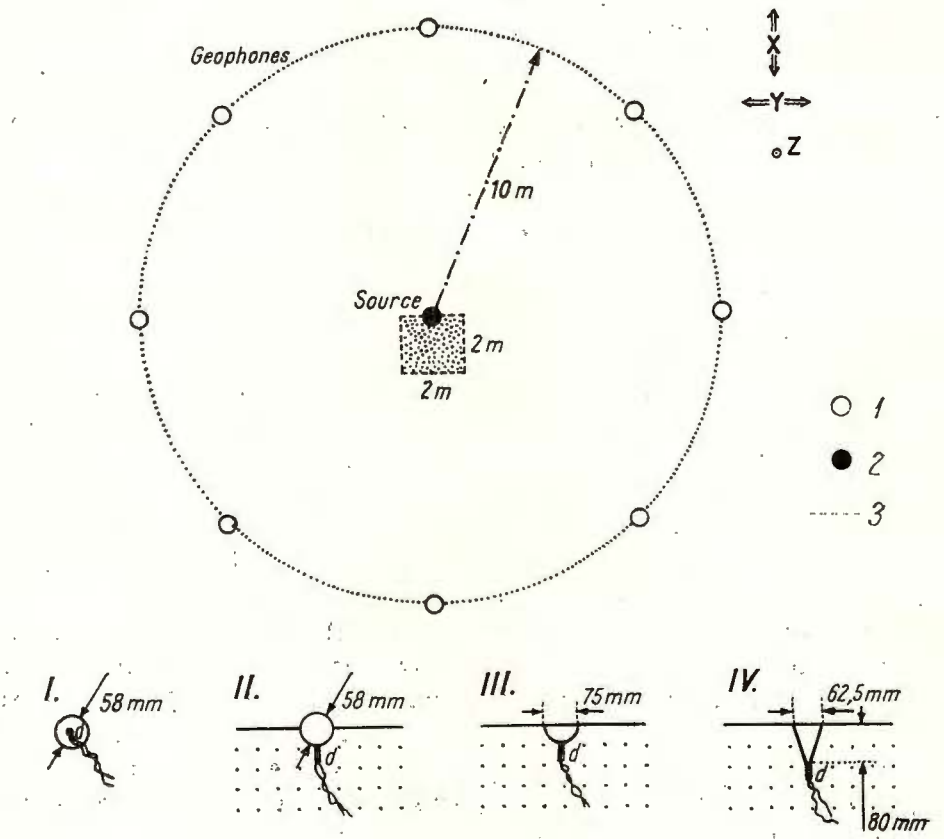

Fig. 1. — Arrangement of the field tests.

1, the pickup sets; 2, the epicentre of the source; 3, the trench: the orientation of the geophones together with the direction of the measured components X, Y and Z are shown by arrows in the right-hand upper corner and the four types of charges are in the lower part.

originating seismic waves. The character of these waves corresponded to the amplitudes of particle velocity. Figure 1 represents a scheme of the arrangement of these experiments.

Four experiments were conducted altogether:

I. spherical source deposited at the bottom of the bore hole, which over the charge was filled with the bored crammed soil;

II. spherical source placed at the wall of the trench;

III. hemispherical source located with its flat side at the wall of the trench;

IV. conical source placed with its base at the wall of the trench.

With the second, third and fourth experiment the trench having the dimensions $2 \times 2 \times 2$ m was after the depositing of the garge again filled with the bored loosely poured soil. In this way the trench enhanced the creation of the directed radiation pattern of the source of seismic waves.

SPECTRAL AMPLITUDE FIELDS OF SEISMIC WAVES

The measured seismic wave records were Fourier analyzed using F i l o n method (F i l o n, 1928—1929) within the frequency range from 0 to 100 c/s. The amplitude spectra served to the construction of spectral amplitude fields (in the next only SAF or SAFs) of seismic waves: the computed values of amplitude spectra were plotted to linear frequency scale on the straight lines starting below the angle of 45° from one point and by graphic interpolation of these values isolines with identical spectral amplitudes were constructed. In this way were created SAFs on individual components X, Y and Z of the originated seismic waves in all four experiments. Each SAF is limited by a circle that corresponds to spectral frequency of 100 c/s and the centre of the SAF is identical with the spectral frequency 0 c/s.

All the SAFs are identically oriented with respect to each other and if we make an imaginary projection of a clock dial on each SAF, the orientation is simple: the component X was always identical with the direction „6—12", the component Y with the direction „3—9" and the component Z was perpendicular to both previous components. From the mutual arrangement of the source and the components measured, it can be deduced that with the SAFs of X components the character of spectra on the line „6—12" can be ascribed to the effect of P waves in medium and on the line „3—9" to the SH waves. On the contrary, with the SAFs of Y components the character of spectra on the line „6—12" corresponds to SH waves and on the line „3—9" to P waves. The SAFs Z then express the character of SV waves in all directions. In the experiments II.—IV. the explosive source energy was regulated to direction „12".

The SAFs of experiment I. (fig. 2) are in good agreement with the results obtained in previous measurements of seismic waves in the vici-

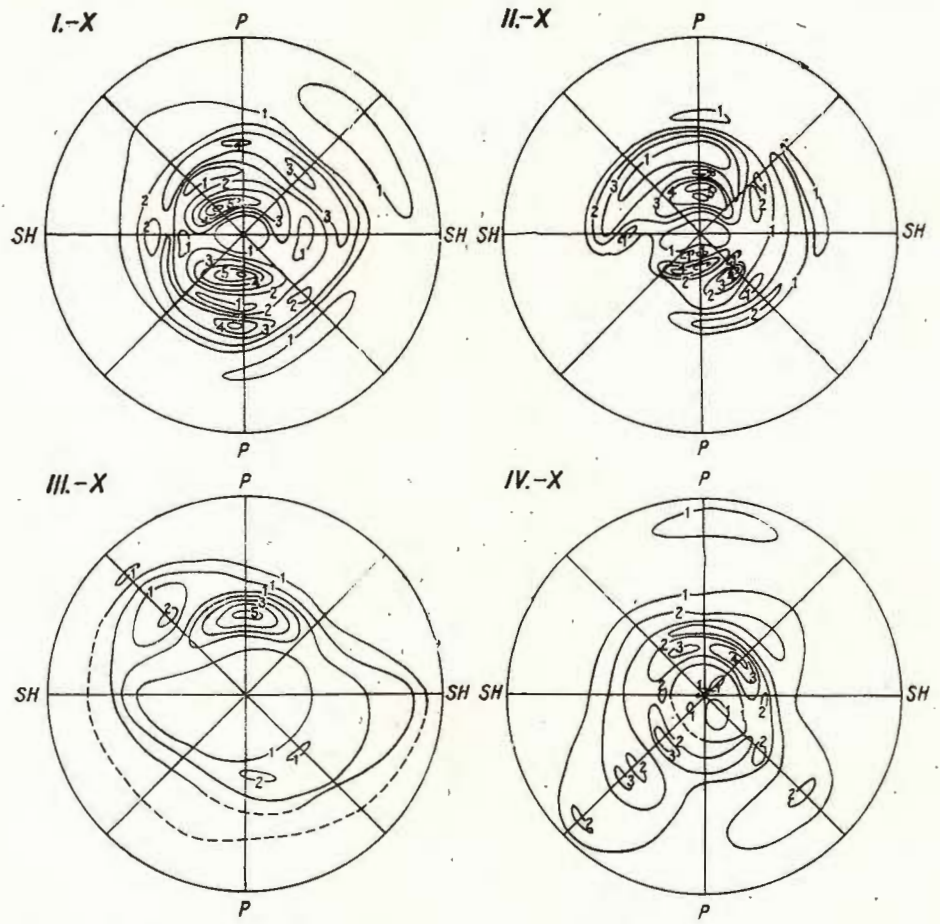

Fig. 2a. — Spectral amplitude fields of spherical (I.) and non-spherical (II.—IV.) explosive sources.

nity of a spherical explosive source [2,3]. The position of the first spectral maximum, which is at the same time the most intensive one, gives the values of the predominant frequencies of individual wave components. The predominant frequency of P waves ranges within the limits from

[2] Schenk V. Stress waves and particle velocities produced by spherical explosive source in loess. 1972. *Trav. Inst. Géophys. Acad. Tchécosl. Sci., Geofis. sbornik*, 376, Academia, Praha (in press).

[3] Schenk V. Stress waves and particle velocities produced by spherical explosive source in limestone. 1972. *Trav. Inst. Géophys. Acad. Tchécosl. Sci., Geofis. sbornik*, 378, Academia, Praha (in press).

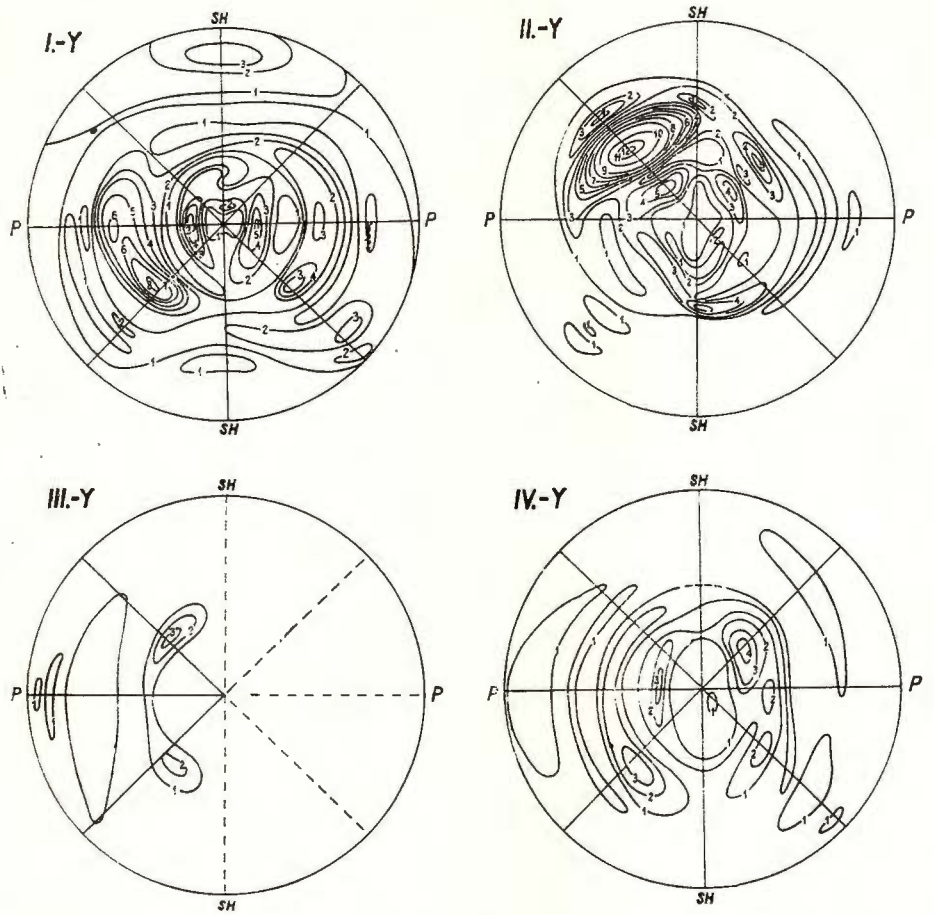

Fig 2b.

16 to 19 c/s, while the predominant frequency of *SV* waves and that of *SH* waves are approximately 30% higher and can be found between 22 and 25 c/s. On comparing the amplitudes of SAFs I.—*X* and I.—*Y* it can be observed that for the same distance and in the same spectral maximum the intensity of *P* waves is two up to three times greater than that of *SH* waves. Identical relations between these frequencies and amplitudes were measured in loess and limestone [4,5,6].

[4] *Op. cit.*, p. 2.

[5] *Op. cit.*, p. 3.

[6] Schenk V. Amplitude relations of *P*, *SV* and *SH* waves in the nearest zone of spherical explosive source. 1973. Proc. 2nd Symp. Earthq. Physics, May 29—Iune 1, 1972, *Publ. Inst. Geophys. Pol. Acad. Sci.*, Warszawa (in press).

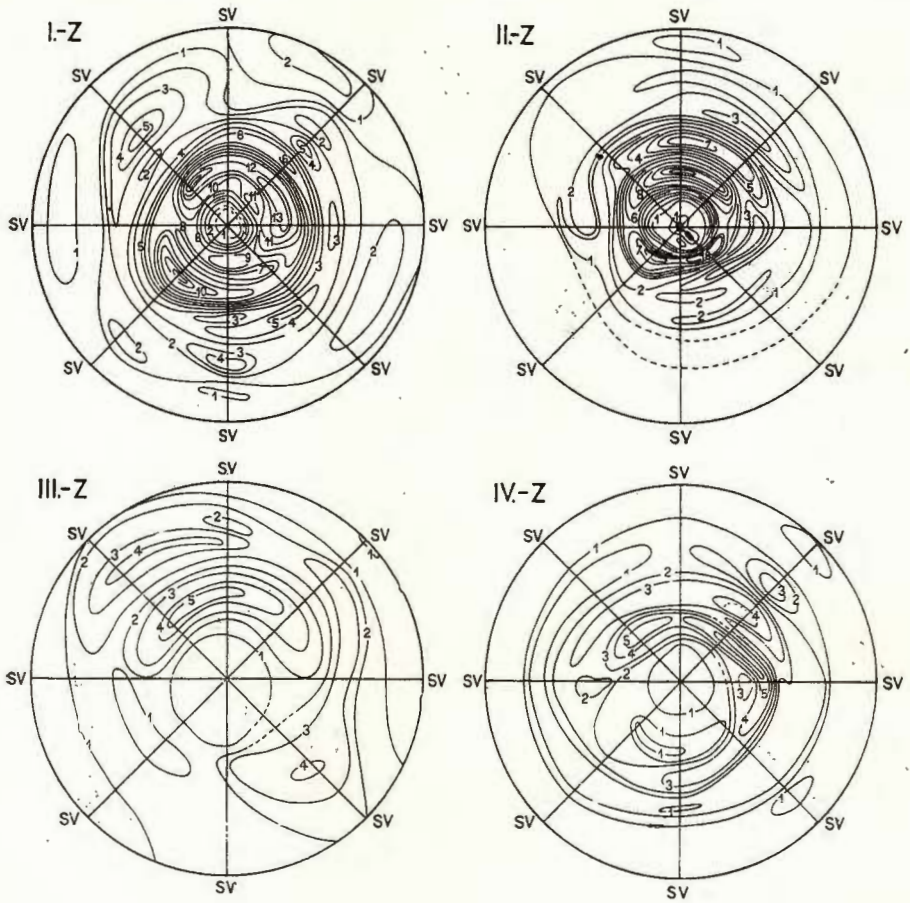

Fig. 2c.

The SAFs of experiment II. correspond to a weakly directed source and SAFs IV. to a strongly directed source. By a comparison of these SAFs with the SAFs for an undirected (spherical) source we can find some dependences between wave groups of P, SV and SH waves, which are caused by the regulation of seismic energy in the source. The position of spectral maxima of P waves and their amplitude values in SAFs of X components (fig. 2) indicates with the increasing degree of the regulation of energy there occurs not only a relative shift of energy of these waves in the direction of its concentration „12", but also a frequency shift of these maxima to higher frequencies in the given direction. This phenomenon is clearly apparent with SAFs II.$-Y$ and IV.$-Y$ (fig. 2)

where these maxima that with an undirected source originally lay on the line „3—9" are deflected in the direction towards „12".

As it was the case with SAFs I.—X and I.—Y, it can also be observed with other SAFs of components X and Y of experiments II.—IV. (fig. 2) that the amplitude of P waves is slightly higher compared with the same amplitude of SH waves. At the same time there occur changes in their position in the SAFs with the increasing degree of the regulation of the source. As a matter of fact, in SAFs X it appears that with the increasing degree of source regulation in the direction towards „12", better conditions are created for the origin of SH waves in the direction „3—9". This causes that a greater part of released energy is transferred to the creation of SH waves. It is well known that with increasing seismic energy of the source, waves of lower frequency originate. That is why in the SAF II.—X it is possible to find the position of P waves on the frequencies 20 up to 22 c/s, whereas in the SAF IV.—X. this maximum for P waves lies approximately on the frequency 30 c/s and for SH waves on the frequency 26 c/s.

Since the SAFs of the Z component (Fig. 2) express the changes of the amplitude spectra of SV waves only, we can observe in them a somewhat simpler course of isolines of spectral amplitudes than it was the case with X and Y SAFs. With an spherical source I. a greater part of energy of SV waves in concentrated into the first spectral maximum (approximately on the frequency 24 c/s). With the SAF II.—Z we can observe a partial division of this energy into the second spectral maximum (about 40—45 c/s) and its concentration in the direction towards „12", to which the source energy was regulated. The SAFs III.—Z and IV.—Z display already quite clearly this shift of energy of SV waves to higher frequencies 35—45 c/s and its concentration in the direction of the regulation of the seismic energy of the source.

CONCLUSION

The results obtained from the interpretation of SAFs of the first series of non-spherical explosive sources of seismic waves suggest that in the future it will be possible to infer not only the amount of energy in the source but also the degree of its regulation from the knowledge of the changes of dynamic parameters of individual groups of these waves.

In closing I should like to express my thanks to all the workers of the Geophysical Institute of ČSAV who contributed to a successful course

of field measurements as well as to the workers of the Institute of Applied Geophysics, Brno, under the guidance of Ing. J. Bernát, without whose help these measurements could not have been realized.

REFERENCES

Filon Z. N. G. (1928—1928) On a Quadrature Formule for Trigonometric Integral. *Proc. R. Soc. Edinb.* 49, 38, Edinburgh.

SEISMIC MODELLING

TWO-DIMENSIONAL MODELLING OF WAVE PROPAGATION IN MEDIA WITH CAVITIES[1]

BY

LOTHAR DRESEN[2]

Shallow seismic soundings of the Earth's crust in the Ruhr-district are frequently disturbed by diffraction due to natural and man-made cavities of cylindrical type, lying in a depth of some decameters.

Field investigations in this area have shown that a range of $0.003 \leqslant h \leqslant 2$ ($h : D/\lambda$; D: diameter of the cavity; $\lambda : P$-wave length) and $0.03 \leqslant l \leqslant 3$ ($l : \Delta X/X$; ΔX: distance cavity — geophone; X: distance source — cavity) should be covered by systematic measurements in order to detect these cavities and to evaluate their influence on wave-parameters.

As a thourough experimental field work in the ranges mentioned above is very complicated and due to theoretical difficulties at the time a two-dimensional model seismic investigation was carried out to find some criteria for the detection of cavities by means of interpreting the amplitudes of direct P- and diffracted $P(P)P$-waves [3].

The investigation of compressional waves diffracted by horizontal and vertical circular cylinders in an unstratified elastic and isotropic medium showed the following results:

a) The features being known in the theory of diffraction of high-frequency waves, i.e. the „illuminated zone", the „transition zone" and

[1] The complete text of this paper will be submitted for publication in *Z. Geophys.*, 39, 1973.

[2] Institut für Geophysik der Ruhr-Universität Bochum, 463 Bochum, BRD.

[3] Dresen L. Modellseismische Untersuchungen zum Problem der Ortung oberflächennaher kreiszylindrischer Hohlräume in Festgestein. 1972. Habilitationsschift, Ruhr-Universität Bochum.

the „deep shadow zone" cannot be quantitatively transferred to the investigated h- and l- ranges,

b) For values of $h < 0.2$ a method of detection using dynamic properties cannot be successfully used.

c) A significant amplitude maximum of the $P(P)P$-wave exists for $\varphi = 0°$, where φ means an angle or a polar coordinate system respectively, and the relevant abscissa $\varphi = 0°$ of a source-located coordinate system is given by the straight line through the source and the centre of the cavity. In connection with a significant amplitude minimum of the $P(P)P$-wave it is possible to detect and to locate a cylindrical cavity by means of the absolut values of these amplitudes.

d) The angle of the effective shadow boundary which indicates a reduction to 50% of the amplitude of the incident P-waves allows in connection with the shift between the effective and the geometrical shadow boundary the construction of the shape of the cavity.

The quantities discussed in *c* are especially useful for a detection in the range $0.3 \leqslant h \leqslant 1$, whereas the angle and the shift mentioned in *d* are good criteria for the range $1 \leqslant h \leqslant 4.3$.

This means that the evaluation of all three quantities enables the detection in the whole interesting range of h and l.

INTERPRETATION OF MACROSEISMIC DATA OF THE EAST ALPINE REGION WITH THE HELP OF MODEL SEISMIC EXPERIMENTS

BY

JULIUS DRIMMEL[1], GEORG GANGL[2], RUDOLF GUTDEUTSCH[2], MANFRED KOENIG[3], ERICH TRAPP[1]

It is wellknown that earthquakes of the East Alpine area are felt predominantly in the NW-direction (S u e s s, 1873; K a u t s k y, 1924; S c h w i n n e r, 1929). As an example the map of earthquake intensity of the Austrian OBDACH earthquake (October 3, 1936; 7.5 °MS) is presented here. The lines of equal intensities deviate from the shape of a circle and form more or less elliptical configurations spreading predominantly to the NW. All earthquakes of this area show this kind of anomaly. It becomes more evident, if the representation

$$\delta I = I_{obs} - \bar{I}(r)$$

is used. $\bar{I}(r)$ is the average intensity of epicentral distance r, I_{obs} is the intensity observed.

We believe that the special geological underground is responsible for the δI -anomalies and have therefore plotted the geological formations into this map (fig. 2), too. Very close to the epicentre we find as many positive as negative δI values. We interpret this behaviour in that way that the resolution of the method used (elements of area of 18.5×18.5 km^2) is not high enough to detect any anomaly. 30 km south of the epicentre

[1] Zentralanstalt für Meterologie und Geodynamik. Hohe Warte 38. A—1190 Wien, Österreich.

[2] Institut für Meteorologie und Geophysik der Universität Wien. Hohe Warte 38. A—1190 Wien, Österreich.

[3] Institut für Geophysik der Univeristät Hamburg. Binderstraße 22. D—2000 Hamburg 13, BRD.

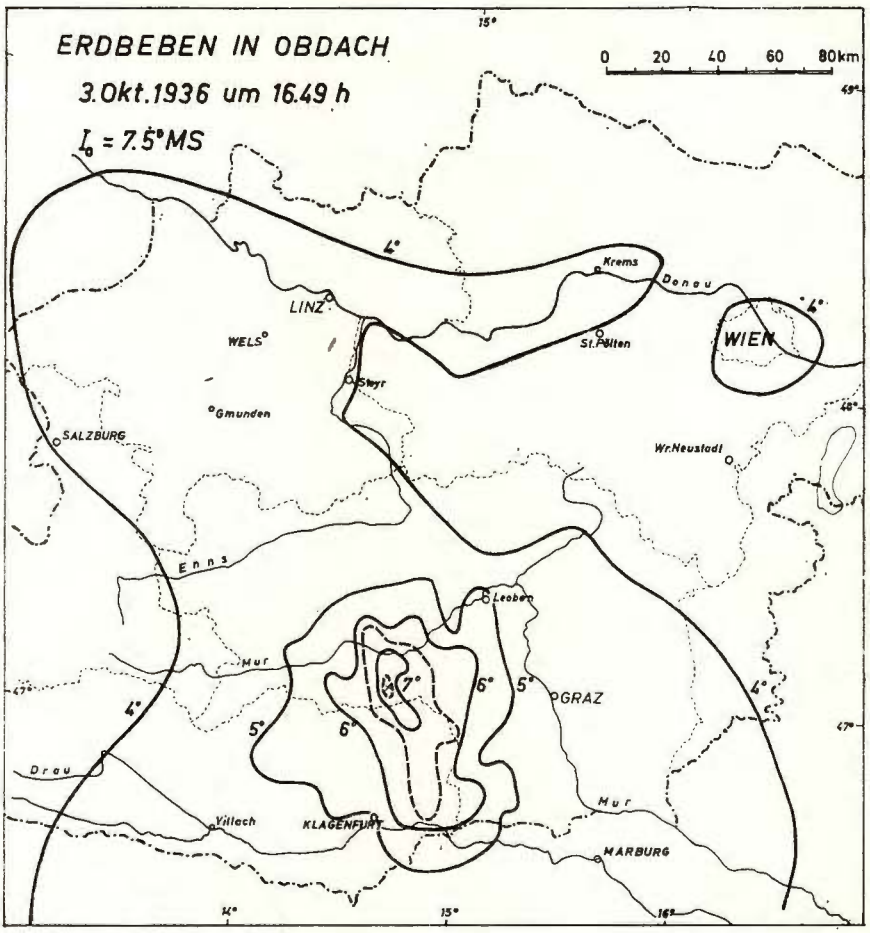

Fig. 1. — OBDACH earthquake, 1936. Isoseismals.

a zone of greater δI occurs which coincides with the Lavanttal-fault. This fault was active in recent geological times.

A strong correlation exists between the area of the Northern Calcareous Alps and negative δI values. This zone is well known as a „shadow zone" with respect to earthquakes of the Mur-Mürz-valley. Further north from this area a broad zone of positive δI occurs. It cannot be by mere chance that this area cioncides with the Molasse and Flysch zone. The Bohemian mass comes to the surface north of a line between Passau and Krems. This line forms the boundary of the shaken area.

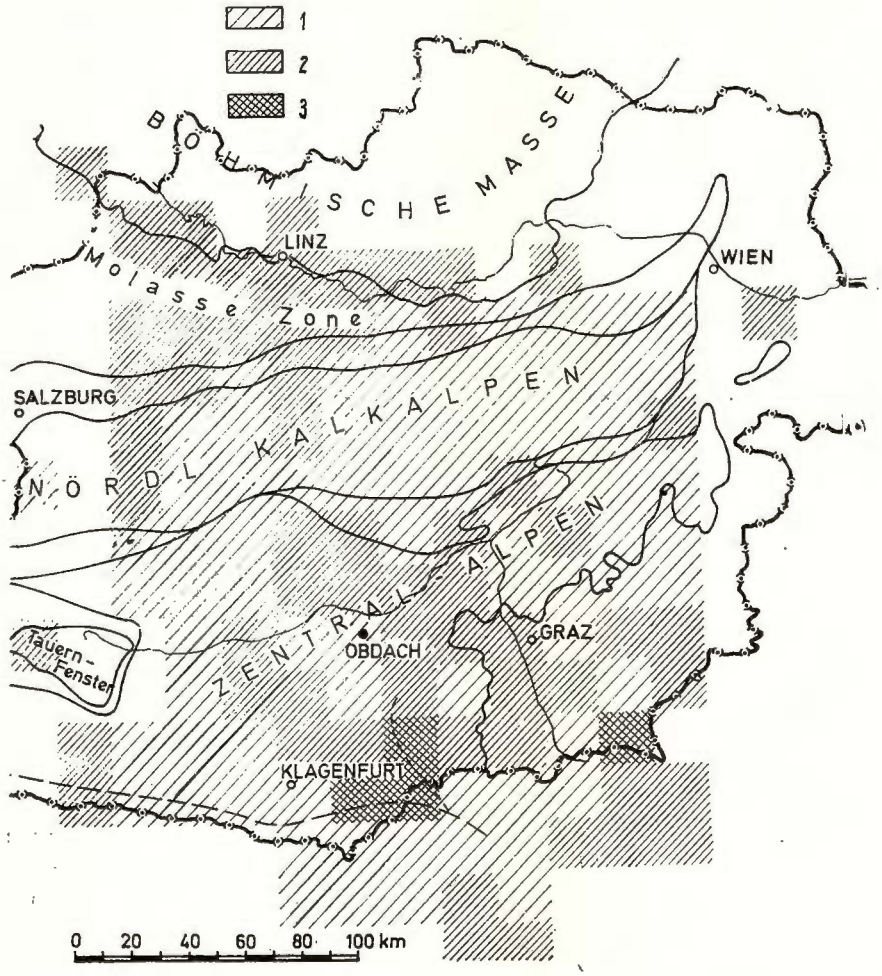

Fig. 2. — OBDACH earthquake, 1936. Map of δI-anomalies:
1, $-1 \leqslant \Delta I \leqslant -0.1$; 2, $0 \leqslant \Delta I \leqslant 0.5$; 3, $0.5 < \Delta I$.

The correlation between the relative intensity δI and the geological formation is evident. — Models of the Eastern Alps are presented by many authors. G a n g l (1969) assumed a wedge of high extinction and high P-velocity. He shows that these conditions may produce a „shadow zone" of the shape observed. This model shall be improved here, making use of more detailed geological information.

MODEL SEISMIC MEASUREMENTS (2-DIMENSIONAL MODELS)

The model of the Eastern Alps suggested by C l a r and S c h l a g e r, 1964 (C l a r, 1965) is represented here. — The Molasse and Flysch zone form layers to the south of the Dunkelsteiner Wald where the Bohemian Mass reaches the surface. This consists of rocks of high wave velocity

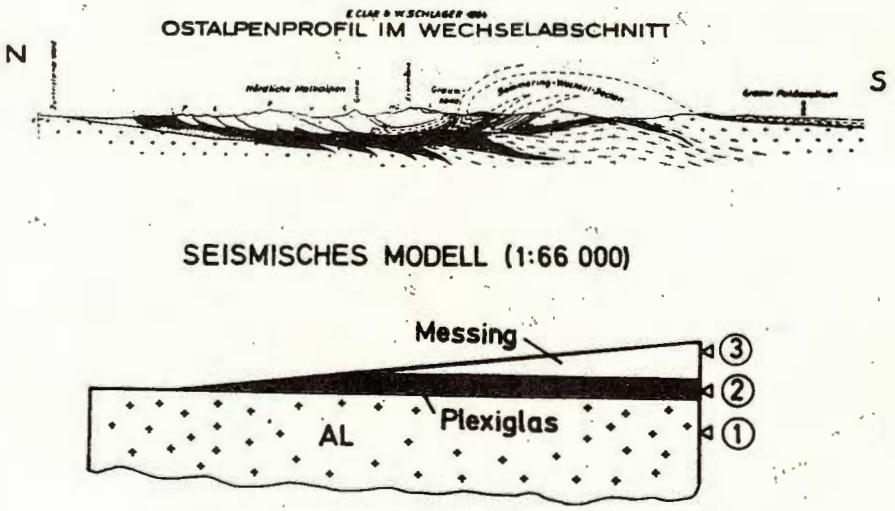

Fig. 3. — Model of the Northern Calcareous Alps.

(5000—6000 m/s) whereas the Flysch and Molasse feature less consolidated sediments with probably a low wave velocity of approximately 2000 to 4 000 m/s. The Northern Calcareous Alps overlap the Molasse from the south. They consist of solid limestone in which high wave velocities have been measured. A n g e n h e i s t e r, B ö g e l, G e b r a n d e, G i e s e, S c h m i d t-T h o m e é, Z e l l (1972) mention values up to 6800 m/s. This cross section approximately represents a wedge resting on a layer of low wave velocity, i.e. on a wave-guide. Below this layer follows material of high wave velocity. This model is used for our investigations (fig. 3). — The scale of our model is 1 : 66000 and holds approximately also for wavelengths and periods. — The physical parameters of the material are as follows :

brass : $v_p = 3750$ m/s $v_s = 2200$ m/s $\rho = 3.5$ g/cm³
epoxy : $v_p = 2400$ m/s $v_s = 1400$ m/s $\rho = 1.2$ g/cm³
aluminium : $v_p = 5500$ m/s $v_s = 3150$ m/s $\rho = 2.7$ g/cm³

In all experiments a ceramic element of 12 mm diameter and 3 mm thickness is used as source of seismic waves. This element is coupled to the model in the positions 1, 2 and 3 consecutively. *P*-waves are transmitted particularly into the normal direction of its surface. *S*-waves are transmitted predominantly at an angle of 45° to this direction. Under this restriction the results obtained from these experiments are to be discnssed but we believe that this special focal mechanism does not greatly deviate from natural conditions. Probably the focal depth strongly affects the distribution of intensities. On the other hand from the viewpoint of geotectonics it is helpful to know whether the foci are confined to certain regions of depths with a high mechanic mobility. Therefore measurements are carried out on the surface of the model while the source is located at the different depths 1, 2 and 3. — The profiles have a length of 108 cm. Both components (*H* and *V*) of the particle motion are received and plotted as a function of time. The receiving device consists of a piezoelectric element which can be turned to be sensitive of particle motion in different directions.

DISCUSSION OF RESULTS

Profile 1 (fig. 4): Waves are generated in the underground. The main part of the energy is concentrated here, *P* and *S* waves attain the surface only by double refraction via the channel. Energy is lost by this process. Therefore only small amplitudes occur on the surface close to the epicentre. Seismic energy with long periods and greater travel times appears on the seismograms. This signal is generated secondarily when a Rayleigh-wave reaches the edge of the model. Therefore it is a disturbance and not to be discussed here. At the distance of 80 cm the profile crosses the boundary from brass to epoxy. The amplitudes of the refracted *P*-wave increase here due to the missing overburden of brass. As the most important feature of the seismograms here the great amplitudes appear at greater travel-times. The seismic energy occurs with long periods obviously having been guided along the low velocity channel of the plexiglass. At greater distances the amplitudes of waves coming from the channel decrease rapidly. They form a system o interference which satisfy the new boundary conditions without the overburden of brass. Its phase velocity varies with the distance in the way K o e n i g [4], described in

[4] K o e n i g M. Das Frequenzverhalten des Rayleighwellensystems in einer keilförmigen Schicht über einem Halbraum grösserer Wellengeschwindigkeit und Dichte. 1972. Dissertation, Universität Hamburg.

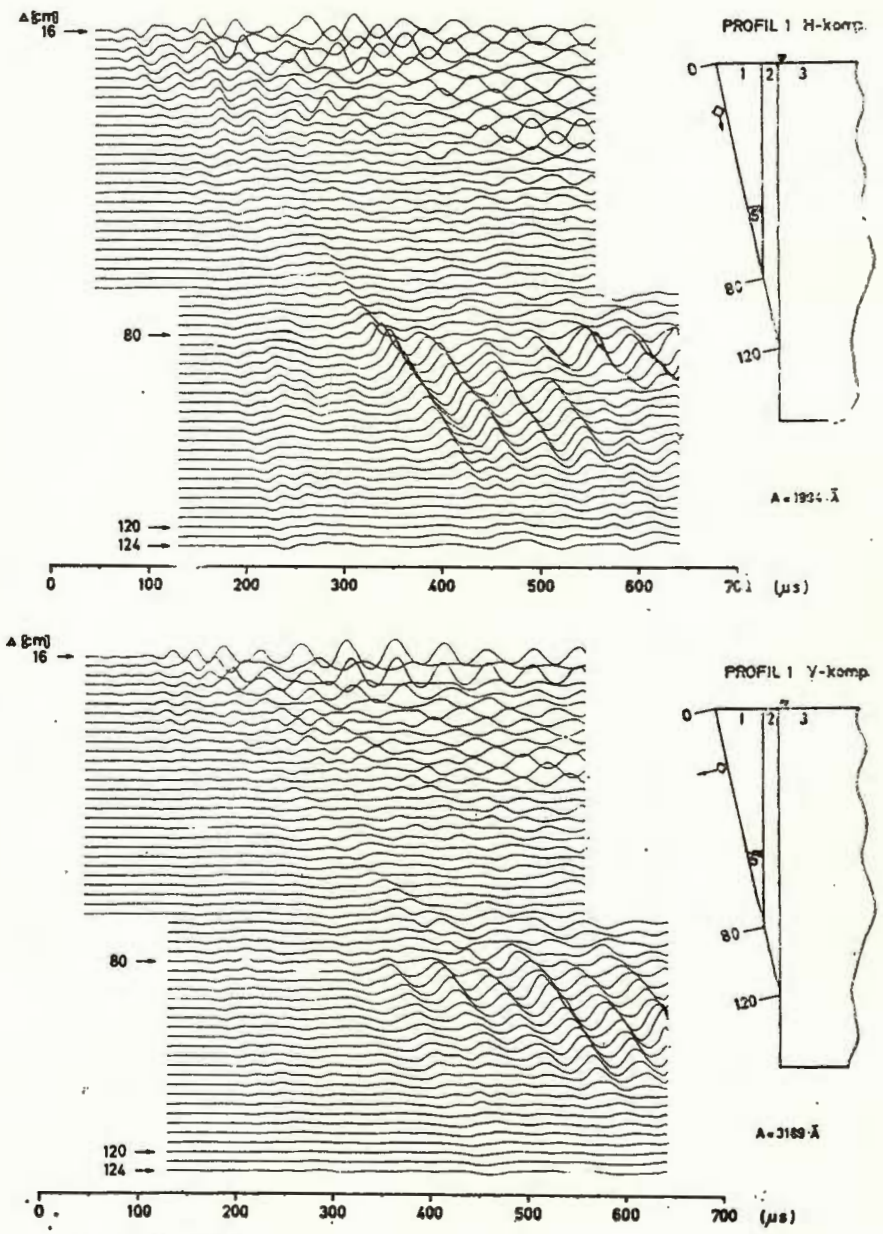

Fig. 4. — Model seismograms; waves are generated in the underground.

his thesis. The amplitude variation is a result of destructive interference and refraction of body waves into the halfspace below the wedge. At 100 cm on the wedge axis this wave disappear. Now the direct P waves play the most important part as well as a long period signal with greater travel time propagating with the velocity of Rayleigh waves.

Profile 2 (fig. 5): The seismic source generates waves which are in contrast to profile 1 predominantly confined to the low velocity channel. Strong onsets in the brass are observed. They can easily be interpreted as refracted P- and S-waves as well as multiple reflections of both. They form many onsets immediately behind the first onset. At a greater distance they build up a new interference system of longitudinal particle motion and long period. Finally this interference system forms the first signal of the seismogram and travels with the velocity of 3600 m/s. This wave apparently is confined to the brass wedge, its amplitude increases with increasing distance. We believe that this wave is similar to the L wave observed by Gutdeutsch (1968) in a solid wedge with free boundaries. In the present paper this wave shall be called L'-wave. The L'-wave is overtaken by the refracted P-wave of the underground at approximately 60 cm. At distances greater than 80 cm the wavegroup coming from the channel show great amplitudes. The phase velocity of the wavegroup measured inside the channel ranges between 2900 and 3600 m/s. According to this high phase velocity it must be expected that this wave radiates shear waves into the underground and the overburden and is therefore subject to rapid extinction. Probably the L'-wave also plays a role in the construction of the channel wave. Between 80 and 120 cm no striking difference is found between profile 2 and profile 1.

Profile 3 (fig. 6): The waves are generated very near the surface. The exitation of short periods is the most striking contrast to the seismograms of profiles 1 and 2. The Rayleigh wave generated at the source posesses a broad spectrum of frequencies. At distances greater than 30 cm this Rayleigh wave is deformed in a very impressive way by a normal dispersion. The signal is approximately sinusoidal where the period increases with time very similar to the B-wave after Gutdeutsch (1968); the main particle motion is transverse. The B-wave is a mechanism occuring on a wedge with free boundaries corresponding to the flexural wave on plates. In this experiment the wedge is coupled onesided to epoxy so this wave must differ from the B-wave. In this paper it is named B'-wave. — The L'-wave is generated strongly on this profile. Its amplitude increases upon approaching the wedge axis. There it interferes

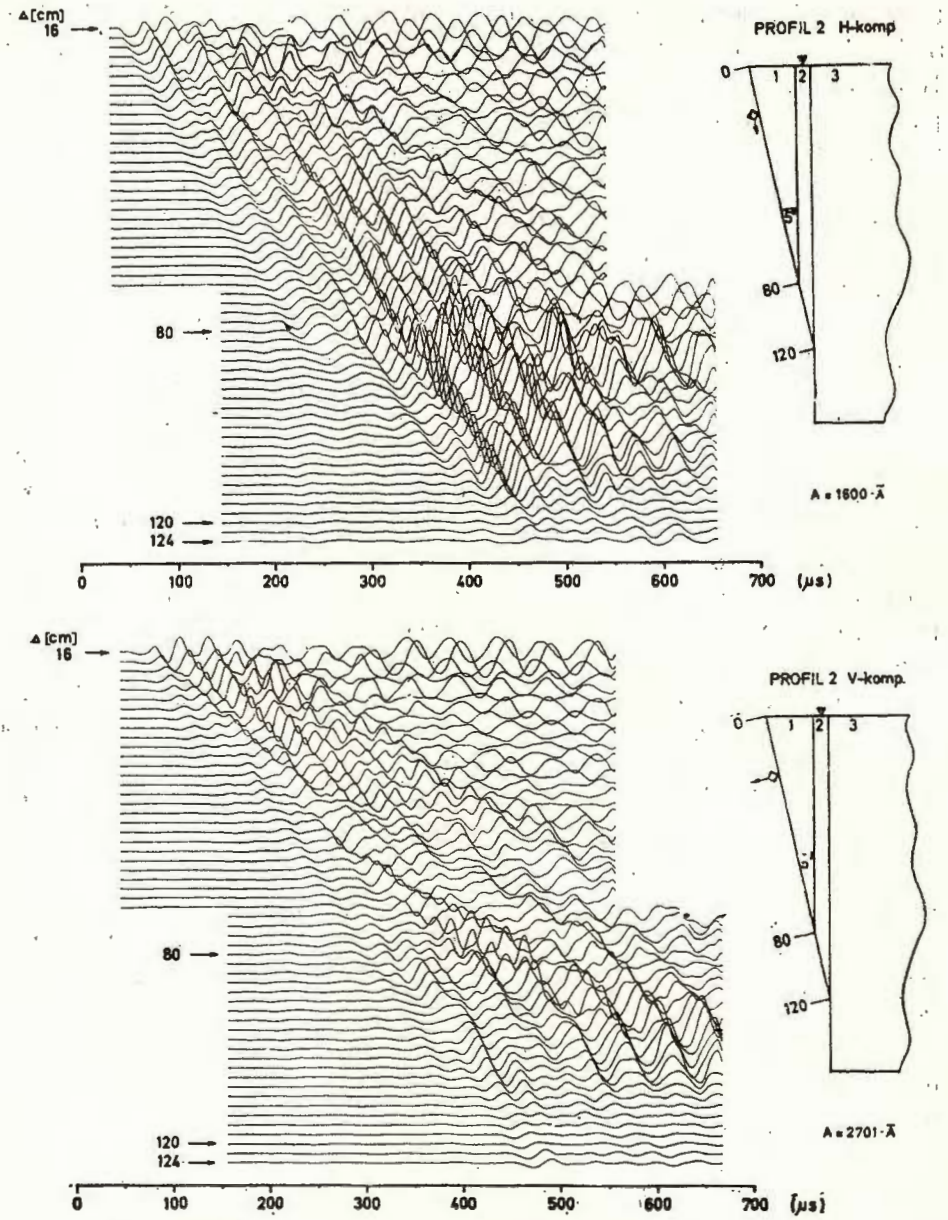

Fig. 5. — Model seismograms; waves are generated in the „channel".

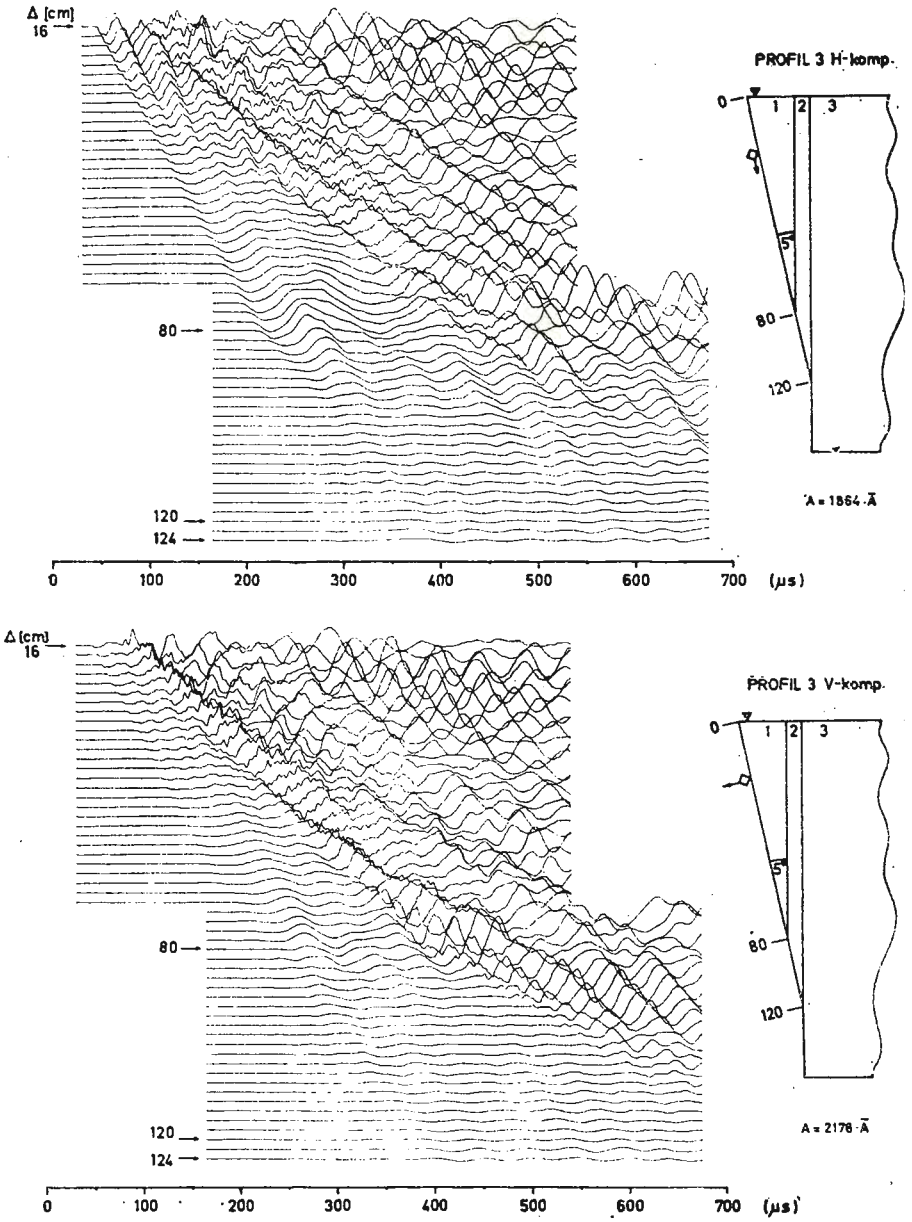

Fig. 6. — Model seismograms; waves are generated near the surface.

with the reflected wave of the same type. L'- and B'-waves give the main contribution to the seismic energy shown in the seismograms. Both waves reach the corner of the brass wedge which works as a source of Huygens' elementary waves. These elementary waves propagate into the low velocity channel. They can be observed at distances greater than 80 cm. Channel waves of the kind discussed before (profile 1 and 2) obviously are not generated in this experiment. It is interesting to see that the B'-wave generates a strong secondary wave in the channel. This wave propagates with normal dispersion and disappears close to 110 cm.

SUMMARY OF RESULTS

On the seismic model investigated here four types of waves play an important part. The first is the channel wave insofar as the main part of its energy is confined to the low velocity channel. The channel wave radiates body waves into the overburden and the underground. Therefore its amplitude must decrease by extinction. Its phase velocity depends on the period. The second mechanism is a dispersive wave generated in the region where the low velocity channel is cut offby the surface. This wave also propagates with dispersion. Shape and amplitude of this wave depend on how it is generated. If the seismic source is found in the underground or the low velocity channel the wave discussed here is generated by the channel wave. If the source is on the surface the wave is generated by waves travelling in the overburden. The third is the L'-wave similar to the L-wave in a wedge with free boundaries. The fourth one is the B'-wave similar to the B-wave which is a kind of flexural wave in a wedge with free boundaries. It depends on the kind of generation which of these mechanisms predominate.

ANALYSIS OF MACROSEISMIC DATA

In order to compare the model seismic results shown here with the macroseismic data from the East Alpine region it is necessary to transfer the model seismic data into macroseismic data. — We used the empirical relation between the earthquake intensity $\bar{I}$ and maximum acceleration B_{max} of the underground

$$\bar{I} = 3 \log (B_{max}) + \text{const.}$$

The maximum amplitude b_{max} are taken from every profile and every seismogram. The expression

$$I = 3 \log (b_{max}) + \text{const.}$$

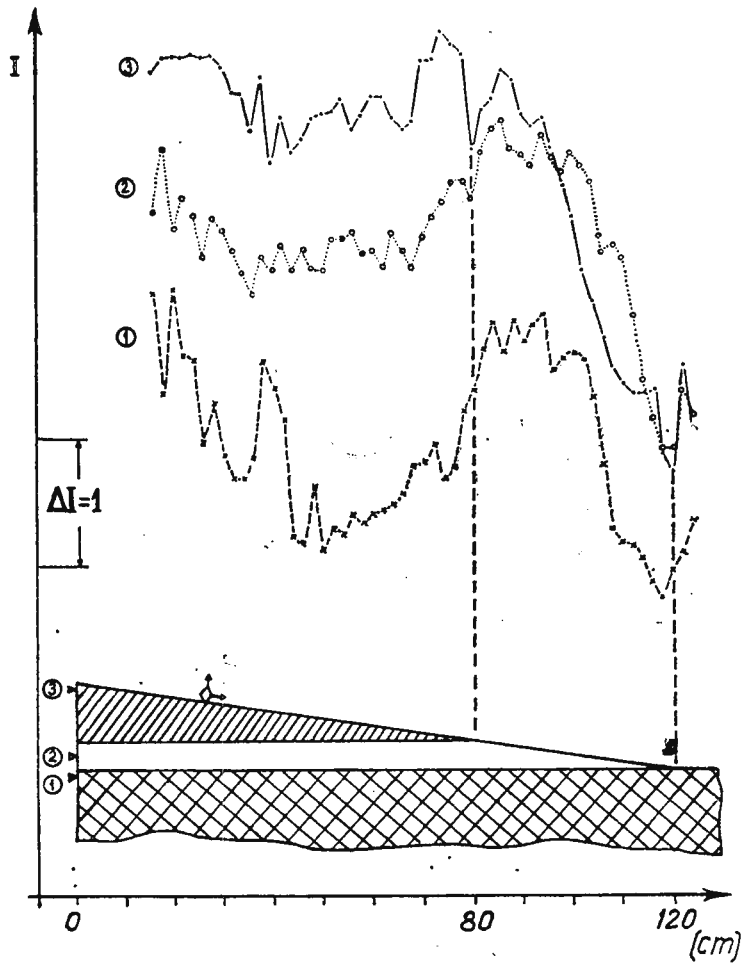

Fig. 7. — Relative variations of the earthquake intensity derived from model seismic experiments.

is comparable to the earthquake intensity if the main frequency does not change with distance. This conditions is approximately satisfied. Relative variations of δI may therefore be regarded as variations of earthquake intensity ($\delta \bar{I}$). We believe that the magnitude of δI in the model experiments are sufficiently representative, though we know that the measure-

ments are taken from a 2-dimensional and not from a 3-dimensional model. — A plot of δI is presented in figure 7. The curves taken from the profiles 1, 2 and 3 all decrease with distance close to the epicentre. The intensity at the different profiles decreases in a different way with distance. From this it can be deduced that the computation of focal depth using a macroseismic method known from literature can yield doubtful results. The curves increase again when approaching the boundary at 80 cm. In the case of a deep focus the maximum can be found in the centre between 80 and 100 cm. At greater distances the intensity decreases rapidly and attains a minimum at 120 cm. When the focal depth is lower the maximum is found at a smaller distance. It is remarkable that the intensity in the case of profile 1 at great distances (about 120 cm) is of the same order of magnitude than at the distance of 60 cm. Evidently the energy is guided predominantly into the direction of the wedge corner. This is not true in the case of small focal depths. Possibly this is an explanation for the macroseismic anomaly of the East Alpine earthquakes. The shadow zone in the area of the Northern Calcareous Alps also can be explained to be a consequence of the underlaying low velocity channel. The model seismic experiments indicate that the focal depths must be great. Probably the main part of the earthquakes occurs in the crystalline basement below the low velocity layer.

REFERENCES

Angenheister G., Bögel H., Gebrande H., Giese P., Schmidt-Thomeé P., Zell W. (1972). Recent investigations of surficial and deeper crustal structures of the Eastern and Southern Alps. *Geol. Rundschau* 61, Schweitzerbarth, Stuttgart.

Clar E. (1965) Zum Bewegungsbild des Gebirgsbaues der Ostalpen. *Verh. Geol. B. A.*, Sonderheft G, Geolog. Bundesanstalt, Wien.

Gangl G. (1969) Ein Beitrag zur Seismizität des Alpenostrandes (Erdbeben in Niederösterreich). *Mitt. d. Erdb.-Komm.*, N.F. 68, Österr. Akad. d. Wiss., math-naturw. Klasse, Springer, Wien.

Gutdeutsch R. (1968) Rayleighwellen am Keil mit freien Grenzflächen. *Hamburger Geophysikal. Einzelschriften.* 10, Cram, de Gruyter u. Co., Hamburg.

Kautsky F. (1924) Die Erdbeben des östlichen Teiles der Ostalpen, ihre Beziehungen zur Tektonik und zu den Schwereanomalien. *Mitt. d. Erdb.-Komm.*, N.F. 58, Österr. Akad. d. Wiss., math-naturw. Klasse. Hölder Pichler-Tempsky, Wien.

Schwinner R. (1929) Zur Deutung der Transversalbeben in den nord-östlichen Kalkalpen. *Zeitschr. f. Geoph.*, V. Friedr. Vieweg u. Sohn, Braunschweig.

ON THE CONVERGENCE OF SOME EXPANSIONS OF SYNTHETIC SEISMOGRAMS USING THE EIKONAL METHOD

BY

EMILE OKAL [1]

Abstract

In this paper, we study the convergence of an expansion of a synthetic seismogram by means of a comparison with the exact solutions, computed through the Cagniard method. We prove that the Eikonal method yields a divergent series for sufficiently large $(t - \tau)$.

The Eikonal method for synthetic seismograms, as it is described in litterature (P e t r a s h e r, 1959) is based upon a number of fundamental hypothesis :

1) The seismic displacement vector $\vec{U}(x, y, z ; t)$ is searched as an expansion :

$$\vec{U}(x,y,z ; t) = \sum_{k=0}^{\infty} f_k(t - \tau(x, y , z) \cdot \vec{W}_k (x,y,z)$$

2) Functions $\vec{W}_k$ (x, y, z) and (x, u, z) are independent from time t and from the excitation function f_0, as long as the symmetry of the seismic source is kept.

3) Functions f_k are subsequent primitives of the excitation function f_0 :

$$f'_k = f_{k-1}.$$

[1] Groupe de Sismologie, Laboratoire de Physique de l'École Normale Supérieure, 24 rue Lhomond. 75231 Paris, France.

These hypothesis enable to separate excitation (f) and propagation ($\vec{W}$, τ).

The problem of the convergence of expansion (1) is very little discussed in litterature. Babich [2] proved that it is always possible to find times t when it converges.

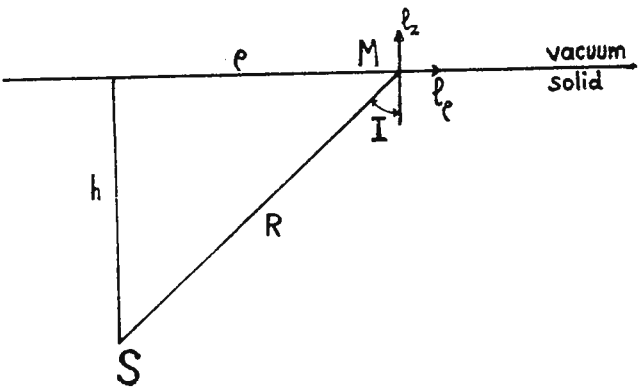

Fig. 1. — Position of geometrical parameters.

As a matter of fact, it is usually very difficult to compute $\vec{W}_2$ or $\vec{W}_3$, and impossible to give a formal expression for $\vec{W}_k$.

Therefore, in order to study the convergence of expansion (1), we will use a particular situation, when the exact solution for the seismic displacement can be computed.

For example, let us consider (fig. 1) a semi-infinite medium under a vacuum with a spherical source S at depth h.

Let us then take an excitation function f_0 in the following way :

$$f_0(\xi) = 1 \text{ for } 0 < \xi < T,\ f_0(\xi) = 0 \text{ elsewhere.}$$

Then it is easy to realise that expansion (1) becomes an expansion into powers of the quantity $(t - R/\Omega_1)$. Here Ω_1 is the P-wave velocity and $R = SM$.

In this case, the C a g n i a r d method (1939) may be used to compute the exact displacement vector at any point. We will study the lon-

[2] Personal communication from Dr. Červený.

gitudinal component e_ρ of the displacement vector of point M located on the surface. According to Cagniard, it is found to be :

$$e_\rho = A f_0 (t - R/\Omega_1) - B \int_{R/\Omega_1}^{t} S_\rho (v)\, f_0(t - v) \cdot dv$$

A and B are two constants depending only on the position of point M ; $\rho = R.\sin I$.

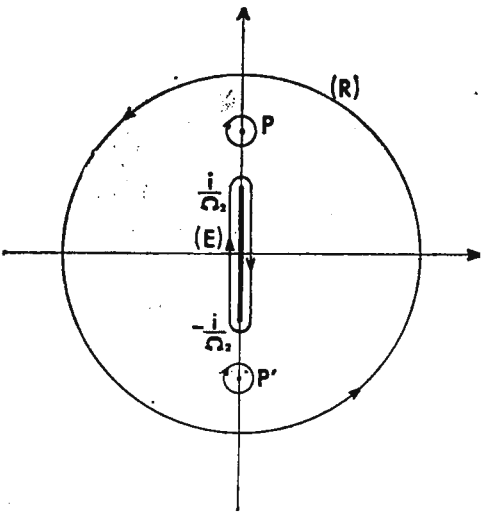

Fig. 2. — Path of integration in the plane of the complex variable u.

$$\text{Then, } S_\rho (v) = C. \int \frac{b \cdot u^3 \cdot du}{D(u) \cdot \{u^2\rho^2 + (v - ah)^2\}^{3/2}},$$

$$\text{with : } \quad a = \sqrt{u^2 + \frac{1}{\Omega_1^2}}\,; \qquad b = \sqrt{u^2 + \frac{1}{\Omega_2^2}}\,;$$

$$D(u) = \left(u^2 + \frac{1}{2\Omega_2^2} \right)^2 - abu^2.$$

The integral in this expression is taken along a contour which is the union of :

1) a large ring of great radius

2) two small rings around the poles of D

3) a contour surrounding a cut from $-\frac{i}{\Omega_2}$ to $+\frac{i}{\Omega_2}$, necessary because of the various determinations of square roots.

This yields three terms :

1) The first term, S_ρ^1 is independent from v and its contribution to e_ρ is a single term, proportional to f_1.

2) The second term, which represents the Rayleigh wave is obtained by a calculus of residues and yields :

$$S_\rho^2 = K \cdot Im\{(\tau^2 - m^2 + cos^2 I + 2i\,\tau \cos I \sqrt{m^2 - 1})^{-3/2}\} = Im(G).$$

Here $\tau = \Omega_1\, v/R$ and m is a numerical constant, which is the ratio of the P-wave velocity to the Rayleigh wave velocity. Its values is about 1.883..., if the two Lamé coefficients of the medium are equal. G is an algebraic function which can obviously be expanded into powers of $x = \tau - 1$.

The radius of convergence of this expansion is the modulus $\mathfrak{R}$ of the pole of G of smallest modulus.

$$\text{This pole is } x_0 = m.\ \sin I - 1 - i.\ \cos I \sqrt{m^2 - 1}.$$

Then, one may easily show[3] that $S_\rho^2\,(v)$ has the same radius of convergence as G.

3) Then, if we look at S_ρ^3, we can see that it is not infinite when x gœs to x_0.

In fact, S_ρ^3 can only go to infinity when the function under the integral sign gœs to infinity for one point of the cut. But $D(u)$ has its zeros outside the cut and, further, $\rho^2 u^2 + (v - ah)^2$ has only $u^2 = 1/\Omega_R^2$ as a root, when $c = v_0$.

As it may be shown[4] that S_ρ^3 is actually expandable into powers of $(x - 1)$ with a non-zero radius of convergence, it is possible to see that $S_\rho^2 + S_\rho^3$ is expandable too, its radius of convergence being not greater than $\mathfrak{R}$.

One can show [5,6] that the vertical displacement e_z has the same radius of convergence as e_ρ. These results may be extended to other functions f_0[7].

---

[3] Okal E. Problèmes posés par l'application de la théorie de l'Eikonal à la Sismologie. 1972. Thèse de 3ème cycle, Paris.

[4] *Op. cit.*, p. 3.

[5] Idem.

[2] Mechler P., Okal E. To be published in B.S.S.A.

[7] *Op. cit.*, p. 3.

In conclusion, we have proved that the expansion (1) certainly diverges for sufficiently large $(t - \tau)$ (O k a l, 1972) provided T is large enough.

Acknowledgement

The author is pleased to acknowledge a valuable discussion with Dr. Č e r v e n ý on the subject of this paper.

REFERENCES

C a g n i a r d L. (1939) Réflexion et réfraction des ondes sismiques progressives. Ed. Gauthier-Villars, Paris.

O k a l E. (1972) *C. R. Acad. Sci.*, B 275, Paris.

P e t r a s h e n G. I. (1959) Problems in the dynamic theory of the propagation of seismic waves. III, Leningrad University Press.

HIGH PRESSURE LABORATORY INVESTIGATIONS

THE EARTH'S CRUST: SEISMIC MODELS FROM DSS AND LABORATORY MEASUREMENTS

BY

M. P. VOLAROVICH, E. I. BAYUK, V. P. VALUS, I. N. GALKIN [1]

Very important for constructing the physical model of the Earth and understanding the processes of the formation and development of its deep structure is a knowledge of how the velocities of seismic waves behave as a function of depth. There has lately been some progress in the problem of learning the vertical velocity distribution in the Earth, owing to the advent of the methods of computational seismology, and to devising new algorithms and programs for solving the inverse problem of seismology by means of the trial-and-error method. The method consists essentially in comparing observed wave characteristics with those computed for a number of alternative models; those models are then picked out which do not differ from the observations by more than the observational error (A z b e l et al., 1966).

The experience gained so far in studying the Earth's velocity distribution leads to the conclusion that the solution always turns out to be non-unique : the observations agree with a whole set of physically different models which are characterized by a certain of variation in the velocity parameters. The non-uniqueness can be weakened by increasing the precision and detailedness of the experiment, and by making use of a large number of characteristics (both kinematic and dynamic ones) of primary and secondary waves.

[1] O. Yu. Schmidt Inst. Phys. of the Earth, Acad. Sci. of the USSR, B. Cruzinskaya 10, Moscow 123242, USSR.

The results of seismic investigations are represented by a strip in the plane „velocity-depth", a strip that symbolizes the discriminative power of the seismic method. The strip can be made thinner, and the velocity distribution be interpreted in physical terms only on the basis of a joint analysis of seismic and other geophysical data.

The present paper reports the results of comparing seismic data about the velocity distribution of the crust with direct measurements of the velocities of elastic waves in various rock samples under pressure. In contrast to similar previous studies, seismic results are used that have been obtained by an objective method, and which describe the whole range of possible solutions, together with mathematically treated results of laboratory data.

VELOCITY MODELS FOR CRUSTS OF VARIOUS TYPES

The structure of the crust has been studied from the data supplied by seismology and deep seismic sounding by means of the trial-and-error method with the help of a computer program (V a l u s, 1968), for regions with different types of crust structure: continental mountainous type (Tyen Shan, the profile Andizhan-Dushanbe), continental transition type (the island of Sakhalin, the pass of Tatarsky), oceanic type (the Pacific). The computations have been done for a thick-layer, local-laterally homogeneous and isotropic structure of the crust according to the formulas of the null approximation in the ray method of the dynamic theory of wave propagation (P e t r a s h e n et al., 1959). 600—900 theoretical models have been treated. The number of models that agree with the observations are [2] (V a l u s et al., 1966, 1971; G a l k i n, 1972): 46 for Tyen Shan (the standard deviation of the P-wave travel times being 1 s, that for PP-1.5 s, and that for the phase velocity of Love waves 0.05 km/s), 27 for Sakhalin (the accuracy of the readings of the first P being 0.2 s, of the amplitudes — 0.2 of a logarithm unity), and 14 for the Pacific (the error being 0.2—0.3 s and 0.3 of a logarithm unity respectively). Those which have „passed" are shown in figure 1. The arabic figures indicate the uncertainty of the velocity, of its gradient, and of interface depths.

Non-uniqueness in the velocity distribution has been found to exist for all the three types of crust structure. It implies an uncertainty in the

[2] V a l u s V. P., V e i t s m a n P.S., G a l k i n I. N., L e v s h i n A. L. On non-uniqueness of the velocity cross-section of the crust in DSS. 1969. Tezisy dokladov 2 vsesoyuznogo soveshaniya po vrzyvnoi seismologii, VNII Geofizika, Alma-Ata (Rotoprint).

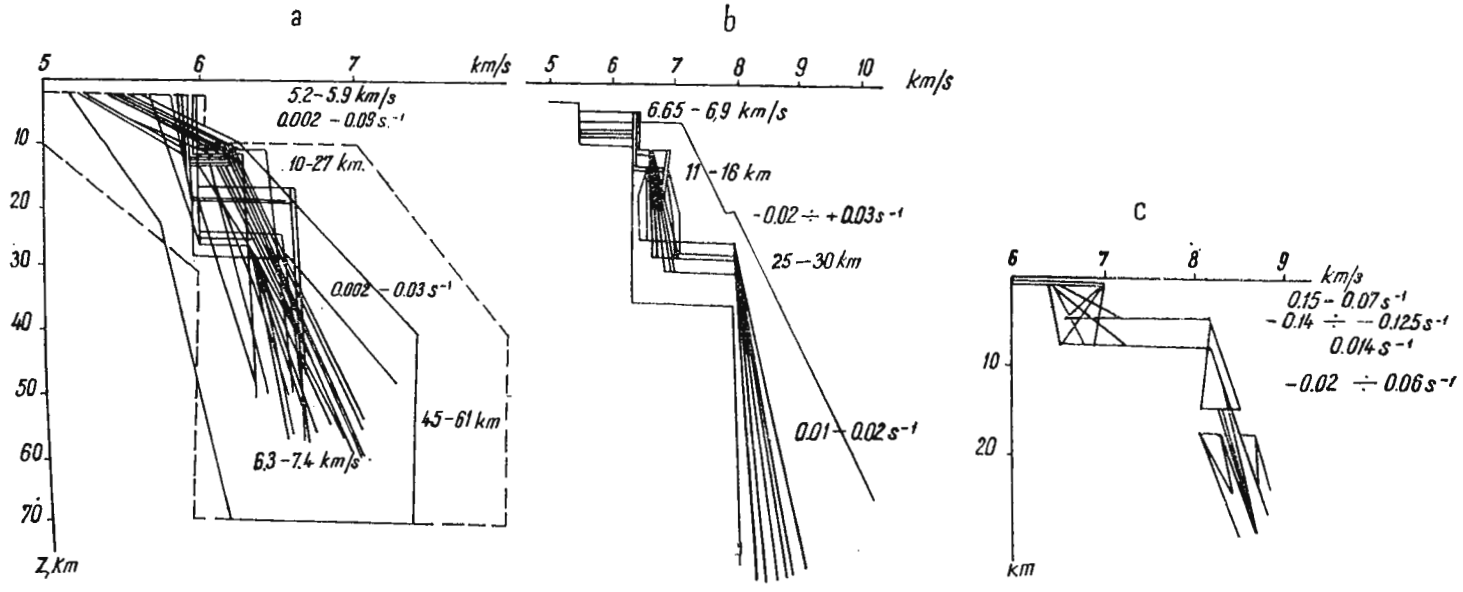

Fig. 1. — Velocity cross-sections of the Earth's crust, determined by the trial-and-error method on an electronic computer for the crust of the continental mountainous type (Tyen Shan) (a), continental transition type (Sakhalin) (b), oceanic type (the Pacific) (c). The Arabic figures show the uncertainty range of the parameters corresponding to the cross-sections.

parameters as well as a basic difference in the models : for Tyen Shan there are discontinuities of the first and the second kind, for the transition zone between Asia and the Pacific — a low velocity channel and a positive velocity gradient in the crust. On the whole, the velocity strips show an essential difference to exist in the three regions studied. There is a decrease in crust thickness and an increase in the velocities when going from the continent towards the ocean.

VELOCITIES IN ROCK SAMPLES UNDER PRESSURE

P-wave velocities in rock samples have been determined at hydrostatic pressures up to 4 kb, and at quasihydrostatic ones — up to 20 kb at room temperature. We studied specimens of igneous rocks from various continental regions of the Soviet Union : the Kola peninsula, the North Caucasus, Central Kazakhstan, Sakhalin, and some other (Volarovich, 1964; Afanasyev et al., 1965; Bayuk et al., 1971; Volarovich et al., 1971, 1970). The experimental data on *P*-wave velocities obtained for more than 100 granite samples, 75 basic rocks (gabbro), and 80 ultrabasic rocks have been used to determine velocity histograms. Then the normal probability law has been fitted to the histograms, with the probability density given by

$$f(x) = \frac{1}{\sigma\sqrt{2\pi}} e^{-\frac{(x-\bar{v})^2}{2\sigma^2}}$$

As is known, the parameters of the normal law are : $\bar{v}$- the mean value, and σ the standard deviation.

The probability density graphs, or velocity distributions for granites, gabbro, and ultrabasic rocks are shown in figure 2 at a pressure of 1 atm, as well as at those of 1, 4 and 15 kb. As the pressure increases, the scatter in the velocities decreases, and accordingly the standard deviation σ decreases. Further, the velocity distribution systematically moves towards higher velocities, since the mean value of the velocity increases. The parameters of the normal distribution law at various pressures are given in the table.

The mean velocities have been calculated also for some rock types of Central Kazakhstan (Volarovich et al., 1971) : granites, gabbro and schists. The data here are more scanty, so that the parameters of the

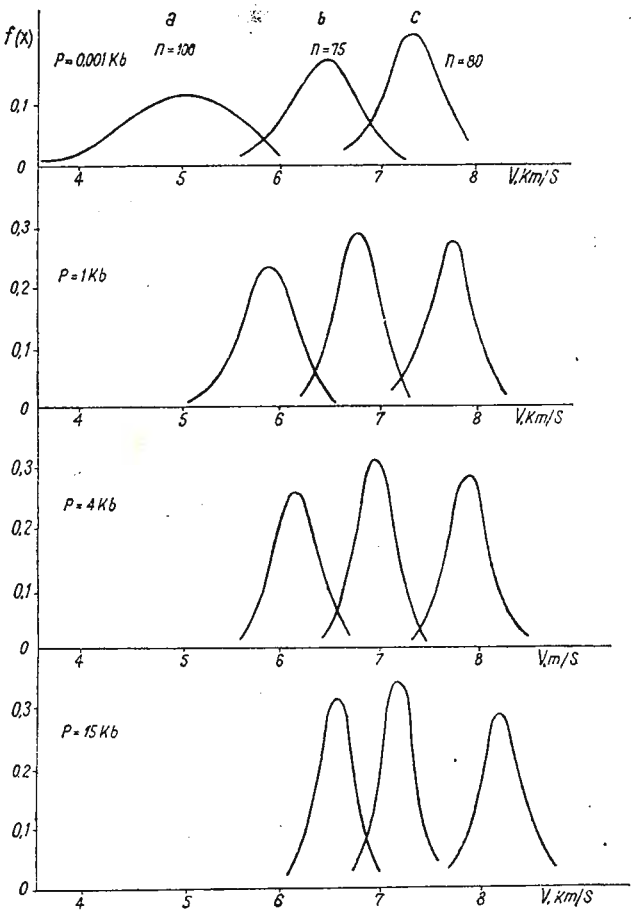

Fig. 2. — Graphs of the probability density of the P-wave velocity for granites (a), gabbro (b), and ultrabasic rocks (c) at various pressures.

TABLE 1

The parameters of the normal distribution law for igneous rocks.

	1 atm	1 kb	4 kb	15 kb
		granites		
$\overline{V}$	5.06	5.87	6.17	6.56
σ	0.33	0.26	0.23	0.20
		basic rocks		
$\overline{V}$	6.42	6.78	6.98	7.17
σ	0.35	0.20	0.18	0.17
		ultrabasic rocks		
$\overline{V}$	7.31	7.70	7.90	8.20
σ	0.28	0.23	0.23	0.24

normal distribution law are less accurate. The same holds for the Sakhalin basalts (Volarovich et al., 1970; Skorikova, 1970).

For the oceanic crust we compared the data of seismology and deep seismic sounding with laboratory determinations of velocities in rocks from the Indian (Bayuk et al. 1972).

The results of the comparison are shown in figures 3, 4, 5. Shaded are the velocity strips from seismic data, lines with various signs — the curves of mean velocities in various samples as functions of pressure (depth), the velocity range for 70% for the samples is given in horizontal shading.

The velocity cross-section for Tyen Shan down to depths of 30—40 km is similar to the regions where the curves for granite are situated. The width of the region is such that the deviation of velocity values from the mean is equal to $\pm \sigma$. In this way an explanation can be found for the variant with no velocity discontinuity in the crust. Just above the Moho seismic velocities reach values characteristic for gabbro. It should be noted that the curves of the mean velocities as functions of pressure for granites and gabbro are almost identical for the whole set of the continental samples and the samples from Kazakhstan. The differ, however, for ultrabasic rocks (the mean velocity is lower for Kazakhstan). The seismic velocities in the upper mantle under Tyen Shan are situated in the 80% strip between the two curves of the mean velocities.

The four-layer seismic model for the consolidated crust and upper mantle under Sakhalin finds a clear lithological interpretation when we compare it with laboratory data: the velocity in the upper layer of the crust falls into the left (low-velocity) part of the 80% values of „granite" velocities and the velocities in the Sakhalin basalt. The velocities in the intermediate layer are identical with those for schists, and the velocities in the lower layer approximate the velocities for gabbro. The curve of the mean velocity for ultrabasic rocks falls into the centre of the velocity strip for the upper mantle (fig. 4).

An analysis of the velocity models for ocean is more difficult, on account of sparsity of rock samples (especially the mantle ones). We have plotted a few curves in figure 5 for basalts from the rift zone of the Indian ocean. If we compare them with the data averaged over the whole Earth it is found that the oceanic crust has the velocities of gabbro, and

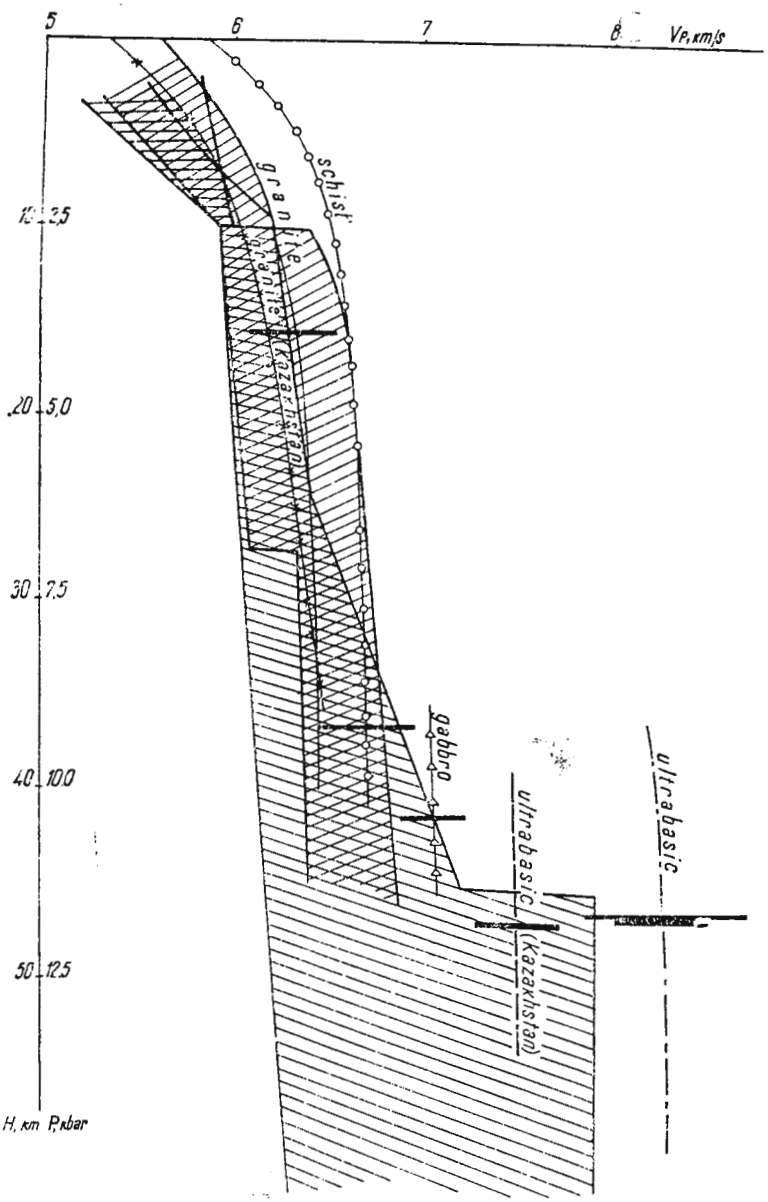

Fig. 3. — The strip of seismic velocities (shaded) and the results of laboratory measurements; the vertical lines represent the mean velocities as functions of pressure (depth), the horizontal ones are strips ($\pm\sigma$) for the crust of the continental mountainous type (Tyen Shan).

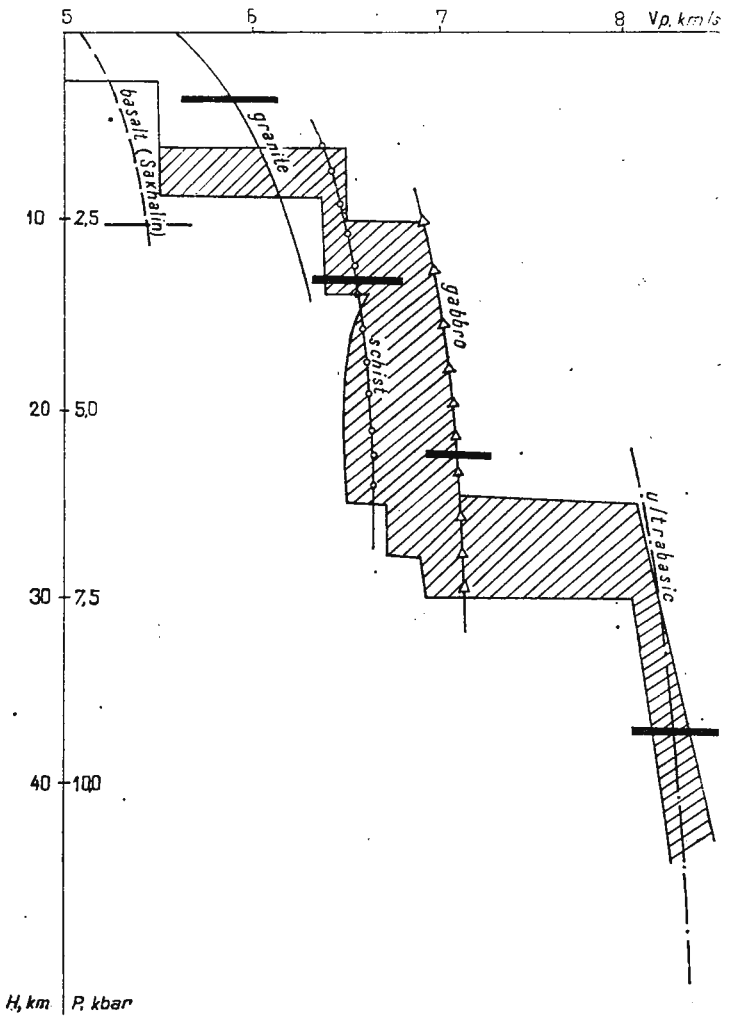

Fig. 4. — The strip of seismic velocities (shaded) and the results of laboratory measurements; the vertical lines represent the mean velocities as functions of pressure (depth), the horizontal ones are strips ($\pm\sigma$) for the crust of the continental transition type (Sakhalin).

the upper mantle falls into the right part of the 80 % strip of "ultrabasic" velocities (fig. 5).

The general conclusion is that a joint use of seismic and laboratory data has proved to be fruitful for preliminary determinations of the constitution of the principal crust layers in regions differing as to structure.

The possibility to narrow the non-uniqueness strip of seismic data with the help of laboratory measurements of velocities should be tested in concrete, localized territories.

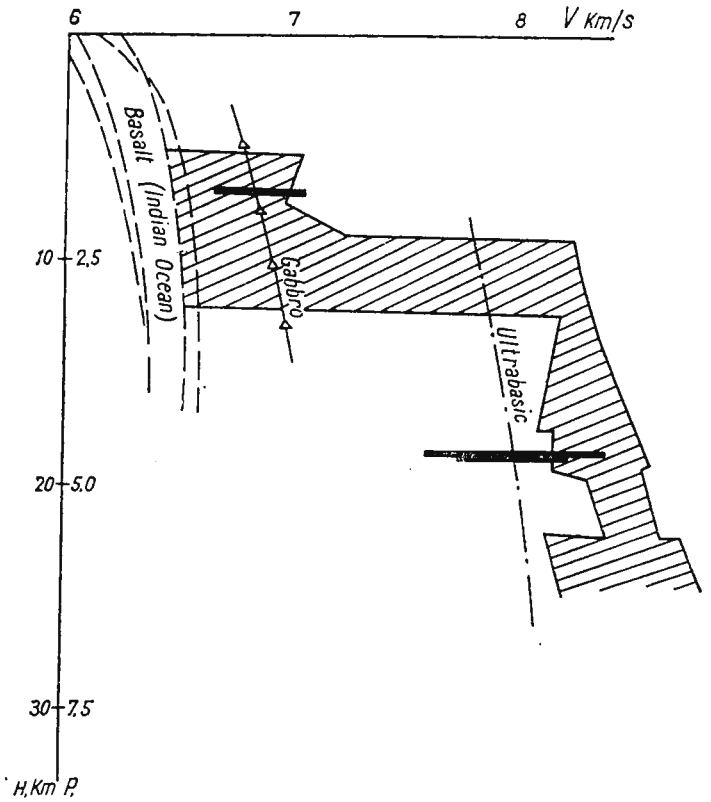

Fig. 5. — The strip of seismic velocities (shaded) and the results of laboratory measurements; the vertical lines represent the mean velocities as functions of pressure (depth), the horizontal ones are strips ($\pm\sigma$) for the oceanic crust.

Lastly, there is one more aspect of the comparison of independent data on the velocities of elastic waves. With measurements of rock samples under pressure, we can prognosticate seismic cross-sections, the wavefield peculiarities, and the technique of seismic observations in regions where no observations have yet been taken, or they are scanty. An example is provided by the experience of seismic investigations in the Moon (L a t h a m et al., 1970). Figure 6 shows the curves of laboratory velocity measurements of the lunar samples from Apollo 11, and the travel-time

curves of the direct P and S waves corresponding to them. The curves coincide with the travel times of the pulses generated by the impact of two spacecraft at distances 63 km and 135 km, which allowed the American

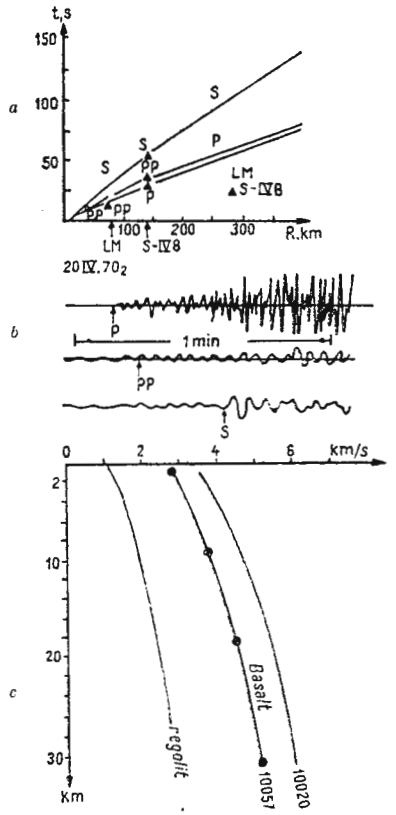

Fig. 6. — Velocity as a function of depth for lunar samples (a) a lunar seismogram (b), theoretical travel-time curves and travel times from the impact of two spacecraft (c).

investigators to draw the preliminary inference that down to a depth of 30 km in the region of lunar seas crease of velocity with depth caused by the increasing density of basalts, and there is no discontinuity like the Moho in the Earth.

REFERENCES

Afanasyev G. D., Bayuk E. I., Belikov B. P., Borsuk A. M., Volarovich M. P., Zalessky B. V., Sin'anov I. Z. (1965) The physical properties of rocks in the formation zones of the North Caucasus and the implications for the interpretation of geophysical data. *Izv. Acad. Sci. USSR. Geol. Ser.*, 9, Moscow.

Azbel I. Ya., Keilis-Borok V. I., Yanovskaya T. B. (1966) A technique for the joint interpretation of travel-time curves and amplitude curves in studying the upper mantle. *Vychislitel'naya seismologiya* 2, Nauka, Moscow.

Bayuk E. I., Volarovich M. P., Skvortsova L. S. (1971) The velocities of elastic waves at high pressures in igneous and metamorphic rocks. *In*: Tectonophysics and the mechanic properties of rocks, Nauka, Moscow.

— Volarovich M. P., Galdin N. E. (1972) High pressure study of the velocities of elastic waves in rock samples from the rift zone and islands of the Indian ocean. *Studies on the problem of the rift zones of the world ocean*, 1, Nauka, Moscow.

Galkin I. N. (1972) Determining the seismic model of the Earth's crust. Nauka, Moscow.

Latham G. et al. (1970) Seismic data from man-made impacts on the Moon. *Science*, 170, 3958, Washington.

Petrashen' G. I., Alekseev A. S., Gel'chinsky B. Ya (1959) Elements of the dynamic theory of the propagation of elastic waves. *Voprosy dinamicheskoi teorii rasprostraneniya seismicheskikh voln*, 3, Leningrad.

Skorikova M. F. (1970) The elastic properties of rocks from Primorye Territory under pressures up to 20000 kg/cm², Nauka Moscow.

Valus V. P., Levshin A. L., Sabitova T. M. (1966) Joint interpretation of bodily and surface waves for a region in Central Asia. *Vychislitel'naya seismologiya*, 2, Moscow.

— (1968). Determination of seismic cross-sections from combined data. *Vychislitel'naya seismologiya*, 4, Moscow.

— Galkin I. N., Levshin A. L. (1971) Computer solution of the inverse problem of DSS from a travel-time curve and an amplitude curve. *Vychislitel'naya seismologiya*, 5, Moscow.

Volarovich M. P. (1964) Studies in the physical properties of rocks at high pressures and temperatures. *Geofizicheskiy sbornik*, 11.

— Levykin A. I., Skorikova M. F. (1970) The elastic properties of rocks from Primorye Territory under pressures up to 20000 kg/cm². *Trudy Sakhknii*, 24.

— Kurskeev A. K., Tomashevshaya I. S., Tuzova I. L., Urazaev B. M. (1971) A study on the velocity of *P*-wave in rock specimens at high pressures in connection with investigation of the deep structure of Central Kazakstan. *In*: Tectonophysics and mechanic properties of rocks, Nauka, Moscow.

DEEP SEISMIC SOUNDING

SYNTHESIS

ON METHODS IN DEEP SEISMIC SOUNDING (DSS)

BY

NIKOLAY PUZYRIOV[1], VSEVOLOD SOLLOGUB[2]

As far back as 10—15 years the methods of DSS studies of the Earth's crust were based on a number of simple assumptions: the crust is composed of two or three layers, seismic boundaries are horizontal or slightily dipping and no significant lateral inhomogeneities of velocity exist.

The said assumptions dictated a simple scheme of observations resulting in single time-distance graphs, at best—in reversed with 250—300 km between the shot points as a rule.

The field observations carried out by the above method have yielded a great amount of data on crustal structure under numerous regions of the globe. At the early stage of crustal investigations these data made is possible to grasp general structural features of the Earth's crust and upper mantle, and to reveal a number of regularities, including those of a global character. These results have paved the way for a deeper insight into the Earth's interior.

More detail observations, however, scarse as they were, have convincingly shown that the crustal structure is not so simple as it was supposed previously. The detail investigations have located numerous deep

[1] Institute of Geology and Geophysics, Academy of Sciences, Novosibirsk, USSR.

[2] Institute of Geophysics, Academy of Sciences, Kiev, UkSSR.

seated faults that cut the crustal mass and probably the upper mantle through and separate individual blocks as big as 30 to 100 and more kilometers. The blocks are of specific structure and may be distinguished by a total crustal thickness, number of seismic boundaries and different ways of their behaviour, by vertical and lateral distribution of elastic velocity, etc. The presence of low velocity layers contributes to the structural complicacy of individual blocks. So do subsurface layers with high velocity (in the regions of ancient shields), velocity anisotropy, the presence of boundary velocity horizontal gradient along a seismic boundary, existence of two or even three boundaries with a velocity above 7.5 km/s, and other factors.

At present, the general regularities of the Earth's crust structure should be considered established in the main, but the relationship between deep and subsurface geology is still uncertain. It invites special detail investigations, on one hand, and sufficiently informative areal observations of a regional character to cover vast territories with various geologic structure — on the other.

Before considering the methods of field observations let us dwell on some problems of DSS data interpretation, for these two questions are closely related to each other.

Nowadays, the forms of representation of final seismic results considerably vary. One group of scientists presents crustal cross-sections in the form of seismic horizons or individual reflectors without any indication of velocity value. This is relative first and foremost, to investigations utilizing subcritical reflections and to crustal studies by conversed waves originated from earthquakes and explosions. It should be noted that the utilization of subcritical reflections results in a most accurate structural plotting. Another group of investigators presents crustal cross-sections as seismic horizons with indications of boundary and layer velocities, all the types of recorded waves being utilized. The third and the last group of investigators offers the final results in the form of velocity columns and velocity cross-sections ignoring a seismic boundary plotting. This yields the information about a general character of velocity distribution in medium in the form of a continuous field, but sufficiently sharp boundaries where persistent groups of waves are originated may well escape our notice. It should be kept in mind that, with a sufficient accuracy of arrival time determinations, this or that isoline on a velocity cross-section may coincide in some cases with a seismic boundary, but as a rule it does not. Hence, it is a general characteristic of physical parameters

of the crust that is shown by the velocity cross-section and is by no means the crust structure itself. Getting ahead, it should be stated that, to our notion, the most correct and expressive representation of seismic results is a cross-section in the form of seismic horizons and individual reflectors

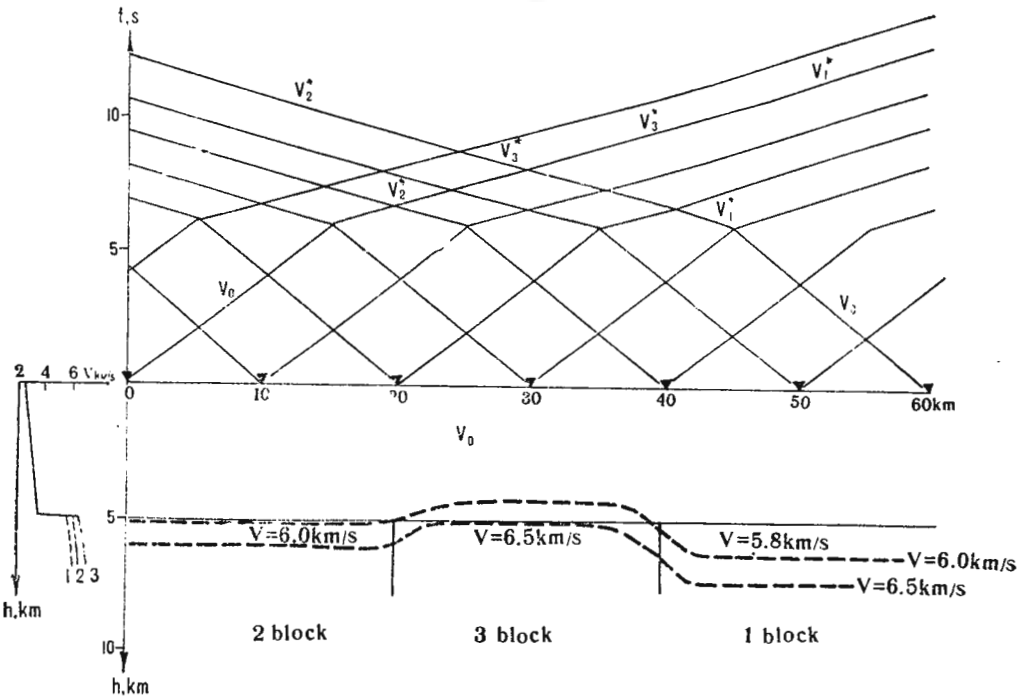

Fig. 1. — Model of upper crust, theoretical time-distance curves and V = const lines

with indication of velocity parameters (in the form of velocity isolines or velocity values). Such a representation gives an idea of the structure of seismic horizons as well as of velocity inhomogeneities along the profile.

Let us dwell on some theoretical and practical examples of rather big errors that may occur in determination of certain parameters at DSS data interpretation. In the first place we shall consider velocity cross-sections to show that the latter are far from being thorough characteristics of the Earth's crust structure.

a) Figure 1 shows the upper crust model where medium with a linear velocity increase with depth (from 2.5 to 3.5 km/s) is underlaid at a depth of 5.0 km by a seismic horizon (say, crystalline basement sur-

face), composed of three blocks (each 20 km wide) with boundary velocities 5.8; 6.0 and 6.5 km/s. Gradients of velocity increase with depth are equal for all the blocks.

Theoretical time-distance curves calculated for the model have made possible to determine velocities and to plot isolines in 6.0 and 6.5 km/s. As it is shown by figure 1, the behaviour of the isoline 6.0 km/s, to which crystalline basement surface is usually associated, does not correspond to that of the horizontal seismic boundary that belongs to the model. In the area (block 3) of higher boundary velocity the isoline 6.0 km/s is a sheer fiction.

The above example shows clearly that with lateral velocity inhomogeneities along one seismic boundary the isolines $V = \text{const}$ may characterize in some cases the boundary under study (block 2) in other cases the real picture is badly distorted (block 1) and, at last, sometimes (block 3) the isoline presents some false data for in this particular area velocity data are not available at all (in our example this is the isoline $V = 6.0$ km/s).

b) For another theoretical example we have taken model of a homogeneously layered medium with constant dips of boundaries ($\varphi = 2°$ and 5°) and velocity increasing in jumps from 5.5 to 8.0 km/s within the depth range from 0 to 42 km. Theoretical time-distance curves of head waves have been plotted as well as the corresponding velocity columns calculated on an assumption of a horizontal layering. Errors in boundary velocity determination increase with depth to the boundary from 1.6 to 4.2 % at $\varphi = 2°$ and from 4.0 to 10.7 % at $\varphi = 5°$. Errors of depths to refracting horizons are of maximum values for the upper boundary; at $\varphi = 2°$ and 5° they amount to 7.6 and 19 % respectively. When passing on to deeper horizons the sign of the error changes to opposite; maximum values do not exceed 3.1 and 7.2 % respectively.

With two chasing time-distance curves available that are treated independently from each other, the velocity isoline dips (with the horizons' dips $\varphi = 2°$ and 5° considered in our example) do not practically differ from the given theoretically and a velocity error is almost the same as for the case of a single time-distance curve.

In the case of two independently treated reversed time-distance curves errors for each curve are of opposite signs. Due to this fact velocity isolines may disagree considerably with the true ones. At $\varphi = 2°$, for example, the dip of the first refracting horizon is equal to that of the model's; the dips of the second and third horizons are considerably distorted, the dips of the fourth and subsequent boundaries are of the signs opposite

to the initial one's. At $\varphi = 5°$ structural distortions are far more striking; in this case it is the first refracting horizon that has the dip opposite to the true one.

The above examples reveal the presence of an inadmissible discrepancy between the results of interpretation (velocity isolines) and the original model.

c) Figure 2 shows a system of time-distance curves obtained on the International Profile VIII in the region of the Ukrainian Shield and the corresponding crustal cross-section plotted from the data on all the recorded waves. Two chasing time-distance curves from the shot points 203 and 98.3 spaced at 100 km, have given a base for calculation of velo-

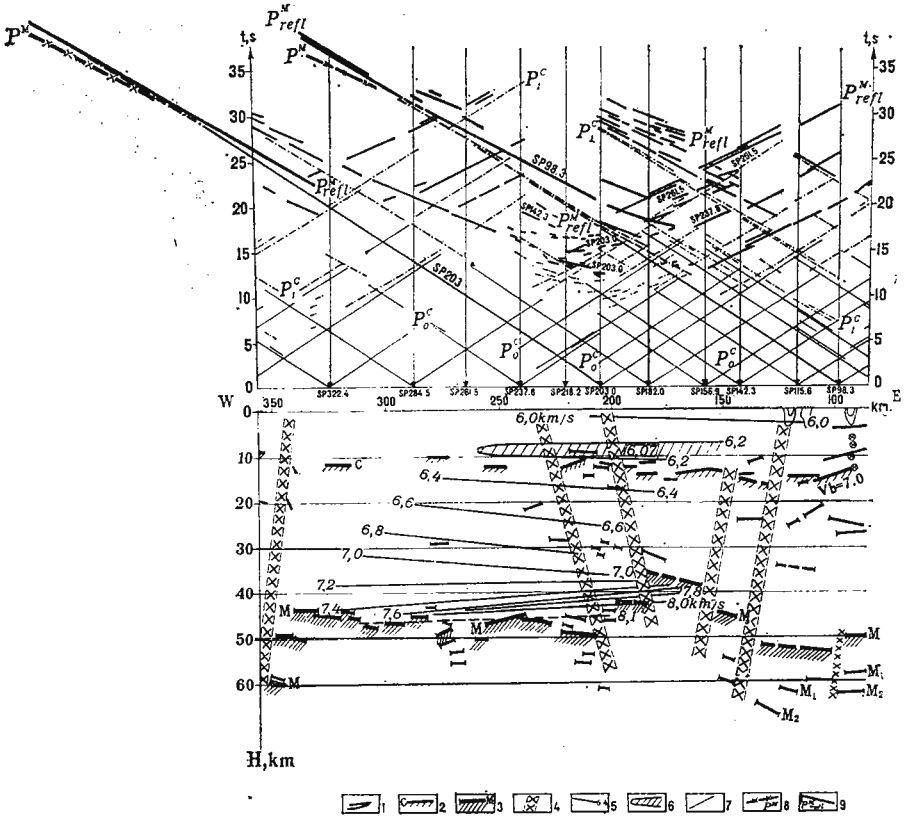

Fig. 2. — Comparison between crustal cross-section along profile VIII and velocity cross-section:

1, reflectors; 2, supposed Conrad surface; 3, M surface; 4, deep seated faults; 5, V = Const lines; 6, low velocity layer; 7, time-distance curves; 8, time-distance curves for waves refracted from M discontinuity; 9, time-distance curves of overcritical reflections from M surface.

city columns (fig. 3), the time-distance curve from the shot point 98.3 suggesting a thin low velocity layer at a depth of 8—12 km. From the said velocity columns velocity isolines have been calculated to be plotted on the seismic cross-section (fig. 2). A comparison between seismic boun-

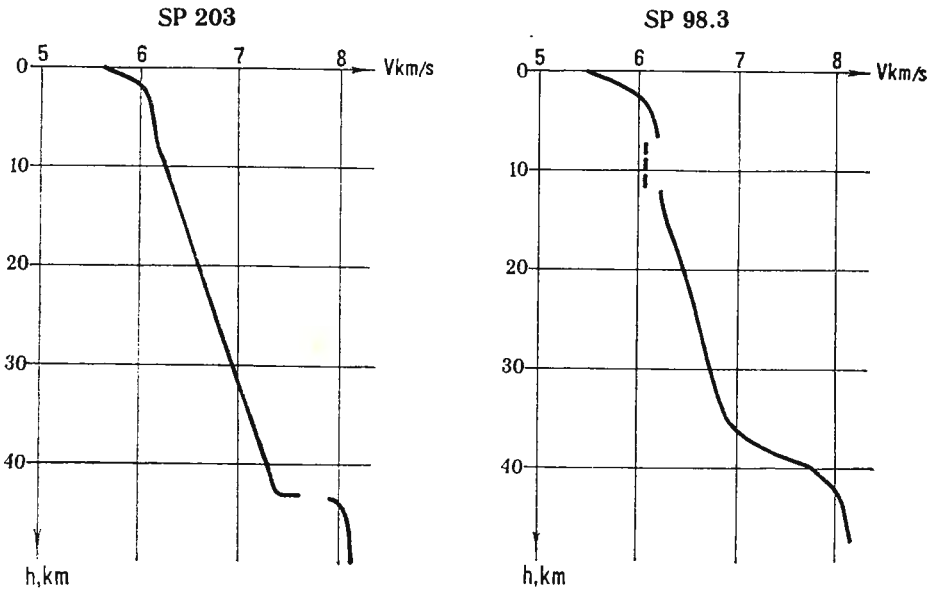

Fig. 3. — Velocity change with depth calculated from time-distance curves from shot points 98.3 and 203.0.

daries (the *M* discontinuity derived from over-critical reflections, in particular) and velocity isolines shows that in general they agree. So, the isoline 8.0 and 8.1 tends to submerge westwards and so does the *M* discontinuity. However, some upwells of the latter (stations 150—200) are not expressed by the velocity isolines : on the said upwelled block, close to the *M* boundary, the isolines 7.8 and even 7.2 have been plotted. Errors in velocity calculations are evident, though a slight decrease of boundary velocity values in upwelled areas of the *M* surface is possible.

The problem of identification of low velocity layers within the crust is being studied by many, however, by this moment, neither a strict solution has been found, nor an adequate observational system worked out to make possible a unique solution of the problem.

One of the main criteria of the existence of a low velocity layer are a break and displacement of the time-distance curve of the first arri-

vals. However, this criterion is not sufficient, for the break in the first arrivals may as well be caused by a fault within the crust. So, the interpretation of a single time-distance curve may bring along errors of principle. It is a more dense observational system that one should have to get a correct idea of the crustal structure.

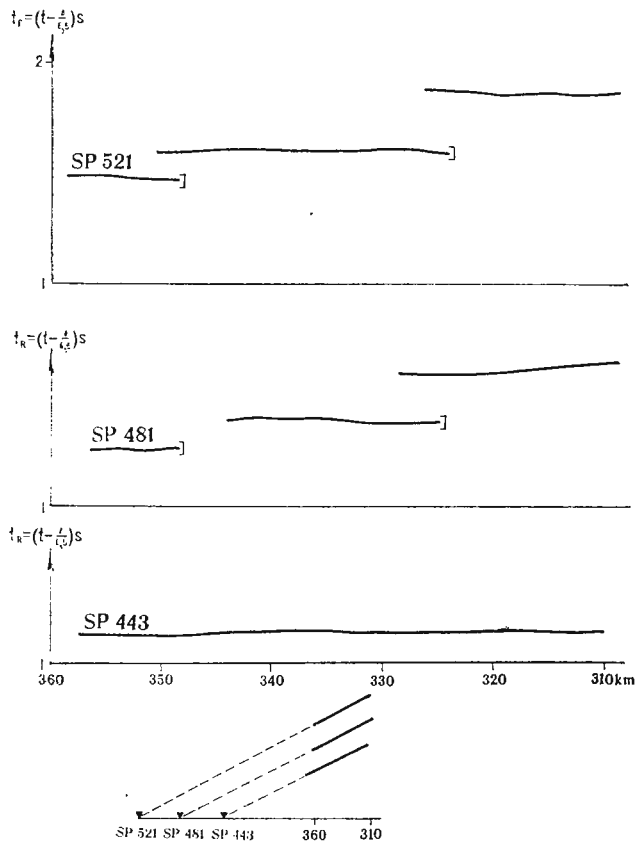

Fig. 4. — Reduced time-distance curves of first arrivals from shot points 443, 481 and 521, showing breaks in wave correlation.

Let us illustrate the above said by an example from the DSS practice. Figure 4 shows three reduced chasing time-distance curves of the first arrivals. Two of them (shot points 521 and 481) have breaks in correlation and displacements in time. The third curve (shot point 443) has no break. The wave pattern observed may be explained like this. The breaks in the two time-distance curves from remote shot points are observed in

approximately the same areas of the line; consequently, these breaks are caused by disjunctive dislocations at a considerable depth. These are naturally not seen on the nearest time-distance curve (shot point 443). With only one of the first two curves available (481 or 521) two low velocity layers would be suggested to account for the break and such an interpretation would be completely wrong.

Thus the above practical example once again shows that the presence of a low velocity layer could not be proved by a single time-distance curve.

As it has already been noted, the method of deep seismic sounding is aiming both at detail and reconnaissance areal study of the Earth's crust and upper mantle. Hence the two stages of the investigations that should be considered.

The first includes a study of the gross structural features of the Earth's interior under vast territories. This is essential for understanding the nature of deep seated regional geologic structures and individual anomalies of natural geophysical fields. The reconnaissance stage should differ from the detail one only by scale and accuracy of the study and not by character of the information obtained. The aims and purposes of the reconnaissance stage may be put like this: location of large (100 and more kilometers across) crustal blocks and zoning faults that separate the blocks; tracing the main persistent boundaries within the crust and, as the first thing, the top and bottom of the crust; investigation of the gross features of velocity distribution within the medium under study.

Consequently, the systems of single and reversed time-distance curves that are being utilized at present do not meet all the requirements of the Earth's crust investigation:

a) Observations with one shot point (single time-distance curves) are known to be carried out by continuous, piecewise-continuous and discrete profiling. The systems of these types provide the possibility to ascertain the nature of the waves recorded in the area under study and to plot a velocity cross-section with an assumption that seismic boundaries and V = Const lines are horizontal. But if the assumption is not valid, simple systems like these may lead to serious errors, as it has been shown on the above examples.

b) Reversed time-distance curves, spaced at 200—300 km, do not always provide the necessary accuracy. In this case we obtain a large information; in particular, an opportunity is offered to take into account the effect of linear horizontal inhomogeneities, provided the correct

identification of waves. But with a seismic boundary of a considerable curvature and horizontal velocity gradients varying, the observational system in question does not provide an adequate recovery of the medium.

In view of the fundamental errors that may arise at the reconnaissance stage with the above described simple observational systems, we recommend a system of the so-called differential sounding that was originally worked out for the areas of Siberia difficult of access and have been tested since in many other regions.

D i f f e r e n t i a l s o u n d i n g is a special kind of reconnaissance work characterised by a small number of recording stations for each shot but with a rather „dense" spacing of shot points (almost as dense as in the detail work by the method of continuous profiling). A distance between a shot point and geophone array (basis of sounding) is chosen to provide a most reliable identification of the waves under study. To ascertain the nature of the waves the data from special piecewise-continuous observations with a single shot point are used. Utilization of a relatively short geophone array (1 km) makes possible to identify regular waves and classify them according to apparent velocities and dynamic features. Utilization of various sounding bases provides a determination of velocity parameters of medium. All the data from various wave types are used in the interpretation. The method of differential sounding is especially helpful in mountaneous, woody and populous regions. The method under consideration does not require too simplified assumptions concerning the medium; it makes allowance, in particular for curvilinear boundaries and velocity variations, both vertical and horizontal. The application of the method results in the behaviour characteristics of the main crustal boundaries (basement and the M discontinuity) and of intracrustal boundaries and $V = \text{Const}$ lines extended over 50—100 km. Velocity data for the crust and upper mantle are obtained as well. Deep seated faults and the corresponding blocks are located by a number of direct and indirect indications. A mode of the method to be applied to a three-dimensional model has been recently developed (areal survey).

The effectiveness of the method of differential sounding may be illustrated by a reinterpretation of the detail and reconnaissance data of the Turkmenia (fig. 5) and the Lake Superior (fig. 6). For the former, the M boundary location disagrees with the results of the continuous profiling by no more than 4 km. Discrepancies for a mantle boundary are of almost the same values. For the upper boundaries the disagreement

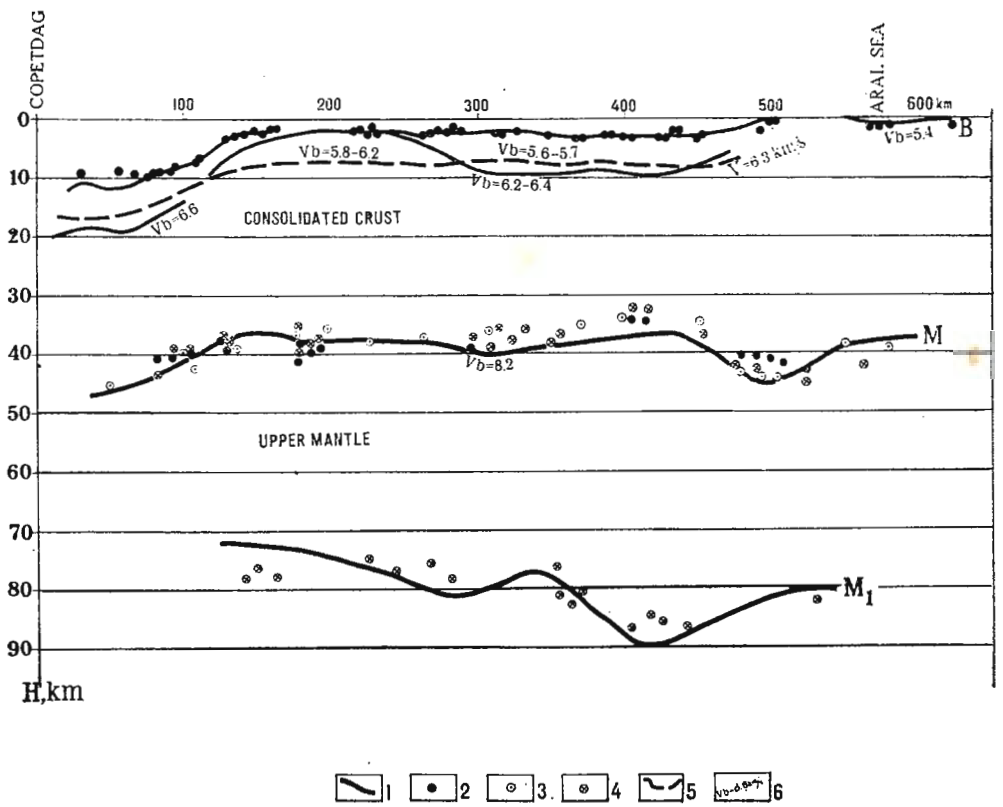

Fig. 5. — Comparison between crustal cross-sections constructed by different methods (Turkmenia);

1. seismic boundaries by detail observations data;
2. depths to seismic boundaries by refracted waves data;
3. ,, ,, ,, ,, combined refracted and reflected waves data;
4. ,, ,, ,, ,, reflected waves data;
5. Velocity isolines from refracted (dipping) waves data;
6. Boundary velocity values.

is not considerable either. In the reinterpretation 10 per cent of all the available seismograms have been used.

In the area of Lake Superior American geophysicists have carried out point (one channel) observations over a dense network. On the bases of the time-distance curves of first arrivals, some authors have plotted several versions of the crustal cross-section with two refracting boundaries at depths of 5—10 and about 40 km (the M discontinuity). Construction of the fields $t(x, l)$ and their transformation have made it possible to plot both the boundaries mentioned and to determine the

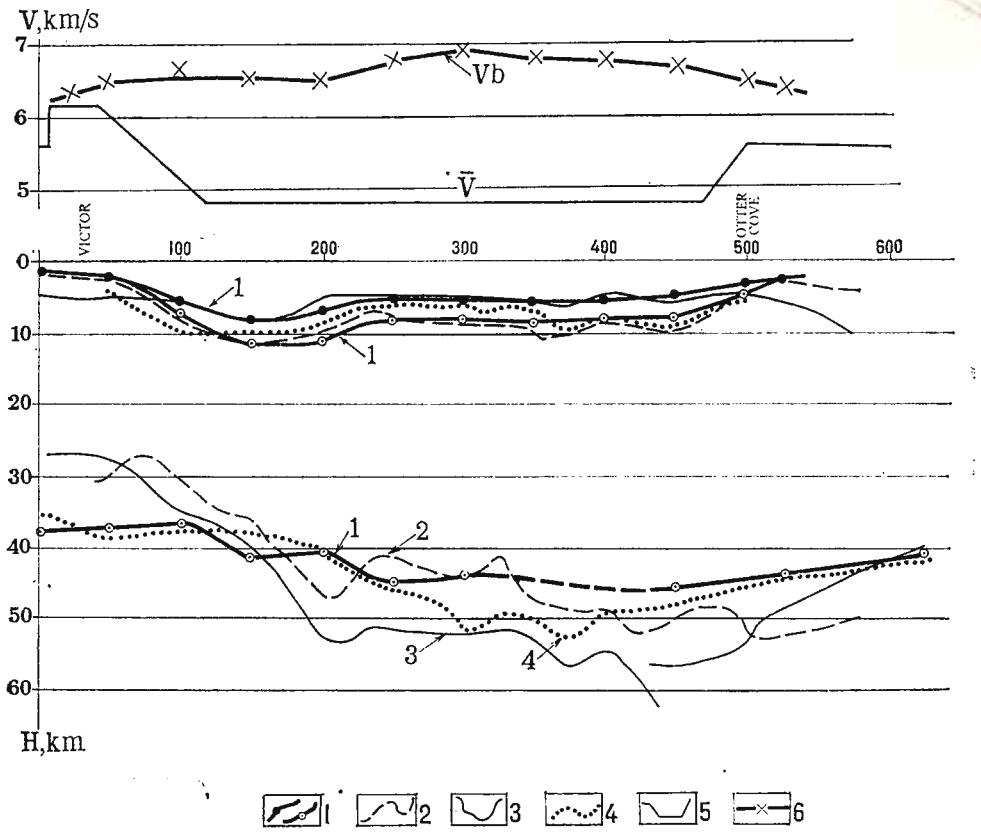

Fig. 6. — Comparison between crustal cross-sections constructed by different methods (Lake Superior region, Canadian Shield).

1, behaviour of seismic boundaries plotted by differential sounding method;
2, " " " " results of Berry et al.;
3, " " " " from results of Smith, et al.;
4, " " " " " " " O,Brien, et al.;
5, $\bar{v}$ change along profile; 6, V_b change along upper seismic boundary from differential sounding data.

distribution of boundary velocity, without any strict assumption concerning the model. The seismic cross-section presented (fig. 6) is not inferior to those obtained by other authors in the sense of a completeness of the information, although just a part of the whole set of data has been used. Our results are in the best agreement with those of O'Brien and strongly differ from the results obtained by M. Berry and B. West with the help of the timeterms method.

The success of the method of differential sounding is strongly dependent on the reliability of a discrete correlation of different types of the wa-

ves recorded. In the course of the correlation a great amount of indications are used including those based on the information about general features of wave fields, behaviour of individual seismic boundaries, velocity distribution, etc. The experience of differential soundings in Siberia and other regions has shown that all the difficulties of the correlation, even in a case of a complicate crustal model, given a skilful approach, may be successfully overcome.

The *second* stage is the study of the fine features of the crustal structure. This invites the detail investigations by the method of continuous profiling. The latter provides a most reliable identification of all the crustal seismic boundaries and deep seated faults; it makes possible to locate smaller crustal blocks and reveal specific features of their structures. Besides, the method lends assurance to determinations of the velocity distribution and identification of low velocity layers.

A special object of the investigations at this stage is a study of the upper part of the consolidated crust. It especially refers to shields where sediments are practically absent.

Detail investigations are carried out mostly along linear profiles with shot points spaced at 15—50 km (depending on the depth under study) and geophones — at 100 — 200 m. A system of time-distance curves is calculated with the view of providing a continuous correlation of the main types of crustal waves. The investigations yield a most reliable information on both horizontal and vertical differentiations of the crust.

A special kind of detail investigations is a recording of subcritical reflected waves from intracrustal boundaries. This elucidates not only short subhorizontal seismic boundaries but also sharply dipping horizons in the upper consolidated crust. All this is of an utmost importance for geologic interpretation of seismic data and for a finalization of the model of the medium in study. The investigations by the method of common reflection point started by Prof. Meissner are of a considerable value as well as anisotropy studies carried out by Morris and his colleagues.

A shortcoming of both detail and reconnaissance investigations at present is a utilization of two-dimensional observational systems that do not always fit to a real model with properties varying in all the three directions.

The upper mantle is poorly heeded both in detail and reconnaissance investigations.

In conclusion it should be noted that conventional field technique and methods of interpretations in DSS could not be considered quite

satisfactory. Their improvement both at reconnaissance and at detail stage of DSS work will require new efforts from the scientists concerned. The main trends of the development of the methods have been outlined above may be summarized in the following :

a) Utilization of the systems providing the investigation of interfaces and distribution of physical parameters for complicated models of media.

b) Elaboration of efficient methods of field procedure aiming at solution of three-dimensional problems.

c) Elaboration of the methods for subcritical reflected waves recording, especially in detail investigations.

d) Realization of special investigations aiming at a further finalization of crustal models, including the study of anisotropy, low velocity layers, blocks, etc.

NORTHERN EUROPE

THE SCOTTISH SEISMIC REFRACTION PROGRAMME

BY

A. W. BRIAN JACOB[1]

This brief account describes the Institute of Geological Sciences' (I. G. S) refraction programme in Scotland. The programme is designed around the I.G.S. seismic network Lownet (Crampin et al., 1970) and it is intended primarily for time-term processing (Willmore, Bancroft, 1960) though it includes two refraction lines with closely spaced shots. The programme was started in 1970 and the shots were completed in the summer of 1972. I.G.S. also has a continuing programme in the Lownet area using the seismic waves generated by quarry blasts to investigate the shallow structure within the network.

H.M.S. Hecla began firing 300 lb depth charges in April 1970. The shots to the East of Lownet (fig. 1) were successfully fired but the ship was unable to complete the work. For these shots there were temporary stations at MK, JU and MS. In late October and early November of the same year another vessel, the Barfoot fired all the shots on the Western side of Scotland South of 58°N (this might be called phase 2). The pattern of 36 depth charges fired includes a line to the South of station MK in which the shots were fired at approximately 3 km intervals. Stations were sited around this subsidiary line to give converage from close range out to full *Pn* range. Finally, the phase 3 shots were fired by Barfoot in the North West segment around station WR in May 1972. Barfoot had been unable to fire these in 1970 because, of very bad weather at the time of phase 2. This last set includes a closely spaced line of shots along the Minch and some stations were put out in this region for the duration of phase 3. Sta-

[1] Institute of Geological Sciences. Edinburgh, Scotland.

tions WR, CL, and MS remained in position for the North Atlantic Seismic Project of Durham University (NASP).

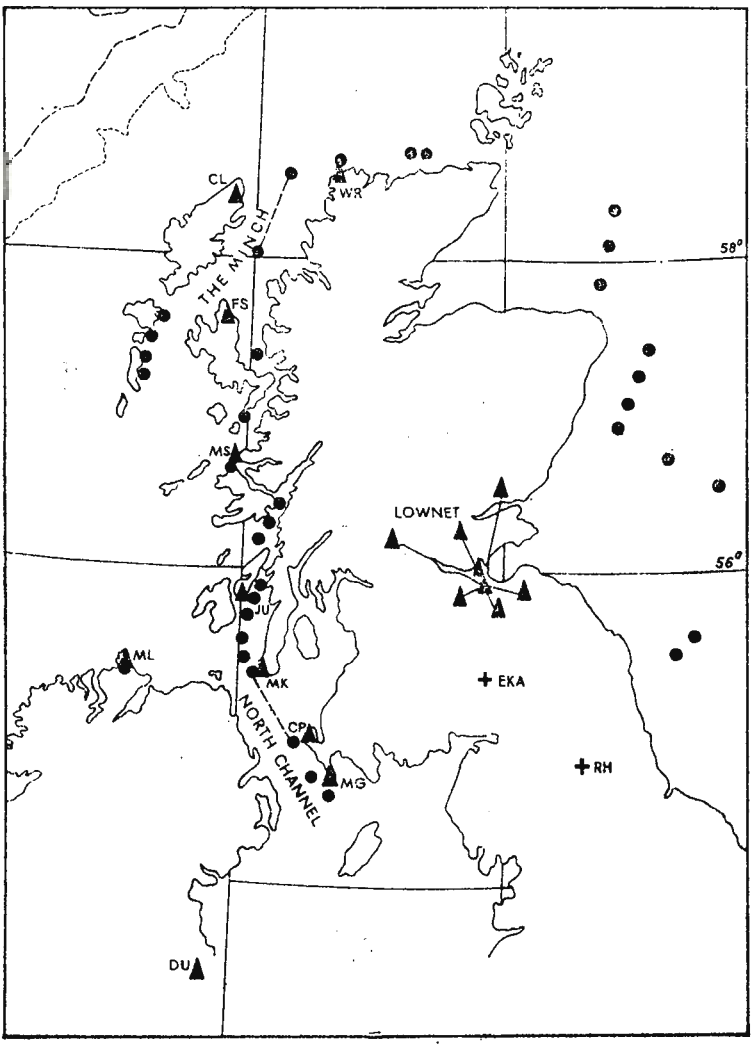

Fig. 1. — Distribution of shots and stations. Lownet is shown as a set if linked triangles in the centre of the map. All the shots are shown as discs.

The shots in phase 1 were fired by depth pistol and these mostly went off on the bottom though in water deep enough to ensure a good seismic signal. All the shots fired by Barfoot in phases 2 and 3 were fired electrically at the optimum depth.

The primary interest has been in the structure in the area of Lownet combined with the measurement of any anisotropy that might exist in the *Pn* wave velocity. The experiment was designed to measure such a variation if it is pressent and, as pointed out by B a m f o r d (1971a), such a variation, if it were not measured and allowed for, could lead to considerable errors in the time terms found, in this case, for the shot positions. It is hoped that the pattern of shots in the North Channel (near MK), and also the results of NASP, will give more information about any lateral changes in the velocity of *Pn* as one moves away from Lownet. The design of the experiment is different from most other ones around Britain (B l u n d e l l , P a r k s , 1969 ; B a m f o r d , 1971b) in that the velocity determining network is the set of stations and that most of the Pn wave paths are under the land mass.

A preliminary straightforward time term processing of most of the *Pn* data (shot-station distances greater than 155 km) has given a *Pn* velocity of 8.10 $\pm$ 0.04 km/s and the distribution of the residuals as a whole appears fairly normal. A more detailed analysis has yet to be carried out. Neglecting for the moment any effects of anisotropy or steep dips it has been found that most of the shot points at sea, except for those in basin structures like the Minch, have *Pn* time terms between 2.5 and 3.0 seconds. Values in the Minch and at some points in the North Sea rise to between 3.0 and 3.5 seconds. The time terms for Lownet are all between 3.5 and 3.7 seconds. These last may be relatively well controlled, even at this early stage, as they are in the velocity determining network and they do not exhibit sharp variations.

Acknowledgement

The work was undertaken with the support of the Natural Environment Research Council and is published with permission of the Director of the Institute of Geological Sciences.

REFERENCES

B a m f o r d S. A. D. (1971a) Applications of simulated data studies to crustal refraction seismology. *Bull. Seism. Soc. Am.*, 61, 4, Berkeley.

— (1971 b) An interpretation of first arrival data from the continental margin refraction experiment. *Geophys. J. R. Astr. Soc.*, 24, London.

Blundell D. J., Parks R. (1969) A study of the crustal structure beneath the Irish Sea. *Geophys. J. R. Astr. Soc.*, 17, London.

Crampin S., Jacob A. W. B., Miller A., Neilson G. (1970) The Lownet radio-linked seismometer network in Scotland. *Geophys. J. R. Astr. Soc.*, 21, London.

Willmore P. L,, Bancroft A. M. (1960) The time term approach to refraction seismology. *Geophys. J. R. Astr. Soc.*, 3, London.

10 TON EXPLOSIONS FIRED IN 1971 AND 1972

BY

A. W. BRIAN JACOB, PATRICK L. WILLMORE[1]

Some results of the 10 Ton explosion fired in 1971 were published in a letter to Nature (J a c o b , W i l l m o r e , 1972 now called Paper I). The present paper presents more data, both from the 1971 explosion and from a second one fired in June, 1972.

On several past occasions, refraction surveyes have produced good signals at surprisingly great range from small explosions. In the Lake Superior Experiments charge sizes down to 1/8 ton were employed and in one case a good signal was measured at a range of 1128 km (M a n s f i e l d, E v e r n d e n , 1966). The seismic programme in 1967 between Scotland and Norway [2], produced good travel times out to over 800 km from similar charges, H a l e s et al. (1970) obtained signals out to 15° from 5 ton shots in the Gulf of Mexico, and the Group Grands Profils Sismique (e. g. 1972) have used the method in Europe. These results illustrate the effect of firing at the so-called optimum depth, i.e. the depth at which the bubble pulse and the water surface reflections are in phase (O' B r i e n , 1967).

In 1969 an experiment was carried out in the North Sea to measure quantitatively the actual amplitude variation produced by varying the depth of a 300 lb charge of *TNT* (J a c o b , 1970). Shots were fired at depths between 18 and 180 metres, the results showed an amplitude variation between the best and the worst cases of about 2½ : 1, and the largest amplitudes were measured for the shot at 91 metres (almost exactly the expected optimum depth for a 300 lb charge of *TNT*). Where the signal

[1] Institute of Geological Sciences. Edinburgh, Scotland.

[2] S o r n e s A. P_n time-term survey Norway-Scotland 1967. 1968. A.R.P.A., Report No.612–1.

to noise ratio at the receiving stations is poor then the results of Bancroft (1966) have shown that such a variation can be critical and demonstrate how worthwhile it is to fire at the optimum depth.

In the course of this development, word was received that a 10-ton lot of surplus military explosive was available, and calculation showed that, if this were to be fired at optimum depth, the resonant frequency would be 1.9 Hz. As this is close to the frequency of maximum sensitivity of the WWSSN network, and as the Q values for much of the teleseismic range are not much less than those for distances at which smaller charges had already been observed, it seemed not unreasonable to hope for teleseismic observations from a charge of this size. Subsequent investigation showed that such a charge was, in fact, about the largest which could easily be handled at sea by available vessels, so that further consideration of the possibilities became tied to this value.

Eventually, shots were fired in July 1971 in the North Sea at 56° 32.5′ N, 0° 41′ E and in June 1972 to the West of Scotland at 57° 03.3′ N, 57° 09.1′ W (fig. 1). In each case the explosives were suspended from a large anchored bouy. They were put in a metal box and countermined with two 300 lb depth charges which were fired electrically. To do this a cable was led up to the surface to a small buoy and there was also a spare cable to another countermining charge in case there was difficulty with the first. The first firing cable was then run along the surface (supported at intervals by small floats) to the ship. The first shot was fired from the ship which was about 1 000 metres from the buoy. The second shot was fired from a small boat to allow the ship to move to a more comfortable distance. Both shots were fired in calm conditions.

Paper I reported that some success had been achieved and that the first shot had been recorded at a number of good stations at teleseismic range. The measured magnitude M_b was 4.4 ± 0.4 for 5 readings and this was an encouragingly high value, as Evernden's work (1970) had suggested that a value of 3.9 ± 0.5 was to be expected in the optimum case. However, at that time most of the data had come from just a few good magnetic tape recording stations. It has since been possible to study a set of microfilm copies of the WWSSN stations and it has been found that while the shot appeared on some European stations it did not appear on any at teleseismic range. This is disappointing but not entirely unexpected. A magnitude of $M_b = 4.3$ (average of both shots) gives the expected

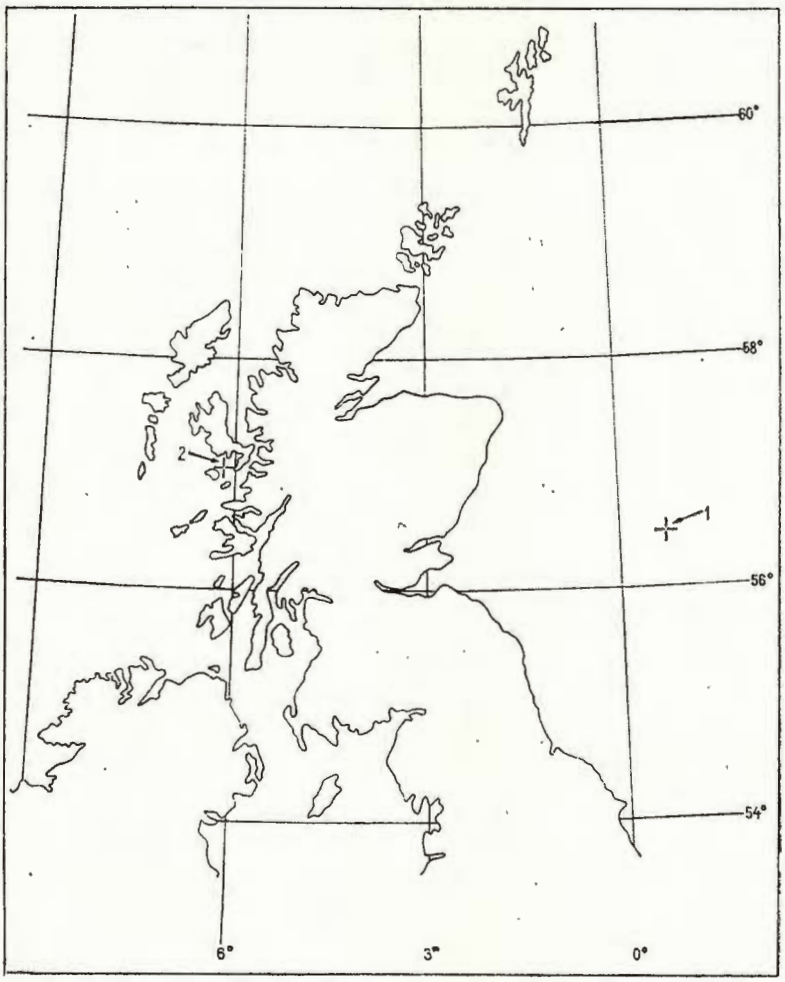

Fig. 1. — Positions of ten ton shots in 1971 and 1972.

ground amplitudes shown (tab. 1) for distances between 30° and 90°. Experience of WWSSN record is that, taking into account the usual line thickness and noise levels, the minimum measurable signal has an amplitude of about 0.3 mm. To produce a trace of this amplitude at the favourable range of 40° a WWSSN station would thus need to be running at a magnification of 50 K, with a well adjusted system and low microseismic levels. At less favourable ranges between 30° and 90°, a station magnification of up to 200 K would be required. The most likely area where the first shot

might have been visible was North America as the shot was fired at 0833 GMT (between 2333 and 0333 local time). Cultural noise levels should therefore have been low, but natural noise was presumably high enough to obscure the signal. The second shot was observed on six Canadian sta-

TABLE 1

Distance (degrees)	Ground Amplitude (nm)
30	3.2
35	2.5
40	5.0
45	2.5
50	2.5
55	2.0
60	2.0
65	1.3
70	1.6
75	2.0
80	2.5
85	1.3
90	1.3

tions, all of which were running at magnifications equivalent to a WWSSN magnification of between 50 K and 150 K when the responses at 1.8 to 1.9 Hz are compared.

The picture is more encouraging when tape-recording stations are considered. Very good signals were observed on single components at tape-recording stations like *YKP* (at which *PcP* was also observed) and *TFO* (fig. 2), and the phased record from *LAO* was very sharp and clear (fig. 3). A tape recording station is not as restricted as a paper recording one and allows subsequent processing to enhance the signal. Even the very simple variation of gain and paper speed on playout of these records makes them far superior to conventional records.

Numerous observations for distances of 200 up to 1500 Km were obtained from European stations, including the temporary stations which were operating at the time of the second shot. The ones which have so far been reduced are plotted in figure 1. If we fit these data to an equation of the form

$$M_b = \text{long } V + K \log R + L$$

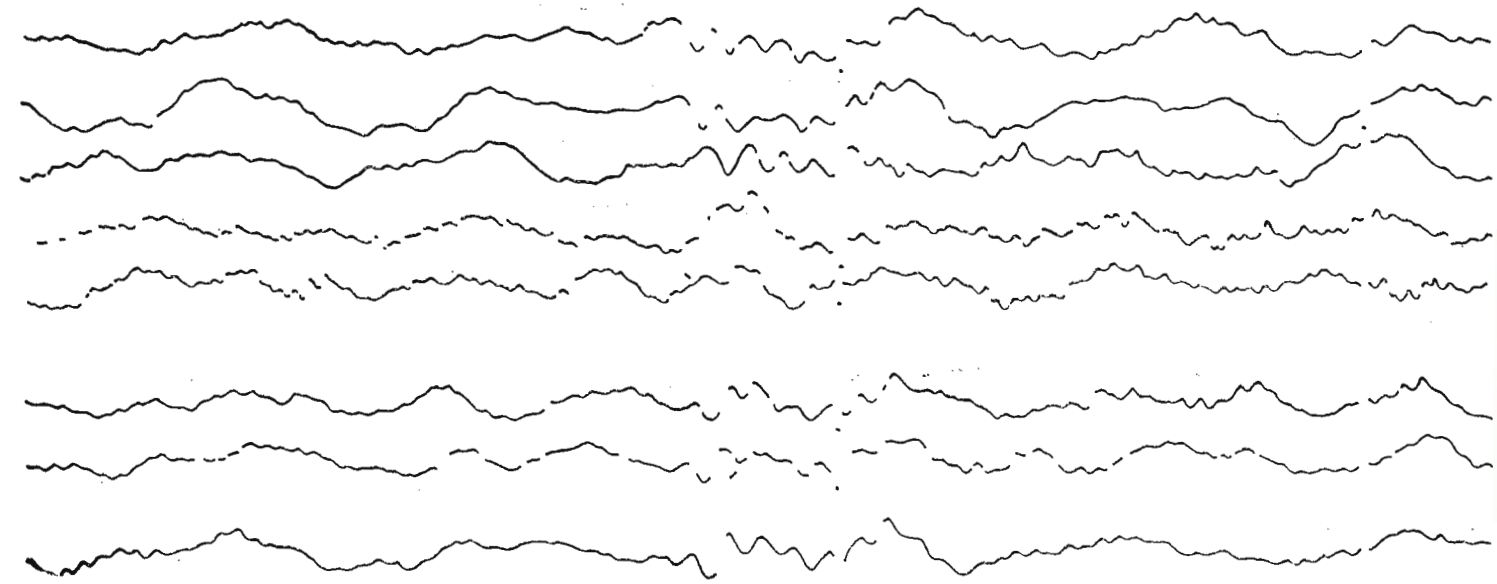

Fig. 2. — Signal on *TFO* — single components. Distance 69.4°.

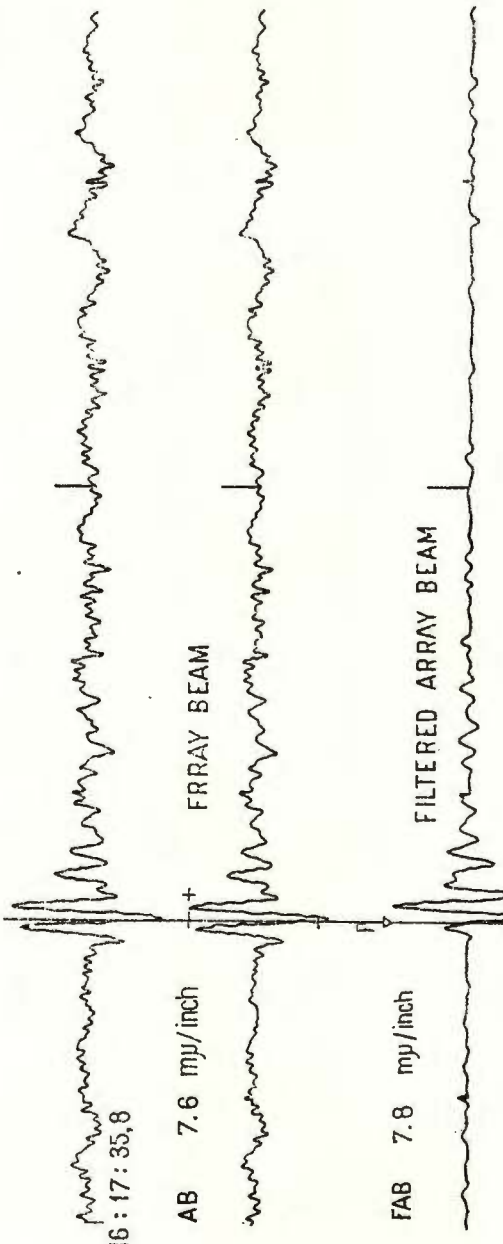

Fig. 3. — Signal (phased) at *LAO*. Distance 57.2°.

(where V is the maximum particle velocity in the P-wave train expressed in microns/s), and set M_b equal to the teleseismic value of 4.34, which is

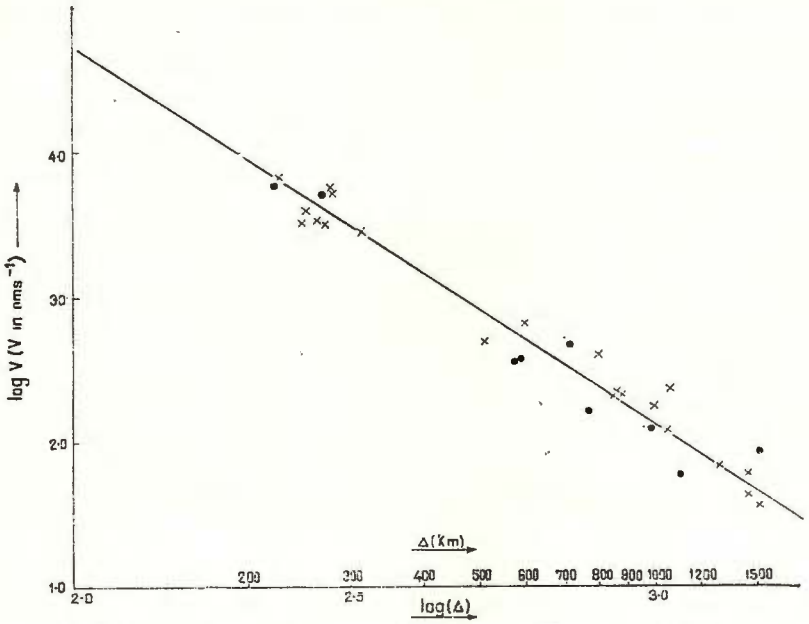

Fig. 4. — Maximum Ground Velocities on European Stations.

TABLE 2

1971		1972	
Station	M_b	Station	M_b
GLM	4.4	BLC	4.4
LAO	3.8	FBC	4.2
BMO	4.2	FFC	4.7
UBO	4.8	INK	4.2
BDF	4.7	MBC	3.7
		YKC	4.5
		LAO	4.3
		TFO	4.5

the mean of all the estimates in table 2, we find $K = 2.5 \pm 0.2$ and $L = -2.3 \pm 0.5$.

In Paper I, trial values of $K = 2.3$, $L = -2$, taken from North American experience, yielded a value, called M_b^* of 4.2.

The experiments have confirmed that explosions equivalent to about 10 Tons TNT can provide a useful tool for investigating velocity and Q structure in the crust and upper mantle of the earth and, that observations can be extended to teleseismic ranges under favourable circumstances. It will not, however, be sufficient to fire shots at random into the existing network of paper recording stations. Tape recording methods, with the resultant availability of more sophisticated data processing, are necessary and for teleseismic work these stations must be on good sites. The possibility exists of investigating particular regions in the mantle by carefully choosing shot sites and receiving stations. On a more ambitious scale, a large pattern of shots fired in oceanic areas into quite a small number of good array stations could give interesting results. Seismology has for long depended on earthquake sources which cannot be well controlled or defined and which occur in regions which are anomalous in terms of general earth structure. Underground nuclear blasts may be available at some sites on land but they are banned from the oceans. Chemical explosions in the kiloton range are rarely feasible and small but carefully controlled sources like those described here offer a significant additional chance of progress.

Acknowledgement

The authors would like to thank those who have supplied data and the Director of the Institute of Geological Sciences for permission to publish this paper.

REFERENCES

Bancroft A. M. (1966) Seismic Spectra and detection probabilities from explosions in Lake Superior, in The Earth Beneath the Continents. *Geophys. Monograph.*, 10, Am Geophys. Un. Washington.

Evernden J. F. (1970) Magnitude versus yield of Explosions. *J. Geophys. Res.*, 75, 5, Richmond.

Groupe Grands Profils Sismiques (1972) A long-range seismic profile in France from the Bretagne to the Provence. *Ann. Géophys.*, 28, 2, Paris.

Hales A. L., Helsley C. E., Nation J. B. (1970) P travel times for an oceanic path. *J. Geophys. Soc.*, 1962, London.

Jacob A. W. B., Willmore P. L. (1972) Teleseismic *P* waves from a 10 Ton explosion. *Nature*, 236, London.

Mansfield R. H., Evernden J. F. (1966) Long range seismic data from the Lake Superior seismic experiments, 1963—1964- in the Earth Beneath the Continents. *Geophys. Monograph.*, 10, Am. Geohpys. Un., Washington.

O'Brien P. N. S. (1967) Quantitative discussion on seismic amplitudes produced by explosions in Lake Superior *J. Geophys. Res.*, 72, Washington.

SOUTH-WESTERN EUROPE

DEEP-SEISMIC SOUNDING EXPERIMENTS IN PORTUGAL

BY

STEPHAN MUELLER[1], CLAUS PRODEHL[2], ALFREDO S. MENDES[3], VICTOR SOUSA MOREIRA[3]

Abstract

First deep-seismic soundings in Portugal were executed in 1970 and 1971. A reversed profile was recorded between Sines and Fuzeta in southern Portugal and another profile was shot parallel to the Atlantic coast (north of Lisboa) between Nazaré and Cabo Raso. The first arrivals of the profiles from Sines and Fuzeta (curve a) indicate a velocity of 6.4 km/s. On the record sections of both profiles strong secondary arrivals have been identified as reflections from the Moho. The velocity-depth function for both profiles indicate the existence of a velocity inversion between a depth of about 10 and 20 km. Beneath that zone a velocity of 7.1 km/s was found. The depth to the Moho at Sines is 30 km and at Fuzeta 34—35 km, indicating an increasing crustal thickness towards the southeast.

The first arrivals of the profile Nazaré-Cabo Raso can be devided into three parts. The first segment up to 25 km shows a velocity of about 5.0 km/s. the second portion between 25 and 55 km corresponds to a velocity of 6.3—6.4 km/s. while first arrivals between 60 and 75 km are associated with a velocity of 6.9—7.0 km/s. If this last branch corresponds to a refracted wave, the secondary arrivals between 25 and 80 km may be interpreted as wide-angle reflections. The depth to the correspondent discontinuity must be about 10 km. Reflected phases from the Moho can also be correlated but are not so well developed as in southern Portugal. They indicate a crustal thickness of about 27 km.

Following recommendations of the International Upper Mantle Committee an agreement was settled between the Serviço Meteorologico Nacional of Portugal, the Geophysical Institute of the „Univerität Frideri-

[1] Institut für Geophysik, Eidgenössische Technische Hochschule. Zürich. Switzerland

[2] Geophysikalisches Institut, Universität Fridericiana. Karlsruhe, Germany.

[3] Serviço Meteorológico Nacional. Lisboa, Portugal.

ciana" at Karlsruhe (Western Germany), the Institute of Geophysics of the „Eidgenössische Technische Hochschule at Zürich (Switzerland) and the Instituto Hidrografico da Marinha of Lisboa to initiate an extensive programme of deep-seismic sounding in Portugal. The first experiments were carried out in 1970 and 1971. Preliminary results have already been published (M e n d e s et al., 1971; M u e l l e r et al., 1971).

In figure 1 is shown the location of the profiles carried out up to now. In July 1970 the profile Sines-Azinhal was the first one to be investigated.

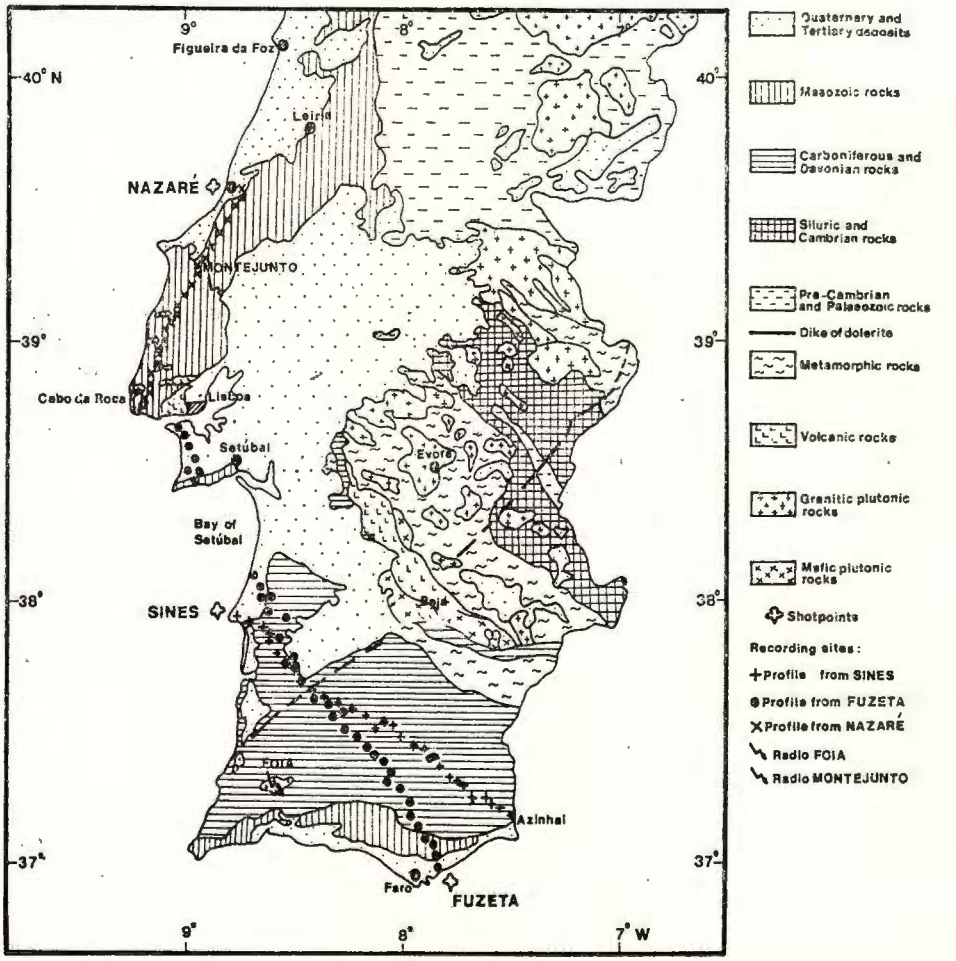

Fig. 1. — Schematic geologic map showing shotpoints, recording sites, and locations utilized for the installation of time signal transmitters.

Because of technical reasons the profile Sines-Azinhal could not be exactly reversed. To reverse this profile a new profile, Fuzeta-Cabo da Roca, was then carried out in November-December 1970. Both profiles were arranged in such a way that critical points fell in about the same distance.

Another profile along the western coast of Portugal (Nazaré-Cabo Raso) was shot in October 1971. This profile was totally reversed in October 1972. Along the profile Sines-Azinhal most of the stations were located on basement rocks of Carboniferous age, consisting generally of schists. The southeasternmost stations occupied on the first twenty kilometers of the profile Fuzeta-Cabo da Roca were located mainly on Mesozoic rocks. In the region of Sines the Paleozoic rocks are overlaid with relatively thin Pleistocene deposits.

Between 160 and 200 kilometers from the shotpoint at Fuzeta, the profile crosses the Bay of Setúbal and continues from Sesimbra to the mouth of the river Tagus and then on to Cabo da Roca. In this part of the profile most of the stations had to be placed on Quaternary deposits except the station close to Sesimbra and the two furthermost stations close to Cabo da Roca, which were located on Jurassic rocks. Along the profile Nazaré-Cabo Raso the stations were located on basement rocks of Miocene, Cretaceous, and Jurassic age.

Accurate time for all records was obtained through time signals broadcast by Radio Foia for the profiles Sines-Azinhal and Fuzeta-Cabo da Roca and Radio Montejunto for the profile Nazaré-Cabo Raso. These short wave stations (3.15 MHz) were installed on top of Mount Foia (902 m above sea level, the highest elevation in southern Portugal) and on top of Montejunto, respectively (fig. 1). The time signals were synchronized with those transmitted by the station HBG (75 kHz), located near Geneva (Switzerland). The position of the recording stations is shwon in figure 1. The average separation of the stations was about 5 km. Each station was equipped with a MARS—66 system consisting of three vertical seismometers (STROPPE FS—60 and GEOTECH S—13) operating into amplifiers whose output was recorded on magnetic tape (Berckhemer, 1970). Good efficiency of the shots in the sea was achieved by firing the charges on the sea bottom at optimum depth, generating standing waves in the water [4].

In tables 1, 2, and 3 the sizes of the charges utilized at Sines, Fuzeta, and Nazaré are listed. Demolition charges, depth charges, and torpedo

[4] Mueller St., Prodehl C., Mendes A. S., Moreira Sousa V. Crustal structure in the southwestern part of the Iberian Peninsula. 1972. (in press).

TABLE 1

List of shots near CABO de SINES, Portugal

Identification code	Date (1970)	Shot Instant (GMT)	Rectangular coordinates (km) X (UTM) Y		Geographic coordinates Latitude (N)	Geographic coordinates Longitude (W)	Water depth (m)	Charge size (kg) TNT
A	20 July	07 : 40 : 30.54	133.960	117.713	38°01'20.15''	8°53'02.35''	58	11.4
D	20 July	09 : 10 : 05.96	133.491	118.351	38°01'40.75''	8°53'21.75''	74	45.6
Z	20 July	11 : 13 : 04.91	133.740	118.571	38°01'47.95''	8°53'11.65''	75	60.0
(E)	20 July	Misfire	132.740	118.106	38°01'32.60''	8°52'52.45''	90	136.0
C	22 July	07 : 35 : 06.07	134.078	117.854	38°01'24.75''	8°52'57.55''	59	34.2
G	22 July	14 : 08 : 05.12	132.872	118.140	38°01'33.70''	8°53'47.05''	87	620.0
E	23 July	06 : 55 : 04.52	132.796	118.016	38°01'29.70''	8°53'50.15''	90	136.0
H−1	23 July	12 : 20 : 04.34	129.165	119.451	38°02'15.20''	8°56'19.50''	120	1240.0
F	27 July	07 : 07 : 03.55	132.228	118.899	38°01'58.15''	8°54'13.75''	100	272.0
H−2	27 July	09 : 30 : 05.16	131.741	118.991	38°02'01.00''	8°54'33.75''	105	1240.0

TABLE 2

List of shots near FUZETA, Portuga

Identification code	Date 1970	Shot Instant (GMT)	Rectangular coordinates (km) X (UTM) Y		Geographic coordinates Latitude (N)	Geographic coordinates Longitude (W)	Water depth (m)	Charge size (kg) TNT
B−1	30 Nov.	09 : 35 : —	237.586	4.597	37°00'17.2''	7°42'34.7''	66	22.8
D	30 Nov.	10 : 15 : 04.24	237.444	3.909	36°59'54.9''	7°42'40.6''	75	45.6
E−1	30 Nov.	11 : 08 : 03.14	238.555	2.947	36°59'23.5''	7°41'55.8''	91	136.0
C	30 Nov.	13 : 52 : 02.38	237.177	4.697	37°00'20.5''	7°42'51.2''	60	34.2
A−1	30 Nov.	15 : 10 : 01.98	236.860	4.627	37°00'18.2''	7°53'04.1''	60	11.4
B−2	1 Dec.	08 : 59 : 59.12	236.420	4.151	37°00'02.9''	7°43'21.9''	65	22.8
F−1	1 Dec.	10 : 30 : 03.27	237.488	0.660	36°58'09.5''	7°42'39.4''	104	272.0
E−2	1 Dec.	13 : 54 : 03.91	237.887	2.708	36°59'15.9''	7°42'22.9''	92.5	136.0
G	3 Dec.	10 : 25 : 04.43	238.075	0.596	36°58'07.3''	7°42'15.7''	109.5	620.0
Y	3 Dec.	15 : 04 : 29.33	237.035	0.066	36°57'50.3''	7°42'57.8''	110	756.0
X	4 Dec.	11 : 40 : 08.71	237.706	0.137	36°57'52.5''	7°42'30.7''	116	408.0
H	4 Dec.	14 : 08 : 03.80	236.622	−0.454	36°57'33.5''	7°43'14.6''	116	1240.0

heads supplied by the Portuguese Navy were used for the explosions. Portuguese war ships „São Jorge" and „Boavista" fired the shots in the sea.

TABLE 3

List of shots near NAZARÉ, Portugal

Identification code	Date 1971	Shot Instant (GMT)	Rectanguoar coordinates (km) X (UTM)	Y	Geographic coordinates Latitude (N)	Longitude (W)	Water depth (m)	Charge size (kg TNT
A—1	6 Oct.	10 : 08 : 02.24	118.108	291.973	39°35'25,7''	9°05'06.5''	56	11.4
B—1	6 Oct.	11 :00 : 00.04	118.111	292.030	39°35'27.5''	9°05'06.5''	66	22.8
E—1	6 Oct.	14 : 22. : 59.85	117.371	291.619	39°35'13.9''	9°05'37.4''	89	136.0
A—2	6 Oct.	15 : 00 : 01.05	117.111	291.569	39°35'12.2''	9°05'48.2''	94	11.4
A—3	7 Oct.	09 : 09 : 29.73	118.125	292.021	39°35'27.2''	9°05'05.9''	58	11.4
E—2	7 Oct.	11 : 07 : 59.82	117.946	292.164	39°35'31.8''	9°05'13.5''	115	136.0
F	7 Oct.	14 : 35 : 02.74	117.864	291.932	39°35'24.4''	9°05'16.9''	120	272.0
A—4	7 Oct.	15 : 09 : 59.99	117.797	292.059	39°35'28.3''	9°05'19.7''	140	11.4
B—2	10 Oct.	11 : 19 : 59.71	118.042	292.118	39°35'30.3''	9°05'09.5''	68	22.8
E—3	10 Oct.	12 : 08 : 31.11	117.774	291.906	39°35'23.4''	9°05'20.6''	95	136.0
B—3	11 Oct.	08 : 34 : 00.84	118.396	291.961	39°35'25.4''	9°04'54.6''	54	22.8
E—4	11 Oct.	09 : 24 :59.92	117.257	291.608	39°35'13.5''	9°05'42.1''	65	136.0

In figure 2 the P-wave record section with correlations for the profile Sines-Azinhal is shown. The first arrivals (curve a) lie on a straight line showing a velocity of 6.4 km/s. P_n arrivals (curve d) can be correlated at the end of the profile. They show an apparent velocity of 8.0 km/s. Strong reflections P_MP from the Moho (curve c) can be observed beyond 65 km. Phases which are identified as reflections from intermediate layers can also be correlated (curves a—b and b).

In figure 3 the P-wave record section for the profile Fuzeta-Cabo da Roca is shown with correlations. The first arrivals up to 20 km show average velocities of 4.3 km/s. Between 20 and 90 km the first arrivals (curve a) lie on a straight line associated with a velocity of 6.4 km/s. The P_n arrivals (curve d) can again be correlated at the end of the profile beyond 150 km. They show an apparent velocity of 8.3 km/s. Strong reflections P_MP from the Moho (curve c) can be observed beyond 65 km. Phases which can be identified as reflections form intermediate layers within the crust can also be correlated (curves a—b and b). These phases can be clearly seen in the record section of the profile Sines-Azinhal, but are not so well developed in the record section of the profile Fuzeta-Cabo da Roca.

The Herglotz-Wiechert and Giese methods (Giese, 1966) have been used to derive starting models for the velocity-depth

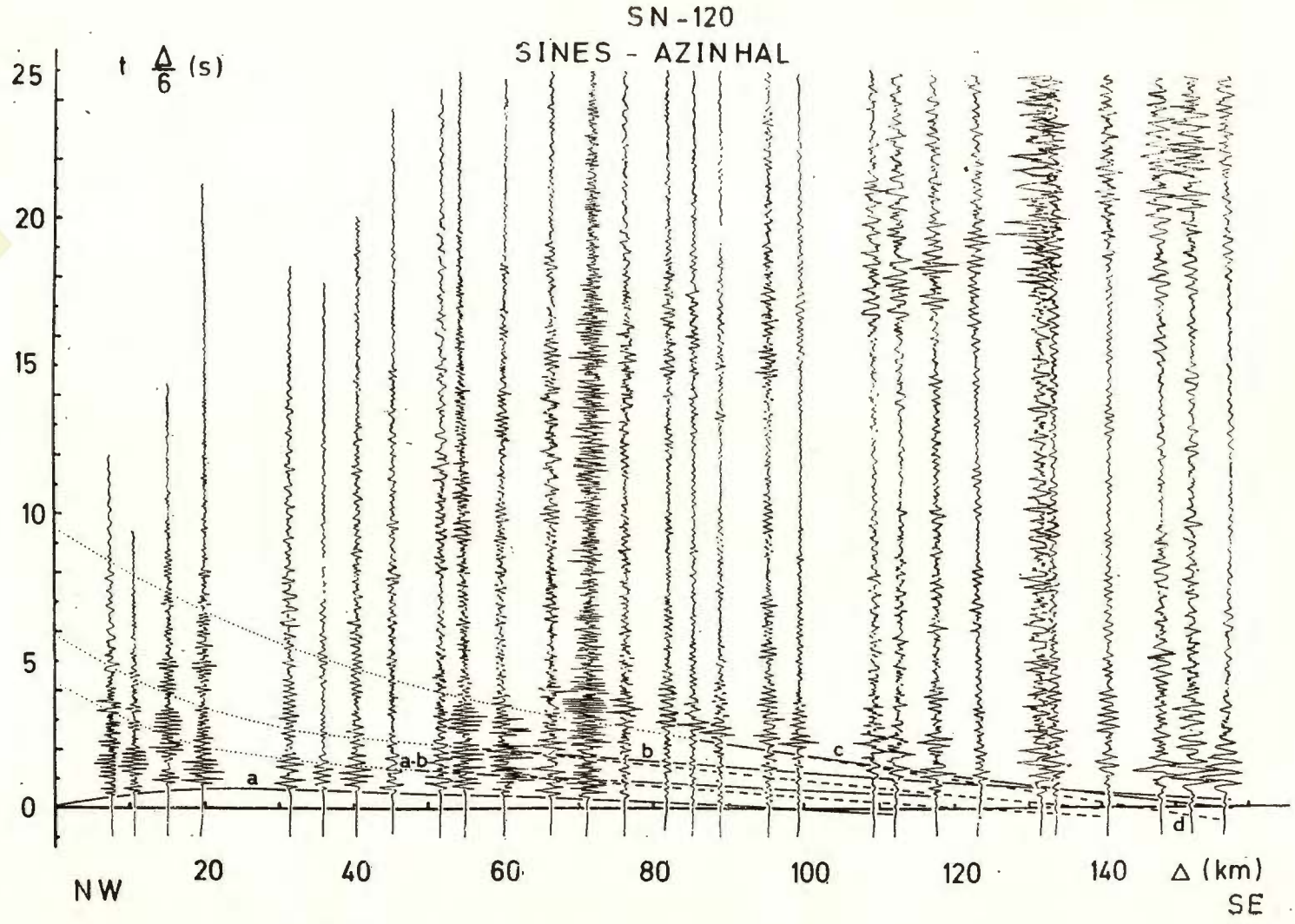

Fig. 2. — *P* wave record section with correlations for the profile Sines-Azinhal.

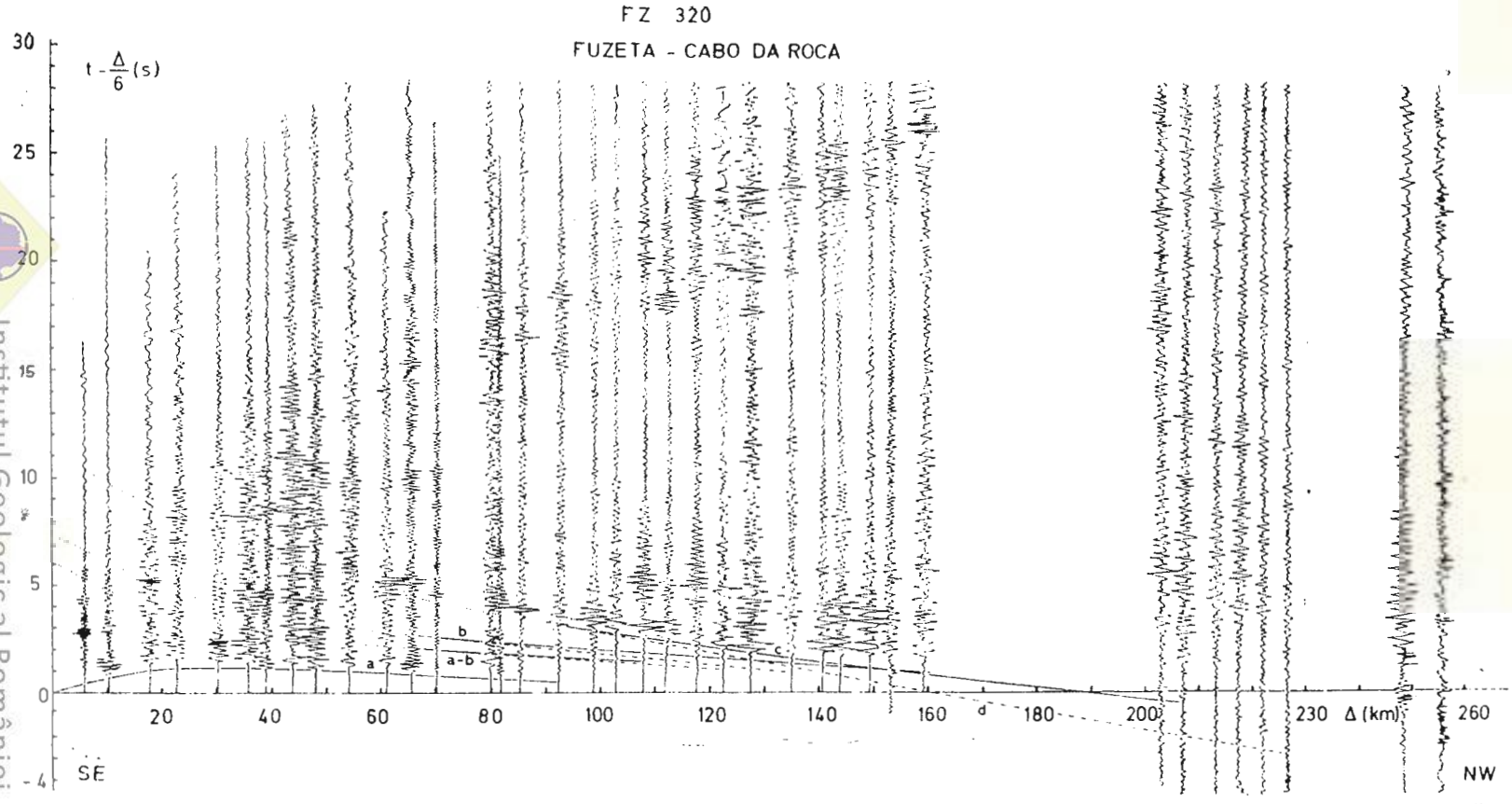

Fig. 3. — *P*-wave record section with correlations for the profile Fuzeta-Cabo da Roca.

function (fig. 4). The models obtained by this procedure were corrected using a method developed by K. Fuchs and G. Müllller (Karlsruhe) for calculating theoretical travel-times. Applying the Herglotz-Wiechert method to the first arrivals of the profile Sines-Azinhal, a velocity distri-

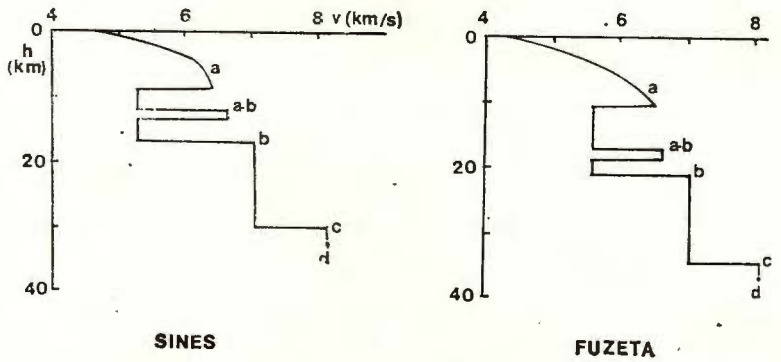

Fig. 4. — Velocity-depth functions for the profiles Sines-Azinhal and Fuzeta-Cabo da Roca. The segments a, a—b, c, and d correspond to the travel-time branches in figures 2 and 3.

bution was obtained where the velocity increases gradually from 4.40 km/s at the surface to 6.20 km/s at 5 km depth, and then more rapidly up to 6.45 km/s at 9 km depth. For the profile Fuzeta-Cabo da Roca the velocity increases from 4.25 km/s at the surface to 6.55 km/s at a depth of 10 km.

The disappearence of the travel-time branch a in both profiles at distances beyond 100 km is explained by a low-velocity zone between about 10 and 20 km depth. For the profile Sines-Azinhal the velocity decreases in this low-velocity layer from about 6.5 km/s to 5.3 km/s, and from about 6.5 km/s to 5.6 km/s for the profile Fuzeta-Cabo da Roca. The thickness of this inversion zone is about 7 km to the southeast of Sines and about 10 km to the northwest of Fuzeta. The travel-time curve a—b which appears in both sections indicates a subdivision of the low-velocity zone represented by a 1.5 km thick layer where the velocity of P-waves is 6.7 km/s (pseudo-laminated structure). Below the low-velocity zone a distinct layer with a velocity of 7.07 km/s was found. The depth to the Moho at Sines is 30.0 km, and at Fuzeta 34.5 km indicating that the thickness of the crust increases towards the southeast. The true velocity in the uppermost mantle just below the Moho is 8.15 km/s. In figure 5 a schematic crustal cross-section between Sines and Fuzeta is shown.

In figure 6 the *P*-wave record section with correlations is shown for the profile Nazaré-Cabo Raso.

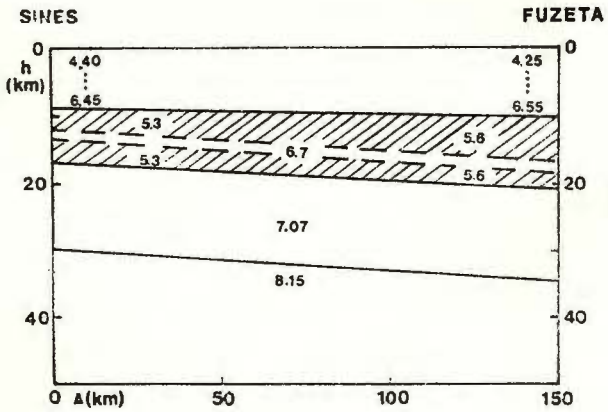

Fig. 5. — Crustal cross section between Sines and Fuzeta in southern Portugal. Velocities are given in km/s.

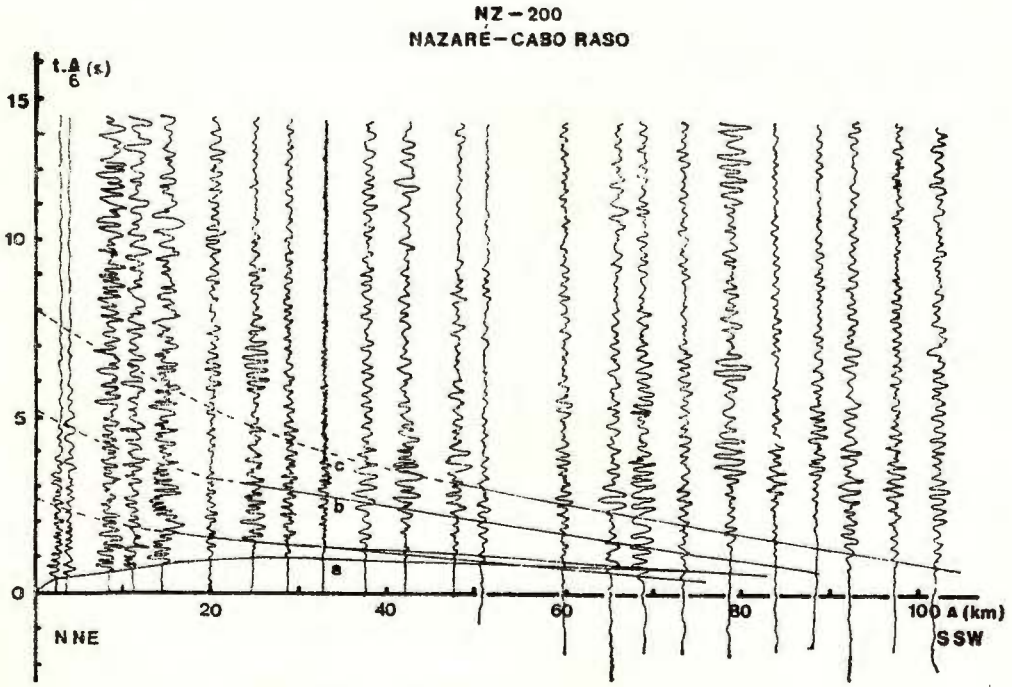

Fig. 6. — *P*-wave record section with correlations for the profile Nazaré-Cabo Raso.

The first arrivals of the profile Nazaré-Cabo Raso can be devided into three parts. The first segment up to 25 km shows a velocity of about 5.0 km/s, the second portion between 25 and 55 km corresponds to a velocity of 6.3—6.4 km/s, while first arrivals between 60 and 75 km are associated with a velocity of 6.9—7.0 km/s. If this last branch corresponds to

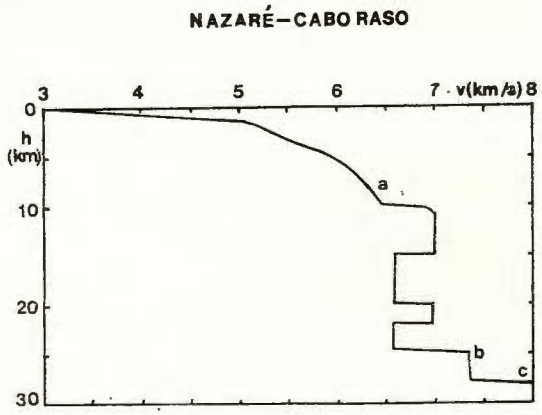

Fig. 7. — First approximation of the velocity-depth function for the profile Nazaré-CaboRaso.

a refracted wave, the secondary arrivals between 25 and 80 km may be interpreted as wide-angle reflections. The depth to the corresponding discontinuity must be about 10 km.

A phase *b* corresponding to a reflection from an intermediate layer in the lower crust can be correlated and phase *c* probably corresponding to a reflection from the Moho can be traced too, but these phases are not so well developed as those obtained for the record sections of southern Portugal. The first approximation of the velocity-depth function which required the insertion section of a low-velocity zone, is presented in figure 7. From this preliminary velocity-depth it seems that the crustal thickness in the region between Nazaré and Cabo Raso is about 27 km. This profile has been reversed in October 1972. A number of shots were fired off Cabo Raso and the observations were carried out along a profile up to Figueira da Foz, that is for a distance of about 200 km from the shotpoint. The results of the interpretation for this profile will be published later in another paper.

REFERENCES

Berckhemer H. (1970) MARS 66—A magnetic tape recording equipment for deep-seismic souding. *Z. Geophysik*, 36, Würzburg.

Giese P. (1968) Versuch einer Gliederung der Erdkruste im nördlichen Alpenvorland, in den Ostalpen und in Teilen der Westalpen mit Hilfe charakteristischer Refraktions-Laufzeit-

kurven sowie eine geologische Deutung. Inst f. Meteorol. und Geophysik d. FU Berlin.*Geophys. Abh.*, I, 2, Berlin.

Mendes A. S., Moreira V. S., Mueller St., Prodehl C. (1971) A estrutura da crosta terrestre no sudoeste da Peninsula Ibérica. *Proceedings* 1 st Cong. Hispano-Luso-Americano de Geologia Económica, 6 (*Geofisica, Geologia e Geologia Submarina*, Lisboa and Madrid.

Mueller St., Mendes A. S., Prodehl C., Moreira V. S. (1971) Preliminary report of the first deep-seismic sounding experiments in the Iberian Peninsula. Observatoire Royal de Belgique *Communications*. Ser. A. 13 (Sér. Géophysique, 101, Brussels).

EASTERN EUROPE

SEISMIC STRUCTURE OF THE MOHO DISCONTINUITY IN THE REGION OF THE FORE-SUDETIC MONOCLINE

BY

A. GUTERCH, R. MATERZOK, J. PAJCHEL[1]

Abstract

Seismic studies of the Earth's crust carried out along international profile VII by means of explosion seismology have revealed the existence of seismic discontinuities of 7.9 km/s and 8.2 km/s in the deep basement of the Earth's crust in the region of the fore-Sudetic monocline. The approximate depth of the 7.9 km/s discontinuity is 30 km, while that of the 8.2 km/s discontinuity varies from 34 to 38.5km. Recorded were the refracted and the well-separated reflected waves. Probably, these two discontinuities determine the upper and lower boundary of the transition zone between the crust and the upper mantle. The thickness of the transition zone defined in this manner changes along the profile from 4 to 8.5 km, locally reaching 12—13 km. Dynamic properties of the reflected waves indicate that the 7.9 km/s discontinuity is sharp in the majority of cases while the 8.2 km/s discontinuity is of diffusion or layer-diffusion nature.

INTRODUCTION

The deep seismic soundings project for Central and Southeastern Europe contained also seismic measurements along international profile VII. This profile runs through Poland and Czechoslovakia. Its location is shown in figure 1. On the territory of Poland its length is 520 km. Until 1972 the measurements planned were completed in about 90 %.

[1] Institute of Geophysics, Polish Academy of Sciences, Warszawa 22, ul. Pasteura 3, Poland.

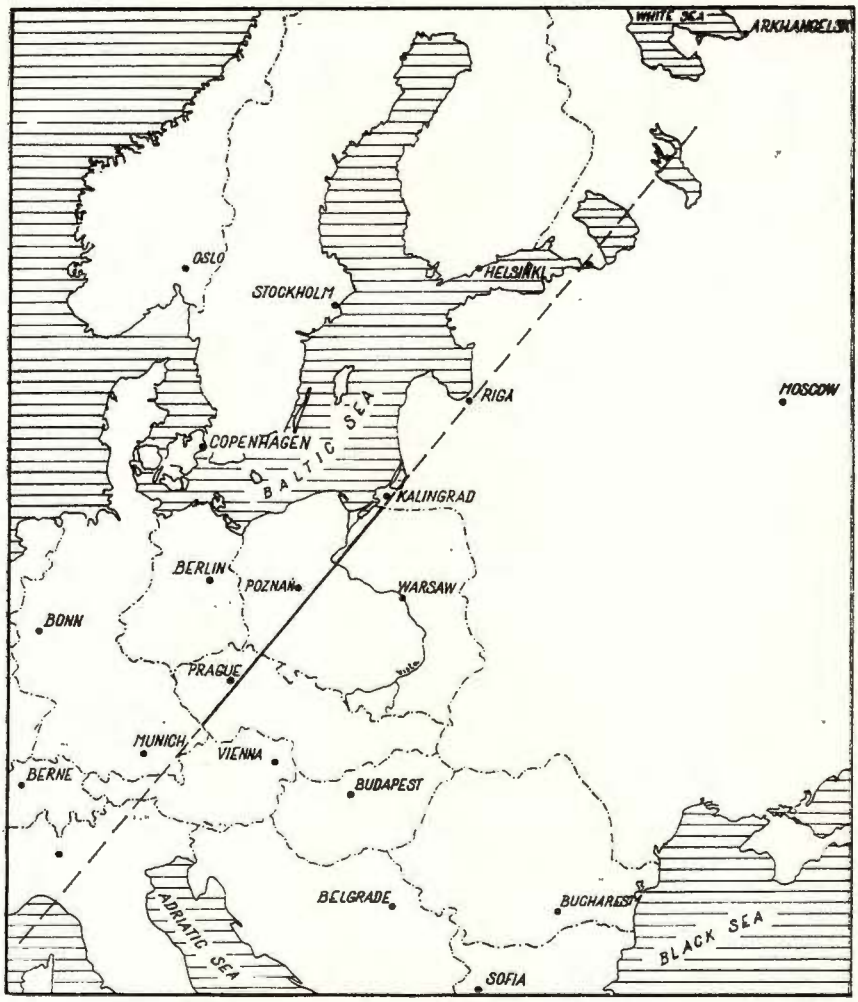

Fig. 1. Location of the international profile VII

Seismic observations were carried out by means of continuous longitudinal profiling to a distance of about 180 to 200 km from shot point. The distances between shot points were about 60—90 km. In the region of the Polish-Czechslovakia border the measurements were made in cooperation between the Institute of Geophysics in Brno and the Institute of Geophysics of Polish Academy of Sciences in Warsaw. The recordings were carried out by means of low-frequency, 6-channel and 24-channel seismic

refraction apparates. Vertical geophones with a frequency of about 2.3 Hz were used. The distances between geophones were 100 or 200 m.

These measurements were supplemented by point observations made by means of 1—Hz vertical and horizontal seismographs with a dynamic amplification of 200 000. The purpose of these point observations was to make a dynamic checking of amplitudes of the waves reflected from the Moho discontinuity in the range of distances from 60 km to 120 km.

GEOLOGICAL SITUATION

On the territory of Poland international profile VII intersects the following three great tectonic units :

1. Precambrian platform of East Europe
2. Paleozoic mountain helts (Caledonides and Variscides), represented on profile VII by the West Sudetes
3. Paleozoic platform of Central and Western Europe

The fore-Sudetic monocline, which is intersected by profile VII, is part of the Paleozoic platform.

SEISMIC STRUCTURE OF THE EARTH'S CRUST BASEMENT

The diagram of crustal structure in the fore-Sudetic monocline region is shown in figure 2. The interpretation of the crustal structure in that region is based exclusively on the data obtained in the years 1970 and 1971. The extensive material obtained in 1972 has not been taken into account yet.

In the region of the fore-Sudetic monocline, two distinct discontinuities, of 7.9 km/s and 8.2 km/s, were determined in the Earth's crust basement. Their depths are 30 km and 34—38.5 km, respectively. Each of them could be regarded as the lower boundary of the Earth's crust. The subcritical and overcritical reflected waves from both discontinuities were recorded very distinctly. In most cases those waves were so well-separated that it would be impossible not to interpret them as independent reflections, in spite of small time differences between them. The interpretation of the structure of the whole Moho-discontinuity zone was based primarily on the reflected waves. In the central part of the profile the 8.2 km/s discontinuity splits into two boundaries. Moreover, about 5 km underneath the 8.2 km/s discontinuity, at depths from 40 to 43 km, there probably exists another discontinuity which produces the weak reflected waves.

The amplitudes of the refracted waves were small. The 7.9 km/s refracted wave was recorded in first arrivals already at a distance of 135 km

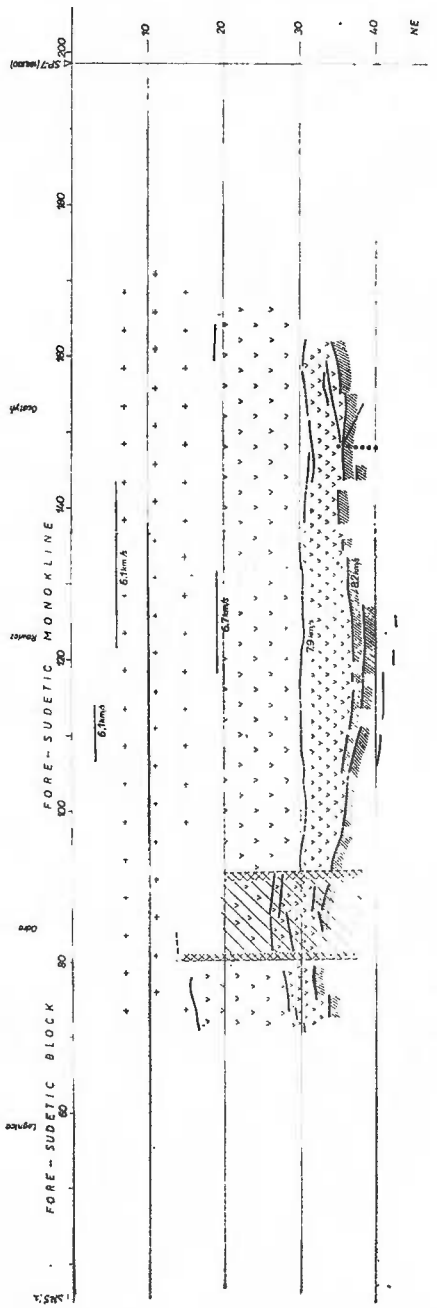

Fig. 2. Diagram of crustal structure in the region of the fore-Sudetic monocline

from the shot point. Later arrivals of refracted waves with a velocity of 8.2 km/s were about 0.3 to 0.2 s delayed in respect to the 7.9 km/s waves. For the central part of the profile, both refracted waves were well-separated. It was, however, much more difficult, or even impossible, to interpret these waves in the southern end of the profile, where they were usually recorded only in fragments.

Examples of records of the reflected waves are shown in figure 3 (a, b, c).

The continuity of travel-time curves enabled us to make a relatively precise correlation of the waves reflected from both discontinuity zones (7.9 km/s and 8.2 km/s). Fading of some phases and the appearence of new ones were observed, notably for the 8.2 km/s discontinuity zone. Therefore, the 8.2 km/s seismic boundary (fig. 2) has a discontinuous and layered nature, which is a consequence of the interpretation of consecutively appearing and fading phases.

The results presented were obtained by means of various methods used to determine mean velocities and the morphology of boundaries. Moreover, the results were tested by model calculations. One of very probable model solutions allows for the existence of a velocity inversion in the upper part of the litosphere, at a depth of about 10—18 km.

In the soutern part of the presented section of the Earth's crust exists a deep fracture, which attains a width of 10—12 km in the Moho discontinuity zone, and is likely to reach the lower lithosphere. The deep fracture zone has a very complex structure. In the region where deep fracture occurs the Moho discontinuity (more precisely the Moho discontinuity zone) is vague and difficult to determine. The diffraction-type waves are observed on seismic records. Recorded were also series of waves with great amplitudes and great apparent velocities, which were interpreted as the waves reflected from local discontinuities occuring in the deep fracture zone, clearly above the Moho discontinuity. The occurence of those local seismic discontinuities producing strong reflected waves maked it possible to believe that the intrusion of a material from the upper mantle into the crust have taken place. In such a case it is impossible to determine precisely the Moho discontinuity in the deep fracture region. The determined deep fracture corresponds to the location of the so-called "Odra fault" which is wellknown in geology. The "Odra fault" separates the fore-Sudetic block from the fore-Sudetic monocline.

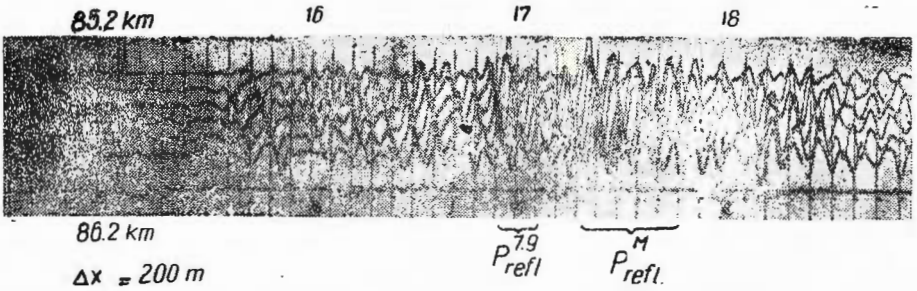

a

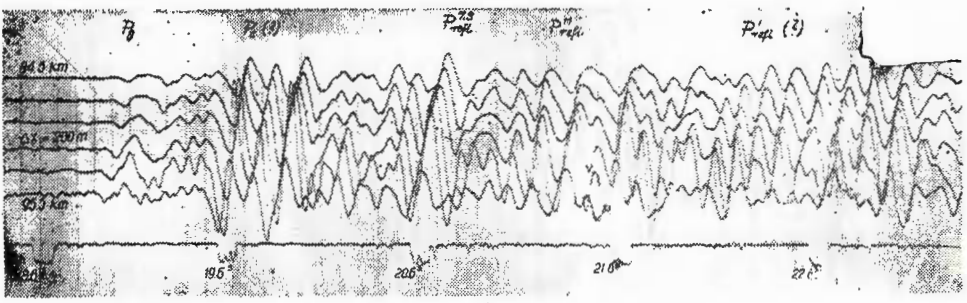

b

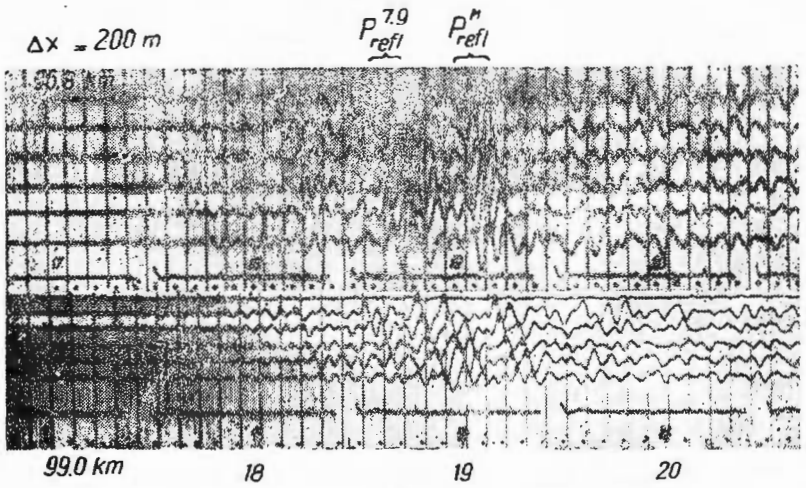

c

Fig. 3. Examples of records of the reflected waves.

a) $P^{7.9}_{refl}$, reflected wave from 7.9 km/s discontinuity; P^{M}_{refl} , reflected wave from 8.2 km/s discontinuity;

b) $P^{7.9}_{refl}$, reflected wave from 7.9km/s discontinuity; P^{M}_{refl} , reflected wave from 8.2 km/s discontinuity; P^{1}_{refl} , reflected wave from boundary beneath the 8.2 km/s discontinuity.

c) $P^{7.9}_{refl}$, reflected wave from 7.9 km/s discontinuity; P^{M}_{refl} , reflected wave from 8.2 km/s discontinuity.

DISCUSSION OF THE RESULTS

The determined seismic discontinuities of 7.9 and 8.2 km/s are likely to be the upper and lower boundaries of the transition zone between the crust and upper mantle of the Earth. In such a case, the thickness of the transition zone changes along the profile from about 4 km to 8.5 km. The amplitudes of the waves reflected from the both discontinuity zones were, in average, of the same order. Qualitative, model-amplitude interpretation of the observed properties of the reflected waves suggests that considerable amount of the total density change should be connected with the 8.2 km/s discontinuity (G u t e r c h , 1970). This may explain the observed fact that the 8.2 km/s discontinuity is not masked by the 7.9 km one which is greater. The hight amplitudes of the reflected waves from the 8.2 km/s discontinuity can also be explained by the model with velocity reversals, proposed by F u c h s (1969) in his studies of the transition zone between crust and upper mantle. Short, usually 2 or 3-phase recordings of the waves reflected from the 7.9 km/s discontinuity suggest that this discontinuity is sharp. The 8.2 km/s discontinuity, however, is rather of a diffuse or "layered-diffuse" nature. The "layered-diffuse" properties of the 8.2 km/s boundary (i.e. of the lower boundary of the transition zone between crust and upper mantle) are confirmed by : *a*) usually multiphase nature of the recording of reflected waves, *b*) comparison of depth values obtained from the interpretation of the reflected and refracted waves — the refraction depths are about 1—1.5 km greater than the reflection depths, *c*) split of this boundary and its discontinuous nature, notably in the central part of the described section of the crust, *d*) appearence of a discontinuity fragments below this boundary, at depths of about 40—43 km, so that the thickness of the transition zone increases there to about 12—13 km.

The nature of the 7.9 and 8.2 km/s discontinuities is somewhat more complicated than its general pattern described above. It was found that the arrivals of both reflected waves may locally join together to form one large wave packet with an extent of about 1 s or more. On few seismograms were also distinctly noted short, 2—3 phase recordings of both reflected waves (fig. 3c). In this case both discontinuities corresponding to them should be sharp. In general however, the 8.2 km/s discontinuity of is "diffuse-layered" nature, while the 7.9 km/s one represents sharp change in velocity (fig. 3a, b).

Determination of the relationship between the seismic and the petrological structure of the transition zone between crust and upper mantle is now of fundamental importance. In the recent years many authors

inclied toward the hypotheses that in some regions the Moho discontinuity can be represented by a phase transition, most generally assuming it to be of a basalt-eclogite type. Those hypotheses were based on experimental petrology data (Yoder, Tilley, 1962; Ringwood, Green 1966). Several serious arguments against the above-mentioned hypotheses have also been pointed out.

Ito and Kennedy (1970, 1971) have shown exactly that the basalt-eclogite transition occurs in two sharp steps, from basalt to garnet granulite and from garnet granulite to eclogite. This basalt-eclogite transition occurs at pressures which are equivalent to the depths of the lower crust and uppermost mantle. The two-step sharp transition ought to produce sharp seismic discontinuities in the lower crust and upper mantle. In general, the petrological interpretation of seismic data on the deep structure of the crust is still very difficult. Nevertheless, we think that the petrological structure of the transition zone between the crust and the upper mantle described above can be relatively close to the explanation given by G. C. Kennedy (see discussion in paper Gangi and Lamping, 1971): "*A sodic basalt gives two sharp transitions in density and velocity: the first where garnet comes in with a velocity jump to 7.5 km/s and the second where the jadeitic feldspar comes in with a velocity jump to 8.1 or 8.2 km/s. If the basalt is not sodic the second step may be masked. The second step may be either sharp or diffuse, depending on the soda content of the basalt. The first transition will occur at the order of 20 to 25 km depth; the second, at 40 to 50, may be as shallow as 35 km depending on the temperature*".

In the seismic experiment described above, the first discontinuity is sharp, while the second has a diffuse or "layered-diffuse" nature. The thickness of the transition zone varies from 5 to 8.5 km, increasing locally to 12—13 km. The thickness of a transition zone depends on temperature. The smaller thickness of the transition zone in the region of fore-Sudetic monocline as compared to Kennedy's data may be explained by the fact that the surface heat flow in that region is higher amounting to about 1.72 μcal/cm²/s (Plewa, 1967).

For example, Lubimova (1966) has shown that the temperatures on the Moho boundary for the regions with low (0.6—0.9 μcal/cm²/s), normal (1.1—1.4μcal/cm²/s) and anomal high (1.8—3.0 cal/cm²/s) heat flow can be about 400°, 650° and 1 000°, respectively. Undoubtedly, the substantial differences in thermodynamical conditions prevailing in the Moho discontinuity zone in various regions have clearly affected the formation of seismic parameters in the basement of the Earth's crust.

REFERENCES

Fuchs K. (1969) On the properties of deep crustal reflectors. *Z. Geophys.*, 35, Würzburg.

Gangi A. F., Lamping N. E. (1971) An in situ method of determining the pressure dependence of phase-transition temperatures in the crust. *In* : The Structure and Physical Properties of the Earth's Crust, *Geophys. Monogr.*, 14, ed. J. G. Heacock, Washington.

Guterch A. (1970) Kinematics and dynamics of seismic waves in selected heterogeneously stratified models of the continental Earth's crust. *Publ. Inst. Geophys. Pol. Acad. Sci.*, 39.

Ito K., Kennedy G. C. (1970) The fine structure of the basalt-eclogite transition. *Mineral. Soc. Amer. Spec. Pap.*, 3,

— K., Kennedy G. C. (1971) An experimental study of the basalt-garnet granulite-eclogite transition. *In* : The Structure and Physical Properties of the Earth's Crust, *Geophys. Monogr.*, 14, ed. J. G. Heacock Washington.

Lubimova E. A. (1966) The distribution on the heat flow and thermal processes in the Earth's mantle (in Russian). *Astron. Zhurn.* 43, 4, Moskva.

Plewa S. (1967) Measurement results of the surface heat flow on the Polish territory. *In* : Selected Problems of Upper Mantle Investigations in Poland, *Publ. Inst. Geophys. Pol. Acad. Sci.*, 14.

Ringwood A. E., Green D. H. (1966) An experimental investigations of the gabbro-eclogite transformation and some geophysical implications. *Tectonophysics*, 3, Amsterdam.

Yoder H. S., Tilley C. E. (1962). Origin of basalt magmas : an experimental study of natural and synthetic rock systems. *J. Petrl.*, 3, London.

Redactor : MARGARETA PELTZ
Tehnoredactori și corectori : ELEONORA SPANOCHE, LIVIA DIACONU
Ilustrația : V. NITU

Dat la cules : dec. 1973, Bun de tipar : aprilie 1974. Tiraj : 900 ex. Hîrtie scris I.A. Format 70 × 100/56 g. Coli de tipar : 22,5 Pentru bibliotecă indicele de clasificare 55 (058).

Tiparul executat la Întreprinderea poligrafică „Informația".
str. Brezoianu nr. 23–25. București – România.